Microcanonical Rates of Unimolecular Reactions Studied by Time-Resolved Photofragment Spectroscopy

Thesis by

Lutfur Rahman Khundkar

In Partial Fulfillment of the Requirements
for the Degree of
Doctor of Philosophy

California Institute of Technology
Pasadena, California
1988

(Submitted May 6, 1988)

To the memory of my parents, whose dreams are mine

Acknowledgements

My life, and therefore the work embodied by this thesis, has been touched and shaped by numerous individuals, some of whom deserve special mention.

First, I thank my family for their unfailing love, the dreams they inspired and the sacrifices thay made for me. I regret that I cannot share with them the thrill of reaching this milestone, especially since I owe everything to their selflessness.

I thank my research advisor, Ahmed H. Zewail, for sharing his experience, enthusiasm and scientific insight. His instinct for devising interesting research problems and his demand for a simple interpretation of all results is inimitable. I would like to express my appreciation for the many long hours he must spend in keeping the research machinery running smoothly and the whole operation generously funded. I must also thank him for the tolerance he has shown toward my own idiosyncrasies. I feel I have grown tremendously through this experience.

Among the many members of the research group, past and present, the two persons who have taught me the most about day-to-day research are Joseph Knee and Norbert Scherer. Dr. Knee's deep interest in experiments, often masked by his easy-going manner, and his patience in teaching a beginning graduate student all the tricks of the trade with zero condescension will be a source of inspiration for me in the years to come. Norbert Scherer, whose company I have enjoyed over countless cups of coffee and dinner platters, has taught me patience and commitment by example. I have learned much about current technology by tapping his fund of knowledge. The comradeship that developed between us over the long lunches at the Athenaeum, the timeless hours in the laboratory, and the late night coffee runs, is something I will miss sorely.

The friendliness and good cheer that the staff members have shown toward me and my demands is also greatly appreciated. Without our favorite Fran Bennett smilingly taking care of the endless stream of requests for URGENT purchase orders, Tom Dunn of the 'One Stop Electronics Repair Shop' and the jocular crowd in the machine/instrument shop, my graduate career would have been considerably longer and more tedious.

I owe a great debt of gratitude to the members of the Caltech community who, through their good humor, have made this experience worthwhile. In particular, Edward Sleva, Jack Syage, Fuad Doany, Paul Hipes and Todd Rose provided moral support in time of crisis by sharing the wisdom of their own experiences. Their distinctive approaches to science and life, and the many discussions about mind, matter and style have enriched me. The two younger members of the group, Chris Sipes and Amy Hoffman, who I have had the opportunity to interact and share expertise with, deserve special thanks for their assistance and comradeship. The newest member, Dr. Jack Breen, who had the luck to inherit the desk next to mine, also deserves thanks for proof reading and assistance in assembling this document.

My debt to Susan is incalculable. When jaded in spirit and at odds with myself I seek solace, she revives my spirits. Without her constant affection, I would accomplish little.

ABSTRACT

The use of modern technology in the study of classic problems in chemistry has afforded researchers the opportunity to understand the dynamics of reactions on a molecular level. This thesis represents one such instance, where the combination of pulsed lasers and molecular beams has made the study of ultrafast reactions of isolated molecules possible.

The optical technique is, in essence, a two pulse pump-probe method. One of the pulses resonantly excites the molecule to be studied, while the second one, delayed in time, measures the population in either the excited parent state or some quantum state of the product. The sample is cooled in a supersonic expansion and observed under collisionless conditions. Atomic and molecular species may be detected by laser-induced fluorescence (LIF) or resonantly-enhanced multiphoton ionization (REMPI), followed by mass-selective detection. The temporal evolution of the state being probed is mapped out as the delay between the pulses is varied. The resolution of this method is determined by the temporal widths of the two pulses, typically $\sim$ 8 picoseconds in the studies presented here.

The technique, termed Time-Resolved Photofragment Spectroscopy (TRPS), has been used to study a number of unimolecular reactions under collisionless conditions. Microcanonical rates of the reaction $NCNO \longrightarrow CN + NO$ have been measured for excitation energies near threshold. The rates are compared with predictions of various statistical theories, including a recently proposed variational method. State-selected studies of the production of iodine atoms in the UV photodissociation of $1,2-$ diiodotetrafluoroethane indicate the existence of a bound intermediate, the iodoperfluoroethyl radical. Energy dependent rates show that the amount of internal energy in the intermediate may be varied by changing excitation conditions, thereby affecting the rate of its decomposition. Time and frequency-resolved studies of the photodissociation of methyl iodide show evidence that perturbed species in a dissociating system (so-called *transition-state* species) may be observed by this technique.

CONTENTS

1.	**Introduction**	1
2.	**Kinetic model for pump-probe experiments**	9
2.1	Description of the model	10
2.2	Solution of the rate equations	12
2.3	Application of the model to experiments	19
2.4	Discussion	22
2.5	References	25
	Figures	27
3.	**Experimental**	34
3.1	Two-color picosecond laser system	35
3.2	The molecular beam apparatus	38
3.3	Detection methods	39
3.4	Data acquisition and analysis	42
3.5	References	43
	Figures	45
4.	**Statistical theories of unimolecular reactions theory**	50
4.1	The Statistical Rate Expressions	52
4.2	Models for rate calculations	55
4.3	References	60
5.	**Time-Resolved Photofragment Spectroscopy. I**	62
A	Picosecond Photofragment Spectroscopy: I. Microcanonical State-to-State rates of the reaction $NCNO \longrightarrow CN + NO$	63
B	RRKM Theory of Flexible Transition States Applied to the Dissociation of NCNO	83
6.	**Time-Resolved Photofragment Spectroscopy. II** Dissociation dynamics of 1,2-diiodotetrafluoroethane	110
6.1	Introduction	111
6.2	Experimental	113
6.3	Results and Discussion	115
6.4	Conclusions	128
6.5	References	129
	Figures	133

7. Observation of intra-collision processes by time- and frequency domain measurements 140

A Picosecond MPI Mass Spectrometry of CH_3I in the process of dissociation 141

B Time- and frequency-dependent absorption spectra of transition states 148

Appendices 171

I Picosecond Photofragment Spectroscopy: III. Vibrational predissociation of van der Waals clusters 172

II Real-time picosecond clocking of the collision complex in a bimolecular reaction: The birth of OH from H + CO_2 185

III Computer program for calculating density of states 189

IV Computer program for calculating PST rates 194

CHAPTER I

INTRODUCTION

The rate of a chemical transformation has been a topic of much interest since the late twentieth century. The length of the period over which this field has remained active attests to its significance. The oldest surviving theory, that of Arrhenius, is a phenomenological description of the temperature dependence of rates of reactions in bulk. The activated complex theory (also referred to as absolute rate theory or transition state theory) postulated more than fifty years ago, provides an useful interpretation of the Arrhenius rate law in terms of molecular properties. The concept of reactions as flux through a hypothetical surface in phase space, the basic idea of transition state theory, is still in vogue.

The questions asked by contemporary kineticists deal with an interpretation of reactivity on a molecular level. The goal of their studies is the detailed understanding of how initial conditions affect the outcome of a chemical reaction. Initial conditions refer to the partitioning of energy in the activation process between the various degrees of freedom (electronic, vibrational, rotational and translational) as well as the structure of the reactant. The outcome must also be specified in quantum detail. In addition to determining the disposal of energy, one desires to know how fast the transition between reactants and products occur, and how the magnitudes of these rates are affected by initial conditions.

Experimental studies of reaction rates thus face the challenge of defining these conditions precisely, as well as the detection of products with quantum state resolution. The two technological advances that have revolutionized experimental chemical kinetics are (i) the adaptation of supersonic molecular beams, and (ii) the invention of the laser. The molecular beam, although used by physicists in the early 1900's, had been neglected by chemists until the 50's. This method allows one to study atomic and molecular processes in the absence of collisions, or under single collision conditions. An added advantage to their use in studying reactivity is that the internal motions of the molecules are quenched during the expansion and the final ensemble on which experiments are performed is approximately a microcanonical one. The application of lasers to molecular spectroscopy followed closely

on the heels of their invention. Lasers, as intense, directed sources of monochromatic light, are sensitive probes of molecular quantum states. The broad range of tunability offered by dye lasers makes selective detection of most organic molecules possible. Their application in reaction dynamics therefore appears as a simple logical step in the development of this field. A combination of lasers and molecular beams has provided an opportunity for us to experimentally verify fundamental issues of reactivity.

The pioneering work of Herschbach and his contemporaries ushered in the era of crossed molecular beam studies.[1–3] Their experiments have now firmly established that chemical reactions may be described in terms of a collision between reactant species. The essential measurements in a crossed beam experiment are the angular and kinetic energy distributions of products from a single collision between reactant species. The analysis of these distributions leads to differential and absolute cross-sections and allows one to deduce the mechanism of the reaction.[4] These elementary mechanisms are categorized as being either *direct* or *complex* mode, the latter meaning that an intermediate species, the collision-complex, is involved. Crude estimates of the lifetime of these complexes may be derived from the measured angular distributions. This technique is best suited for measuring post-collision observables. The impact energy, a pre-collision parameter, may be varied over a small range using velocity selectors. Inhomogeneous fields may be used to select particular quantum states, e.g. specific rotational states, preferentially over others.[4]

The use of lasers in the field of kinetics is widespread. The technique of photofragment spectroscopy[5,6] , developed in the 70's, is a crossed-beam experiment closely related to the one mentioned above, where a photon beam (laser) replaces one of the molecular beams. The method studies so-called 'half-collision' reactions; namely, unimolecular dissociations. The quantities measured are the same — angular and translational energy distributions of products. One advantage of this method is that the initial energy may be varied over a much wider range and with greater resolution.

In the wake of chemiluminescence and infra-red fluorescence studies of vibrationally excited products of reactions[3] , the more sensitive technique of laser-induced fluorescence (LIF) has proved to be the method of choice for studying nascent product state distributions.[7] The two-beam method can be augmented by a third beam, one of photons, which acts as a sensitive probe of the internal states of the products. One of them, the photolysis laser, prepares the system in a metastable state which decays with a characteristic lifetime. The detection laser, a tunable dye laser for instance, is used to record the spectrum of products from which the nascent population distribution is derived. In addition to state distributions, angular distributions may also be crudely determined by measurements of the polarization anisotropy.[8] Translational energy distributions associated with each resolvable product quantum state may be obtained indirectly from measurements of the Doppler profile of the absorption lines.[9]

The use of lasers in studying reaction rates require a prior understanding of the nature of matter-radiation interaction and the influence of other intramolecular processes.[10] How well one can define initial conditions following optical excitation is determined by the rate of the photophysical processes involved, such as intramolecular vibrational redistribution (IVR)[11,12] , internal conversion or intersystem crossing. If the rate of reaction is intrinsically faster than the rate of energy redistribution, then one would expect the outcome of the reaction to be deterministic — initial state influences both rates and product distributions. This question is related to the validity of ergodicity in highly energized, isolated molecules[13] , i.e., whether time-averaged behavior is indeed equivalent to the ensemble average in such systems. If the redistribution rate is much faster than the reaction rate, the system behaves ergodically. Under these conditions, the only relevant initial parameters that may be specified are the total energy and angular momentum, the global constants of motion.

Unimolecular rates have been studied by a number of methods, both direct and indirect. The indirect methods, line-width measurements, 'collisional clocking' methods[14] , quantum yield measurements, all suffer from the fact that some

additional assumptions have to be made in order to determine the dynamics of the system. Time-resolved measurements of the evolution of population of some molecular species monitor the dynamics directly. Gas-phase as well as beam studies of excited state population decays have been measured as a function of energy previously.[15,16] These experiments are limited to molecules with appreciable quantum yield.

We have recently implemented a three-beam technique — one molecular, the other two, photon — for the study of ultrafast reactions. This method, time-resolved photofragment spectroscopy (TRPS), is essentially a two-color pump-probe arrangement which allows us to measure reagent decay and product rise-times as a function of the initial energy and the final product rotational or electronic quantum state. The optical scheme is one that has been extensively used for photophysical studies in condensed phases[17] , and to a limited extent, in the gas phase.[18] Two laser pulses, overlapped in time, are focused in the sample, a beam of molecules. One of the pulses, the pump, is resonant with a transition in the reagent molecule, while the other, the probe, selectively excites or ionizes either a product or the excited reactant. The temporal evolution of the species selected by the probe is mapped out as the delay between the two pulses is varied.

The temporal resolution of this method is the correlation width of the pump and probe pulses. The pulses themselves may be on the order of a few picoseconds or less, the lower limit being set by the current state of ultrashort laser technology. The spectral resolution is determined by the frequency spectrum of the pulses, generally close to the uncertainty limit. Resonance-enhanced multiphoton ionization (REMPI), possible because intense pulses are used, allows us to selectively ionize the species of interest. This has a two-fold advantage: (i) the ions can be identified with a mass-spectrometer built into the instrument, and (ii) non-fluorescing species may be detected, thus broadening the range of molecules that may be studied.

The versatility of TRPS is demonstrated by the range of problems that have been studied. The list includes predissociation of rare gas-molecule or hydrogen-bonded van der Waals' clusters[19] , complex mode unimolecular reactions initiated

by overtone[20] or electronic excitation[21] , direct photodissociation on a repulsive surface[22] , oriented bimolecular reactions[23] and detection of collisionally perturbed transient species present during the dissociation process.[24] The dynamics of bond breakage is currently being examined using an extension of this technique to the femtosecond domain.[25]

The results presented in this thesis constitute a few of the applications cited above. We have measured microcanonical rates of a prototypical statistical reaction, the dissociation of nitrosyl cyanide into the diatom nitric oxide and the cyanogen radical. Product state distributions for this reaction has been shown to be in agreement with the predictions of the standard statistical theories. Rates of product appearance in different fragment quantum states were observed to be the same within the limits of experimental accuracy. The energy dependence of the rates near threshold (5-700 cm^{-1}) measured in small energy increments allow us to test statistical theories of rates at the microcanonical level.

For a second example, we present results on the UV fragmentation of the polyhaloethane, $C_2F_4I_2$, to tetrafluoroethane and atomic iodine. Our experiments showed that the dissociation proceeded by a two-step process, one I atom being removed at each step. The intermediate radical, C_2F_4I, previously believed to be unstable, exhibited a lifetime of 30 ps, suggesting that it was bound. Energy dependent studies show that the distribution of internal energies in the radical may be varied by changing the pump energy, which is reflected by an increase in the lifetime of the radical.

Results demonstrating the detection of collisionally perturbed I atoms in the dissociation of methyl iodide are presented as a final example. Frequency-selected transient behavior and the complementary time-dependent excitation spectra measured by resonant multiphoton ionization show that the pump-probe technique is a tenable detection method for the observation of so-called *transition-state* species.

The body of this thesis is organized into six chapters. In chapter 2, we derive the appropriate expressions for obtaining rate constants from the measured transients, in the presence of fields of arbitrary strengths. Chapter 3 describes the ex-

perimental apparatus in brief. A short review of the theories of unimolecular rates constitutes chapter 4. The last three chapters represent the fruits of our labors — experimental results and discussions of the studies mentioned above, in the order specified. Published work on additional topics constitute two of four appendices. Appendix I reports on the dissociation of van der Waals' clusters and a preliminary account of the detection of OH produced in the reaction $H + CO_2 \longrightarrow OH + CO$ appears in appendix II. The last two contain listings of FORTRAN programs for calculating density of states (direct count method) and phase space distributions and rates for a reaction producing two diatoms (Hund's case *a* and *b*).

References

1. D. R. Herschbach, *Angew. Chem. Int. Ed. (Eng.)*, **26**, 1221, (1987).

2. Y. T. Lee , *Angew. Chem. Int. Ed. (Eng.)*, **26**, 936, (1987).

3. J. C. Polanyi, *Angew. Chem. Int. Ed. (Eng.)*, **26**, 952, (1987).

4. See, e.g., R. D. Levine and R. B. Bernstein, in *Molecular Reaction Dynamics and Chemical Reactivity*, Oxford Univ. Press, NY, (1987) .

5. S. J. Riley and K. R. Wilson, *Farad. Disc. Chem. Soc.*, **53**, 132, (1972).
   G. E. Busch and K. R. Wilson, *J. Chem. Phys.*, **56**, 3626, (191972).

6. M. J. Dzvonik, S. Yang and R. Bersohn, *J. Chem. Phys.*, **61**, 4408, (1974).

7. H. W. Cruse, P. J. Dagdigian and R. N. Zare, *Farad. Disc. Chem. Soc.*, **55**, 277, (1973).
   R. N. Zare and P. J. Dagdigian, *Science*, **185**, 739, (1974).

8. C. H. Green and R. N. Zare, *Ann. Rev. Phys. Chem.*, **33**, 119, (1982).
   C. H. Green and R. N. Zare, *J. Chem. Phys.*, **78**, 6741, (1983).

9. J. L. Kinsey, *J. Chem. Phys.*, **66**, 2560, (1977).

10. See, e.g., *Radiationless Transitions*, ed. S. H. Lin, Acad. Press, NY (1980).

11. K. F. Freed and A. Nitzan, *J. Chem. Phys.*, **73**, 4765, (1980).
R. E. Smalley, *J. Phys. Chem.*, **86**, 3504, (1982).

12. A. H. Zewail, *Ber. Bun. Phys. Chem*, **84**, 1184, (1984).

13. I. Oref and B. S. Rabinovitch, *Acc. Chem. Res.*, **12**, 166, (1979).
D. W. Noid, M. L. Koszykowski and R. A. Marcus, *Ann. Rev. Phys. Chem.*, **32**, 267, (1981).
N. Bloembergen and E. Yablonovitch, *Phys. Today*, **31**, 23, (1978).

14. C. S. Parmenter, *Farad. Disc. Chem Soc.*, **75**, 7, (1983).
R. A. Coveleski, D. A. Dolson and C. S. Parmenter, *J. Chem. Phys.*, **72**, 5774, (1980).

15. Thesis by P. M .Felker, C.I.T., 1985.
J. J. Ramaekers, L. B. Krijnen, H. J. Lips, J. Langelaar and R. P. H. Rettschnick, in *Proc. Int. Conf. on Photochem. and Photobiol.*, ed. A. H. Zewail, Harwood, NY (1983).

16. R. E. Moore, F. E. Doany, E. J. Heilweil and R. M. Hochstrasser, *Farad. Disc. Chem Soc.*, **75**, 331, (1983).
S. M. Beck, J. B. Hopkins, D. E. Powers and R. E. Smalley, *J. Chem. Phys.*, **74**, 43, (1981).

17. J. W. Shelton and J. A. Armstrong, *IEEE J. Quan. Electron.*, **QE-3**, 302, (1967).
M. M. Malley and P. M. Rentzepis, *Chem. Phys. Lett.*, **3**, 534, (1969).
R. M. Hochstrasser, H. Lutz and G. Scott, *Chem. Phys. Lett.*, **24**, 162, (1974).

18. J. W. Perry, N. F. Scherer, A. H. Zewail, *Chem. Phys. Lett.*, **103**, 1, (1983).
B. I. Greene and R. C. Farrow, *J. Chem. Phys.*, **78**, 3336, (1983).

19. J. L. Knee, L. R. Khundkar and A. H. Zewail, *J. Chem. Phys.*, **87**, 115, (1987).

20. N. F. Scherer and A. H. Zewail, *J. Chem. Phys.*, **87**, 97, (1987).

21. L. R. Khundkar , J. L. Knee and A. H. Zewail, *J. Chem. Phys.*, **87**, 77, (1987).
A. J. Hoffman, L. R. Khundkar and A. H. Zewail, unpublished results.

22. J. L. Knee , L. R. Khundkar and A. H. Zewail, *J. Chem. Phys.*, **1996**, 85, (19).
N. F. Scherer, J. L. Knee, D. D. Smith and A. H. Zewail, *J. Phys. Chem.*, **89**, 5141, (1985).

23. N. F. Scherer, L. R. Khundkar , R. B. Bernstein and A. H. Zewail, *J. Chem. Phys.*, **87**, 1451, (1987).

24. L. R. Khundkar and A. H. Zewail, *Chem. Phys. Lett.*, **142**, 426, (1987). M. Dantus, M. J. Rosker and A. H. Zewail, *J. Chem. Phys.*, **87**, 2395, (1987).

25. T. S. Rose, M. J. Rosker and A. H. Zewail, *J. Chem. Phys.*, in press.

CHAPTER 2

A KINETIC MODEL FOR PUMP-PROBE EXPERIMENTS

In a pump-probe experiment, two pulses, overlapped in time, interact with some molecular species. The pump is tuned to a resonance frequency of the molecule, while the probe is used to interrogate the population induced by the pump in some molecular state. This may be the resonant state directly excited by the pump, or some other state that is coupled to it *via* a molecular dephasing process. If this process is dissociation, the state detected by the probe may correspond to a different molecular species.

The signal from such experiments, recorded as a function of the delay between the two pulses, is clearly dependent on the rate of the molecular processes involved. In this chapter we derive expressions for the exact time-dependent signal in such an experiment and show how these solutions may be used to determine the molecular parameters sought. This treatment allows us to take into account the finite width of the pulses, as well as the effects of stimulated emission.

2.1. Description of the model

We use a phenomenological approach and describe matter-radiation interaction in terms of the commonly applied kinetic model for a two-level system.[1,2] Following general convention, we label the lower state (1) and the upper state (2) (figure 2.1). The standard low-signal rate equations are:

$$\dot{N}_1(t) = -B_{12}\rho(\nu)N_1(t) + [A + B_{21}\rho(\nu)]N_2(t) \qquad (2.1)$$

$$\dot{N}_2(t) = B_{12}\rho(\nu)N_1(t) - [A + B_{21}\rho(\nu)]N_2(t) \qquad (2.2)$$

Here A, B_{12} and B_{21} are the Einstein coefficients and can be expressed in terms of molecular parameters. B_{12} is proportional to the integrated absorption cross-section, σ, and may also be related to the transition moment. $\rho(\nu)$ is the radiation density and is simply the quotient of the intensity of the incident light, I(ν), and c, the speed of light in the medium.

Pump-probe experiments are generally performed on a multilevel system. The level scheme may be treated as sets of two-level systems interacting by population exchange. Thus we need to consider an open two-level system, i.e., one in which

the total population is not a constant in time. We assume that equations (2.1) and (2.2) are valid even for a time-varying $\rho(\nu)$. We wish to consider two variations on this theme. First, we allow the two-level system to be open in a limited way. Levels 1 and 2 are allowed to have an intrinsic, known time-dependence, $n_1(t)$ and $n_2(t)$, in the absence of a field. It is assumed that $\dot{n}_1(t)$ and $\dot{n}_2(t)$ do not depend explicitly on the population in the respective levels. Second, we allow $n_2(t)$ to depend on the population in level (2) as a generalization of the previous case.

The effect of the radiation field is to couple the two levels and thereby change their populations. Using $N_1(t)$ and $N_2(t)$ to denote the population in the respective levels of the open system in the presence of a field, we may write the rate equations as

$$\dot{N}_1(t) = \dot{n}_1(t) - B_{12}\rho(\nu,t)N_1(t) + [A + B_{21}\rho(\nu,t)]N_2(t) \quad (2.3)$$

$$\dot{N}_2(t) = \dot{n}_2(t) + B_{12}\rho(\nu,t)N_1(t) - [A + B_{21}\rho(\nu,t)]N_2(t) \quad (2.4)$$

An additional constraint imposed by conservation of mass is

$$N_1(t) + N_2(t) = n_1(t) + n_2(t). \quad (2.5)$$

The separation of the dynamics in the absence of a field can be rigorously done only if the actual values of n_1 and n_2 are not affected by the presence of the field. Thus the coupled pair of equations describes the dynamics exactly if the time derivatives $\dot{n}_1$ and $\dot{n}_2$ do not depend explicitly on the population in either 1 or 2. They are approximately correct if the net change in population $N_1 - n_1$ and $N_2 - n_2$ is small compared to n_1 and n_2 respectively.

Our experimental applications involve laser pulses of ultrashort duration. The time scale is much shorter than typical radiative lifetimes, and we can safely ignore A in equations (2.3) and (2.4). Since our light pulses have finite energy, they are integrable, and we may collect all constants and rewrite the $B\rho$ factors in (2.3) and (2.4) as

$$B_{12}\rho(\nu,t) = \alpha_1 f(t)$$

$$B_{21}\rho(\nu,t) = \alpha_2 f(t).$$

$f(t)$ is a normalized representation of the laser pulse, i.e.,$\bar{f}(s) \equiv \int_{-\infty}^{s} f(t)dt$ approaches unity as s approaches ∞. Equations (2.3) and (2.4) become (2.6a) and (2.6b) below, with the constraint still given by equation (2.5).

$$\dot{N}_1(t) = \dot{n}_1(t) - \alpha_1 f(t)N_1(t) + \alpha_2 f(t)N_2(t) \qquad (2.6a)$$

$$\dot{N}_2(t) = \dot{n}_2(t) + \alpha_1 f(t)N_1(t) - \alpha_2 f(t)N_2(t) \qquad (2.6b)$$

As an extension of the simple model, we then treat the case where the temporal behavior of one of the levels (for convenience chosen to be 2) depends explicitly on the transient population of that level. We treat the case where each level is singly degenerate, which implies α_1 and α_2 are equal. The differential equations are simple to write down (equations 2.7a and 2.7b).

$$\dot{N}_1(t) = -\alpha f(t)N_1(t) + \alpha f(t)N_2(t) \qquad (2.7a)$$

$$\dot{N}_2(t) = \alpha f(t)N_1(t) - \alpha f(t)N_2(t) - kN_2(t) \qquad (2.7b)$$

Note that the mechanism of depletion excludes repopulation of the ground state. Equation 2.7 differs from the Einstein relations in this respect. k is the rate constant for loss of population from level 2. The equation of constraint (equation 2.5) is no longer strictly applicable and a unique solution is obtained only when initial conditions are specified.

2.2. Solution of the rate equations

In the following sections we derive solutions of (2.6) and (2.7) and show how they may be used to analyze the signal from a pump-probe experiment. The difference between the two equations lies in the direction of population flow in the system whose dynamics they describe. Equation 2.6 is applicable when the field-free dynamics does not involve the population in either level. An example of such a situation is one in which population accumulates in the system, but there is no mechanism for its loss. It may be pointed out that equation 2.5 is a time-dependent constraint and does not necessarily reflect population conservation in the system. Equation 2.7 corresponds to loss of population from the system via the upper state.

The cases are distinguished in order to simplify the solution of the respective rate equations.

2.2.1. Case of intrinsic dynamics independent of population in either level

The system of equations (2.6) is easily solved using equation (2.5) and the appropriate integration factor. A brief derivation of the solution for $N_1(t)$ is presented below.

Substituting $N_2(t) = n_1(t) + n_2(t) - N_1(t)$ in equation (2.6a) and rearranging terms leads to

$$\dot{N}_1(t) + (\alpha_1 + \alpha_2)N_1(t) \quad = \quad \dot{n}_1(t) + \alpha_2 f(t)[n_1(t) + n_2(t)]$$

Using $exp[(\alpha_1 + \alpha_2)\bar{f}(t)]$ as the integrating factor and invoking the boundary condition $N_1(-\infty) = n_1(-\infty)$, the above equation is reduced to

$$N_1(t) = n_1(t) \; - \; \alpha_1 \left(\int_{-\infty}^{t} n_1(x) f(x) \Omega(x) dx \right) \; + \; \alpha_2 \left(\int_{-\infty}^{t} n_2(x) f(x) \Omega(x) dx \right). \tag{2.8}$$

A new function, $\Omega(x)$, has been defined for compactness of notation.

$$\Omega(x) \; \equiv \; \Omega(x;t) \; \equiv \; e^{(\alpha_1+\alpha_2)[\bar{f}(x)-\bar{f}(t)]}$$

$\Omega(x;t)$ is defined on $(-\infty, t]$ and is bounded by $e^{-(\alpha_1+\alpha_2)}$ and 1, which in turn implies that the integrals are well-defined. Figure 2.2 shows $\Omega(x)$ for various values of $\alpha_1 + \alpha_2$ and a gaussian pulse shape. t has been chosen to be large and positive, so that $\bar{f}(t)$ is essentially unity. The expression for $N_2(t)$ may be derived similarly, or simply by substituting the solution for $N_1(t)$ in equation (2.5).

$$N_2(t) = n_2(t) \; + \; \alpha_1 \left(\int_{-\infty}^{t} n_1(x) f(x) \Omega(x) dx \right) \; - \; \alpha_2 \left(\int_{-\infty}^{t} n_2(x) f(x) \Omega(x) dx \right) \tag{2.9}$$

It is useful to consider a few special cases relevant to our discussion below. These case studies have been selected to illustrate some physical aspect of the problem.

2.2.1.1. Relating α to transition probabilities

We begin by considering a two-state system with initial population in the lower state and no intrinsic evolution. The system is closed and the relevant conditions are $n_1(t) = n_1$, a constant, and $n_2(t) = 0$. Since each of the levels are non-degenerate, $\alpha_1 = \alpha_2 = \alpha$. This is the common two-level problem (with no spontaneous relaxation) and equations 2.8 and 2.9 yields the standard solution.

$$N_1(t) = n_1 - \alpha \int_{-\infty}^{t} n_1(x) f(x) \Omega(x) dx$$

$$N_2(t) = \alpha \int_{-\infty}^{t} n_1(x) f(x) \Omega(x) dx.$$

The integrals may be further simplified

$$N_1(t) = 0.5 n_1 \left[1 + e^{-2\alpha \bar{f}(t)}\right] \tag{2.10}$$

$$N_2(t) = 0.5 n_1 \left[1 - e^{-2\alpha \bar{f}(t)}\right] \tag{2.11}$$

At long times (after the pulse) the population in (2) is

$$N_2 = 0.5 n_1 \left[1 - e^{-2\alpha}\right]$$

In the limit of very strong fields, the population in (1) approaches that in (2), i.e., $N_1 \approx N_2$. Plots of N_2 (equation 2.11) for a gaussian pulse and a range of values of α are shown in figure 2.3.

Since α is related to the intensity of the incident radiation, equations (2.10) and (2.11) give the intensity dependent signal (proportional to $N_2(t)$) as a function of time. The latter may be used to identify α with a physical quantity. The net probability, P, of a transition having occurred is the change in population in level 2 divided by the total population.

$$P = 0.50 \left(1 - e^{-2\alpha}\right)$$

which implies $\alpha = -0.5 \ell n(1 - 2P)$.

It is no surprise that α is related to the probability of a transition having occurred, since B_{12} is the microscopic equivalent of the transition moment. When $P << 1$, it follows that $\alpha \sim P$ and equation (2.11) simplifies to $N_2 = \alpha n_1$. Thus the net change in the population of the excited state depends on the intensity of the incident radiation in the same way as α, e.g., linear for a one-photon transition.

2.2.1.2. Saturation effects on an evolving system

To illustrate the effects of stimulated emission, we consider the case of a two-level system, only one of which has an intrinsic time dependence. We choose $\dot{n}_2(t) = 0$ since this will be relevant to our discussion later. The appropriate conditions are then $\dot{n}_2(t) = n_2(t) = 0$ and $\dot{n}_1(t)$ is non-zero. Under these conditions, the solutions (equation (2.3) and (2.4)) have the following simplified form

$$N_1(t) = n_1(t) - \alpha_1 \int_{-\infty}^{t} n_1(x) f(x) \Omega(x;t) dx \tag{2.12}$$

$$N_2(t) = \alpha_1 \int_{-\infty}^{t} n_1(x) f(x) \Omega(x;t) dx. \tag{2.13}$$

The integral in equation (2.13) may be thought of as a convolution. If α_1 is small, $\Omega(x) \sim 1$ and $N_2(t)$ has the form of an intrinsic molecular response $n_1(x)$ convoluted with an excitation pulse, $f(x)$. If the incident radiation is strong enough to cause significant changes in the populations of the two levels, the population in level 2 is given by the convolution of $n_1(x)$ with an effective pulse $f_e(x)$ defined by equation (2.14).

$$f_e(x) = f(x) e^{2\alpha \bar{f}(x)} \tag{2.14}$$

The origin of the factor, $e^{2\alpha \bar{f}(x)}$, lies in the change in population in level 1 as a result of the radiation being present. The interaction of population $N_1(x)$ and the excitation pulse $f_1(x)$ can be visualized in two equivalent ways. First, when α is significant, competition between stimulated emission and absorption becomes important sooner since the initial rate of upward transitions is higher. Thus $n_1(x)\Omega(x)$ represents an effective population in level 1 which is affected by a pulse of radiation $f(x)$. In other words, the incident pulse sees an effective population

$n_1(x)\Omega(x)$ different from $n_1(x)$ due to the interaction. The alternative visualizes an unperturbed population interacting with a pulse whose temporal profile has been affected by the interaction. The latter perspective will be used in interpreting pump-probe transients in a general format, irrespective of the intensity of the radiation field.

In figure 2.4, we show profiles of $f(x)$ and $f_e(x)$ for different values of α (intensity) and a gaussian pulse shape. Symmetric pulses become effectively asymmetric and the peak of $f_e(x)$ is shifted in time from the peak of $f(x)$. The new peak position is the algebraic solution, ξ, to equation (2.15)

$$f'(\xi) \quad + \quad 2\alpha f^2(\xi) \quad = 0 \tag{2.15}$$

Here, $f(x)$ is the known temporal profile of the incident pulse and f' is its time derivative. In particular, $\xi = \alpha(\frac{a}{\pi})$ for a lorentzian pulse whose half-width at half-maximum is a. For a gaussian pulse of the form e^{-ax^2}, ξ is the solution of the transcendental equation $\xi = (\alpha/a)exp(-a\xi^2)$. Note that ξ is dependent on α in both cases and unbounded. From a physical perspective, the validity of the basic equations have to be considered for reasonable bounds on α, which will then impose a limit to these shifts.

2.2.2. Solution of the non-conservative system of equations including population loss

The coupled pair of differential equations (2.7a ,2.7b) cannot be reduced to a single first order equation since the equation of constraint (2.5) is no longer valid. The solutions can be readily derived for limiting values of α and k. Each case is treated individually below. It will be seen that except for the case where both α and k are large, the solutions may be represented by a convolution integral. For simplicity, we assume that initially only the ground state is populated.

2.2.2.1. Case 1: α small, k arbitrary

If either the radiation field is weak or its coupling to the material is small, α is small and $\alpha f(t)N_2(t)$ may be neglected. The solutions are obtained using the same techniques as in the previous section.

$$N_1(t) \approx N_1(-\infty)\left[1 - \alpha\bar{f}(t)\right] \tag{2.16a}$$

$$N_2(t) \approx \alpha N_1(-\infty)\int_{-\infty}^{t} e^{-k(t-s)}f(s)ds \tag{2.16b}$$

where only terms up to first order in α have been retained. Clearly, the solutions reduce to the solutions for case 1 of the previous section (equations 2.10 and 2.11) if k is small enough to be neglected.

Equation (2.16b) may be recognized as the convolution of the intrinsic molecular response e^{-kx} with the normalized excitation pulse. An intuitive explanation for this may be developed without recourse to the Einstein equations. A general kinetic scheme has a unique solution once the proper boundary conditions are specified. The solution for a set of initial conditions can be obtained if the conditions are specified in the absence of evolution, i.e., with k set equal to zero. For a discrete set of conditions the solution is the sum

$$n_2^s(t) = \sum_j n_2(t-\xi_j)\left[(n_2^0(\xi_j) - n_2^0(\xi_{j-1})\right]$$

Here, $n_2(t-\xi)$ is the unique solution with initial value n^0 specified at ξ, and n^s is the solution accounting for the set of initial conditions. For a continuous set of initial conditions, the sum becomes the integral

$$n_2^s(t) = \int_{t_0}^{t} n_2(t-\xi)\dot{n}_2^0(\xi)d\xi \tag{2.17}$$

It is easy to show that equation (2.16) is an equivalent representation of this integral.

2.2.2.2. Case 2: α arbitrary, k small

The restriction of k to small values amounts to a separation of time scales. Thus k can be numerically large, e.g. 10^8 s^{-1}, as long as it is negligible compared

to the inverse of the duration of the pulse. This assumption allows one to solve equation 2.7 for $N_1(t)$ with k set equal to zero and the solution is equation 2.10.

The behavior of the upper level is slightly more complicated since the long-time dynamics is determined by k. We can write the differential equation for $N_2(t)$ as

$$\dot{N}_2(t) \quad = \quad -\dot{N}_1(t) \quad - \quad kN_2(t) \tag{2.18}$$

Since $\dot{N}_1$ can be calculated from equation 2.10, the d.e. is an inhomogeneous, first order equation which can be solved easily using integration factors.

$$N_2(t) \quad = \quad n_1\alpha \int_{-\infty}^{t} e^{-k(t-s)} f(s) e^{-2\alpha \bar{f}(s)} ds \tag{2.19}$$

The solution, $N_2(t)$, can be rewritten in the form of equation (2.17) above. A simple derivation from equation (2.11) (which is $n_2^0(t)$ in the notation of this section) leads to the familiar convolution.

$$N_2(t) \quad = \quad \int_{-\infty}^{t} e^{-k(t-\xi)} \left(\frac{dn_2^0(\xi)}{d\xi} \right) d\xi \tag{2.20}$$

2.2.2.3. Case 3: large α, large k

The solution of this case may be derived using Picard iteration. Equations (2.7) may be written in matrix form

$$\dot{\vec{x}} \quad = \quad \mathbf{A}(t) \cdot \vec{x}$$

where the two components of $\vec{x}$ are $x_1 = N_1 + N_2$ and $x_2 = N_2 - N_1$, and the matrix $\mathbf{A}(t)$, defined as

$$\mathbf{A}(t) \quad = \quad -\frac{k}{2} \begin{pmatrix} 1 & 1 \\ 1 & 1 + \frac{4\alpha f}{k} \end{pmatrix},$$

is time-dependent. The solution is obtained iteratively from an initial guess[3] using the following recursion relation

$$\vec{x}_n(t) \; = \; \vec{x}_{n-1}(0) \; + \; \int_0^t \mathbf{A}(s) \vec{x}_{n-1}(s) ds. \tag{2.19}$$

The convergence of this series is guaranteed, as is the uniqueness of the solution.[3] Although a formal solution may be derived, there appears to be no simple (closed form or integral) representation for it. The cross terms in the matrix multiplication in equation (2.19) lead to multiple integrals which are not readily simplified. It may be argued that this case, which corresponds to the saturation of a greatly homogeneously broadened transition, is unlikely to arise in an experimental situation, i.e., the bulk of pump-probe experiments fall into the domain of the cases explicitly solved above.

2.3. Application of the simple model to pump-probe experiments

A general pump-probe experiment can be treated in terms of two two-level open systems, the initial pair (i_1, i_2) connected by the pump pulse and the final pair (f_1, f_2) coupled by the probe field. The evolution of the level i_2 to f_1 is an intrinsic molecular property and may be described in terms of an appropriate kinetic scheme. In this section we use this simple picture to derive expressions for the delay-dependent signal in such an experiment. The two cases are treated separately.

2.3.1. The three-level system

This case is relevant to transient absorption experiments (figure 2.5a). The i_2 and f_1 levels are the same. We can conceive of the experiment as occurring in two steps, with no coherence between them. In the first step, the pump excites absorbers from level i_1 to level $i_2(f_1)$. Population in i_2 decays spontaneously with a rate-constant k. Assuming that initial population is in the ground state (i_1) exclusively, the population in i_2 as a function of time is given by equation 2.20.

$$N_{i_2}(t) = \int_{-\infty}^{t} e^{-k(t-x)} \dot{N}^0_{i_2}(x) dx$$

In the second step the probe pulse excites population from $i_2(f_1)$ to f_2. This is the case treated in section 2.2.1.2 above, with the intrinsic molecular response

(in the absence of the probe pulse) being $N_{i_2}(t)$. Using the solution (equation 2.13) with the appropriate substitution, we get

$$N_{f_2}(t;T) = \alpha_{prb} \int_{-\infty}^{t} f_{prb}(\tau;T)\Omega_{prb}(\tau;t) \int_{-\infty}^{\tau} e^{-k(\tau-x)} \dot{N}^0_{i_2}(x)dxd\tau \qquad (2.21)$$

Assuming that the detected signal is proportional to the population in f_2, the transient behavior of the signal is given by equation (2.21). The variable T which appears in the integral is the time-delay between the pulses and is used to parametrize the signal. For a fixed value of T, $N_{f_2}(t;T)$ depicts the evolution of population in f_2. A typical experiment measures this quantity at long times (large enough t so that $f_{prb}(t;T) \sim 0$) and the measured signal, $S(T)$, is given by

$$S(T) = n_1 \alpha_{pmp}\alpha_{prb} \int_{-\infty}^{\infty} f_{prb}(\tau - T) f_{prb} e^{2\alpha_{prb}\bar{f}_{prb}(\tau-T)} \cdot e^{-2\alpha_{prb}} \int_{-\infty}^{\tau} e^{-k(\tau-x)} f_{pmp} e^{-2\alpha_{pmp}\bar{f}_{pmp}(x)} dxd\tau \qquad (2.22)$$

As shown elsewhere,[4] the convolution of an arbitrary molecular response $M(t-t_0)$ with the pump and probe pulses of finite temporal width can be written as a single convolution. We write $f_1 \equiv f_{pmp}e^{-2\alpha_{pmp}\bar{f}_{pmp}}$ and $f_2 \equiv f_{prb}e^{2\alpha_{prb}\bar{f}_{prb}}$. The molecular response $M(\xi)$ is the exponential decay with constant k. If we also suppress the constants before the integral, we obtain a more compact form for equation 2.22.

$$S(T) = \int_{-\infty}^{+\infty} \int_{-\infty}^{\tau_2} f_1(\tau_1)M(\tau_2 - \tau_1)f_2(\tau_2 - T)d\tau_1\, d\tau_2$$

A change of variables ($s \equiv \tau_1 - \tau_2 + T$) then leads to

$$S(T) = \int_{-\infty}^{T} \int_{-\infty}^{+\infty} f_1(\tau_1)f_2(\tau_1 - s)M(T - s)d\tau_1\, ds$$

The system response function, $R(t)$, defined as the function obtained by setting $M(t)$ equal to the Dirac delta-function, is easily recognized as the cross-correlation of the two pulses f_1 and f_2.

$$R(T) = \int_{-\infty}^{+\infty} f_1(\tau_1) f_2(\tau_1 - T)\, d\tau_1$$

The measured molecular transient can then be written as in equation 2.23.

$$S(T) = \int_{-\infty}^{T} R(s) M(T-s)\, ds \qquad (2.23)$$

For the three-level system, the molecular response is simply e^{-kz}, while the characteristics of the pulses are included in $R(s)$.

2.3.2. Four-level system

In this case i_2 and f_1 are distinct and the evolution of population from the former to the latter has to be explicitly considered (figure 2.5b). Thus it models the detection of fragment species. The relevant molecular kinetic scheme is the simplest possible one.

$$A(i_2) \xrightarrow{k} B(f_1)$$

Thus $B(t)$ is simply the integral of $A(t)$ multiplied by a constant factor $-k$.

Following the arguments presented above for the pump excitation, we obtain the solution for $B(t)$, i.e., $N_{f_1}(t)$.

$$N_{f_1}(t) = -k \int_{-\infty}^{t} \int_{-\infty}^{s} e^{-k(s-x)} \dot{N}^0_{i_2}(x) dx ds$$

After some simple manipulations and an integration by parts, this integral is reduced to the simpler form

$$N_{f_1}(t) = \int_{-\infty}^{t} [1 - e^{-k(t-x)}] \dot{N}^0_{i_2}(x) dx$$

The derivation of the delay-dependent signal in this case is identical to the three-level case from this point and we eventually get

$$S(T) = \int_{-\infty}^{T} [1 - e^{-k(T-s)}] R(s) ds \tag{2.24}$$

where $R(s)$ is again the cross-correlation of f_1 and f_2.

2.3.3. Response function

The response function derived above is the cross-correlation of the pump and probe pulses when α is small. In general, it contains additional factors that account for the effects of stimulated emission.

$$R(s;T) = \int_{-\infty}^{\infty} f_{pmp}(x) e^{-2\alpha \bar{f}_{pmp}(x)} f_{prb}(s-x) e^{2\alpha_{prb} \bar{f}_{prb}(s-x)} dx$$

The exponential factors describe the distortion of the response due to saturation of either of the two transitions. Typically, one measures the cross-correlation function in a non-linear crystal under conditions such that saturation is not significant. In order to use this as the correct response function, the relevant pump-probe experiment must be done under similar conditions, i.e., α_{pump} and $\alpha_{prb} \sim 0$. If the parameters being measured are significantly longer than the time-scale of the response, the experiments may be performed under conditions where the signal is saturated in either pump or probe, with the *proviso* that the distortion of the true response function is considered in determining the precision of the measurement.

2.4. Discussion

In this chapter we have derived the exact time-dependence of the signal measured in a pump-probe experiment, assuming the validity of Einstein's kinetic model. We showed that this signal may be represented as a convolution of a molecular response with an instrument response function, $R(s)$. In the weak field limit, where stimulated emission may be neglected, $R(s)$ is the cross-correlation of the pump and probe pulses. When this condition is not satisfied, $R(s)$ includes an additional multiplicative factor. In the next few sections, we elaborate on the relevance of these results to pump-probe experiments.

2.4.1. Effect of Saturation

We illustrate these effects by a simple example. Figure 2.6 shows $R(s)$ for various values of the parameters α_{pmp} and α_{prb}. The most noticeable point is the asymmetry and shift in the peak position as their values increase, the rising edge appearing sharper. For comparison with typical data, we show convolutions of these responses with exponential decays and buildups (figure 2.7). We have restricted the values of α used in the simulations to be less than 1.0,[5] which corresponds to a transition probability of ~ 0.43 within each two-level subsystem. At this point it is instructive to consider the range of α that is typical of our experimental conditions. From its definition, we realize that the quantity is dimensionless and simply the product of the absorption cross-section and the average, time-integrated intensity. For a pulse energy of 100 μJ at 300 nm focused to a minimum spot size $\sim 10\,\mu^2$ in area, we calculate $\alpha \sim 10^{-3}$ using an absorption cross-section of 10^{-18} cm^2. This corresponds to a transition probability of $\sim 10^{-3}$. The spatial intensity distribution of the pulse has not been considered in this estimate.

It is worth mentioning that $R(s)$ is a smooth function, even for large values of α. Thus saturation effects cannot give rise to additional features on the measured transients.

2.4.2. Effect of pulse width

The effect of pulse width on the measurement of a fast process is of relevance to the discussion in the following chapters. One of the questions we may ask ourselves is that given a fast process, what are the limits of detection when the response function has a much longer duration. A cursory attempt to evaluate this simply by plugging in numbers for k that are much larger than the characteristic constants in describing f_{pump} and f_{prb} would lead to an unreasonable result. The clue lies in assessing the matter-radiation interaction for such a case at the primitive level (equations 2.6 and 2.7). The innocuous α factor describes the coupling strength between the field and the two-level system. As the molecular processes get fast, the coupling term is affected — the α parameter gets smaller for the same value of

intensity and pulse-width. A heuristic argument following the derivation of two-photon absorption cross-sections for atoms[6] may be used to derive an absorption cross-section that depends on the lifetime of the intermediate state. The overall rate for a two-photon transition is approximately equal to $\sigma_1\sigma_2\tau$, where the σs are the absorption cross-sections of the pump and the probe, and $\tau = k^{-1}$ is the lifetime of the intermediate state. Thus α is proportional to k^{-1}. This result may also be derived from equation 2.16b by considering the limiting behavior for large k. Thus the temporal behavior dependence of the upper level still follows the description given above, but the effective coupling constant (i.e. α) is reduced. In physical terms, one may say that even though the pulse is long-lived, the system is too short-lived to sample the pulse for its duration.

Since the signal is proportional to α, as k increases, the overall signal goes down. This dependence is expected to be linear and the range of detection of large k with pulses of longer duration is therefore linearly proportional to the dynamic range of the signal.

2.4.3. Relevance to pump-probe experiments

Some final comments regarding the impact of these results on pump-probe experiments are in order. From a purist's point of view, all experiments must be done in the weak field limit. If the time-scale of the molecular process is long compared to the cross-correlation of the pump and probe, one may use intense pulses for both pump and probe without introducing significant error into the measured time-constant. This is advantageous because intense pulses generally mean large signals. On the other hand, when the time-scale of the dynamics is of the same order as the cross-correlation, weak pulses must be employed. The measured zero-time is then intimately related to the saturation conditions and one is at risk of drawing a false conclusion if both the response function and the molecular transient behavior are not measured under identical conditions.[7] The simplest way to avoid this artifact is to perform both measurements with weak pulses, thereby ensuring that stimulated emission is insignificant.

In using pump-probe methods to study processes whose lifetimes are comparable to or faster than the pulse duration, one is often able to use more intense pulses because population in the intermediate state (upper state for the pump) does not build up as rapidly as when there are no decay channels. If the probe is resonant with an asymptotic product state, its intensity should be adjusted to avoid saturation.

2.5. References

1. J. I. Steinfeld in *Molecules and Radiation*, 2nd. ed., MIT Press, Cambridge (1985), 25.
2. A more accurate description would be obtained by using the optical Bloch equations or the complete Rabi solutions as derived in, e.g., L. Allen and J. H. Eberly, *Optical Resonance and Two-Level Atoms*, J. Wiley, NY, 1975. We do not pursue this any further since our objective is a simple description of the problem.
3. R. D. Driver in *Ordinary and Delay Differential Equations*, Springer Verlag, NY (1977).
4. L. R. Khundkar, J. L. Knee and A. H. Zewail, *J. Chem. Phys.*, **87**, 73 (1987).
5. The validity of the kinetic model is questionable for larger values of α. The cutoff value used here (1.0) was chosen arbitrarily and is probably too large to be physically relevant. For a discussion of this point, see e.g., S. Feneuille, *Rep. Prog. in Phys.*,40, 1257 (1977).
6. See, e.g., G. Mainfray and C. Manus, in *Multiphoton Ionization of Atoms*, ed. S. L. Chin and P. Lambropoulos, Acad. Press, Orlando FL (1984).
7. It should be noted that saturation is not synonymous with intensity. If different transitions are studied in the measurement of the transient and the instrument response, their respective oscillator strengths, as well as the intensity, determines the extent of saturation.

Table 2.1

Parameters and symbols used in simulations.

				Symbol	
α_{pmp}	P_{pmp}	α_{prb}	P_{prb}	Fig. 5	Fig. 6
1.0	0.43	1.0	0.43	– – –	——
5.0×10^{-3}	0.0005	1.0	0.43	– · – · –	– – –
1.0	0.43	5.0×10^{-3}	0.0005	·····	
0.1	0.09	0.5	0.32	– ··· – ··· –	– · – · –
5.0×10^{-3}	0.0005	5.0×10^{-3}	0.0005	——	·····

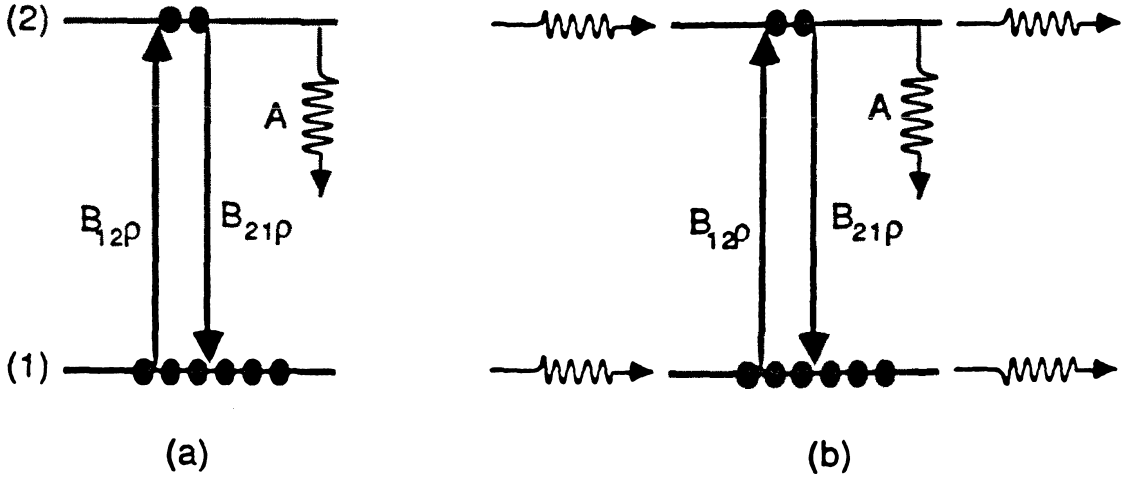

Figure 2.1. Kinetic model for interaction of radiation with a two-level system. $B\rho$ depicts the rate of stimulated absorption and emission, while A denotes spontaneous emission. (a) closed system, i.e., no loss of population. (b) open system.

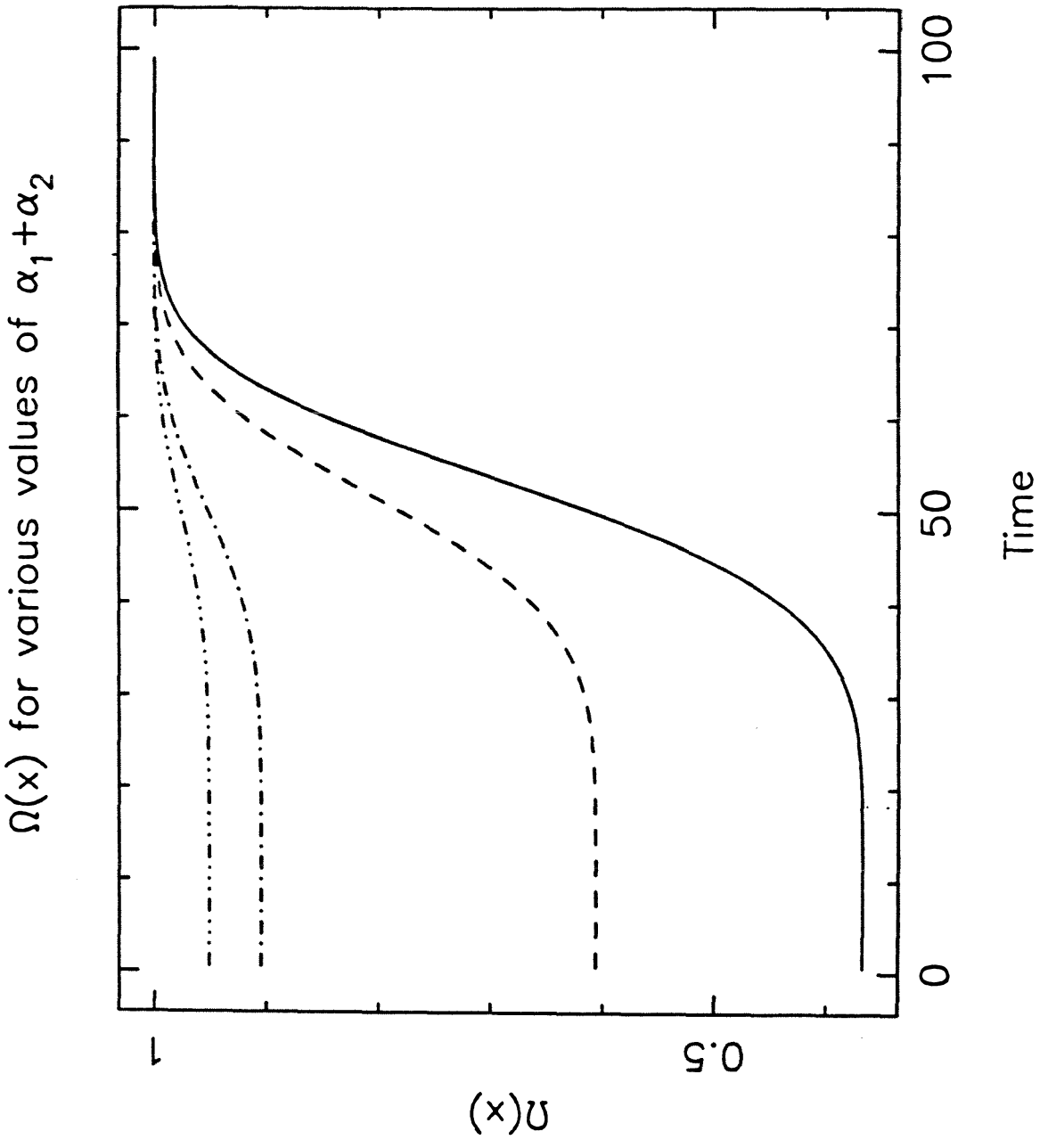

Figure 2.2. Plots of the form factor $\Omega(x;t)$ for a gaussian pulse and various values of $\alpha_1 + \alpha_2$, ranging from 10^{-3} to 0.5.

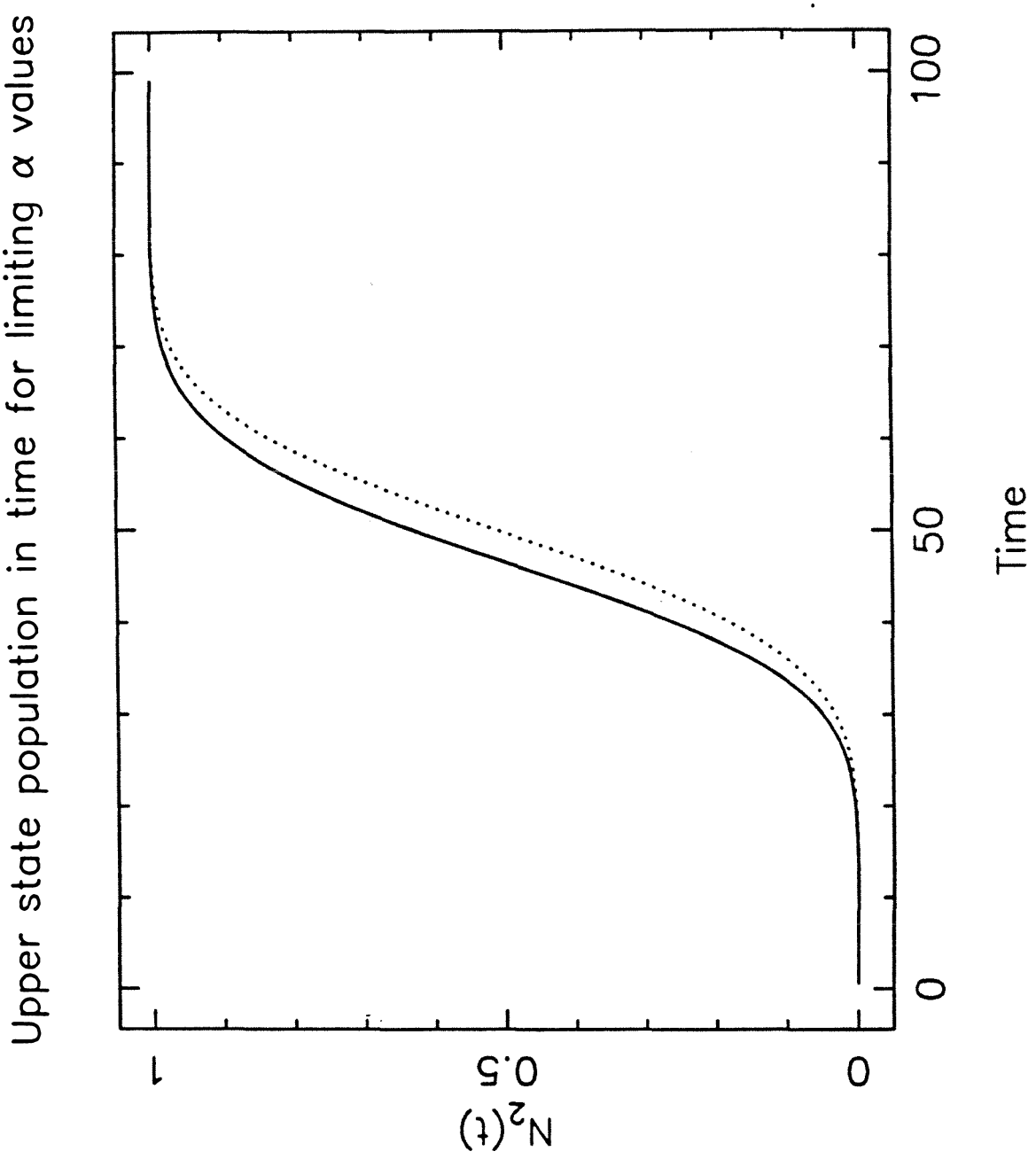

Figure 2.3. Temporal evolution of the upper state population for a gaussian excitation pulse and limiting values of α. Dotted line for a value of 0.0005, solid line for 0.5.

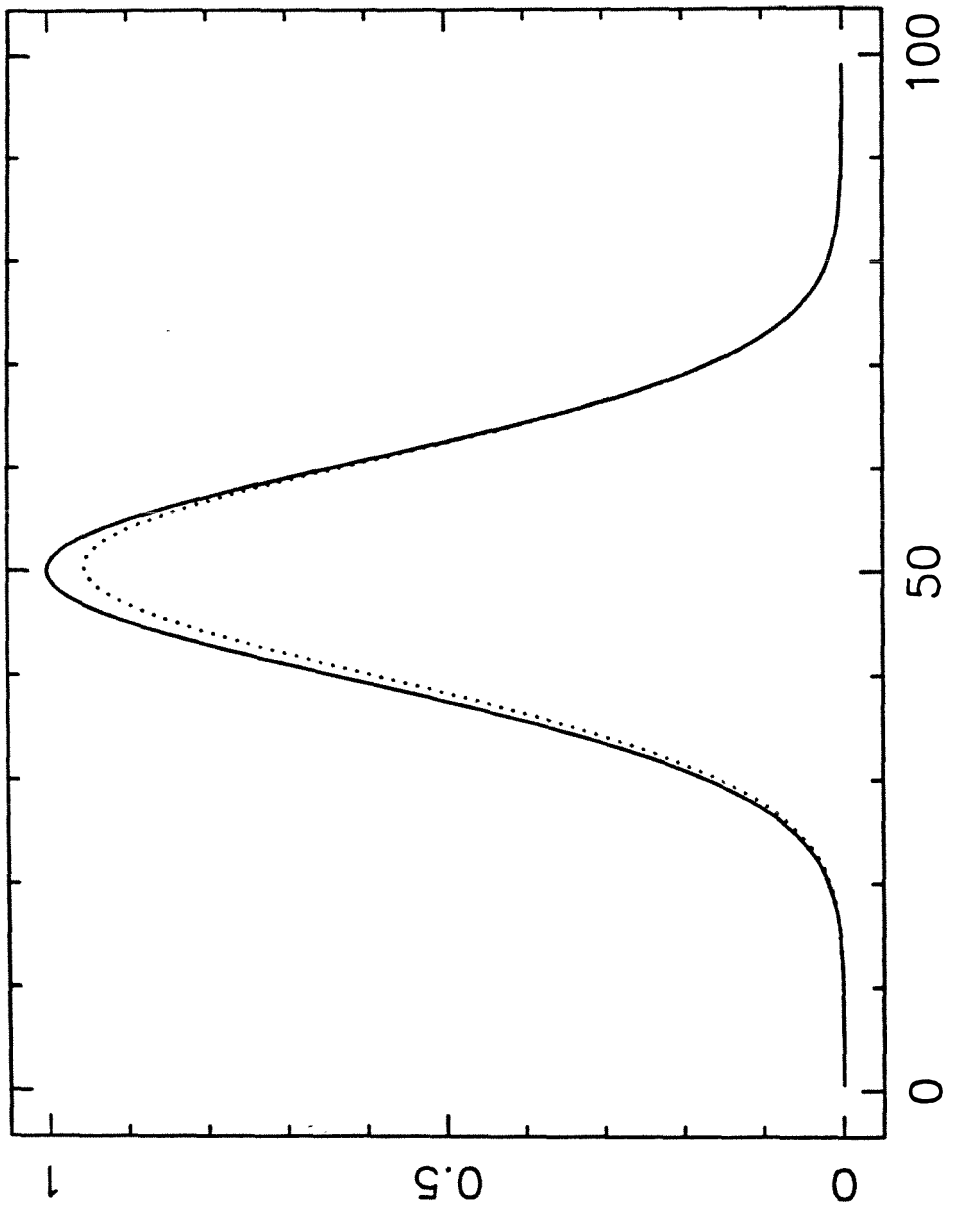

Figure 2.4. Plot of the effective pulse for different values of α. t has been chosen large for convenience. The solid line corresponds to $\alpha = 0.0005$ while the dotted line is for $\alpha = 0.5$. Notice the asymmetry in the pulse for the larger value of α.

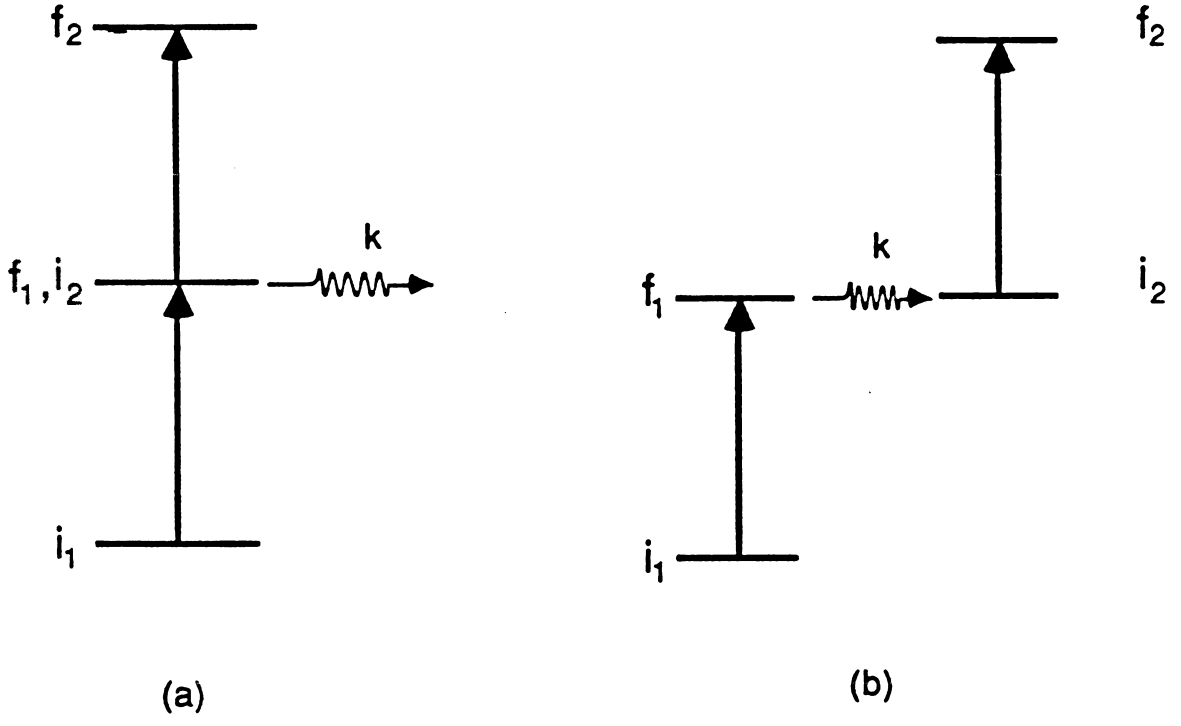

Figure 2.5. Level schemes for probing (a) initial (reactant) state or (b) final (product, fragment) state.

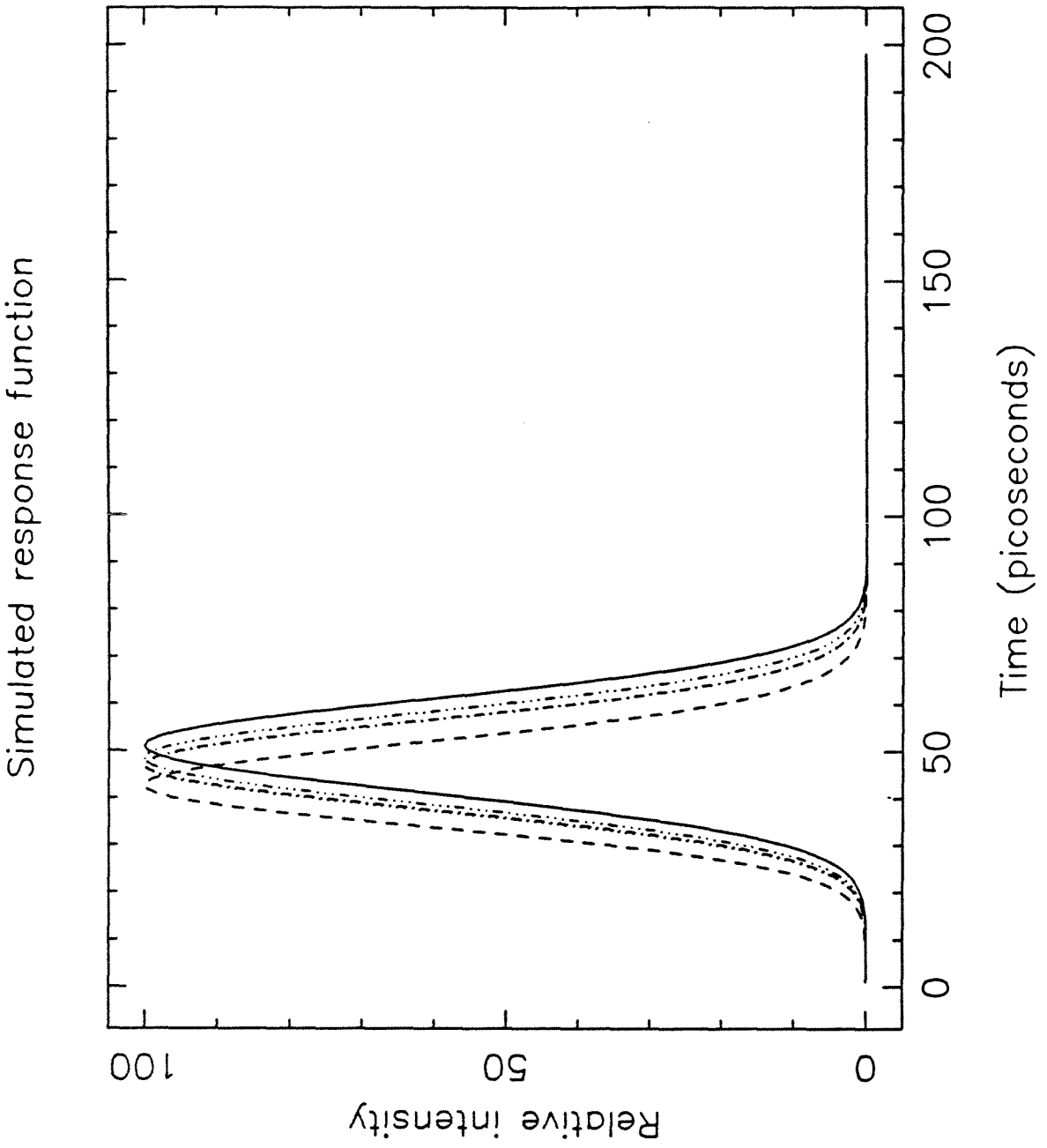

Figure 2.6. Calculated $R(s)$ for various combinations of α_{pmp} and α_{prb}. The actual values used given in Table 2.1. Note the change in shape and shift in peak position for large values of α.

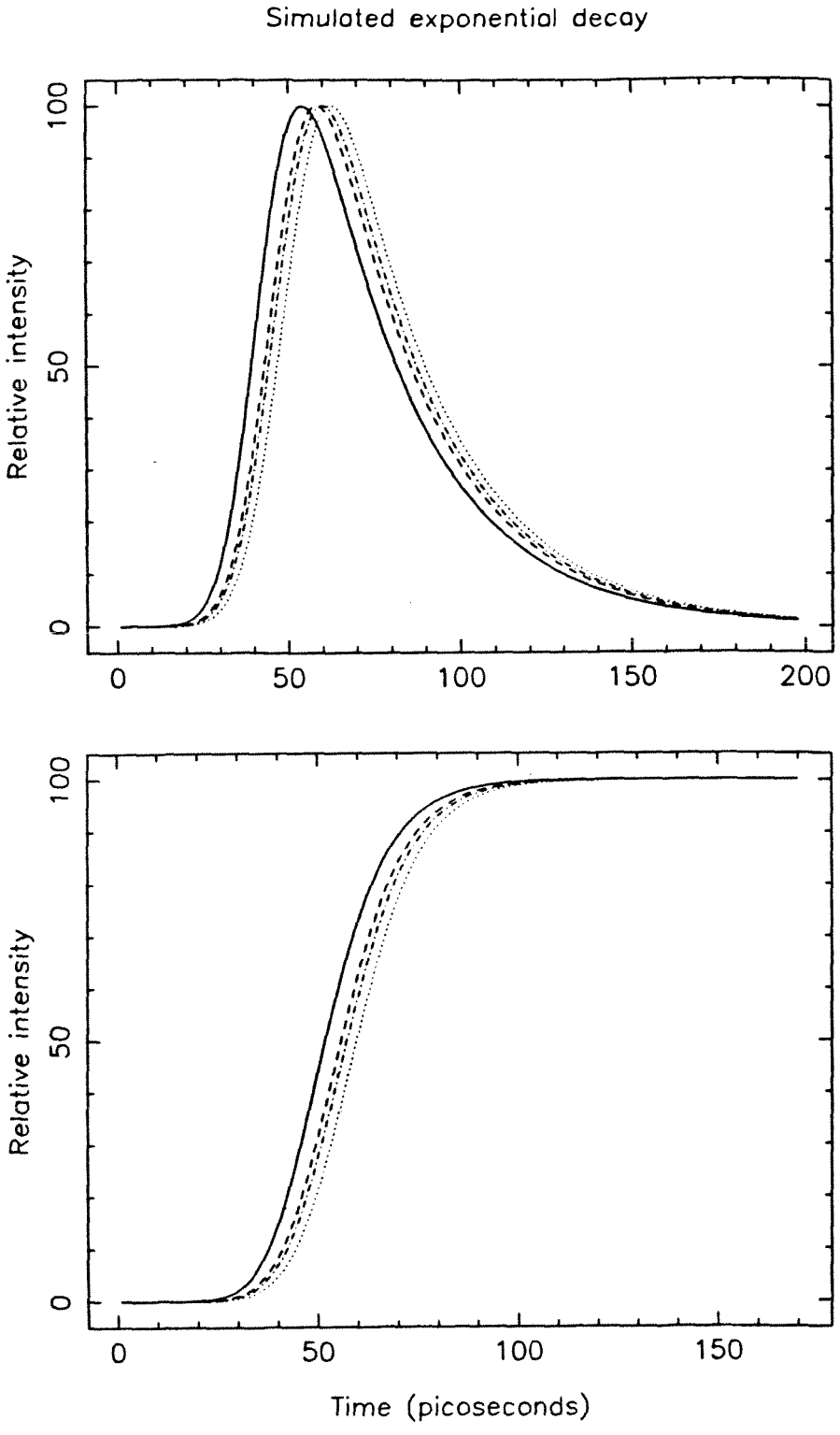

Figure 2.7. (a) Simulated transients for a 30 ps decay (eqn 2.21) using gaussian pump and probe pulses, each of width 10 ps. The curves correspond to various values of α_{pmp} and α_{prb}, as indicated in Table 2.1. (b) Simulated transients for a 10 ps. rise using the same $R(s)$ as in (a) above. Note the distortion due to saturation.

CHAPTER 3

EXPERIMENTAL

Since molecular resonances are discrete, it is necessary to use two independently tunable sources to spectroscopically identify both the initial state accessed and the specific product state whose temporal behavior is to be studied. The temporal resolution of the experiment is determined by the duration of the pump and probe pulses and the relative jitter between them. It should be noted that since frequency and time constitute a fourier transform pair and are related by the Heisenberg Uncertainty Principle, one compromises spectral resolution in attaining better temporal resolution and vice versa.[1]

In addition to having ultrashort, tunable pulses, we also need to have high photon flux (intensities) for a number of reasons. First, the concentration of molecules of interest in a supersonic expansion is small. Second, the volume of interaction of the two beams (laser and molecule) is small as in all crossed-beam experiments. Third, most small organic molecules that can be conveniently seeded in a MB absorb in the UV. These colors have to be generated from the visible light of tunable dye lasers by taking advantage of the large nonlinear susceptibility of special materials. Conversion efficiencies depend on the intensity of the light beam and therefore intense pulses are particularly useful.

The work described here employed picosecond pulses. The following sections describe the methods used to generate pulses of the appropriate color and intensity, the molecular beam apparatus used to achieve internally cold distributions and the mass- spectrometer and LIF detection systems. The apparatus has been described in a number of publications[2–4] and is briefly summarized here. A comprehensive account will be given elsewhere.[5] A schematic diagram is shown in Figure 3.1.

3.1. Two-color Picosecond Laser System

3.1.1. The picosecond sync-pumped dye lasers

The 1064 nm output of a commercial, actively mode-locked Nd-YAG is frequency doubled by focusing in a KTP crystal. The 532 nm visible light ($\sim$ 800 mW) is divided into two beams of approximately equal intensity and each one used as the pump source for a synchronously pumped dye laser. The output wavelength of

each dye laser is selected by an intracavity 3-plate quartz birefringent filter. Both dye lasers use R6G in ethylene glycol as the gain medium. One of them (DL1) is used to generate the pump while the other (DL2) is used for the probe. The typical energy for each laser is $\sim$ 50 mW, which corresponds to 0.6 nJ per pulse. Typical pulses from each dye laser have approximately gaussian temporal profiles with a full-width at half maximum (FWHM) value of $\sim$ 8 ps. The measured spectral bandwidth is also approximately gaussian with $\sim$ 3 cm^{-1} FWHM. The third plate of the frequency tuning element can be removed or purposely misaligned to obtain pulses of shorter duration.[6] The gain condition existing in the laser is such that additional pulses may be formed under these circumstances. This problem is countered by introducing a saturable absorber into the cavity. The dye laser is of a single fold, single jet design and the nonlinear absorber is usually mixed with the gain medium.[7] The pulse energies and widths are monitored as the concentration of the absorber is carefully increased. Enough absorber is added to ensure proper mode-locking and that a single pulse per cavity round trip time is obtained. Pulses with auto-correlation widths (FWHM) half as much as those obtained with the 3-plate filter could be achieved with this combination (hybrid mode-locking).

3.1.2. Pulsed dye amplifiers

The picosecond dye laser pulses were amplified in a multi-stage optical amplifier of conventional design.[8] The second harmonic of an amplified Q-switched Nd:YAG laser operating at 20 Hz (300 mJ/pulse @ 532 nm) is split into two beams of nominally equal intensity. Each half is used to pump a number of dye-amplifier stages (three or four). Each picosecond pulse is propagated through one of these multi-stage amplifiers. The Q-switch of the YAG laser is synchronized to the mode locking frequency synthesizer of the CW Nd-YAG laser so that a 532 nm pulse and a picosecond pulse arrive at the first stage of the dye amplifier simultaneously. The overall gain in each amplifier is nominally 10^6. A train of 0.5 - 1.0 mJ visible pulses at 20 Hz is thus obtained. The temporal shape of the amplified pulses is very similar to that of the input pulses as long as the gain of the amplifier is not

much greater than 1×10^6. The variety of available laser dyes makes it possible for us to obtain the maximum gain for most wavelengths in the range 560 - 620 nm.

3.1.3. Generation of the proper colors by nonlinear techniques.

As mentioned above, most small molecules absorb UV light, which must be generated from the amplified visible pulses by nonlinear methods.[9] We have employed second harmonic generation and nonlinear mixing in crystals of special materials (e.g. KDP and KD*P). In some cases, Raman scattering in a high pressure gas may be used to extend the range of UV wavelengths accessible. A brief description of this method is given below.

The output of the amplified dye laser is focused (1 meter lens) into a 1 meter long high pressure Raman cell. Methane has a large cross-section for scattering and is therefore a good first choice. The amplified picosecond pulses are scattered by the gas ($\Delta\nu = 2914\ \mathrm{cm}^{-1}$) and various orders of Stokes and anti-Stokes light are generated. The intensity distribution among them can be varied by changing the pressure in the cell. Best results for the first Stokes and anti-Stokes lines are obtained with 90 and 120 psig of technical grade methane (Matheson, 98%). The light, Raman orders and fundamental, is recollimated with a .5 meter lens. The necessary UV light may be generated by doubling the Raman order directly, or by mixing the appropriate order with the unconverted visible light immediately after the collimating lens. Best conversion efficiency for mixing is obtained with this lens close to the output window of the Raman cell as the scattered radiation diverges, and good overlap with the fundamental is lost quickly as the beams propagate. We used the first raman order (Stokes' or anti-Stokes')in the experiments requiring this method for generating the proper wavelength.

3.1.4. The optical delay

The time delay between the two beams is set up in a Michelson interferometer. The pump beam (DL1) is directed through a fixed delay, while the probe beam (DL2) is directed through a variable delay consisting of a 2.5 inch hollow corner cube mounted on a stepper-motor driven translator (10.0 μ per step). The beams

are combined on a dichroic mirror after which they are propagated collinearly and focused into the sample. Each method of detection requires a different focal-length lens. Typically, a 1 m lens is used for the LIF measurements while a 25 cm lens is used for the MPI experiments. In some cases, a telescope with two converging lenses appropriately spaced is used in one arm to ensure that both beams are focused at the same point. This is necessary because the quartz lens before the sample is not an achromatic lens.

3.1.5. Pulse characterization

A home-built real-time spinning-block autocorrelator is used to monitor the pulses from the synchronously pumped dye lasers. A beam-splitting cube sends 50% of each laser beam into each arm of the interferometer and also serves to recombine the return beams. The returned beams are focused into an appropriate nonlinear crystal (usually $LiIO_3$) with a 10 cm converging lens. The second harmonic generated by this non-collinear arrangement is negligible except when the pulses are temporally overlapped in the crystal, thus affording a zero-background method for observing their autocorrelation.[1] With appropriate adjustments of spatial overlap, relative pathlengths and phase-matching angle, the cross correlation between the two dye laser outputs can also be obtained.

The cross-correlation of DL1 and DL2 after amplification is measured by generating the sum frequency in a 1 cm KDP crystal. The cross-correlation of the doubled light and the fundamental may be obtained by generating the difference frequency and spatially or spectrally separating it from the visible beam.

3.2. Molecular Beam Apparatus

The method of cooling the internal degrees of freedom of a molecule by supersonic expansions is well established.[10] As shown by previous workers, the expansion results in a non-Boltzmann distribution of energy among the various degrees of freedom. Each class, i.e., vibrations, rotations and translation can be characterized by an effective temperature, T_{vib}, T_{rot} and T_{trans} respectively. This means that energy distribution among the different vibrational degrees of freedom can be

described as that of a Boltzmann ensemble of the same species at a temperature T_{vib}. Generally $T_{vib} > T_{rot} > T_{trans}$ with typical values 10 K, 3 K and 1 K.

A free jet expansion is used to eliminate internal energy in the parent molecule. The expansion chamber consists of two cylindrical halves approximately 12 inches in diameter, bolted together. A thin (1/16 ") stainless steel sheet with a central cutout serves to divide the chamber into two compartments. Each half is pumped by a single VHS–6 oil-diffusion pump equipped with a liquid nitrogen cooled baffle. A nickel skimmer (Beam Dynamics, 1.3 mm aperture, 1.5 inches high) is mounted over the cutout in the stainless-steel septum. Thus the geometric axis of the vacuum chamber is the symmetry axis of the molecular expansion. Each half also has a built-in four-way cross near the end which is bolted to the other half. One compartment houses the source and is used exclusively for LIF studies, while the second one is devoted to mass-spectrometry. The sample is introduced through a pulsed nozzle made of Kel-F, a perfluorinated, machinable plastic. The nozzle is operated at 20 Hz and triggered by the Q-switch of the YAG amplifier. The nozzle design and controller electronics were developed by Syage *et al.* and the details are given elsewhere.[11] Some modifications to the pulse amplifier circuit had to be made to ensure reliable operation and the currently used circuit is shown in figure 3.2. The nominal aperture diameter, d, is 500 μ and with typical backing pressures of 1000 Torr He and nominal valve open-time of 500 μs, an ambient pressure of 2×10^{-4} Torr in the first chamber can be maintained at steady- state. The pressure in the second chamber is $\sim 10^{-6}$ torr under these conditions.

3.3. Detection Methods

3.3.1. Laser induced fluorescence

The laser beams typically intersect the expansion 10 mm downstream from the nozzle, corresponding to $x/d \approx 20$. Short optical baffles are used on both input and output sides to reduce scattered light in the chamber for these measurements. Fluorescence can be detected using a single $f/1$ quartz lens 2 inch in diameter which is adjusted to focus a point image defined by the laser beams and the axis

of the expansion slightly beyond the detector. A three-lens and slit combination is used for experiments that have low signal and therefore require greater scattered light rejection. Appropriate UV sharp-cut filters (Corion, Schott) and visible blocking filters (7-59 and interference-coated 7-54, Corning) are used to define the spectral window of detection. The detector is a high gain photomultiplier typically operated close to its maximum gain of 10^8. The output of the PMT is amplified and used as input to a variable gain boxcar integrator which is triggered off a fast photodiode illuminated by 532 nm light from the Q-switched laser. The gate for signal averaging is set to bias against laser scatter.

3.3.2. Time-of-Flight mass spectrometer

Ions can be created by laser multiphoton ionization or electron impact methods. The MPI method is used for time-resolved measurements while the latter method is used for diagnostic purposes. A time-of-flight (TOF) mass-spectrometer is used for mass analysis. The spectrometer and the methods of ionization are described briefly.

The principle of TOF mass-spectrometry is well-known.[12] Positive ions are accelerated through a fixed potential so that they acquire a kinetic energy which is independent of their mass. The ions are allowed to travel through a field-free drift tube and detected by an appropriate ion multiplier (IM). Since the velocity of a particular ion depends on its mass, the arrival time at the detector is proportional to the square-root of the mass. If the signal is resolved in time, one can deduce the mass-spectrum of the ions. The simplicity of this instrument is counterbalanced by the moderate resolution that can be achieved. A simple variation due to Wiley and McClaren[13] , employing a double acceleration zone for first-order space focusing, was implemented. Sophisticated methods have been employed to improve the resolution,[14] but these were not incorporated into this particular instrument since mass-resolution was not the most severe limitation for the experiments reported here.

The vertical drift tube is 1 m long and contains an ion multiplier, EMI 9642/3B, to detect the ions which have been dispersed in time. The arrival of

the ions can be recorded by a 100 MHz transient digitizer, Lecroy TR8818, which is based in a CAMAC crate interfaced to an LSI 11/23+ minicomputer. The signal from a number of laser shots is averaged in the computer to build up a mass spectrum. In cases where just one mass is to be observed, the amplified output of the ion multiplier is fed into a gated integrator/boxcar averager (EG&G 162/164), and the gate positioned to sample the mass peak of interest, with near unit mass resolution in the region of interest. It should be noted that the resolution achieved by this method is determined by the minimum gate-width of the boxcar (2 ns), which is better than that obtained with the digitizer.

The laser enters the second chamber perpendicular to the molecular beam and intersects it $\sim$ 10 cm downstream of the nozzle. The intersection of the laser and molecular beam is in the acceleration region of the mass spectrometer. The ionizing electron beam is derived from a source similar to the one described in ref. 15. Figure 3.3 (lower half) is a schematic diagram of the source. The coiled tungsten filament is mounted on a Macor (machinable glass) piece and enclosed in a stainless-steel cup which is open at the top. Holes for the necessary electrical connections are provided at the bottom of the cup and isolated from the body by Macor spacers. A stainless-steel disc (Gate) with a central 0.5 cm circular aperture fits over the cup, but remains electrically isolated. The aperture, covered with 90 % transmitting Ni-mesh, is directly over the filament.

The cup and the filament are biased to the same, constant positive DC voltage. The gate is held at a voltage slightly lower ($\sim 10 - 20$ V less) than the filament. It is pulsed high (amplitude of $\sim$ 40 V) for a short period ($\sim 1\mu s$) in tandem with the molecular beam valve. The repeller grid is simultaneously pulsed down to the same voltage as the accelerator grid for the duration of the electron pulse. The electron impact energy is assumed to be equal to the voltage difference between the filament and the accelerator grid. This is typically set to 60 V or less.

Schematics of the high voltage pulse circuits are shown in figure 3.4 and the timing sequence in figure 3.5, along with typical operating voltages. The grid

voltages for the TOFMS are kept below 550 V at all times in order not to exceed the maximum ratings of the MOSFET chips used in the circuit.

3.4. Data Acquisition and Analysis

A pump-probe transient is obtained by sampling the detected signal (LIF or ion current) with a boxcar gate of appropriate width as a function of the position of the stepper-motor controlled optical delay line. The boxcar output is routed through a voltage-frequency converter and into a multichannel analyzer (MCA) operated in the multichannel scaling mode. The channel step for the MCA is enslaved to the stepper-motor controller (SMC). The delay line is repetitively scanned for signal averaging and the data averaged in the MCA. They are later transferred to a PDP 11/23+ minicomputer where the transients are analyzed and stored. A single scan takes 20 – 40 minutes and typically 10 scans are averaged to obtain a transient with a reasonable signal-to-noise ratio. A number of such transients are recorded for a given combination of pump and probe wavelengths. Since the two colors may be independently varied, one may obtain a two-parameter map of transient behavior *vs.* initial and final state.

The system response function is approximately gaussian. The standard non-linear least squares analysis based on the Marquardt algorithm[16] is used to fit the cross-correlations to this functional form. Typical pulse FWHM values obtained with a three-plate filter were in the range 9.5 to 11.5 ps. Cross-correlations of narrower temporal extent could be obtained with a combination of hybrid mode-locking and detuning (or removal) of the third plate. This typically results in cross-correlations of $\sim$ 5 ps FWHM.

The pulse width obtained from a fit of the cross-correlation to a gaussian form is used to derive accurate rate constants from the molecular responses measured. In cases where the cross-correlation of the two visible beams is not the true system response, the transients are fitted with a calculated gaussian response function whose width is chosen to best match the rising edge of the transients. The width of the calculated response function is constrained to be less than the fitted gaussian widths of the visible cross-correlations. This is justified since the true system

response is of higher order in the intensity of both pump and probe than the visible cross-correlation. In other words, the UV pulses that are typically used in our experiments are shorter than the visible pulses from which they are generated. Therefore the cross-correlation between the UV pulses is narrower in time than that between the visible pulses. It is difficult to quantify the extent by which the UV cross-correlations are shorter since the jitter between the two lasers is not well-characterized.

3.5. References

1. E. P. Ippen and C. V. Shank, *Top. Appl. Phys*, **Vol. 18**, (Springer-Verlag, NY, 1984) .

2. N. F. Scherer, J. L. Knee, D. D. Smith and A. H. Zewail, *J. Phys. Chem.*, **89**, 5141, (1985).

3. J. L. Knee, L. R. Khundkar and A. H. Zewail, *J. Chem. Phys.*, **87**, 115, (1987).

4. L. R. Khundkar , J. L. Knee and A. H. Zewail, *J. Chem. Phys.*, **87**, 77, (1987).

5. Norbert F. Scherer, Ph. D. Thesis, C. I. T., Pasadena, to be submitted.

6. See, e.g., David P. Millar, Ph. D. Thesis, C. I. T., Pasadena, (1982).

7. Although this is not the best method, we found it to be adequate.
8. E. P. Ippen and C. V. Shank, in *Ultrafast Light Pulses*, ed. S. L. Shapiro (Springer-Verlag, NY, 1977) .
   A. Migus, C. V. Shank, E. P. Ippen and R. L. Fork, *IEEE J. Quan. Electron.*, **QE-18**, 101, (1982).
   R. L. Fork, C. V. Shank and R. T. Yen, *Appl. Phys. Lett.*, **41**, 223, (1983).

9. A. Yariv, *Quantum Electronics*, 2nd ed. (J. Wiley, NY, 1975).
   Y. R. Shen, *Principles of Nonlinear Optics* (J. Wiley, New York, 1984).

10. J. B. Anderson, R. P. Andres and J. B. Fenn, *Adv. Chem. Phys.*, **10**, 275, (1965).
    A. Kantrowitz and J. Grey, *Rev. Sci. Inst.*, **22**, 328, (1951).
    G. M. McClelland, K. L. Saenger, J. J. Valentini and D. R. Herschbach, *J. Phys. Chem.*, **83**, 947, (1979).

D. M. Lubman, C. T. Rettner and R. N. Zare, *J. Phys. Chem.*, **86**, 1129, (1982).

11. B. W. Keelan, J. A. Syage, J. F. Shepanski and A. H. Zewail, *Proc. Int. Conf. Lasers*, (STS, McLean, VA, 1985), p. 718.

12. See, e.g., R. S. Lehrle and J. E. Parker , *MTP Int. Rev. Sci., Phys. Chem. Ser. 1* , Vol. 5 (North-Holland, 1972), p. 219..
T. D. Märk, *Int. J. Mass Spec. Ion Phys.*, **45**, 125, (1982).
C. Bruneé, *Int. J. Mass Spec. Ion Phys.*, **45**, 51, (1982).

13. W. C. Wiley and I. H. McClaren, *Rev. Sci. Inst.*, **26**, 1150, (1955).

14. U. Boesl, H. J. Neusser, R. Weinkauf and E. W. Schlag, *J. Phys. Chem.*, **86**, 4857, (1982).

15. J. E. Pollard and R. Cohen, *Rev. Sci. Inst.*, **58**, 32, (1987).

16. D. W. Marquardt, *SIAM*, **11**, 431, (1964).
W. H. Press, B. P. Flannery, S. A. Teukolsky and W. T. Vetterling, *Numerical Recipes*, Cambridge Univ. Press, Cambridge, 1986.

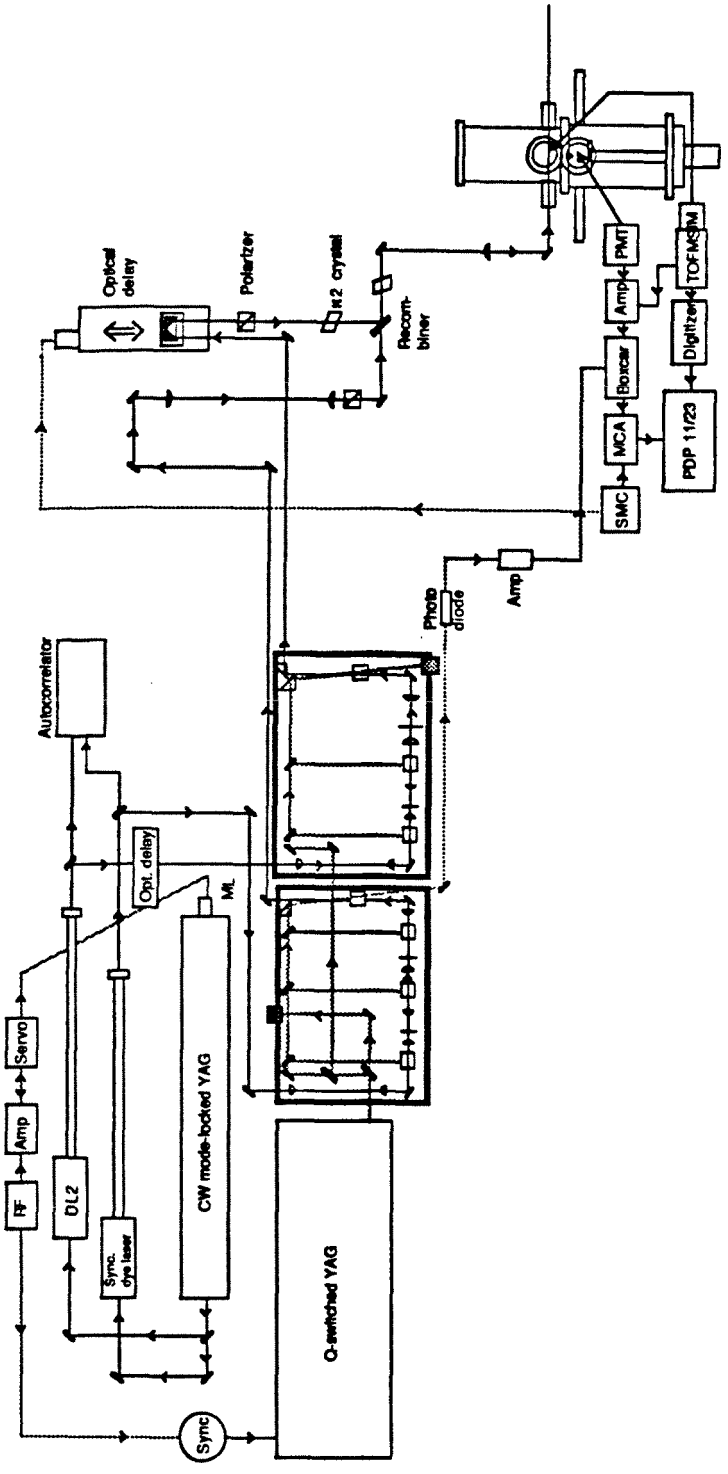

Figure 3.1. Layout of apparatus for time-resolved photofragment spectroscopy. Pulses are generated in the left half. The upper section of the right half shows the interferometer while the lower section shows the molecular beam apparatus. The two methods of detection and the data acquisition protocol are shown in block flow-diagram form. The figure has been adapted from ref. 2.

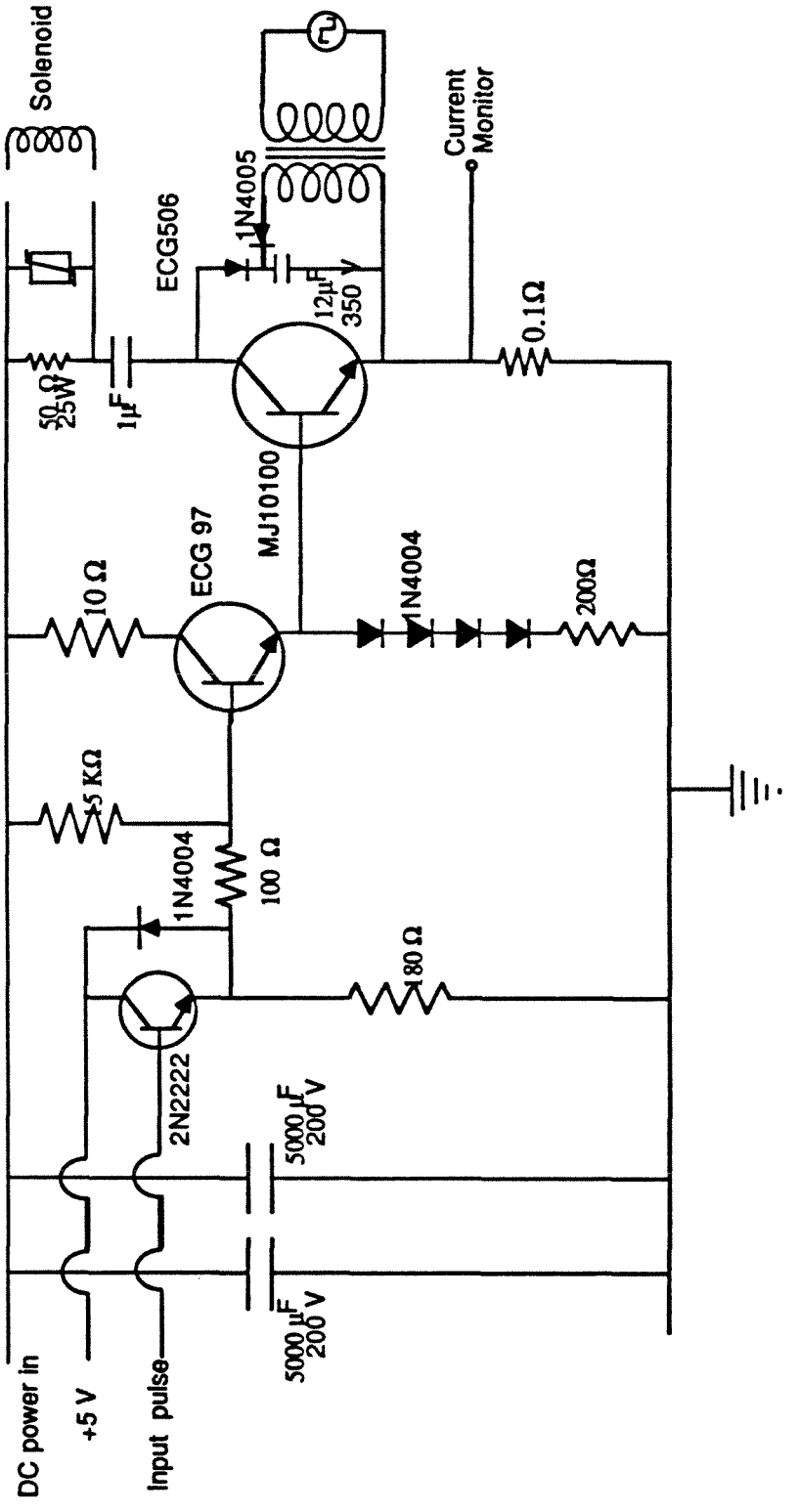

Figure 3.2. Schematic of modified circuit for a pulse amplifier. The input pulse is shaped by TTL components (not shown[11]). The output pulse drives the solenoid of the pulsed valve.

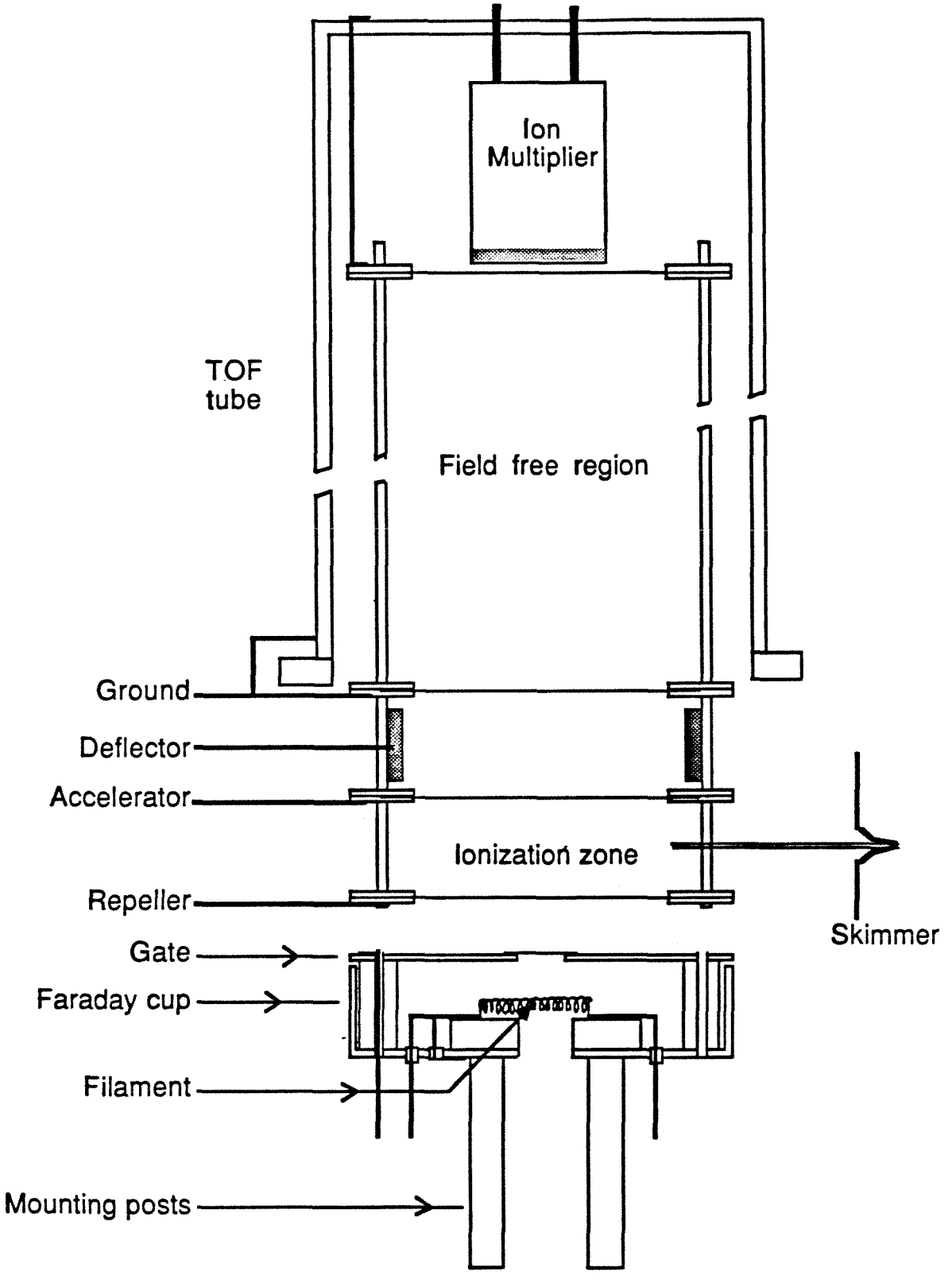

Figure 3.3. Time-of-Flight mass spectrometer and electron source.

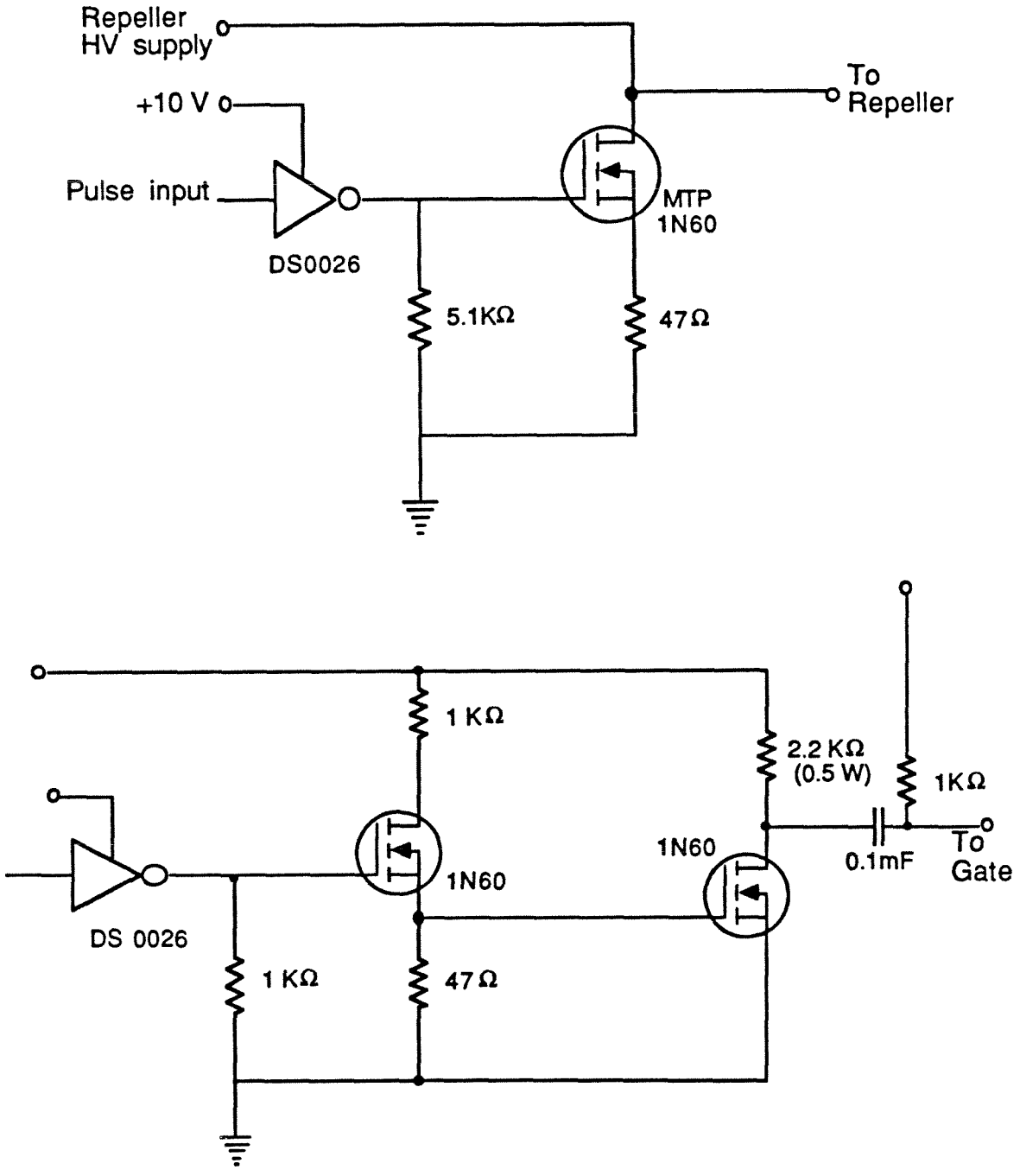

Figure 3.4. High-voltage pulser circuit for EI–TOFMS.

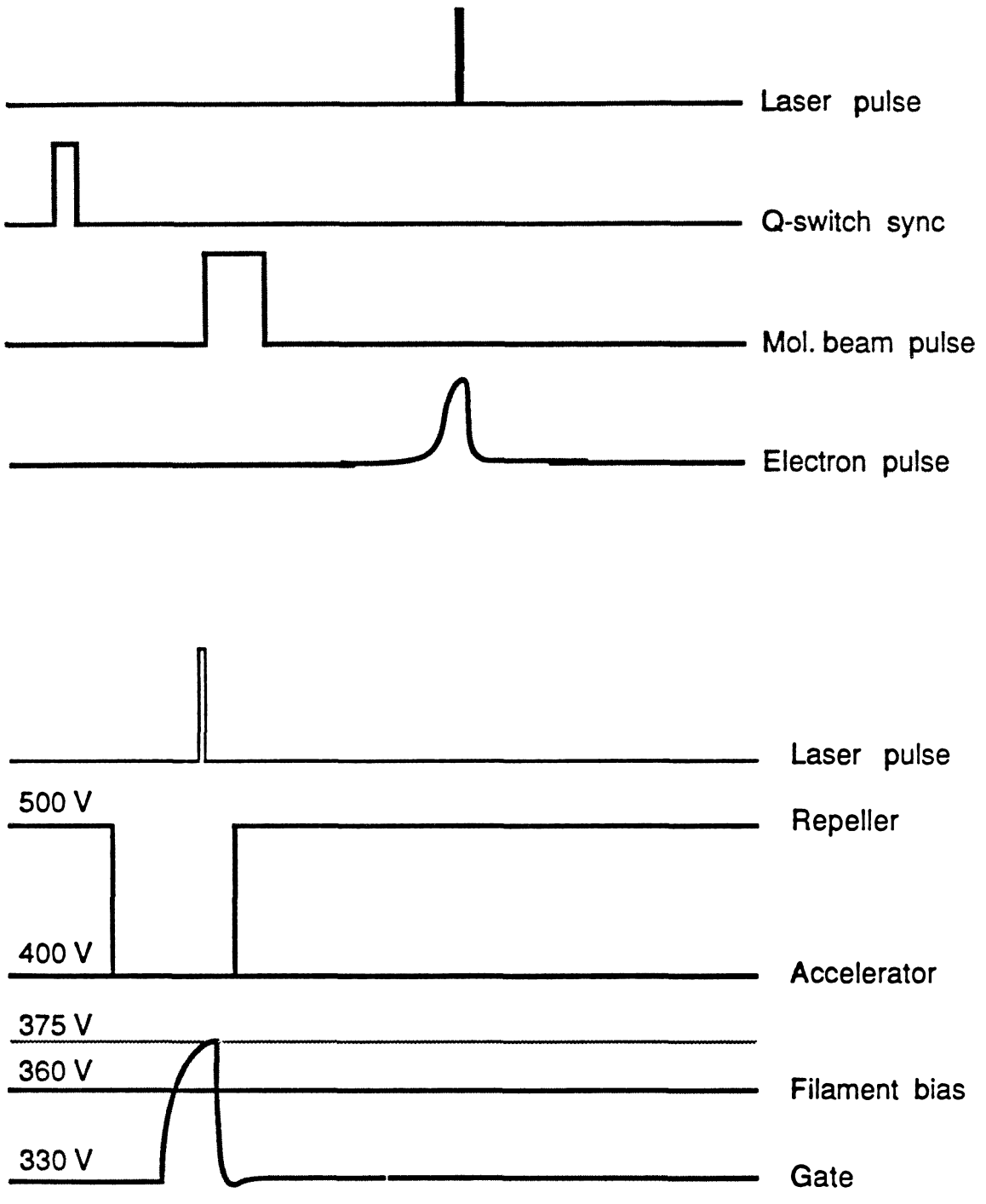

Figure 3.5. Schematic of time-ordering of the various pulsed events that need to be synchronized for EI–TOFMS.

CHAPTER 4

STATISTICAL THEORIES OF UNIMOLECULAR REACTIONS

Unimolecular dissociation can be regarded as the spontaneous decay of a metastable molecular state.[1] Speaking in quantum mechanical terms, one would say that the bound state is coupled to a translational continuum, and the strength of this coupling determines the rate of fragmentation. The approximate Hamiltonian describing the bound part of the potential surface has complex eigenvalues, $E - i\Gamma$.[2] An ensemble of isolated states (resonances) decays with a random distribution of lifetimes and its temporal behavior is an exponential decay with a characteristic rate-constant 2Γ. For polyatomics at energies high enough to cause dissociation of a covalent bond, these resonances are numerous, each of them having a finite energy spread as dictated by the uncertainty principle. The average spacing between states at these energies is often comparable to or smaller than the width of each resonance. The evolution of a large number of overlapping resonances is a difficult problem to treat analytically,[3] except in certain idealized cases. For instance, if the states are uniformly distributed and equally coupled to the continuum, the time behavior approaches an exponential form as the average spacing tends to zero.[3]

Such a theory of unimolecular rates demands that the values of the coupling constants be known *a priori*. In order to be of any value to kineticists, it must provide a scheme for estimating these constants from readily observable molecular parameters, as well as a means for predicting rates as a function of initial conditions, energy and angular momentum. Although quantum scattering calculations are, in principle, capable of determining reaction cross-sections as a function of energy, from which resonance widths may be estimated,[1,4] such methods are still not practical for systems other than the simplest three atom reactions. Classical and semiclassical approaches based on the transition state theory have been developed[5], but these are generally computationally intensive.

Transition State Theory[6] (TST), the time-honored description of reactions, is the basis of most unimolecular rate theories. Its appeal stems from the intuitive picture of a reaction it presents. The fundamental assumptions of the theory are the existence of a dividing surface that separates reactants and products and a reaction

coordinate, which parametrizes the 'extent of reaction'. We are immediately forced into a classical, or at best a semiclassical, theory of rates, since the idea of a well-defined 'moment of decision' is fundamentally classical.[7] For most theories, statistical or dynamical[8] , these assumptions are the starting point; one of the major tasks of the theory being the identification of the reaction coordinate and the dividing surface.

The statistical approximation, which asserts that the time scale on which energy is completely randomized is much faster than that of any dissociation, has been overwhelmingly successful in predicting rates of thermal reactions. Recent experiments in molecular beams, which allow one to study essentially microcanonical systems, have renewed interest in the issue of fast and complete energy redistribution as well as the scope of these approximations.[9] A brief summary of the various statistical theories of microcanonical rates[10] is presented in this chapter.

4.1. The Statistical Rate Expressions

The essence of a statistical theory is that all choices satisfying a given set of constraints are equivalent. Evaluating physical quantities then becomes reduced to the task of calculating the number of possible ways the system can satisfy the conditions imposed on it.

4.1.1. Ramsperger-Rice-Kassel (RRK) theory

In the RRK theory[11] , the rate of dissociation of a molecule consisting of s quantum oscillators is equated to that of a hypothetical system having the same number of identical oscillators. The energy-dependent rate constant, $k(E)$, is assumed to be proportional to the fractional number of dissociative configurations. A dissociative configuration is one in which the threshold (or barrier) energy is accumulated in a single oscillator. A simple exercise in combinatorics leads to the expression

$$k_{RRK}(E) \quad = \quad A\left(\frac{E-E_0}{E}\right)^{s-1} \tag{4.1}$$

Stirling's approximation for large numbers and the assumption that the total energy, E, is much greater than the threshold energy, E_0. This expression, sometimes

referred to as the classical rate, is usually regarded as an empirical theory, a microcanonical analog of the Arrhenius rate law. Measured rates are fitted to equation (4.1) using A and s as adjustable parameters, although the derivation shows s to be the total number of oscillators in the reactant. The overwhelming success of the more detailed theories described below in predicting rates has rendered this expression almost obsolete.

4.1.2. Ramsperger-Rice-Kassel-Marcus (RRKM) theory

This semiclassical theory[12] treats the general molecular system in an abstract way. The dispersion of the molecular vibrational frequencies, their mutual interaction and their coupling with molecular rotations, are included in the theory *via* their effects on the energies of the molecular states. In this derivation of the RRKM expression[10] , the microscopic equilibrium between energized (random distribution among possible states) molecules (A^*) and the transition state ($A^\dagger$) is evaluated.

$$A^*(E) \overset{k_a(E,x)}{\longrightarrow} A^\dagger \overset{k^+(E,x)}{\longrightarrow} products \tag{4.2}$$

The rate constants k^+ and k_a are partial rate constants characteristic of those configurations where $A^\dagger$ has less than the total energy, the balance of energy x appearing as translational energy in the reaction coordinate. The overall rate of dissociation, k_{RRKM}, is obtained as the sum (or integral) of these partial constants over allowed values of x. k_a is estimated from a steady-state assumption on $A^\dagger$.

$$k_a(E,x) \quad = \quad k^+(E,x)\frac{1}{2}\left(\frac{[A^\dagger(E,x)]}{[A^*(E,x)]}\right)$$

The factor $\frac{1}{2}$ arises from the assumption that at equilibrium, the critical complex would have equal probability of forming reactants or products.

The partial rate constant $k^+(E,x)$ is evaluated as the time-of passage of a hypothetical particle of mass μ through a one-dimensional box of length δ. A quantum-mechanical treatment of the number of translational energy states in the box leads to an equilibrium concentration of $A^\dagger$ which also depends on μ and δ.

Fortuitiously, these hypothetical quantities cancel and we are left with the familiar expression after integration over all x less than the total energy, E.

$$k_{RRKM} = \frac{N^{\dagger}(E - E_0)}{h\rho(E)} \tag{4.3}$$

where $\rho(E)$ is the density of states of the reactant, and $N^{\dagger}(E - E_0)$ is the total number of internal energy states of the critical configuration whose energy is less than the available energy, $E - E_0$, E_0 being the threshold energy.

4.3. Classical Transition State Theory

If a system has n degrees of freedom, then its corresponding phase space is a $2n$-dimensional hypersurface, whose basis consists of n generalized coordinates q_i $\{i = 1,\ldots,n\}$ and their conjugate momenta, p_i $\{i = 1,\ldots,n\}$. The dividing surface is a $(2n-1)$ dimensional hypersurface which is specified by the coordinates only.[13] It is also assumed that the reaction coordinate, q_1, is separable and that the critical surface obeys the simple constraint $q_1 = q_1^0$. The Hamiltonian for the system may be written as a sum of two terms

$$H(p;q) = H^{\dagger}(p_1;q_1) + H'(p';q')$$

We have used p' and q' to denote the set of coordinates and momenta $\{p_i, q_i; i = 2,\ldots,n\}$ and the same notation with no primes for the full set of p_i and q_i. The flux of phase space points through the surface is given by

$$\Phi = \int P(p;q_1^0)\vec{\mathbf{u}}\cdot\vec{\mathbf{k}}\, dS$$

where $P(p;q_1^0)$ is the density of phase space points in the vicinity of the surface, $\vec{\mathbf{u}}$ is the velocity and $\vec{\mathbf{k}}$ denotes the unit normal to the surface. In terms of phase space variables, the flux equation is

$$\Phi = \int dp_1 \int dq_1 \int dp' \int dq' \delta\left(E - H[p',q'] - \frac{p_1^2}{2\mu}\right) \delta\left(q_1 - q_i^0\right) \frac{p_1}{\mu} G(p_1)$$

$H(p,q)$ is the hamiltonian defined on the dividing surface and $G(x)$ is the unit step function,

$$\begin{aligned} G(x) &= 1 && x \geq 0 \\ &= 0 && x \leq 0, \end{aligned}$$

which ensures that only flux leading to products is taken into account. The rate is equal to the flux divided by the total volume of phase space accessible.

$$k_{MC} = \frac{\int dp' \int dq'\, G\,[E - H'(p',q')]}{\int dp \int dq\, \delta(E - H(p,q))} \tag{4.4}$$

The numerator can be recognized as the microcanonical (MC) partition[13] function, the total number of states less than E, on the dividing surface. The denominator is the number of reactant states in a differential energy shell, i.e., it is the state density at energy E. With proper quantization, equation (4.3) is obtained exactly.

4.2. Models for Rate calculations

Of the two terms in equation (4.3) that have to be evaluated, the density of states, ρ, is the easier one to calculate.[10] Algorithms have been defined for counting quantum states and an implementation of one is given in appendix III. For large densities of states ($\geq$ 1000 per cm^{-1}) this method is inefficient and not the method of choice because fairly accurate estimates may be obtained using semiclassical methods. The equilibrium frequencies of the reactant are usually used for state counting, each individual oscillator being treated as a harmonic or a Morse one.

Various methods for estimating the factor $N^{\dagger}$ have been proposed. The precise definition of the dividing surface is the essential difference between the various theories. Following the derivation of the classical rate constant as flux, one could envision the rate being limited by a dynamic bottleneck, one where the flux is minimum.[14] This criterion amounts to defining the surface as the one with the minimum number of trajectory recrossings. In transition state theory, no trajectory is allowed to cross the surface more than once in its history, while physical trajectories may. Thus TST rates are an upper bound to physical rates.

4.2.1. Modelling the transition state

The structure of the transition state is often guessed at following chemical intuition. The frequencies and rotational constants are estimated[15] and standard counting schemes used to evaluate $N^{\dagger}$. One such prescription, so-called 'standard RRKM', is to choose the frequencies of the complex equal to those of the reactant, with the exception of the reaction coordinate. This is a rather crude approximation and works only when the energetic barrier to reaction is much greater than the thermodynamic heat of reaction.

In the regular RRKM treatment, rotational energy is excluded from the available energy in calculating $N^{\dagger}$ or ρ.

$$E_{av} \quad = \quad E_{tot} \; - \; E_{rot} \; - \; V^0_{min}$$

where V^0_{min} is the energy of the vibrationless level on some arbitrary scale. Usually V^0_{min}(reactants) is chosen to be the zero of the energy scale. This specification implies that the rotational constants of the complex have to be estimated as well. Not surprisingly, they are taken to be equal to those of the reactant in the standard RRKM procedure.

4.2.2. Phase-Space Theory

For endoergic reactions with no additional barrier, the 'standard RRKM' assumptions are not valid and a different approach is taken.[16] The radial coordinate, r, (distance of the centers of the dissociating species) is effectively the reaction coordinate. Fragments are allowed to rotate freely in the transition state (TS), which is assumed to be located at the local maximum of the effective potential, V_{eff}, obtained from the sum of a long range attraction, $V_b(r)$, and centrifugal repulsion due to orbital motion of the separating particles.

$$V_{eff}(r) \quad = \quad V_b(r) \; + \; \frac{\hbar^2 \ell(\ell+1)}{2\mu r^2} \tag{4.6}$$

The location of the maximum depends on ℓ, the orbital momentum quantum number. Energy and angular momentum conservation principles impose constraints on ℓ, the latter being given by the triangle inequality

$$|J - k| \leq \ell \leq J + k,$$

where k is a quantum number corresponding to the addition of the angular momenta, j_1 and j_2, of the (two) products. It satisfies a second such inequality

$$|j_1 - j_2| \leq k \leq j_1 + j_2.$$

Generally, V_b is approximated by the attractive part of the Lennard-Jones 6-12 potential. $N^\dagger$ is then obtained by counting all possible combinations of product quantum numbers, vibrational and rotational ($j_1, \kappa_1, j_2, \kappa_2, \ell$ and k) satisfying energy and angular momentum conservation.

For simple systems, the states may be counted directly, using true quantum numbers and appropriate energy expressions (appendix IV). When the fragments are polyatomic, the inefficiency of a strict counting procedure outweighs the accuracy of the results. Approximate treatments using integrals instead of sums (classical PST) have been developed that are of greater practical worth in calculating $N^\dagger$. This method also provides estimates of the internal state distributions of the fragments.

PST is inherently inaccurate as a rate theory since it allows free rotation of fragments within the TS. It has been more widely applied in predicting internal distributions than for predicting absolute rates, partly because of this weakness. It is useful in the sense that it models the loosest possible TS, and therefore gives an upper bound for rates.

4.2.3. Generalized TS and RRKM theory

Variational treatments of rates that attempt to find the minimum flux have been used in most dynamical theories. Recently, Wardlaw and Marcus[17] have exploited the minimum flux criterion in deriving rates of reactions involving flexible

transition states. The TS is assumed to be orthogonal to the reaction coordinate and parametrized by it. The number of states on a number of such orthogonal surfaces located at different values of r is calculated and the overall minimum number determined by inspection or a simple interpolation.

$N^\dagger$ is a function of the energy, E, and the total angular momentum, J. It is calculated in the following way. The set of internal coordinates can be separated into two disjoint subsets, one consisting of motions that are present in both reactants and products, so-called *conserved modes*, and the other set consists of bending modes and rotations that eventually appear as product rotations and relative motions. The non-harmonic modes, termed *transitional modes*, constitute the latter set and are often strongly coupled among themselves. This separation allows the sum of states $N_{EJ}(R)$, on the dividing surface (located at a value R of the reaction coordinate) to be written as the convolution

$$N_{EJ} \quad = \quad \int_0^E N_v(E-x)\Omega(x)dx$$

where N_v is the number of states of conserved modes alone and $\Omega(x)$ is the density of transitional states. The term N_v is treated quantum mechanically, while Ω is estimated classically by a Monte Carlo integration over the subspace defined by these modes. Explicit knowledge of the potential energy hypersurface in the transition region between reactants and products is required before these calculations may be performed.

4.2.4. *Vibrationally Adiabatic TST — a hybrid theory*

The Statistical Adiabatic Channel Model (SACM)[18] is in essence a vibrationally adiabatic, transition state theory.[19] The distinction is made between conserved and transitional modes in this method as well. Adiabatic channel curves connecting reactant and product quantum states which involve the conserved modes are constructed using an interpolation scheme.

$$E_c(\{n_i\}) \; = \; \sum_i \left[(n_i + \frac{1}{2})h\nu_i^R)g(\xi) \; + \; (n_i + \frac{1}{2})h\nu_i^P)(1-g(\xi)) \right]$$

The switching function, $g(\xi)$ is usually defined as $exp(-\alpha[\xi - \xi_0])$. ξ is the reaction coordinate and ξ_0 is the equilibrium value for reactants. The superscripts R and P on the vibrational frequencies denote reactants and products, respectively. The sum is over all conserved modes, with α being an adjustable parameter, typically 1.0 $Å^{-1}$.

A second set of channel curves is determined from the transitional modes in the following way. A sequence of reactant states, arranged in order of increasing energy, is constructed using the equilibrium frequencies of the bending motions and internal rotations of the reactant. A similar, ordered sequence of product states is constructed using rotations and orbital motions of the products. A one-to-one correspondence map between the lowest states in these two sequences is drawn up. Angular momentum conservation is ensured at this step, i.e., the triangle inequalities mentioned in section 4.2.2 are enforced. The next step is to obtain channel energies, E_τ, for these curves as a function of the reaction coordinate. The centrifugal energy of the relative motion of the fragments must be considered along with the energies of the reactant and products modified by the switching function. The reactive flux is then determined by counting the number of such channels that are uniformly bounded by the total energy, i.e., $E_c(\xi) + E_\tau(\xi)$ is less than the total available energy for reaction for all ξ greater than ξ_0. This method is computationally intensive and various simplifications have been suggested.[18]

The brief survey of statistical theories presented above highlights the similarities and differences between them. Its purpose is to remind the reader of the different ways of calculating rates of a reaction based on the statistical hypothesis. In the following chapters, we compare energy-resolved experimental rates with the predictions of these theories.

4.3. References

1. See, e.g.,M. L. Goldberger and K. M. Watson, in *Collision Theory*, ch. 8, Krieger, NY, (1975).

2. See, e.g., L. D. Landau and E. M. Lifschitz, *Nonrelativistic Quantum Mechanics* (Pergamon, NY, 1982).

3. U. Fano, *Phys. Rev.*, **124**, 1886, (1961).
   F. H. Mies and M. Krauss, *J. Chem. Phys.*, **43**, 4455, (1966).
   F. Mies, *J. Chem. Phys.*, **51**, 787, (1969).
   S. A. Rice, in *Excited States*, **V2**, (ed. E. C. Lim), 111, (1975).

5. See, e.g., E. Pollak, in *Theory of Chemical Reaction Dynamics*, ed. M. Baer (CRC Press, FL, 1985).

6. See, e.g., D. G. Truhlar and B. C. Garrett, *Ann. Rev. Phys. Chem.*, **35**, 159, (1984).
   P. Pechukas, *Ann. Rev. Phys. Chem.*, **32**, 159, (1981).

7. E. Wigner, *Trans. Farad. Soc.*, **34**, 29, (1938).

8. W. L. Hase, *J. Phys. Chem.*, **90**, 365, (1986).
   D. L. Bunker, *J. Chem. Phys.*, **40**, 1946, (1964).

9. I. Oref and B. S. Rabinovitch, *Acc . Chem. Res.*, **31**, 117, (1979).
   D. W. Noid, M. L. Kozykowski and R. A. Marcus, *Ann. Rev. Phys. Chem.*, **32**, 267, (1981).

10. P. J. Robinson and K. A. Holbrook, in *Unimolecular Reactions* Wiley, New York, (1972).
    W. Forst, *Theory of Unimolecular Reactions* Acad. Press, NY, (1973).
    R. E. Weston and H. A. Schwarz, *Chemical Kinetics* Prentice-Hall, Englewood Cliffs, NJ, (1972).
    D. M. Wardlaw and R. A. Marcus, *Adv. Chem. Phys.*, **70**, 231, (1988).

11. O. K. Rice and H. C. Ramsperger, *J. A. C. S.*, **49**, 1617, (1927).
    L. S. Kassel, *J. Phys. Chem.*, **32**, 225, 1065, (1928).

12. R. A. Marcus, *J. Chem. Phys.*, **20**, 359, (1952).
    R. A. Marcus and O. K. Rice, *J. Phys. Colloid. Chem.*, **55**, 894, (1951).
    R. A. Marcus, *J. Chem. Phys.*, **43**, 2658, (1965).
    R. A. Marcus, *ibid.*, **52**, 1018, (1970).

13. See, e.g., W. H. Miller, *J. Chem. Phys.*, **65**, 4343, (1976).

14. W. A. Wong and R. A. Marcus, *J. Chem. Phys.*, **55**, 5625, (1971).
D. L. Bunker and M. Pattengil, *J. Chem. Phys.*, **48**, 772, (1968).

15. S. W. Benson and D. M. O'Neil, *Kinetic Data for Gas Phase Unimolecular Reactions*, **NBS–21**, US Dept. of Comm., 1970.

16. P. Pechukas and J. C. Light, *J. Chem. Phys.*, **42**, 3281, (1965).
P. Pechukas, R. Rankin and J. C. Light, *J. Chem. Phys.*, **44**, 794, (1966).
C. Klotz, *J. Phys. Chem.*, **75**, 1526, (1971).
C. Klotz, *Z. Naturforsch.*, **A27**, 553, (1972).
W. Chesnavich and M. Bowers, *J. Chem. Phys.*, **66**, 2306, (1977).

17. D. M. Wardlaw and R. A. Marcus, *Chem. Phys. Lett.*, **110**, 230, (1984).
D. M. Wardlaw and R. A. Marcus, *J. Chem. Phys.*, **83**, 3462, (1985).
D. M. Wardlaw and R. A. Marcus, *J. Phys. Chem.*, **90**, 5383, (1986).

18. M. Quack and J. Tröe, *Ber. Bunsen. Phys. Chem.*, **78**, 240, (1974).
M. Quack and J. Tröe, *ibid.*, **79**, 170, (1975).
M. Quack, *J. Phys. Chem.*, **83**, 150, (1979).

19 R. A. Marcus, *J. Chem. Phys.*, **43**, 1598, (1965).
J. O. Hirschfelder and E. Wigner, *J. Chem. Phys.*, **7**, 616, (1939).

CHAPTER 5

TIME-RESOLVED PHOTOFRAGMENT SPECTROSCOPY

CHAPTER 5A

Picosecond photofragment spectroscopy. I. Microcanonical state-to-state rates of the reaction NCNO → CN + NO

Lutfur R. Khundkar, Joseph L. Knee,[a] and Ahmed H. Zewail
Arthur Amos Noyes Laboratory of Chemical Physics,[b] California Institute of Technology, Pasadena, California 91125

(Received 9 December 1986; accepted 11 February 1987)

This paper, the first in a series of three papers, gives a detailed account of our studies on picosecond photofragment spectroscopy. The unimolecular reaction NCNO → CN + NO is examined in detail here. Microcanonical state-to-state rates are measured in molecular beams at different energies in the reagent NCNO using pump–probe techniques: one picosecond pulse initiates the reaction from an initial (v,J) state and a second pulse, delayed in time, monitors the CN radical product in a specific rovibrational state, or the reagent NCNO (transient absorption). The threshold energy for reaction is determined to be 17 083 cm^{-1} (bond energy = 48.8 kcal/mol). Measured rates are found to be sharply dependent on the total energy of the reagent, but independent of the rotational quantum state of product CN. Results of transient absorption measurements are used to argue that the ground state potential energy surface dominates the reaction in the range of excess energies studied. The energy dependence of the rates, $k_{MC}(E)$, is compared with that predicted by statistical theories. Both standard RRKM (tight transition state) and phase space theory (loose transition state) fail to reproduce the data over the full range of energies studied, even though nascent product state distributions are known to be in accord with PST at these energies. Furthermore, $k_{MC}(E)$ is not a strictly monotonically increasing function of energy but exhibits some structure which cannot be explained by simple statistical theories. We advance some explanations for this structure and deviations from statistical theories.

I. INTRODUCTION

In preliminary publications from this laboratory, we have reported on the technique of pico-[1] and femtosecond[2] photofragment spectroscopy and its application to the measurement of absolute rates of different classes of reactions. In a series of forthcoming papers we present detailed accounts of these studies, focusing on the following reactions in this set:

(I) Predissociation of a stable molecule

$$NCNO \rightarrow CN + NO .$$

(II) Local-mode overtone-initiated predissociation[3]

$$H_2O_2(v_{OH} = 5) \rightarrow 2OH .$$

(III) Predissociation of van der Waals clusters[4]

$$\text{phenol–benzene} \rightarrow \text{phenol} + \text{benzene} ,$$
$$\text{cresol–benzene} \rightarrow \text{cresol} + \text{benzene} .$$

In these experiments, two picosecond (or femtosecond) pulses are overlapped spatially and temporally in a seeded supersonic molecular beam (or in a low-pressure gas). The first pulse initiates the reaction from an initial state $(v,J)_i$ and the second pulse, delayed in time, probes the population of nascent products in a specific final vibrational/rotational state $(v,J)_f$, or monitors the evolution of the initial state of the reagent. In the former case, the state-to-state rate constant $(k_{i\rightarrow f})$ is measured with picosecond or subpicosecond time resolution. Product state distributions (PSD) may also be obtained by comparing the population in different final states at delay times much longer than the lifetime of the initial state. Information on alignment and correlation of angular momenta can also be deduced from studies where the polarization of the pump pulse relative to the probe pulse is varied.

The systems we have studied so far each possess some features that merit discussion individually. In NCNO, the oscillator strength is carried by a bound, excited electronic state. Reaction is preceded by energy redistribution to a lower electronic state, presumably because the density of vibrational states is large for the lower state at the energies of interest. In H_2O_2, an overtone of the OH stretch is excited directly on the ground-state surface and the mixing with other internal degrees of freedom is an important component of the dynamics of bond dissociation. The van der Waals' system has elements common to the other two. The vibrational densities are large, yet there is a large disparity between the frequencies of the complex modes and those of the internal modes of the uncomplexed molecules. One may expect separability of the two sets of modes, which would lead to nonstatistical effects in a large system. Studies on these model systems will improve our understanding of the domain of validity of the assumptions commonly used to describe unimolecular reactions.

A reaction may be considered fully characterized when the multidimensional potential energy surface (PES) governing the motions of the constituent atoms is exactly known. Product angular and translational energy distribu-

[a] Present address: Dept. of Chemistry, Wesleyan University, Middletown, CT 06547.
[b] Contribution No. 7513.

tions measured in crossed molecular beams[5] offer important experimental data that can be used to test a model PES. Unimolecular reactions, or half-collisions, constitute a special subset of the infinite number of fragment internal energy and impact parameter combinations possible in the reverse reaction, a bimolecular scattering experiment. The measurable quantities in this simpler case are product internal and external (translation) energy distributions as well as absolute rates. Consider the typical unimolecular reaction from state α to the final state (β,γ):

$$A^*(v_\alpha J_\alpha) \xrightarrow{k_{\alpha-(\beta,\gamma)}} B(v_\beta J_\beta;b) + C(v_\gamma J_\gamma;b) .$$

Several parameters may be defined—the rate of disappearance of A ($K_\alpha \equiv \Sigma_{\beta,\gamma}\, k_{\alpha-(\beta,\gamma)}$), the rate of formation of B or C and the impact parameter b. The state-to-state rate constant is the characteristic time constant for the appearance of products B or C in specific final states. The temporal behavior of A, B, or C can be measured in principle, b cannot be directly measured, but may be inferred from the distribution in different final states. K_α, the absolute reaction rate, cannot be derived from PSDs since the ratio of nascent population in different product states is simply the ratio of the state-to-state rates, $k_{\alpha-(\beta,\gamma)}$, of dissociation into those channels.

The measurements of rates and PSDs yield different information relevant to the dynamics. PSDs contribute information on the distribution of impact parameters that include effects of long range interactions (dispersion forces and electron correlation). These measurements are made after the entire ensemble has reacted and involves time delays of several tens of nanoseconds between initiation and probing. In rate measurements, the time evolution of the ensemble is of primary interest; energy redistribution and early time dynamics leave their signature on the form of the transient. The hope here is to be able to view the dynamics at early times and to compare rate measurements with predictions of statistical theories such as RRKM, phase space theory (PST), or the statistical adiabatic channel model (SACM). The combination of time resolution and molecular beams makes it possible to measure directly the rates (and PSDs) of an ensemble which is essentially microcanonical, with specified energy and angular momentum. This affords a stringent test of the theories of energy redistribution and unimolecular dissociation.

This first paper (I) in the series presents measurements of the state-to-state reaction rates of the unimolecular dissociation of nitrosyl cyanide (NCNO) to nitric oxide (NO) and the cyanogen radical (CN). The PSDs for this reaction have been studied in a complete series of experiments by Wittig and co-workers[6] and found to be in agreement with PST. Our experiments reported here are performed in a supersonic beam to obtain initial states with a narrow spread in energy and angular momentum, in contrast to the previously reported work[1(c)] performed in a low pressure, ambient temperature bulb or in an effusive beam. By continuously and independently varying the pump and probe photon energies, we provide k_{i-f} for different initial total energy in the reagent and for different rotational states of the CN product. The functional dependence of the rates on energy shows a threshold for reaction which is the bond energy in the absence of an exit channel barrier. We find phase space theory (PST) and simple RRKM treatments inadequate for explaining the energy dependence of the rates, $k_{MC}(E)$, over the range of excess energies studied. We observe "structure" in $k_{MC}(E)$ and offer a number of possible explanations for these deviations, including the idea of *dynamical trapping* in the exit channel of the PES whose details are presently unknown.

This paper is structured as follows. The experimental section (Sec. II) contains a summary of our apparatus. The results and analysis section (Sec. III) give specific details of the different experiments done and their results, followed by a description of how the raw data was analyzed. The fourth section develops the theoretical background relevant to the discussion and includes a summary of statistical theories. The discussion (Sec. V) is broken up into several subsections. The first one (Sec. V A) presents some spectroscopic information on the reagent and the products. The next one addresses the significance of measuring the time dependence of product appearance in different channels (Sec. V B). The dependence of rates on the initial angular momentum is briefly discussed next. The influence of intramolecular energy redistribution on reaction rates is considered in the light of transient absorption and recent fluorescence measurements (Sec. V D). Calculated phase space theory and RRKM rates are compared with the experimental rates (Sec. V E), showing the inadequacy of both models in explaining the energy dependence. Possible explanations for the structure in $k(E)$ are also explored.

II. EXPERIMENTAL APPARATUS

A. Two-color picosecond laser system

It is necessary to have two independently tunable sources of high energy picosecond pulses in order to measure the excess energy dependence of the temporal behavior of a given product channel. A detailed description of the laser system is presented in paper II,[3] and only a summary is presented here. The 1064 nm output of an actively mode-locked Nd–YAG was frequency doubled by focusing in a KTP crystal. The 532 nm visible light (~800 mW) was divided into two beams of approximately equal intensity and each one used as the pump source for a synchronously pumped dye laser. The output wavelength of each dye laser was selected by an intracavity three-plate quartz birefringent filter. Both dye lasers used R6G in ethylene glycol as the gain medium. One of these (DL1) was used to generate light at 580–565 nm, while the other (DL2) was used to generate light at ~610 nm. Typical pulses from each dye laser had Gaussian temporal profiles with a full-width at half-maximum (FWHM) value of ~8 ps. The measured spectral bandwidth was approximately Gaussian with ~3 cm^{-1} FWHM.

The pulses from the sync-pump lasers were amplified in two three-stage dye-amplifiers pumped by the doubled output of a Q-switched Nd–YAG laser operating at 20 Hz. A number of different dye solutions (R640, R610/R640, R610, KR620, R620/R590, and R590, all in methanol) were used to obtain proper amplification as the frequency of DL1 was changed. The visible output of amplified DL1 was

used as the pump with no further processing. The amplified output of DL2 was mixed with the 1064 nm fundamental of the DCR/2A in a KDP crystal to generate light at 388 nm and used to probe specific rotational states of the nascent ground-state CN radicals produced on dissociation.

The time delay between the two beams was set up in a Michelson interferometer. The pump beam (DL1) was directed through a fixed delay, while the probe beam (DL2) was directed through a variable delay consisting of a 2.5 in. hollow corner cube mounted on a stepper-motor driven translator (10.0 μ per step). The beams were combined in a dichroic mirror after which they were propagated collinearly and focused softly with a 1 m quartz lens into the expansion chamber. The focus was adjusted to be beyond the free jet, so that scatter and multiphoton processes could be minimized simultaneously.

The cross correlation of DL1 and DL2 after amplification was measured by generating the sum frequency[7] in a 1 cm KDP crystal. A typical cross correlation (Fig. 1) could be represented by a Gaussian envelop (FWHM $\approx$ 10 ps). The response functions for the transient absorption experiments described below were obtained by generating the difference frequency of the UV light (doubled DL1 or DL2) and the visible fundamental (DL1) in a KDP or $LiIO_3$ crystal. In this case the light generated had exactly the same frequency as the fundamental, but could be separated from it by using a spatial filter to give an essentially zero-background two beam signal. Figure 1 also shows typical cross correlations for this experiment when the tuning element in the laser was a two-plate birefringent filter. This configuration was used for some of the transient absorption studies described below.

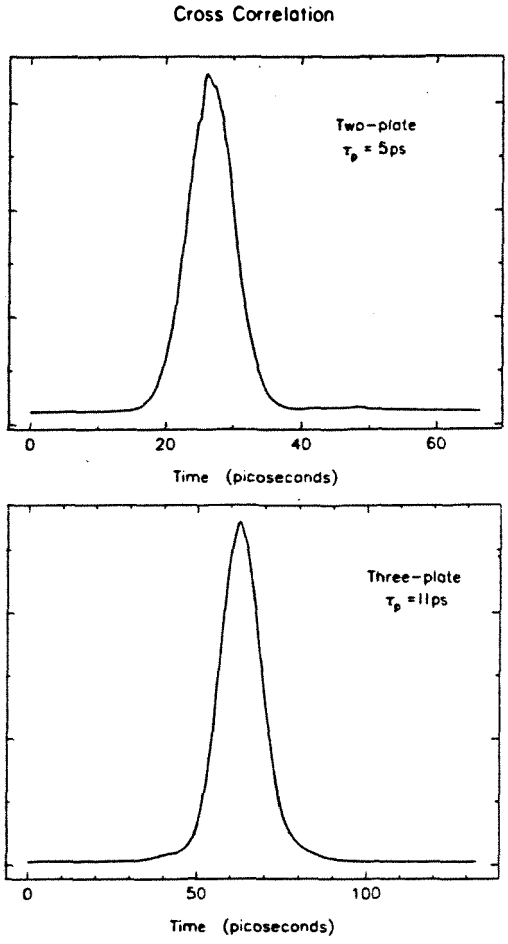

FIG. 1. Cross correlation of pump and probe lasers. The top figure was obtained by generating the difference frequency between the doubled output and the fundamental of DL1. A two-plate birefringent filter was used to reduce the temporal widths of the pulses. The lower trace was obtained by generating the sum frequency of DL1 and DL2. A three-plate birefringent filter was used in each sync-pump laser.

B. Molecular beam apparatus with LIF detection

A free jet expansion was used to eliminate internal energy in the parent NCNO molecule. The expansion chamber was pumped by two oil-diffusion pumps. The sample was introduced through a pulsed nozzle made of Kel-F, a perfluorinated, machinable plastic. The nozzle was operated at 20 Hz and triggered by the Q-switch of the YAG amplifier. The nominal aperture diameter d was 500 μ and the laser beams intersected the expansion 10 mm downstream from the nozzle, corresponding to $x/d \approx 20$. The results were not affected by decreasing d. Typical backing pressures of 1000 Torr He and nominal valve open-time of 100 μs resulted in an ambient pressure of 2×10^{-5} Torr at steady state. Short optical baffles were used on both input and output sides to reduce scattered light in the chamber.

Fluorescence was detected using a single $f/1$ quartz lens 2 inches in diameter which was adjusted to focus a point image defined by the laser beams and the axis of the expansion slightly beyond the detector. A UV sharp-cut filter (Corion LDS-370) and visible blocking filters (7-59 and interference-coated 7-54, Corning) were used to define the spectral window of detection. The detector was a high gain photomultiplier operated close to its maximum gain of 10^8. The output of the PMT was amplified and used as input to a variable gain boxcar integrator which was triggered off a fast photodiode illuminated by 532 nm light from the Q-switched laser. The gate for signal averaging was set to bias against laser scatter. The boxcar output was routed through a voltage to frequency converter and into a multichannel analyzer operated in the repetitive scaling mode. The channel step for the MCA was enslaved to a programmable stepper-motor controller which drives the optical delay translator. The data was averaged in the MCA and later transferred to a PDP 11/23+ minicomputer where it was analyzed and stored on floppy disks.

C. Sample preparation and handling

NCNO was prepared by the reaction of NOCl with AgCN according to the procedure of previous authors.[6,8] NOCl was prepared following a documented procedure.[9] Reagent grade chemicals were used in the syntheses without further purification. AgCN (Aldrich) was dried thoroughly under vacuum and cooled to -40 °C. NOCl was introduced

into the bulb containing AgCN and the gas–solid mixture was vigorously stirred. As the reaction proceeded, the vessel was kept cold with a bath of dry ice and acetone maintained below − 30 °C. After 15–20 min, the gaseous products were trapped out into a separate bulb immersed in liquid N_2. This procedure was repeated a number of times. The crude products which always contained a large amount of unreacted NOCl was purified by repeated bulb to bulb distillation from a hexane-liquid N_2 slush bath. Extreme care was taken during the synthesis as several reports of explosions have been made.[8]

A 22 l bulb was evacuated to ~100 mTorr and pure NCNO introduced to ~1 Torr. The bulb was then pressurized to 1000 Torr with He and connected to the input line for the pulsed nozzle. The bulb was refilled with pure He every 2 h, during which time the pressure in it dropped to ~800 Torr. This procedure could be repeated 20 times before the total signal level would start to affect the quality of the data. At that point the bulb was evacuated and fresh sample introduced. Except where specifically stated, this was our operating condition for all transients recorded.

The experiments to elucidate initial J dependence of dissociation rates were done similarly, with the following differences. A much smaller bulb (5l) was used and N_2 was the carrier gas employed. The bulb was pressurized to 100 Torr and the drop in pressure over 1.5 h was ~10 Torr. The sample delivery manifold was checked carefully against leaks to the atmosphere. These expansions are referred to later as *warm*.

III. RESULTS AND DATA ANALYSIS

Several different types of experiments were undertaken and a short description of each type is given below, with the results obtained in each case. The molecular transient response for a combination of pump and probe wavelength was obtained by varying the delay between the pulses. Care was taken to ensure that the range of the delay was $\gtrsim 4\tau$, where τ is the characteristic constant of a single exponential fit to the data. This was possible for all cases except at threshold, where τ was longer than 1 ns.

A. Product rotational state dependence

In this set of experiments, the pump laser (DL1) was tuned to a known absorption band of the parent molecule.[6] The probe laser (DL2) was tuned to a wavelength such that the sum frequency obtained after mixing with the 1064 nm was resonant with a specific transition in the R branch of the $\Delta v = 0$ band of the $B\,^2\Sigma^+ \leftarrow X\,^2\Sigma^+$ electronic transition of CN.[10] With the pump laser frequency fixed, the wavelength of the probe laser was tuned to various resonances in the R branch corresponding to different rotational levels (N'') of ground state CN. A series of transients corresponding to different N'' and a fixed pump wavelength showed characteristic risetimes which were identical within experimental error. This was observed for several different pump energies in the range of excess energies covered in this study.

B. Excess energy dependence

These experiments were similar in concept to the ones described above. The pump laser was tuned to a vibronic transition in the $S_1 \leftarrow S_0$ absorption band. The probe laser was tuned to monitor a single N'' state in the ground state of CN, typically the one with maximum probability for population on dissociation of NCNO. In this set, the probe laser remained fixed for the most part, while the pump laser was tuned through the absorption spectrum.

The dissociation rate of NCNO, as manifested by the appearance rate of the fragment CN, as a function of the excess energy in the parent was measured from 5853 to 5630 Å. The threshold for reaction derived from this data set is 17 083 cm^{-1}, in excellent agreement with the reported value of 17 085 cm^{-1}.[6] In the range of energies studied, the characteristic constants varied from >2.0 ns at threshold to 10.0 ps at 690 cm^{-1}. Typical transients are shown in Fig. 2 and the fitted rate constants are plotted as a function of excess energy in Fig. 3. A study of the signal intensity as a function of the pump laser power showing linear dependence is presented in Fig. 4. The signal was also found to vary linearly with the intensity of the probe laser.

C. Total angular momentum dependence

In order to investigate the effect of parent rotation on the rate of decomposition, we changed the expansion conditions. A *warm* expansion would leave significant population in higher J states of the parent. The pump wavelength was held fixed at 5846 Å which lies in the middle of an unstructured region of S_1 absorption. The probe was tuned for different N'', as described in Sec. III A, and the responses measured are shown in Fig. 5. These rates show a marked dependence on N'', the effect being particularly striking for the highest N'''s, which show a biexponential temporal behavior.

D. Transient absorption

This set of experiments was designed to probe the bound parent molecule. As before, DL1 was tuned to a resonance in S_1. The amplified light of DL1 was frequency doubled to generate 285 nm, which was then used as the probe. The UV probe may also be obtained by frequency doubling the output of DL2. Fluorescence dependent on both fields was observed and identified as spontaneous emission from the $B\,^2\Sigma$ state of CN using appropriate cutoff filters. The measured lifetime of this fluorescence was found to be 56 ns, which is identical to that of the fluorescence observed using a probe resonant with the CN $B \leftarrow X$ transition.[10] The signal was linearly dependent on the intensity of both fields. In this scheme, molecules absorbing photons from both pump and probe fields dissociate to the electronically excited B state of CN (Fig. 6).

The transient absorption of the parent was measured at a number of different energies above and below the threshold for dissociation. For excitation below threshold, the pump laser was tuned to a weak S_1 resonance at 5912 Å.[11] The

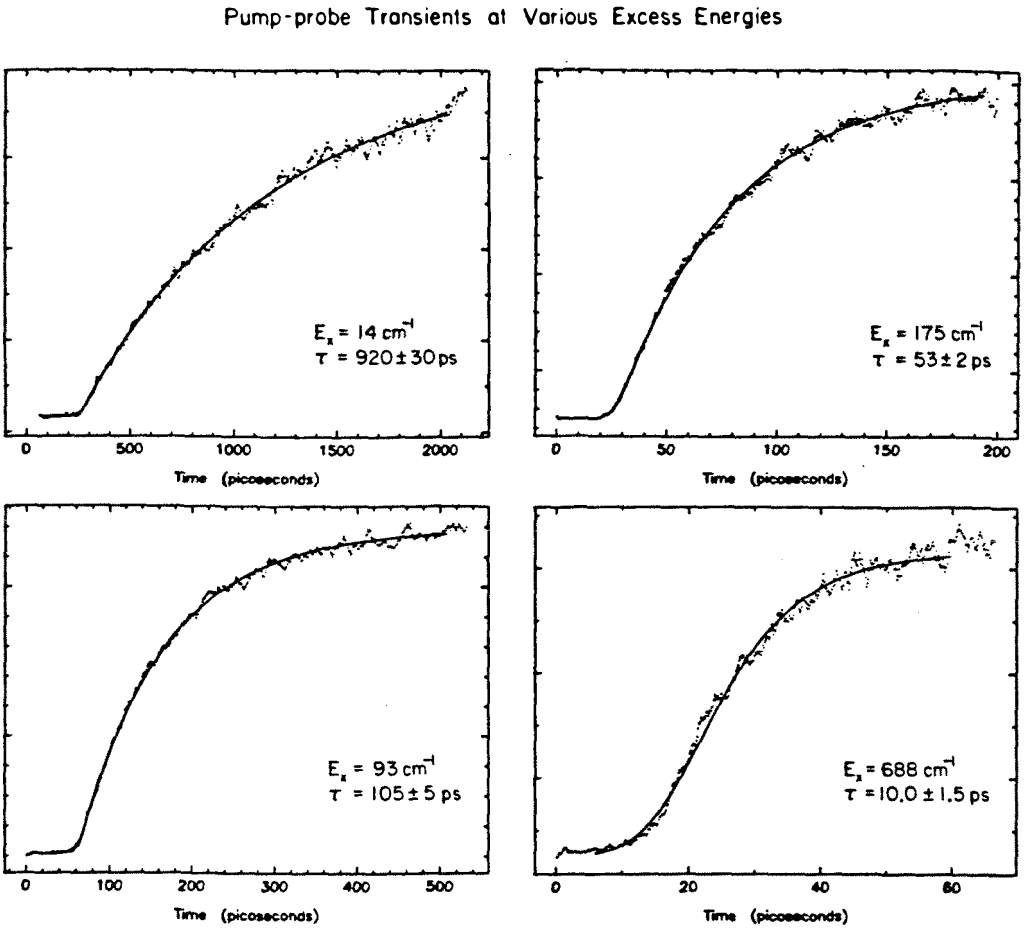

FIG. 2. Typical transients observed at different pump energies. The solid lines are our best fit of the data to single exponential buildup (see the text). The same applies to other related figures.

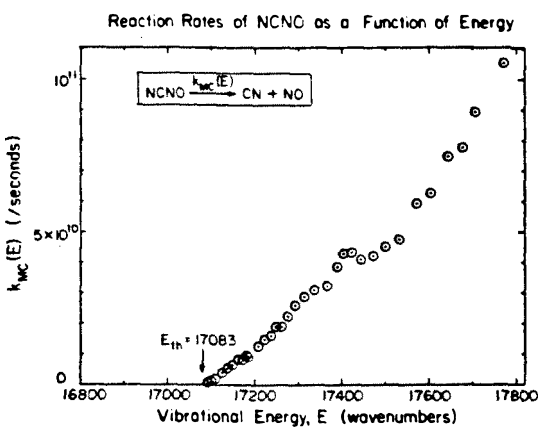

FIG. 3. The excess energy dependence of measured microcanonical rates from 5853 to 5630 Å. Included in this data are the rates measured for different N'' states of CN. As mentioned in the text, different N'' show the same rate when measured in a cold expansion.

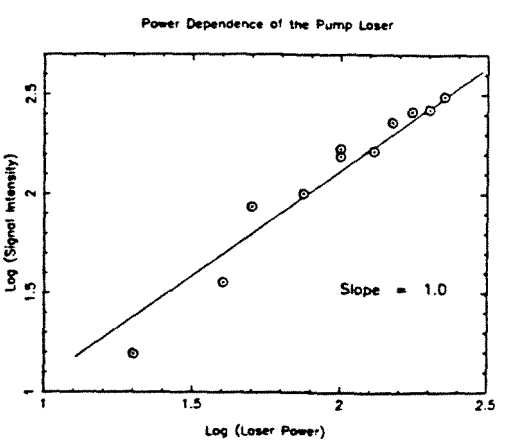

FIG. 4. Observed signal intensity as a function of the intensity of the pump laser. The background was obtained by measuring the signal at large negative time and subtracting it from the signal at large positive time.

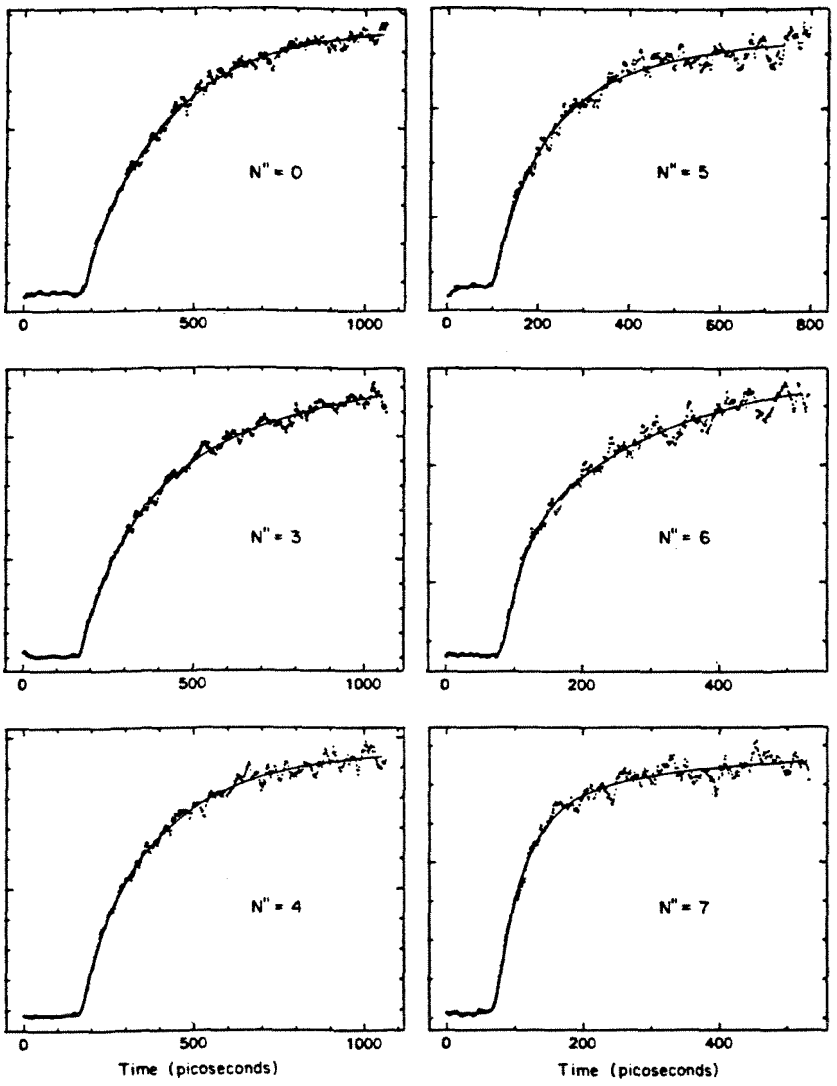

FIG. 5. Transients observed while probing different CN(N'') with pump frequency fixed at 5845 Å. These experiments were done on the *warm* expansion (see the text).

measured response showed an instantaneous rise and no subsequent decay on our time scale. At all excess energies above threshold, the measured decays were exponentials, with the time constant equal to that of the corresponding rise of CN at the same pump energy. Typical transients at different energies are presented in Fig. 7.

E. Data analysis

The system response function was approximately Gaussian. The standard nonlinear least-squares analysis based on the Marquardt algorithm[12] was used to fit the cross correlations to this functional form. Typical pulse FWHM values were in the range 9.5 to 11.5 ps.

The pulse width obtained from a fit of the cross correlation to a Gaussian form was used to derive accurate rate constants from the molecular responses measured in the experiments described in Secs. III A–III C. Although the cross correlation of the two visible beams is not the true system response, the 388 nm radiation used in these experiments appears to have the same temporal profile as that of the fundamental visible used to generate it. A simple argument supporting this observation is that the temporal fluctu-

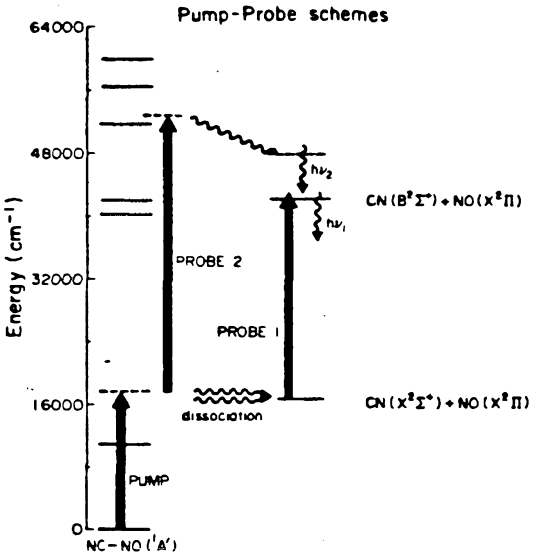

FIG. 6. Experimental schemes for transient absorption and CN state selected detection. Pump and probe wavelengths are independently tunable. PROBE 1 corresponds to resonant excitation of specific rotational states of product CN. PROBE 2 is absorbed by the bound molecule; the highly excited NCNO dissociates into electronically excited CN, and the spontaneous fluorescence is detected.

ations in the intensity of the ~3 ns, 1064 nm beam from the Q-switched YAG should be negligible over 10 ps, the time range of interest. The measured cross-correlation functions were used to deconvolute the transient decays described in Sec. III D. The fitted decay lifetimes were found to be the same as those obtained by deconvoluting the transients with a Gaussian pulse simulating the cross correlation.

The data reduction code was also based on the same algorithm and set up for the analysis of fluorescence decays. As shown in the Appendix, the convolution of a pulse with an exponential rise has the same mathematical form as the convolution of the integral of the pulse with an exponential decay having the same time constant. We used the second approach to deconvolute our data to derive the reported dissociation rates.

The transients presented in the figures were all smoothed using a three-point averaging algorithm.[13] Since the exponential constants were typically 100 channels, averaging has little effect on the derived rate constants. Reduced χ^2 values obtained with statistical weighting were in the range 2.0 to 5.0. The weighted residuals showed that the nonrandom noise distribution responsible for these large values had high frequency components that may be due to the mode quality of the pulsed YAG amplifier and imperfect alignment of the interferometer.

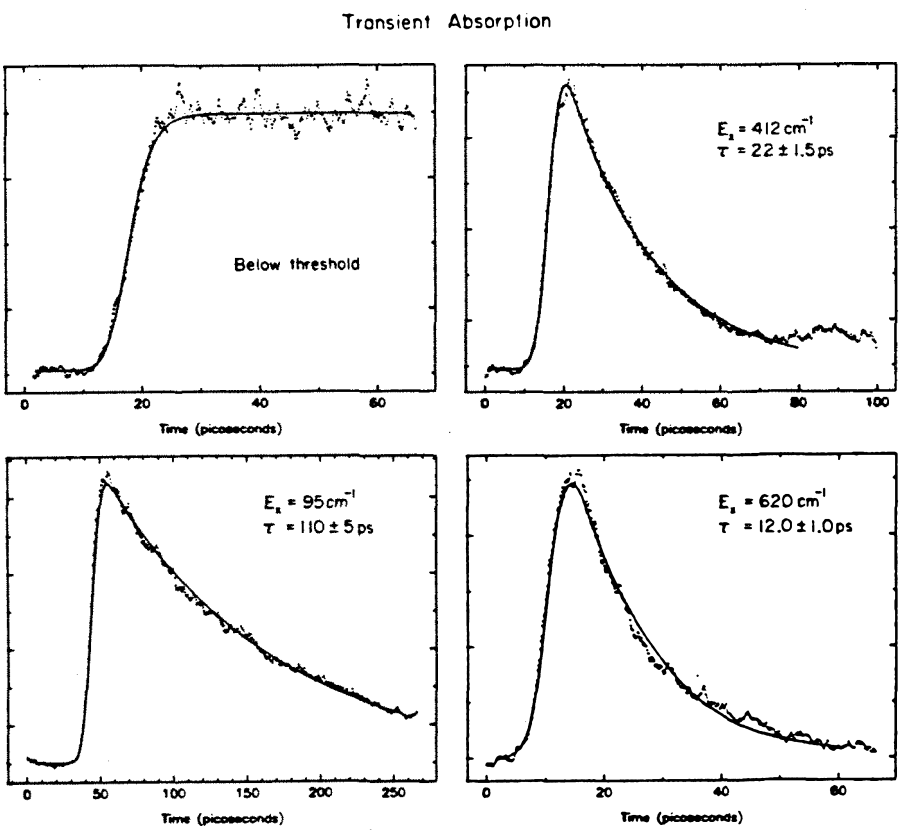

FIG. 7. Transient absorption signals measured at different pump energies. Note the agreement with results in Fig. 2 for $E_x = 95\ cm^{-1}$. The same agreement was found at other excess energies studied.

IV. THEORY

A. Kinetic model

A quasibound or metastable state has a wave function which can be represented in a low-order approximation by a superposition of a bound state and continuum wave functions.[14] The bound states form a basis in a local sense, i.e., if the system is restricted to a small volume in configuration space. It is well known that an isolated level coupled to a continuum can be represented quantum mechanically as a state having a complex energy.[15] Population in these states, if observable, would decay exponentially with a time constant proportional to Γ, the effective coupling constant. A polyatomic molecule dissociating into two fragments can be formally represented in the same way. The true bound states of the parent molecule may be used to construct an approximate basis set. Each set of bound state quantum numbers of the fragments has an associated translational energy continuum to which the bound states of the parent polyatomic are coupled. Thus so-called *state-to-state* rates of an unimolecular dissociation process are simply measures of the coupling strength of an approximate molecular state to each continuum channel.

The obvious kinetic scheme for the dissociation of a polyatomic molecule A into two fragments B and C is shown in Fig. 8. The sets $\{v_i, J_i, \tau_i\}_X$ designate the vibrational (v_i) and rotational (J_i, τ_i) quantum numbers of the molecule X and identify the initial state i. Population in the ith state of X at time t is abbreviated to $[X_i(t)]$ below. The solutions to the three simultaneous linear first-order differential equations describing the temporal behavior of each molecule are readily obtained. If the initial conditions are that only $[A_\alpha(0)]$ is nonzero,

$$[A_\alpha(t)] = [A_\alpha(0)]e^{-K_\alpha t}, \tag{1}$$

$$[B_\beta(t)] = [A_\alpha(0)] \sum_\gamma \frac{k_{\alpha-(\beta,\gamma)}}{K_\alpha}\left[1 - e^{-K_\alpha t}\right], \tag{2}$$

$$[C_\gamma(t)] = [A_\alpha(0)] \sum_\beta \frac{k_{\alpha-(\beta,\gamma)}}{K_\alpha}\left[1 - e^{-K_\alpha t}\right], \tag{3}$$

where $K_\alpha = \Sigma_{\beta,\gamma}\, k_{\alpha-(\beta,\gamma)}$. The sums in Eqs. (2) and (3) are to account for the correct counting of channels for, say, fragment B in a quantum state β with all possible concomitant states γ of fragment C. The observed time dependence will be exponential, a decay for A and buildup for B or C, with time constant equal to the *total rate* of depopulation of the initial state. The probability of products appearing in channel (B_β, C_γ) is $k_{\alpha-(\beta,\gamma)}/K_\alpha$. Therefore, analysis of product state distributions must be used with measurements of absolute rates to derive estimates of $k_{\alpha-(\beta,\gamma)}$. Furthermore, PSDs cannot provide absolute rates (K_α) since they only give ratios of $k_{\alpha-(\beta,\gamma)}/K_\alpha$.

This description of a unimolecular reaction is useful for comparison between theory and experiment only if the nature of the initial state(s) and their coupling(s) to the translational continua are known. The true molecular basis of the bound molecule cannot be exactly specified since all the interactions between the internal degrees of freedom are typically not known. In practice, additional simplifying assumptions that allow one to predict $k_{\alpha-(\beta,\gamma)}$, K_α and other quantities of interest as functions of globally conserved quantities E and J are made. One of these, the statistical approximation, is discussed briefly.

B. Statistical models for microcanonical rates

A proper statistical treatment of rates conserves all constants of motion and weights all degeneracies equally. For a typical potential energy surface with a single saddle point (Fig. 9) representing the unimolecular reaction A → B + C, the classical microcanonical rate is proportional to the flux of points through a hypothetical surface S_m in phase space. If S_m is drawn such that a given trajectory will intersect it at most once, the rate is given by[16,17]

$$k = \frac{1}{h^n \rho^{(n)}(E)} \int dp \int dq\, \delta[E - H(p,q)] \times \delta[f_0(q)]\left(\frac{\partial f_0}{\partial q}\cdot\frac{p}{\mu}\right) G_0\left[\frac{\partial f_0}{\partial q}\cdot p\right].$$

q and p are generalized coordinates and momenta, each integral is n-dimensional, E is the total energy, $H(p,q)$ is the n-dimensional Hamiltonian, $G_0(x)$ is the unit step function, $\rho^{(n)}(E)$ is the density of states in the vicinity of the well respresenting A, and $f_0 = 0$ defines the $(n-1)$-dimensional dividing surface, S_m. $\delta[E - H(p,q)]$ in the integral specifies a microcanonical (MC) ensemble, $\delta(f_0)$ restricts the integral over coordinate dimensions to S_m, and the last two factors constitute the forward flux from A to products through

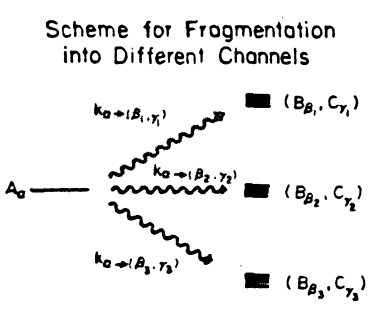

FIG. 8. Kinetic model for dissociation into various fragment channels identified by quantum numbers.

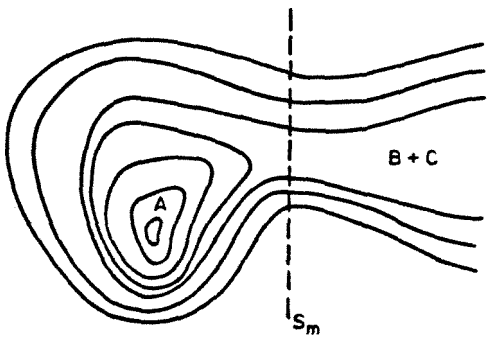

FIG. 9. A two-dimensional contour representation of a typical potential energy surface for unimolecular dissociation of A into B and C.

it. The integral reduces to the microcanonical partition function of the system restricted to the dividing surface which is the usual juncture for introducing quantization.[16,17] The MC partition function is the total number of bound states with energy less than E, $N(E)$. Using a superscript † to emphasize that the relevant integral has one less degree of freedom, the rate assumes the familiar expression associated with RRKM theory[16]:

$$k_{MC}(E) = \frac{N^{\dagger}(E^{\dagger})}{h\rho(E)} . \tag{4}$$

An application of this formula requires knowledge of the shape and position of the dividing surface as well as ρ. How correct a calculation of the rate constant is will be determined by how accurately S_m is described and how well $\rho(E)$ is assessed. The choice of S_m must satisfy a minimum flux ($N^{\dagger}$) criterion,[18] but its shape cannot be completely specified without detailed knowledge of the potential energy surface (PES). Standard methods of approximating $N^{\dagger}$ without recourse to the PES are described below.

1. RRKM theory

The zero-order approach is to model S_m by a surface perpendicular to q, the coordinate that best describes the bond being broken, and similar in shape to one drawn through the local minimum of the potential corresponding to A, and also perpendicular to q. This approximation, known as *standard* RRKM, is clearly an idealized case and will be good if the true S_m lies close to the equilibrium position of the reactants. In more familiar terms, S_m represents a fictitious molecule (*critical configuration* or *transition state*) with one less degree of freedom than the reactant. This lost degree is the reaction coordinate and is used to parametrize the extent of reaction in an intuitive sense. A standard RRKM calculation thus assumes a transition state whose vibrational frequencies and rotational constants are the same as the corresponding ones in the reactant. In the literature, this is referred to as a *tight* transition state.

2. Phase-space theory

For transition states of infinite looseness, yet another idealized case has been used to estimate $N^{\dagger}$ with explicit conservation of angular momentum. In this model,[19] S_m is placed at the local maximum of an effective potential, V_{eff}, obtained from the sum of a long range attraction, $V_b(r)$, and centrifugal repulsion due to orbital motion of the separating particles. Energy conservation imposes an upper limit on the orbital momentum quantum number. For a tetraatomic molecule (A) dissociating into two diatomic fragments (B and C), the conservation laws are

$$\mathbf{J} = \mathbf{J}_A = \mathbf{J}_B + \mathbf{J}_C + \mathbf{l} , \tag{5}$$

$$E_{avail} = E - \max\{V_{eff}(r)\} > \sum_{n=B,C} E_n(\text{vib}) + E_n(\text{rot}) , \tag{6}$$

$$V_{eff}(r) = V_b(r) + \frac{\hbar^2 l(l+1)}{\mu r^2} . \tag{7}$$

E is the energy in the parent and $V_b(r)$ is a one-parameter representation of the potential energy along the bond dissociation coordinate. The dissociation energy E_0 is $V_b(\infty)$. Note that E_0 includes the zero point energies of the reactant and products. $\mathbf{J}_A$ is the total angular momentum of the parent, $\mathbf{J}_B$ and $\mathbf{J}_C$ the total angular momentum of B and C, respectively, and $\mathbf{l}$ the angular momentum of the relative motion of the separating fragments. $E_n(\text{vib})$ and $E_n(\text{rot})$ are the vibrational and rotational energies of the fragment n. μ is the reduced mass and the second term in the right-hand side of Eq. (7) is the centrifugal potential. $E - E_0$ is the total energy available for product translation and internal motion at large distances. E_{avail} is this energy minus the centrifugal barrier to recombination (the reverse reaction) for each value of l. The barrier energy appears exclusively as translational energy in the separated products. Generally, V_b is approximated by the attractive part of the Lennard-Jones 6-12 potential. $N^{\dagger}$ is then obtained by counting all possible combinations of product quantum numbers satisfying energy and angular momentum conservation:

$$N^{\dagger}(E - E_0) = \sum_{v_n} \sum_{J_B J_C l} \kappa . \tag{8}$$

The parameter κ is a measure of the contribution of a combination of quantum numbers to the reaction rate and should be a constant for a proper statistical theory. It may be regarded as the microscopic transmission coefficient and is generally chosen to be unity. The sum in Eq. (8) is over all allowed J_B, J_C, l and vibrational states, v_n. It is convenient to define J', an intermediate quantum number corresponding to the sum of $\mathbf{J}_B$ and $\mathbf{J}_C$, in performing the calculation of $N^{\dagger}$. The conservation of angular momentum imposes the following restrictions on J' and l:

$$|J_B - J_C| < J' < J_B + J_C ,$$
$$|J' - l| < J < J' + l .$$

It should be noted that the degeneracies of J_B, J_C, and l have been included in the sum, but they do not appear explicitly in Eq. (8).[20]

3. Refined models

Standard RRKM and PST represent two extreme cases. A number of modifications have been proposed to better mimic physical situations which most probably lie between these cases. The frequencies and rotational constants of the transition state can be modified following intuitive semiquantitative prescriptions.[21] Another variation (SACM) proposes a method for parametrizing molecular quantum numbers by the reaction coordinate and examining each such adiabatic channel to determine whether it is energetically accessible at all points between reactants and products.[22] PST has been criticized because it allows free rotation of the fragments within the transition state complex. A method (SSE)[6] for calculating PSDs that treats vibrations and rotations somewhat differently has been recently proposed and applied to the dissociation of NCNO at energies where product vibrations are excited and PST overestimates the extent of rotational excitation in the fragments. Classical trajectory calculations[23] offer a means of avoiding the statistical assumptions but require explicit knowledge of the PES.

The minimum flux criterion mentioned is derived from treating k_{MC} variationally. Several treatments have formalized this approach as microcanonical variational transition state theory.[24] A recent treatment of the dissociation of small polyatomic molecules involving transition states of arbitrary looseness uses canonical variables and Monte Carlo techniques for numerically estimating the multidimensional integrals in Eq. (4).[25] All of these methods presume a model of the PES which may be altered to obtain better agreement with experimental observations. We leave applications of these more elaborate models for future work.

V. DISCUSSION

A. Preliminary considerations

Before embarking on a detailed analysis of our results, we summarize the spectroscopy of NCNO and the fragment radicals CN and NO in this section. We also address the issues related to the selectivity of these experiments, namely, how well do we know our initial and final states.

1. Spectroscopy of parent and fragment molecules

NCNO has been thoroughly studied by microwave,[26] infrared,[27] and visible[28] spectroscopy. Studies by Wittig and co-workers on jet-cooled NCNO has provided rich information on the spectra.[28] Molecular constants for both ground state and excited state NCNO taken from the current literature are listed in Table I. The molecule is bent and planar in the ground state and has C_s point group symmetry. In the first excited singlet state ($n\pi^*$), the molecule is also planar and bent. Strong perturbations in the spectrum have been attributed to extensive mixing with the ground singlet state promoted by the bending modes. Near the S_1 origin, the rotational structure has been resolved and the band assigned[28] as a C-type transition, i.e., the transition moment is perpendicular to the molecular plane and parallel to the c axis of inertia.[29] At higher energies, vibronically induced A /B-type transitions to nontotally symmetric bands are observed.

TABLE I. Spectroscopic parameters of NCNO, CN, and NO.

NCNO: Vibrational frequencies and rotational constants (Refs. 26–28) (cm^{-1})				
ν_1''	CN stretch (*terminal*)	2170	A''	2.71
ν_2''	NO stretch	1501	B''	0.18
ν_3''	CN stretch (*central*)	820	C''	0.16
ν_4''	CNO bend	216.5	A'	4.77
ν_5''	NCN bend	588.5	B'	0.16
ν_6''	out of plane bend	269.6	C'	0.16
	CN: Molecular constants (Ref. 32) (cm^{-1})			
$^2\Sigma$				
	ν	2068.7		
	B_v	1.889 8		
	γ	0.007 25 spin–rotation constant		
	NO: Molecular constants (Ref. 32) (cm^{-1})			
$^2\Pi_i$				
	ν	1904.03		
	B_v	1.672		
$^2\Pi_j$				
	ΔE_{so}	119.62 spin–orbit splitting		
	ν	1903.68		
	B_v	1.720		

Overtones and combinations of the ν_4 bending mode are considerably broader than other transitions at comparable energies, indicating its role as a promoting mode for S_1–S_0 mixing.[28] Similar effects have been observed in the absorption spectrum of HNO[30] and likewise attributed to perturbations between the two lowest states. A sharp onset for the production of CN radicals occurs at 17 085 cm^{-1}. The S_1 absorption spectrum in this energy region shows structure reminiscent of C-type bands, but the rotational substructure of these bands cannot be resolved with laser linewidths of 0.04 cm^{-1}. This must be due to perturbations of the levels, since the measured dissociation rate at threshold ($\sim 10^8\ s^{-1}$) implies homogeneous widths $\sim$0.001 cm^{-1}. Fluorescence measurements have been recently made on expansion cooled NCNO (see Sec. V D) and estimates of the radiative lifetime (20 μs) can be made for these nitroso compounds.

The fragment CN is a typical Hund's case (b) diatomic.[29] The ground state is a $^2\Sigma$ state and the angular momentum without spin (N) is an approximate quantum number. N is the sum of nuclear rotational angular momentum (R) and the electronic orbital angular momentum (Λ), and is coupled weakly to the electron spin. The appropriate energy expressions[31] are given below and an energy level diagram showing some of the rotational levels is presented in Fig. 10:

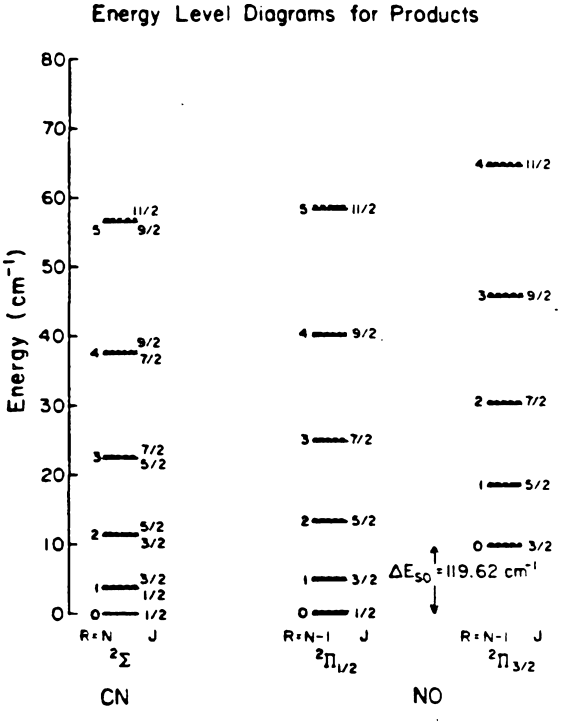

FIG. 10. Energy level diagram showing rotational states of CN and NO. The numbers on the left of each set of levels (R) identify it with the nuclear rotational angular momentum. The labels to the right correspond to the *total* angular momentum J. Note that the spin–orbit splitting of NO is not represented to scale. The spin–rotation and λ-doublet splittings (dashed levels) are exaggerated for clarity. For CN, N is a good quantum number, while J is the quantum number for NO.

$$F_1(N) = B_v N(N+1) + \tfrac{1}{2}\gamma N,$$
$$F_2(N) = B_v N(N+1) - \tfrac{1}{2}\gamma(N+1).$$

The total angular momentum J is given by $N \pm \frac{1}{2}$ for the states F_1 and F_2, respectively. B_v is the rotational constant in a particular vibrational state and γ is the spin–rotation coupling constant.

The fragment NO is a typical Hund's case (a) molecule. The ground state is $^2\Pi$ and nonnegligible spin–orbit coupling breaks the degeneracy due to the nonzero projection of the electronic spin angular momentum on the internuclear axis. The total angular momentum (J) is the sum of the rotational angular momentum and the electronic angular momentum including spin. Each level is doubly degenerate, corresponding to the two possible ways of electron motion about the figure axis. For high values of J, this degeneracy is also removed (λ-doubling). The appropriate energy expressions for the $^2\Pi_{1/2}$ and $^2\Pi_{3/2}$ states are[31]

$$E_J(^2\Pi^{\pm}_{1/2}) = B_v^{(1/2)} J(J+1) \pm \xi_{1/2}(J),$$
$$E_J(^2\Pi^{\pm}_{3/2}) = B_v^{(3/2)} J(J+1) + \Delta E_{so} \pm \xi_{3/2}(J).$$

The energy scale is referenced to the lowest rotational level ($J = 1/2$) of the $^2\Pi_{1/2}$ state. $\xi_{1/2}$ and $\xi_{3/2}$ are the J dependent corrections to the energy due to orbital–rotation (spin–uncoupling) interaction and are important only for high J. These terms are ignored in the discussion below. ΔE_{so} is the spin–orbit splitting which is the energy of the lowest rotational level ($J = 3/2$) of the $^2\Pi_{3/2}$ state. It is important to note that the energy in this case is determined primarily by J and not N, in contrast to CN. The spectroscopic constants are collected in Table I.

2. Resolution of initial and product states

The final distribution of internal energy in molecules in a free-jet expansion is generally described in terms of effective vibrational, rotational, and translational temperatures.[33] These values depend on the carrier gas used and are typically small, ~10 K for vibrational, ~5 K for rotational, and ~1 K for translational distributions. In NCNO, the smallest ground state vibrational fundamental is 216 cm^{-1} which has an occupation probability of 0.002 at 50 K. Thus vibrational energy in the parent may be ignored for cold expansions. On the other hand, the rotational constants are small and a significant fraction of the molecules lie in states with $J > 0$. Under similar expansion conditions Noble *et al.*[28] determined rotational temperatures of 2 K by resolving the rotational fine structure of the origin band. Their estimate of the average rotational quantum number is $J = 3$. On scanning the frequency of the probe laser at a number of fixed pump energies, we observed a sharp drop in signal intensity for probe frequencies greater than that required to detect CN fragments with the maximum rotational quantum number that is energetically allowed, as reported by Nadler *et al.*[6] This suggests that the spread of internal energies in NCNO in our expansion is also small and we assume that the terminal rotational temperature in our studies is also ~2 K.

The $S_1(^1A'') \leftarrow S_0(^1A')$ transition in NCNO is dipole allowed (orbitally forbidden[28]) having its moment parallel to the principal axis of largest moment of inertia (C-type). The approximate symmetric top selection rules (perpendicular-type transition) are

$$\Delta J = 0, \pm 1 \quad \Delta K = \pm 1.$$

At excitation energies near dissociation threshold where mixing with another electronic state is believed to be extensive, the pure rotational quantum number is not a good one but the total angular momentum must be conserved. The reactive ensemble is essentially microcanonical with angular momentum $J = 3$ and energy equal to the sum of the photon energy and the rotational energy. The spectral bandwidth of the excitation laser is 3 cm^{-1} FWHM, which determines the spread in energy in the reactive ensemble.

The probe laser is tuned to a specific transition in the R branch ($\Delta N = +1$) of the $B \leftarrow X$ band of CN. This transition shows a bandhead in the P branch when the diatom is rotationally very excited. The R branch was chosen to avoid spectral overlap between transitions from different N'' levels at the higher excitation energies. The spectral bandwidth of the probe laser (3 cm^{-1}) is smaller than the spacing between adjacent peaks in this branch. Thus different N'' states of CN can be monitored quite cleanly, although the different spin–rotation states (F_1 and F_2) are not resolved. Since simultaneous measurements on NO were not made, the population of CN in a particular N'' state observed at any time is the sum over all open product channels having that value of CN(N'').

3. Electronic state correlation

The concept of a PES on which nuclear motion takes place is entrenched in the Born–Oppenheimer approximation. The terms in the complete Hamiltonian that are ignored in the approximate treatment result in small coupling terms between the zero-order eigenfunctions. The separability of nuclear and electronic coordinates implies that the electronic quantum numbers are conserved independently. For a system where the nuclei are constrained near their equilibrium configuration, this approximation is quite successful. On the other hand, one expects it to be inadequate for the quantitative description of a system which is undergoing dissociation into fragments that are very different from the parent molecule. Nevertheless, correlations between states with the same electronic quantum numbers may be used to obtain qualitative knowledge of the shape of the PES as the nuclei rearrange or separate during a chemical reaction.

For the case at hand, it is simplest to consider the reverse process, recombination of the radicals CN and NO, proceeding through a linear complex which then rearranges to the equilibrium structure of NCNO (Fig. 11). If spin–orbit interaction in NO were ignored, the ground state diatomics would combine to form a $^1\Pi$ and a $^3\Pi$ state in a linear NCNO. At the equilibrium geometry each doubly degenerate Π state also splits into two (A' and A'' in C_s). The singlet states are nondegenerate whereas the three spin components of the triplet states remain quasidegenerate. Similar arguments must be developed for all combinations of electronically excited states of CN and NO and correlated to electronic states of NCNO. The ordering of the electronic states

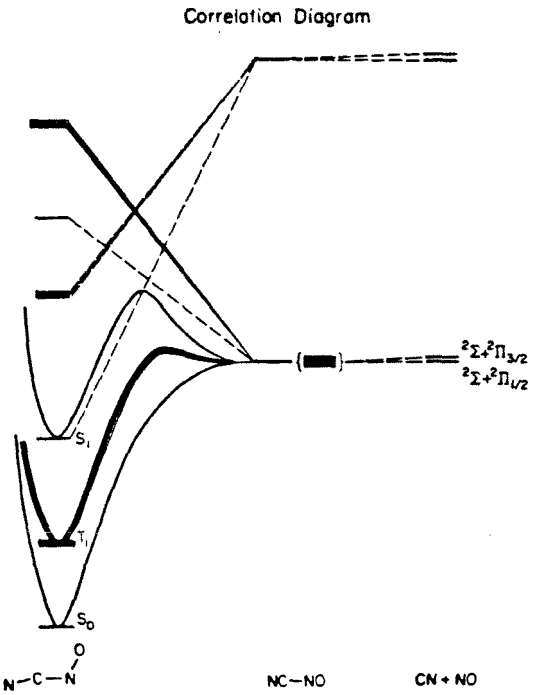

FIG. 11. Correlation diagram for the dissociation of NCNO. The leftmost column shows the order of energy levels in the parent molecule schematically. The far right column shows the energy of the products at infinite separation. The center column represents the molecule with the central CN bond greatly extended and the fragments arranged in a linear geometry.

by energy cannot be deduced without detailed calculations of its electronic structure. Recent calculations[34] show that the ground singlet and lowest triplet states are derived from ground state CN and NO, but the next most energetic singlet and triplet states are obtained from CN(X) and a highly excited configuration of NO. Topological constraints demand that these curves intersect the higher NCNO states correlating to CN(X) and NO(X). The pairs of states involved have the same symmetry and their interaction leads to an avoided crossing, which predicts a substantial barrier to dissociation from S_1 and T_2 to ground state CN and NO fragments.

B. Product rotational state dependence

As shown above for an isolated resonance coupled to a finite number of continua, the rise time observed in any channel is the absolute rate of depopulation of the resonance state. We define such a state as an eigenfunction of an approximate molecular Hamiltonian which includes all terms except those which couple the bound states to the translation continua. Thus intramolecular vibrational redistribution and nonradiative transitions other than fragmentation would be manifested only in the relative phases of the states included in the initial superposition created by the excitation. For the purposes of this discussion, we ignore the relative phase factors and consider only population loss from the bound states. Differences in the rate of appearance of fragments in different channels can be observed if the following two conditions are satisfied: (i) multiple resonances are excited simultaneously and (ii) relative coupling strengths of the resonance states to continua are different. It is easy to verify by a contrapositive argument that these are necessary conditions. The second criterion has to be quantified in order for the pair to be sufficient conditions as well.

The observed temporal evolution of population in each CN rotational state can be modeled as a single exponential buildup with the time constants for different N'' being equal within experimental error. At least one of the two conditions just stated is therefore not satisfied. Although our experiments cannot distinguish between the cases of one resonance state coupled to the continua and many such states equally coupled to the translational states, the former is an unlikely possibility because of energy redistribution (discussed in later sections), which leads to the excitation of multiple resonance states prior to reaction.

If we assume that many resonance states are populated by or following photoexcitation, the second condition insists that the coupling strengths are determined by the constants of motion—total energy and angular momentum. The possibility that only one state in the set of excited states dissociates can be ruled out on the basis of the single exponentials observed in transient absorption (see discussion below).

If the reaction were statistical in the reagent, rates of nonradiative decay and vibrational redistribution would be much faster than the rate of reaction. All quasidegenerate resonance states would be coupled to the optical state and to the dissociation continua. The discussion above makes no claim about the *extent* of redistribution, although experimental results suggest that all resonance states that are populated are equally coupled to products. Thus measurements of equal rates in different product channels indicate rapid redistribution among the set of resonance states which are coupled to the optical state. It is important to note this set does not necessarily include all accessible states.[35]

In our initial communication we reported rates changing as a function of CN(N''). At that time, we were unable to determine whether the observed dependence was a manifestation of nonstatistical effects or simply an ensemble effect. Our current results show unambiguously the latter is the correct interpretation of our previous study.

C. Initial angular momentum dependence

Figure 5 illustrates the effect of a finite spread in the distribution of initial energy and angular momentum. The photon energy promotes molecules in the vibrationally and rotationally cold ground state to states 25 cm^{-1} above the threshold for dissociation. If this were the maximum energy available for distribution among product degrees of freedom, the rotational quantum number of CN would be $N'' < 4$. Clearly, product channels with CN($N'' > 4$) must originate from internally excited NCNO. Since the distribution of vibrational states at low energies is sparse, we assume that most of the excitation is rotational.

These measurements dramatize the need for performing experiments in molecular beams where extensive cooling of

TABLE II. $N^{\prime\prime}$ dependent lifetimes of *warm* expansion (ps).

$N^{\prime\prime}$	Lifetime 1	Lifetime 2	Fraction
0	107	289	0.296
3	123	532	0.425
4	95	380	0.392
5	64	230	0.433
6	26	213	0.352
7	37	183	0.730

the internal degrees of freedom is achievable. They also support our claim above that the previously observed $N^{\prime\prime}$ dependence of the dissociation rates in a bulb was due to ensemble energy. In Table II we list the fitted rate constants for each transient with the fraction of the fast component to the total amplitude. It is not possible to accurately represent a distribution of rate constants with average values and this was reflected in the sensitivity of the fit to the initial guess. The values listed in the table are therefore the average of fitted values obtained with a range of initial guesses.

The observed quasibiexponential behavior in Fig. 5 reflects the dissociation of molecules from different J,K states. For molecules in high J, low K states, the centrifugal barrier is expected to be higher than for molecules in low J states. Accordingly, the dissociation rates from these states will be relatively slow. On the other hand, the dissociation rates for molecules in high $K(K \simeq J)$ states should be faster. This is because the initial J (good quantum number) is converted to average l, especially if the rotational constants of the fragments are much larger than those of the reagent. States with high K are not as constrained with angular momentum conservation laws and behave more like vibrational states.

The results for the higher $N^{\prime\prime}$ channels corroborate the discussion above. The $N^{\prime\prime} = 7$ channel is closed for energies less than 105 cm^{-1} so that only rotationally excited molecules ($J \geq 6$) can contribute. Table II shows that a significant fraction of molecules decay into this channel with rates $\sim 5 \times 10^9\ s^{-1}$ (slow component of the quasibiexponential), a value which is a factor of 2 smaller than the rate of dissociation of NCNO with $\sim 100\ cm^{-1}$ of excess vibrational energy and no rotational excitation. This slow component is derived from the high J, low K states. The fast component is faster than the rate measured in the cold expansion ($E_x = 105\ cm^{-1}$), indicating the involvement of high $K(K \sim J)$ states. This ensemble effect was also observed in the lower $N^{\prime\prime}$ channels.

D. Energy redistribution and reaction mechanism

The model we adopt here is described in Fig. 12. The S_1 singlet level, which carries most of the oscillator strength, is quasidegenerate with many levels from S_0 and/or T states. Since the barrier to dissociation on S_1 is high (estimated to be more than 5000 cm^{-1} [6]), and the density of levels in $S_0^{\dagger}$ and $T^{\dagger}$ is appreciable, energy redistribution from the state of S_1 character to $S_0^{\dagger}$ (or $T^{\dagger}$) states is the primary step for dissociation. This intramolecular process requires electronic coupling between the initial and final states, which may involve promoting modes that mediate vibrational/rotational

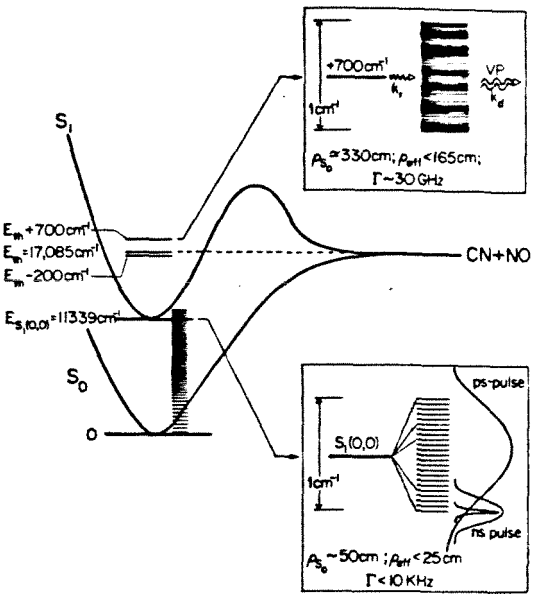

FIG. 12. A pictorial representation of energy redistribution, predissociation and the effect of coherent excitation. The lower right inset shows the detailed energy level structure near the S_1 origin. The "broad band" ps pulse can excite the state of S_1 character, whereas the ns ("narrow band") pulse cannot. The upper insert shows the structure above dissociation threshold. The greater density of states and lifetime broadening makes the spectrum of quasibound states appear continuous.

energy redistribution on the final state surface. The reaction proceeds from the final state surface. We therefore consider both processes (i.e., energy redistribution and dissociation) explicitly.

Below the dissociation threshold, the redistribution discussed here is quite similar to the case of intermediate sized molecules, such as pyrazine and isoquinoline.[37] As shown in the case of pyrazine, a picosecond pulse with a coherence width spanning the eigenstates of the system leads to the preparation of the zero-order state (or close to it), in this case the S_1 state. Intramolecular dephasing is the primary decay process (*in pyrazine it was observed to be 100 ps*[37]) which leads to the population of long-lived states, in this case the $S_0^{\dagger}$ (or $T^{\dagger}$) states. For NCNO near the S_1 origin, the vibrational density of states is $\rho_v \sim 50$ per cm^{-1}. The effective (including symmetry restrictions and limited couplings) density is less than 25 cm, ignoring rotations for the sake of simplicity. The linewidth of the states is < 10 kHz, indicating that below the dissociation limit, the spacing between levels is greater than the intrinsic width. The two-color picosecond transient absorption experiments reported here and the recent fluorescence lifetime measurements of Reisler *et al.*[38] support this view. Our transient absorption studies show (Fig. 7) a rise (< 8 ps) and no decay at longer times. The fluorescence experiment below threshold of Reisler *et al.*[36] determines the long decay component to be $> 100\ \mu s$. The laser coherence width in their case is probably less than 0.5 cm^{-1}, while in our picosecond experiments it is 3 cm^{-1}. Thus in the ns experiments one is measuring the

long-time ("dilution effect") decay of an eigenstate or a bunch of eigenstates (Fig. 12). The ps experiment coherently excites the distribution of eigenstates which following dephasing (ps's) produce the long-lived $S_0^\dagger$ (or $T^\dagger$) states that are subsequently probed in the transient absorption experiment. The early-time dephasing is also supported by the fact that below (or near) threshold the rotational structure of the absorption bands was not resolved using a 0.04 cm^{-1} bandwidth laser.[6] Finally, the difference (27 vs 3 cm^{-1}) in linewidths observed below threshold for different absorption bands could be due to the influence of the promoting mode(s) on electronic couplings of nearby states. This proximity effect is also found in isoquinoline S_1/S_2 coupling.[37]

Above the dissociation threshold the picture is somewhat different. For example at $E_{th} + 700\ cm^{-1}$, $\rho_{eff} < 150$ per cm^{-1} and the linewidth (from our dissociation rate measurements) is ~30 GHz. Both the density and level width have increased considerably and the picture here is that of fast and reversible energy redistribution followed by predissociation (see Fig. 12). If we ignore coherence effects, then we can evaluate the relative importance of the redistribution vs predissociation rates. Simple kinetics indicate that the initial state S_1 decays by the redistribution rate constant (k_r):

$$S_1(t) = S_1(0)e^{-k_r t}$$

while $S_0(t)$ will build up and decay according to

$$S_0(t) = S_1(0)\frac{k_r}{k_r - k_d}(e^{-k_d t} - e^{-k_r t}) .$$

It is important to note that if $k_r - k_d$ is positive, the decay of $S_0(t)$ will be given by k_d. The product buildup in this limit ($k_r > k_d$) is simply given by

$$P(t) \approx S_1(0)(1 - e^{-k_d t})$$

and exhibits the same rate as $S_0(t)$, consistent with experimental observation. We have ignored reversible processes, since ρ is large and detailed balance implies very long recurrence times. The important point here is that the picosecond product appearance times, transient absorption decay rates and other spectroscopic data are all consistent with this model. This allows us to separate the redistribution from predissociation processes, within the context of the model, and to conclude that the measured rates are k_d. These k_d change by three orders of magnitude on going from near threshold to 700 cm^{-1} above threshold, yet the absorption spectrum still shows sharp features. The linewidth above dissociation threshold is given by the dephasing rate. An estimate of k_r is ~(3 ps)$^{-1}$, which is still larger than the observed rates (ns^{-1} at threshold to 10 ps^{-1} at 700 cm^{-1} above threshold).

Finally, in the above discussion we tacitly ignored the contribution of the triplet state below S_1. This is not known for certain, although there are a number of points that may be presented in favor of the S_0 choice. First, if the triplet were involved in addition to S_0 then the product buildup should be a biexponential rise with the ratio of the two components of the rise determined by the relative redistribution rate constants to S_0 and T. This has not been observed in our experiments—all transient absorption decays and product buildup rates are matching single exponentials. Second, extensive perturbations of the levels of S_1 have been attributed to mixing with S_0.[6] ρ is ~280 cm in the ground state, compared to ~20 cm in T (assuming the same frequencies and that T is ~6000 cm^{-1} above S_0, which is not known for NCNO) at threshold. The choice of S_0 over T has been favored before for NCNO by Wittig's group. It is also interesting that in HNO, threshold dissociation proceeds via S_0.[30]

E. Reagent excess energy dependence

Figure 3 shows rate constants for the appearance of CN as a function of excess energy. A plot of the rates near threshold is presented in Fig. 13 with a smooth curve drawn through the data and extrapolated to lower energy to obtain the threshold energy for reaction. Scanning DL1 with DL2 tuned to probe CN($N'' = 0$), we were able to reproduce the results of Nadler *et al.* for excitation wavelengths shorter than 5853 Å. Relative positions of peaks and the absolute value of the threshold energy are in excellent agreement. The lifetimes vary smoothly from >2 ns at 5853 Å to ~10 ps at 5630 Å. It is interesting to note that we do not observe the peak just at threshold. Previous experiments show evidence for very long appearance times (70–20 ns) corresponding to tunneling through a small rotational barrier.[6] Our experiments are not designed to measure the long rise times (~10 ns) close to threshold expected on the basis of previous work.

The rapid increase in the rates from threshold requires further consideration of the effect of finite spread in energy. Since the pump pulse has a finite spectral width (3 cm^{-1}), the initial ensemble is not strictly a microcanonical one, and the observed rates are larger than the rate at the mean energy. Molecules absorbing the redder photons have less total energy and therefore dissociate more slowly than the ones which absorb the bluer photons. There are two possible sources of bias in our measurements. At threshold, the reactive part of the ensemble has a skewed energy distribution and the average rate is faster than the rate of a true MC ensemble having the mean energy of the excitation pulse.

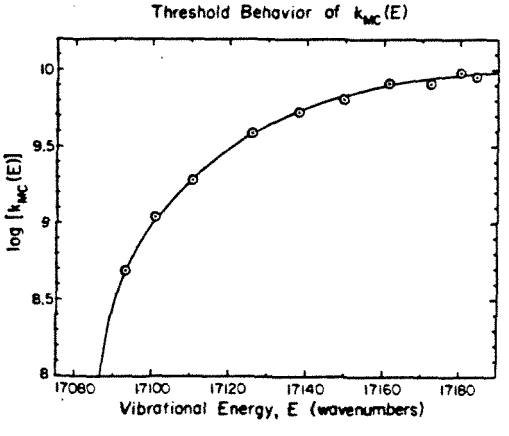

FIG. 13. Rates of dissociation measured near threshold showing the onset of reaction.

This effect becomes of lesser consequence if tunnelling effects are taken into account. The second point regarding threshold measurements is that the limited time range over which the appearance of products is measured constitutes a biased sampling of the ensemble (within 3 cm^{-1}). The severity of this unavoidable systematic error can be reduced simply by carrying out measurements to time delays of several τ. Since both of these effects are expected to be small in magnitude and nonnegligible only near threshold, we make no effort to adjust our results to correct for these errors.

Calculations of MC rates using PST and RRKM theory are compared with our rate measurements below, in an attempt at understanding their dependence on excess energy in the reagent.

1. Comparison with statistical theories: Phase space theory

Although it is well known that PST overestimates rates, we present results of these calculations as an upper bound for the observed rates at all energies. These rates should be a good approximation very close to threshold. The calculations were performed on a PDP 11/23 + computer using a Lennard-Jones attractive potential ($C_6 = 1.60 \times 10^5$ erg·Å^6). The molecular constants are collected in Table I.

It is crucial to assess all degeneracies for a correct absolute rate calculation. The total angular momentum is the sum of electron spin and orbital angular momentum, rotational angular momentum and nuclear spin. We assume that the nuclear spin coordinates are separable and the total nuclear spin is conserved independently. As the dissociated fragments are distinguishable, the Pauli principle imposes no restrictions on possible combinations of angular momentum quantum numbers in the products. The total angular momenta of the fragments are good quantum numbers and are easily computed. In a singlet state electron spin is zero and the total angular momentum of NCNO is the spectroscopically assigned quantum number J. The phase space volume for the transition state is estimated using Eq. (8). The two spin–orbit states of NO are treated as independent channels with equal weighting.

We have performed a full PST calculation ($\kappa = 1$) and the results are shown in Fig. 14 (curve C). We also make an attempt at conserving electronic quantum numbers by proposing a value less than unity for κ, the transmission coefficient. Ignoring differences in electronic energy in the products, we notice an eightfold degeneracy for a given combination of CN and NO rotational states. This arises from a twofold degeneracy of the electron spin in each of the two fragments and an additional twofold degeneracy (λ-doubling) of the electron orbital motion in NO. Each combination of electronic quantum numbers should correlate with a different electronic state of NCNO. As discussed in Sec. V A 3, some combinations correlate with the triplet and excited singlet states and therefore represent closed channels. Correlation between the states of the two radicals and a linear NCNO can be made, but enough information for detailed correlations to the bent NCNO is not available. If we take recourse in statistical adiabaticity, i.e., on the average these quantum numbers are preserved, only one-eighth of all

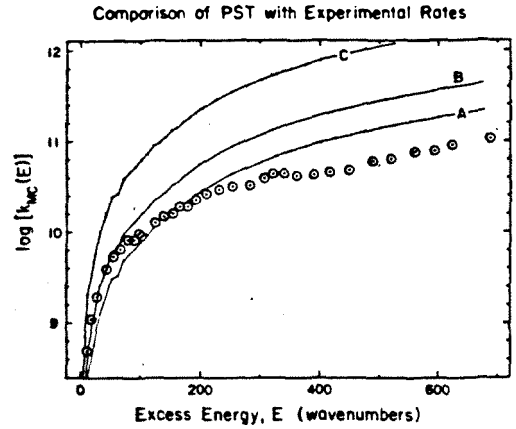

FIG. 14. Comparison of PST theory with experiment. Calculated rates ($J = 3$) are shown as connected lines. Curves A, B, and C correspond to $\kappa = \frac{1}{8}, \frac{1}{4}$, and 1, respectively. The density of states was approximated by the Whitten–Rabinovitch method for harmonic vibrations and summed over allowed K. The circles are the experimentally measured values. Note that the structure is somewhat deemphasized because the rates are plotted on a logarithmic scale.

final states correlate with the ground singlet state. This is implemented in our calculations by setting $\kappa = \frac{1}{8}$. It must be emphasized that the full count ($\kappa = 1$) includes all electronic degeneracies in the products, in particular the spin states of CN and the orbital degeneracy of NO(Π). These states have to be considered explicitly because the total angular momentum of each product is important for momentum conservation, while the energy can be approximately represented by the spectroscopic "good" quantum numbers.

The domain of applicability of this choice needs some consideration. The value $\frac{1}{8}$ was chosen assuming the electronic quantum numbers do not appear in the energy expression except as small corrections that may be neglected to a good approximation. In reality, spin–orbit interaction in NO is nonzero (~ 120 cm^{-1}). In the energy range 0–120 cm^{-1} above threshold, the electronic degeneracy is effectively 4, rather than 8. Therefore $\kappa = \frac{1}{4}$ should be used in this range, while at higher energies $\kappa = \frac{1}{8}$ is more appropriate. It should be noted that the transmission coefficient is expected to be a continuous function of energy and the change from 0.25 to 0.125 is likely to occur over a range of energies. Curves A and B in Fig. 14 were calculated with $\kappa = \frac{1}{8}$ and $\frac{1}{4}$ respectively, but it should be emphasized that this is done simply to illustrate the effect of $\kappa < 1$ on the PST calculation of rates.

The density of states was calculated using the Whitten–Rabinovitch approximation for harmonic vibrations.[16] For $J = 0$, the vibrational state density in S_0 at threshold was ~ 280 per cm^{-1}, which is large enough for the approximation to be valid. The density was corrected for contributions from states with different values of K with the formula

$$\rho(E,J) = (2J+1) \sum_{K=0,J} \sigma \rho_v [E - B^* J(J+1) - (A^* - B^*)K^2], \quad (14)$$

where $\sigma = 1$ for $K = 0$, and $\sigma = 2$ otherwise. $\rho(E,J)$ is the total density of rovibrational states at energy E that have angular momentum J. In contrast to Eq. (8), this expression displays all degeneracies $(2J + 1)$. $\rho_v(E,J,K)$ is the subset of ρ containing only states having K as the projection of J along the figure axis. Thus ρ is simply the sum over all allowed K of ρ_v.

In Fig. 14, calculated rates using different values of κ are superimposed on a plot of $\log k_{MC}(E)$ vs E. The agreement between theory and experiment is reasonable at low energies. Clearly the range of energy over which κ changes its value is small and occurs where $E \simeq \Delta E_{\infty}$. At the high end of the energy range studied, PST rates are indeed higher than the measured rates. It should be emphasized that ρ was calculated using the harmonic approximation. Spectroscopic studies demonstrate that the bending potentials are quite harmonic.[28] The value of C_6 was chosen for consistency with the calculations which reproduced the measured PSDs.[6] Sample calculations show that decreasing or increasing its value by an order of magnitude does not affect the rates significantly. Finally, the same algorithm used for calculating rates was used to produce the PSD obtained in Ref. 6, and good agreement was found.

2. RRKM rates

A standard RRKM calculation using only vibrational frequencies of the reactant yields a discontinuous distribution of rates as a function of energy and is obviously incorrect. We attempt to model the transition state in the following way. We choose the frequencies for the CN and NO stretch modes to be equal to their free radical values. The three bending motions are represented by three harmonic oscillators of very low frequency (see Table III). The reaction coordinate is the central bond stretch mode. The vibrational zero-point energies are assumed to have been included in the threshold energy. The rotational constants are estimated for the equilibrium geometry with an extended central bond. $N^{\dagger}(E)$ was calculated using a direct count algorithm[39] with no symmetry restrictions and the densities were obtained using the semiclassical approximation as in the previous section. Angular momentum was conserved by holding J constant. For a given energy, a sum over K analogous to Eq. (14) was used:

$$N^{\dagger}(E^{\dagger},J) = (2J+1) \sum_{K=0,J} \sigma N_v^{\dagger}(E^{\dagger} - B^{\dagger}J(J+1) - (A^{\dagger} - B^{\dagger})K^2),$$

TABLE III. Frequencies in model TS for RRKM calculations.

TS rotational constants (cm^{-1}): A = 2.0, B = 0.015, C = 0.015			
TS Vibrational frequencies (cm^{-1}):			
Model A	Model B	Model C	Model D
1904	1904	1904	1904
2068	2068	2068	2068
10	10	5	20
12	12	12	25
50	200	200	50

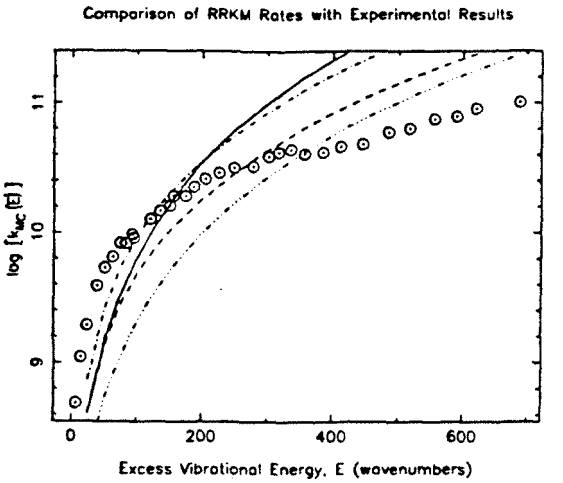

FIG. 15. Comparison of RRKM theory with experimental results. The densities were obtained as for the PST calculations. $N^{\dagger}$ was obtained from a direct quantum count of harmonic vibrations. The different connected lines correspond to different combinations of frequencies (see Table III). The following representation is used: model A (—), model B (- - -), model C (– · –), and model D (– ··· –).

where $E^{\dagger}$ is the difference of the total energy (E) and the dissociation energy (including zero point energies). σ is as in Eq. (14) and $N^{\dagger}$ is the total number of rovibrational states with energy less than or equal to the total energy and having angular momentum J. $N_v^{\dagger}$ is a subset of these states whose angular momentum has a projection K along the figure axis. Note that we have implicitly assumed the TS is a symmetric top. Varying $A^{\dagger}$ and $B^{\dagger}$ changes the results by a small amount.

Some representative cases are shown in Fig. 15. The frequencies used in these calculations are listed in Table III. It is apparent that a TS with harmonic frequencies is unable to reproduce experimental results. With very low frequencies, the low energy behavior can be approximated at the cost of reasonable agreement at higher energies and vice versa. This is not too surprising since a loose transition state, as proposed on the basis of PSDs and supported by our PST calculations, will imply larger separation between energy levels at higher quantum numbers. This is a crude method for modeling a loose transition state and should be considered in that spirit only since the number of possible choices is quite large. A proper treatment using a recent modification of the theory developed for flexible transition states of arbitrary looseness is currently in progress.

Although neither PST nor RRKM models can quantitatively account for the observed results, the general trend shows that the TS is indeed fairly loose. This is clearly borne out by the small harmonic frequencies we have to assume in the RRKM model to obtain rates having the correct order of magnitude.

It has been conjectured that PST predictions of the rate will be accurate at energies close to threshold but that the infinitely loose TS is not a good approximation at higher energies. This statement borrows from concepts of the vari-

ational theories—the exact location of the TS changes with the energy available for reaction. If the dissociation of NCNO were a simple process that could be described as a fast redistribution of vibrational energy and slow (adiabatic) passage through a single dividing surface, PST should reproduce the experimental results. We showed that the effects of electronic correlation could be accounted for by simple heuristic arguments very close to threshold. The position of the dividing surface changes slowly and continuously with increasing energy, provided the reaction remains direct, i.e., a single dividing surface exists such that any trajectory intersects it at most once. The ratio of the observed rates and PST rates may be interpreted as an energy dependent transmission coefficient $\kappa(E)$, and is plotted in Fig. 16 for this purpose. The first few points have been corrected for tunneling ($10^8\ s^{-1}$) and the corresponding PST rates averaged over a Boltzmann distribution of rotational states at 2 K. The gradual change in $\kappa(E)$ with increasing energy can be interpreted as reflection of a smooth transition from a completely loose to a tighter TS.

3. Structure in the excess energy dependence

The plot of the rates vs excess energy (Fig. 3; see also Fig. 15) shows an inflexion and a weak maximum around $320\ cm^{-1}$. Although no conclusive interpretation of this unusual behavior can be made at this time, we discuss several plausible explanations. Detailed knowledge of the PES(s) is required to identify which of these possibilities most closely resembles nature.

PST and RRKM theory assume a radially isotropic potential. In reality, NO and CN have permanent dipole moments and the long range potential is determined by dipole–dipole interaction which is dependent on their relative orientation. In the limiting cases of linear approach, head-to-head or head-to-tail, the electrostatic potential is repulsive in one case and attractive in the other. The central bond stretching

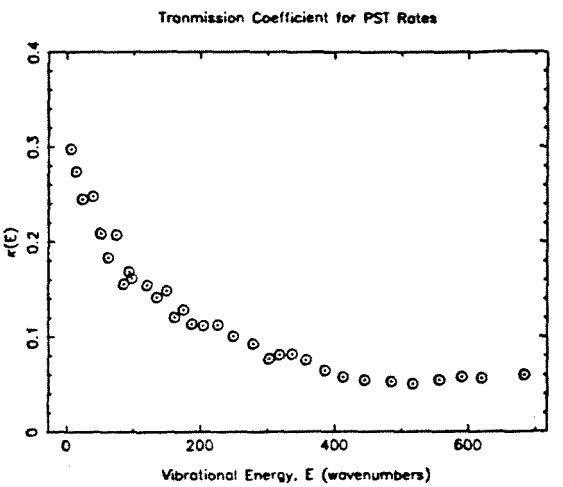

FIG. 16. The energy dependent transmission coefficient of PST rates. The first two data points near threshold are corrected for the distribution in internal energies at 2 K.

motion would not be separable and the proper reaction coordinate would be some complicated motion with projection along multiple normal modes. Estimating proper statistical rates for such a system is not a tractable problem as yet.

Related to the radial anisotropy of the PES is the possibility of complex formation and reactions leading to other products. One postulated reaction[40] is

$$NCNO \rightarrow [NC{\cdot}ON] \rightarrow N_2 + CO\,.$$

Loss of NCNO into this channel would be manifested in the rate of CN production, but not necessarily in the relative distributions of $CN(N'')$. A cyclic intermediate has been proposed as a transient species along the exoergic path for CO production. The distribution of energy in the internal and translational degrees of freedom in a particular channel will reflect the existence of other product channels as will the absolute rates. PSDs in a given channel will be affected by the global shape of the PES only if trajectories entering the channel may return to the reactant region of phase space.

The experimental results could be presented from an operational perspective. All simple theories predict a smooth monotonic dependence of the rates on energy. Such an empirical curve drawn to approximate the data at the high energy end of the range studied underestimates the rates in the range 200 to 400 cm^{-1}. A simple interpretation of the enhanced rates is that the vibrational phase space is restricted. The maximum at $\sim 320\ cm^{-1}$ would then correspond to the energy regime for transition from restricted to complete redistribution in the reactant and the close agreement between PST and the data at low energies is fortuitous. The statistical adiabatic channel model considers strict conservation of vibrational quantum numbers of those motions which can be clearly identified in reactants and products. In this reaction, they are the terminal CN and NO stretches. From an extension of this idea, one could conceive of the restrictions in reactant phase space being due to weak coupling between these modes and the others. This picture does not contradict the observation of equal appearance times in all product channels and the transient absorption measurements if we assume that redistribution cannot populate these modes directly. Some fluctuations in the rate is expected as the nature of the optical state changes with the photon energy in the transition regime, which may explain the observed structure in $k_{MC}(E)$.

Although the involvement of other electronic states as direct channels of reaction have been argued against, they may be important in determining the shape of the S_0 PES in the reaction channel. It is believed that S_1 and T_1 correlate with ground state CN and NO. Spin–orbit coupling may induce mixing between the vibronic manifolds of S_0 and T_1, leading to avoided crossings and multiple minima (Demkov resonances) along the reaction coordinate.[41] Similar effects would also arise from interactions between the manifolds of the two singlet surfaces. It must be noted that such minima can occur only if some vibrations are adiabatic, i.e., redistribution is not complete among all vibrational modes. This may be visualized as dynamical trapping, molecules vibrating in a particular mode see potential minima greater in number and different in position than molecules executing a

different form of vibrational motion. The purely electronic S_0 PES cannot have a minimum along the reaction path (except at the equilibrium geometry of the reactants) and the rates can be compared to PST or RRKM for energies such that only this surface is important. At energies greater than 200 cm^{-1}, the reaction must then proceed through multiple transition states. The complex mode of the reaction should manifest itself in the absolute rate, but not necessarily in PSDs. The rates may be estimated only if the contribution from each adiabatic PES (electronic and vibrational) can be estimated.

It is interesting to note that there is no obvious correlation between the sharp features in the absorption (photodissociation yield) spectrum and the structure in $k_{MC}(E)$. In the bimolecular scattering of ground-state CN and NO radicals, fluctuations in the scattering cross section corresponding to orbiting or compound (Feshbach) resonances may be present.[42] In this example of predissociation, the reaction is initiated in such compound states at all energies. Structure in the unimolecular rate as a function of energy is therefore a manifestation of restrictions to the redistribution of energy.

4. Rates vs product state distributions

Although a complete interpretation of the energy dependence of the rates is not possible without a proper description of the PES in full detail, we can assert that the dissociation rates are sensitive to different aspects of the potential than PSDs. Nascent distributions obtained under similar experimental conditions for CN and both spin–orbit states of NO are in good agreement with PST, with no evidence of restricted IVR or nonadiabatic effects. Comments on the intrinsic differences between measurements of rates and PSDs are clearly appropriate.

Absolute reaction rates are affected by the global features of the PES, in contrast to PSDs. Reactive channels which do not yield CN and NO as products are not presented in the PSDs of CN (or NO) but will be manifested in the absolute rate. In other words, the total yield in the CN + NO channel will be affected by the presence of other, chemically distinct, open channels, even though the relative population of product quantum numbers within a single rearrangement channel might not be influenced.

There are also subtle considerations in a single channel which influence rates and PSDs differently. Rates are thought to be determined by a hypothetical surface in phase space that minimizes the flux of trajectories through it. This dynamic bottleneck to reaction may be located somewhere other than at the maximum (saddle point of PES) of V_{eff} [Eq. (7)]. PSDs are determined at this critical point which is generally further toward products than S_m. An equivalent statement is that exit channel effects (long range collisions) are important for this reaction, even near threshold. As the energy available for reaction increases, the position of the TS (S_m) migrates slowly towards the reagent, thus accentuating the differences between PSDs and rates. The rates are sensitive to IVR and the short-range interactions on the PES, while product state distributions are mapping long-range influences and impact parameter distributions. This is strong motivation for examining photofragmentation on ultrashort timescales.

VI. CONCLUSIONS

This paper, the first in the series, presents direct measurements of state-to-state rates (and product state distributions) of the dissociation of beam-cooled NCNO as a function of reagent and product energy. The studies provide an opportunity for examining the picosecond time-resolved dynamics of this reaction. The primary experimental findings reported here are:

(a) State-to-state rate constants are found to be independent of the character of the final product rotational state. A simple model is used to argue that energy randomization is fast in the accessible (subject to energy and possibly dynamical constraints) region of phase space.

(b) Rates as a function of energy exhibit a threshold (17 083 cm^{-1}, the bond energy, 48.8 kcal/mol) and increase with total energy in the reagent. The functional dependence of the rates on energy is not strictly monotonic but shows some structure, which cannot be explained using simple statistical theories. Comparison with RRKM and PST provides insight into the nature of the transition state and the effects of recoil during fragmentation.

(c) Transient absorption measurements show a population decay at a rate equal to the buildup of products. In the light of these experiments, we consider energy redistribution and predissociation explicitly. It is reasoned that only one potential energy surface is important at the energies considered.

(d) Differences between product state distributions (statistical – PST) and absolute rates (nonstatistical) are rationalized as manifestations of the global vs local features of the PES, or early-time vs long-time dynamics of the reaction process. *Ab initio* or semiempirical calculations of the full S_0 PES would be of great use in gaining further insight into this prototype and elementary reaction.

ACKNOWLEDGMENTS

This research was supported by a grant from the National Science Foundation (CHE-8512887). Some initial support was provided by the President's Fund and the Keck Foundation. We thank Professor R. B. Bernstein and Professor R. A. Marcus for many illuminating discussions. We also wish to thank Professor C. Wittig and Professor H. Reisler, and Dr. M. Noble for many helpful discussions throughout this work and assistance in the safe and successful synthesis of NCNO. We are particularly grateful to Dr. Hanna Reisler for communicating her results on the fluorescence lifetime and for an indepth discussion of NCNO dissociation.

APPENDIX: CHARACTERISTIC CONSTANTS FROM PUMP–PROBE TRANSIENTS

In cases where the dynamics occur on a time-scale much longer than the duration of the excitation or probe pulses,

the experimental response can be analyzed without explicitly accounting for their finite temporal widths. More accurate estimates of the constants of the molecular response are obtained if the instrumental response function is included in the analysis. The problem has been solved in the context of fluorescence lifetime measurements by photon-counting techniques[43] and is given by a convolution integral, and in transient absorption experiments.[44] Here, we show explicitly that a pump–probe transient may also be analyzed by a mathematically similar form, which we utilize in the analysis of our data.

First, we consider the effect of the excitation pulse which has a temporal profile, $f(t)$. If the molecular response has a functional form $M(t-t_0)$, the measured response, $S(t)$, is represented by the Riemann sum over the range with $f(t)$ nonzero:

$$S(t) = \sum_n f(n\delta\tau)\cdot M(t-n\delta\tau)\,. \tag{A1}$$

In the limit of infinitesimal $\delta\tau$ the sum is the definite integral in Eq. (A2), which can be recognized as a convolution integral of f with M:

$$S(t) = \int_{-\infty}^{t} f(\tau)M(t-\tau)d\tau\,. \tag{A2}$$

In a pump–probe scheme where both pulses have finite temporal spread, the time parameter is generally chosen to be the peak-to-peak delay, T. Including the probe pulse in Eq. (A2) results in

$$S(T) = \int_{-\infty}^{+\infty}\int_{\tau_1}^{+\infty} f_1(\tau_1)M(\tau_2-\tau_1)f_2(\tau_2-T)d\tau_2\,d\tau_1\,.$$

Defining a new variable $\tau' = \tau_2 - T$,

$$S(T) = \int_{-\infty}^{+\infty}\int_{\tau_1-T}^{+\infty} f_1(\tau_1)M(\tau'-\tau_1+T) \times f_2(\tau')d\tau'\,d\tau_1\,.$$

Another substitution $s = \tau_1 - \tau'$ and a change in the order of integration results in

$$S(T) = \int_{-\infty}^{T}\int_{-\infty}^{+\infty} f_1(\tau_1)f_2(\tau_1-s)M(T-s)d\tau_1\,ds\,.$$

The system response function, $R(t)$, obtained by setting $M(t)$ equal to the Dirac delta-function is seen to be the cross correlation of the two pulses. This shows that the cross-correlation function is indeed the true system response function

$$R(T) = \int_{-\infty}^{+\infty} f_1(\tau_1)f_2(\tau_1-T)d\tau_1\,.$$

The measured molecular transient can then be written as in Eq. (A3):

$$S(T) = \int_{-\infty}^{T} R(s)M(T-s)ds. \tag{A3}$$

In our experiments, $M(x)$ has the form of an exponential buildup. Next, we show that the convolution of a pulse with zero amplitude at long positive and negative times with an exponential rise is identical to the convolution of the integral of that response with an exponential decay. In other words, we want to show that the following equality holds:

$$\int_{-\infty}^{t} f(\tau)A'[1-e^{-k(t-\tau)}]d\tau = \int_{-\infty}^{t}\left(\int_{-\infty}^{\tau} f(s)ds\right)A'e^{-k(t-\tau)}d\tau\,.$$

The right-hand side can be integrated by parts:

$$\begin{aligned}\int_{-\infty}^{t}&\left(\int_{-\infty}^{\tau} f(s)ds\right)A'e^{-k(t-\tau)}d\tau \\ &= A'e^{-kt}\left[\int_{-\infty}^{\tau} f(s)ds\cdot\frac{e^{k\tau}}{k}\right|_{-\infty}^{t} \\ &\quad - \int_{-\infty}^{t}\frac{e^{k\tau}}{k}\cdot\frac{d}{d\tau}\left(\int_{-\infty}^{\tau} f(s)ds\right)d\tau\Bigg] \\ &= A'e^{-kt}\left[\int_{-\infty}^{t} f(s)ds\cdot\frac{e^{kt}}{k} - \int_{-\infty}^{t}\frac{e^{k\tau}}{k}f(\tau)d\tau\right] \\ &= \frac{A'}{k}\int_{-\infty}^{t} f(\tau)[1-e^{-k(t-\tau)}]d\tau\,.\end{aligned}$$

This shows that the deconvoluted lifetimes are the same, but the amplitude is changed by a multiplicative factor. This has to be accounted for in deriving the correct fraction for a multicomponent rise. For a biexponential rise deconvoluted using the integrated pulse method, the correct ratio F of the amplitude of the fast component to the total amplitude is related to the fraction obtained in the fit F' by

$$F = \frac{k_2F'}{k_1(1-F') + k_2F'}\,,$$

where the exponential constants satisfy $k_1 > k_2$.

[1] (a) J. L. Knee, L. R. Khundkar, and A. H. Zewail, J. Chem. Phys. **82**, 4715 (1985); (b) **83**, 1996 (1985); (c) J. Phys. Chem. **89**, 4659 (1985); (d) N. F. Scherer, F. E. Doany, A. H. Zewail, and J. W. Perry, J. Chem. Phys. **84**, 1932 (1986).

[2] N. F. Scherer, J. L. Knee, D. D. Smith, and A. H. Zewail, J. Phys. Chem. **89**, 5141 (1985).

[3] N. F. Scherer and A. H. Zewail, J. Chem. Phys. **87**, 97 (1987).

[4] J. L. Knee, L. R. Khundkar, and A. H. Zewail, J. Chem. Phys. **87**, 115 (1987).

[5] See, e.g., R. B. Bernstein, *Chemical Dynamics via Molecular Beams and Laser Techniques* (Clarendon, Oxford, 1982).

[6] I. Nadler, M. Noble, H. Reisler, and C. Wittig, J. Chem. Phys. **82**, 2608 (1985); I. Nadler, J. Pfab, H. Reisler, and C. Wittig, *ibid.* **81**, 653 (1984); I. Nadler, J. Pfab, G. Radhakrishnan, H. Reisler, and C. Wittig, *ibid.* **79**, 2088 (1983); C. Wittig, I. Nadler, H. Reisler, M. Noble, J. Catanzarite, and G. Radhakrishnan, *ibid.* **83**, 5581 (1985); C. X. W. Qian, M. Noble, I. Nadler, H. Reisler, and C. Wittig, *ibid.* **83**, 5573 (1985).

[7] E. P. Ippen and C. V. Shank, *Topics in Applied Physics* (Springer, New York, 1984), Vol. 18.

[8] P. Horsewood and G. W. Kirby, Chem. Comm. **1971**, 1139.

[9] J. R. Morton and H. W. Wilcox, Inorg. Synth. IV, 48 (1953).

[10] *Spectroscopic Data*, edited by S. N. Suchard (Plenum, New York, 1975), Vol. I.

[11] I. Nadler, H. Reisler, M. Noble, and C. Wittig, Chem. Phys. Lett. **108**, 115 (1984).

[12] D. W. Marquardt, SIAM **11**, 431 (1964); David P. Millar, Ph.D. dissertation, California Institute of Technology, 1982.

[13] P. R. Bevington, *Data Reduction and Error Analysis for Physical Sciences* (Academic, New York, 1981).

[14] See, e.g., P. Brumer and M. Shapiro, Adv. Chem. Phys. **60**, 371 (1985); F. H. Mies and M. Krauss, J. Chem. Phys. **43**, 4455 (1966); S. A. Rice, in *Excited States*, edited by E. C. Lim (Academic, New York, 1975), Vol. 2, p. 111.

[15]L. D. Landau and E. M. Lifschitz, *Nonrelativistic Quantum Mechanics* (Pergamon, New York, 1982).
[16]W. Forst, *Theory of Unimolecular Reactions* (Academic, New York, 1973); P. J. Robinson and K. A. Holbrook, *Unimolecular Reactions* (Wiley-Interscience, London, 1974).
[17]See, for example, W. H. Miller, J. Chem. Phys. 65, 4343 (1976).
[18]W. A. Wong and R. A. Marcus, J. Chem. Phys. 55, 5625 (1971); D. L. Bunker and M. Pattengil, *ibid.* 48, 772 (1968).
[19]P. Pechukas and J. C. Light, J. Chem. Phys. 42, 3281 (1965); P. Pechukas, R. Rankin, and J. C. Light, *ibid.* 44, 794 (1966); C. Klotz, J. Phys. Chem. 75, 1526 (1971); C. Klotz, Z. Naturforsch, Teil A 27, 553 (1972); W. Chesnavich and M. Bowers, J. Chem. Phys. 66, 2306 (1977).
[20]The expression for N^+ or ρ is for a specific value of J_z. The degeneracy associated with this quantum number appears in both numerator and denominator in Eq. (4) and therefore cancels out. For details, see Refs. 6 (Wittig *et al.*) and 19.
[21]S. W. Benson and D. M. O'Neil, *Kinetic Data for Gas Phase Unimolecular Reactions*, Natl. Bur. Stand. (U.S.) 21 (1970).
[22]M. Quack and J. Tröe, Ber. Bunsenges. Phys. Chem. 78, 240 (1974); 79, 170 (1975); M. Quack, J. Phys. Chem. 83, 150 (1979).
[23]See, e.g., E. Pollak, in *Theory of Chemical Reaction Dynamics*, edited by M. Baer (Chemical Rubber, Boca Raton, FL, 1985); D. L. Bunker, J. Chem. Phys. 40, 1946 (1964); W. L. Hase, J. Phys. Chem. 90, 365 (1986).
[24]See, e.g., D. G. Truhlar and B. C. Garrett, Ann. Rev. Phys. Chem. 35, 159 (1984).
[25]D. M. Wardlaw and R. A. Marcus, J. Chem. Phys. 83, 3462 (1985); D. M. Wardlaw and R. A. Marcus, Chem. Phys. Lett. 110, 230 (1984).
[26]R. Dickinson, G. W. Kirby, J. G. Sweeny, and J. K. Tyler, J. Chem. Soc. Faraday Trans. 2 74, 1393 (1978).
[27]B. Bak, F. M. Nicolaisen and O. J. Nielsen, J. Mol. Struct. 51, 17 (1979); J. Pfab, Chem. Phys. Lett. 99, 465 (1983).
[28]M. Noble, I. Nadler, H. Reisler, and C. Wittig, J. Chem. Phys. 81, 4333 (1984).
[29]G. Herzberg, in *Molecular Spectra and Molecular Structure* (Van Nostrand, New York, 1965).
[30]R. N. Dixon, K. B. Jones, M. Noble, and S. Carter, Mol. Phys. 42, 455 (1981); R. N. Dixon, M. Noble, C. Taylor, and M. Delhoume, Faraday Discuss. Chem. Soc. 71, 125 (1981).
[31]H. W. Kroto, *Molecular Rotational Spectroscopy* (Wiley-Interscience, London, 1975).
[32]*Landolt-Börnstein, Physical Constants for Atoms and Molecules* (Springer, Berlin, 1983), Part II (Sup.).
[33]See, e.g., G. M. McClelland, K. L. Saenger, J. J. Valentini, and D. Herschbach, J. Phys. Chem. 83, 947 (1975).
[34](a) M. Dupuis and W. A. Lester Jr., J. Chem. Phys. 83, 3990 (1985); (b) M. Marudarajan and G. Segal, Chem. Phys. Lett. 128, 1 (1986).
[35]In the language of classical mechanics, trajectories with initial conditions specified by the excitation do not fill the entire phase-space.
[36]H. Reisler, private communication [see Ref. 34(b)].
[37]See, e.g., P. M. Felker and A. H. Zewail, Chem. Phys. Lett. 128, 221 (1986), and references therein; J. L. Knee, L. R. Khundkar, and A. H. Zewail, J. Phys. Chem. 89, 3201 (1985).
[38]C. X. Qian, A. Ogai, H. Reisler, and C. Wittig (private communication).
[39]L. R. Khundkar, R. A. Marcus, and A. H. Zewail, J. Phys. Chem. 87, 2473 (1983).
[40]B. G. Gowenlock and L. Radom, Aust. J. Chem. 31, 2349 (1978).
[41]M. S. Child, in *Atom–Molecule Collision Theory*, edited by R. B. Bernstein (Plenum, New York, 1979).
[42]R. B. Bernstein, Phys. Rev. Lett. 16, 385 (1966); R. J. LeRoy and R. B. Bernstein, J. Chem. Phys. 54, 5114 (1971).
[43]See, e.g., D. V. O'Connor and D. Phillips, in *Time-Correlated Single Photon Counting* (Academic, London, 1984).
[44]See, e.g., B. I. Greene, R. M. Hochstrasser, and R. B. Weisman, J. Chem. Phys. 70, 1247 (1979).

CHAPTER 5B

RRKM Theory of Flexible Transition States Applied to the Dissociation of NCNO [a]

[a] The results presented in this chapter are to be submitted for publication: S. J. Klippenstein, L. R. Khundkar, A. H. Zewail and R. A. Marcus

In part A of this chapter, we presented energy resolved rate constants for the unimolecular dissociation of NCNO[1] and compared them with several simple models of the transition state. In particular, we calculated PST[2] rates, using various electronic degeneracy factors, as well as RRKM theory[3] for tight transition states, with harmonic frequencies chosen small enough so as to obtain rates of the correct order of magnitude. PST predictions were reasonably accurate very close to threshold, but deviated significantly at higher energies. Rates from models of tight transition states agreed with the measured rates over a subrange of the energies studied, but not over the entire range from threshold to 700 cm^{-1} above it. We speculated that such behavior could be a manifestation of the change in the transition state with energy. Thus a more detailed model of the transition state seems warranted.

A scheme for calculating rates of reactions involving flexible transition states has been proposed recently.[4] This method is capable of treating the transformation of the bending modes of the reactant to the hindered rotations of the transition state and then finally to the free rotations of the products, including the coupling between hindered rotational modes and overall rotations, explicitly. Examples of this variational implementation of RRKM theory for flexible transition states of other systems are given in several recent papers.[4–6] In this part, we calculate rates of dissociation of NCNO using this method.

Since the potential energy surfaces (PES) for the transition state (TS) region of unimolecular dissociations are not well known, we consider a number of model surfaces. The results obtained may then be used as a guide for the subsequent determination of an *ab initio* or improved semi-empirical potential energy surface in the TS region.

A brief description of the theoretical aspects of the dissociation rates is given in section 5B.1. Details of the model potentials are in section 5B.2, and the numerical results follow in 5B.3. The final section includes a discussion of the results.

5B.1. Theory

The specific rate constant k_{EJ} for unimolecular dissociation at a given energy E and total angular momentum quantum number J is given by[3]

$$k_{EJ} = N^{\dagger}_{EJ}/h\rho_{EJ} \ , \qquad (5B.1)$$

where ρ_{EJ} is the density of states for the reactant at the given E and J. The quantity $N^{\dagger}_{EJ}$ is the number of available quantum states of the transition state with energy less than or equal to E and with the given J.

The essentials of the theory have been described earlier (chapter 4). In the earlier studies[4] , a transformation to action-angle variables was used to facilitate conservation of angular momentum. In refs 5 and 6 it has been shown how the constraint of fixed total angular momentum may be implemented conveniently using conventional coordinates. In these studies an approximate separation of variables into the conserved and transitional modes mentioned earlier is introduced. In this chapter the method of refs 5 and 6 is used in all determinations of $N_{EJ}(R)$. In particular, a computational method based on eqs 12, 13 and 17 - 21 of ref 6 is employed.

Several points are discussed before we proceed with the determination of k_{EJ}'s. There are four electronic surfaces that are quasi-degenerate for large internuclear separations, two of them singlets and the other two triplets. The fragments CN and NO each have a doubly (spin) degenerate ground state. The ground state of NO is a Π state whose electronic degeneracy is removed by a weak spin-orbit interaction ($j_{el} = 1/2, 3/2$) of 120 cm^{-1}. As discussed earlier[1] , these states correlate with the four states of NCNO. A schematic diagram for the photodissociation of NCNO is reproduced in Figure 5B.1. The zero of energy has been chosen to be the energy of the fragments at infinite separation. The initial photoexcitation involves excitation to the S_1 state.[7] The latter state is calculated[8] to have a barrier height above the value at $R = \infty$ of 6674 cm^{-1}, and thus for excess energies below this amount dissociation must occur *via* either internal conversion to the S_0 (cf. Figure 5B.1) or intersystem crossing to the T_1 state. Arguments supporting the choice of rapid

internal conversion were presented in part A. Following the initial redistribution step, there may be "intersystem crossings" and "internal conversions" between the various states beyond the barriers on the excited states, where the different states have similar energies. The calculated barrier of 6674 cm^{-1} for the S_1 state indicates that crossings between the S_1 and S_0 can occur only at very large separations and therefore the excited singlet probably has little influence on the rates. A similar argument may be used to justify neglecting the second triplet state, which is of higher energy than S_1, in these calculations. In principle, they could play a role in a determination of the product state distributions in the case of PST, since in PST itself no detailed dynamics are postulated to restrict such usage of these states, intersystem crossing, etc., and the states may be nearly degenerate at the large $R^\dagger(l)$'s involved in PST.

A general discussion of the role of the triplet level in RRKM calculations has been given in ref 6. The discussion there indicates that when the intersystem crossing rates and triplet potential energy surfaces are not well-known, the best current approach to the rate calculations is to consider only the singlet state S_0. An alternative model is to consider a limiting case where the intersystem crossing rates are very rapid and calculate an $N^\dagger_{EJ}(R)$ as the sum of the number of states for both the S_0 and T_1 states ($N_{EJ} = N^{S_0}_{EJ} + N^{T_1}_{EJ}$, each of which contains a degeneracy factor g_e which is one for the singlet state and three for the triplet state). Then the $R^\dagger$ at which this $N_{EJ}(R)$ has a minimum is calculated.

In order to perform the above calculation a potential energy surface for the triplet state, T_1, is needed. This triplet state is expected to be slightly repulsive at large R, before becoming attractive by an amount of about 11000 cm^{-1} at its equilibrium configuration.[7] Recent *ab initio* calculations[8] of the T_1 potential surface indicate that the barrier height above the value at infinite separation is 4597 cm^{-1}. This reasonably large barrier height indicates that the T_1 triplet state is not likely to play a major role in the determination of the dissociation rates.

We consider a simple barrierless model for the T_1 state (which overestimates the possible effect of the triplet state based on the *ab initio* results of ref 8) to

indicate the difference between a PST and a RRKM treatment of an excited triplet state for the case in which the intersystem crossing rates are rapid. In PST one typically considers the degeneracies at $R = \infty$ (because the $R^{\dagger}(l)$'s of PST are usually quite large) in which case the T_1 contributes an extra factor of 3. For comparison with the contribution of T_1 with RRKM theory the triplet potential energy is set to zero throughout the transition state region (the dashed line in Figure 5B.1.)

The determination of the density of states for the reactant molecule deserves mention. For the present NCNO dissociation reaction the number of vibrational modes for the reactant is small enough that a direct count of the number of states is easily performed. Diagonal anharmonicities were included in the direct count used here. These diagonal anharmonicities were estimated through consideration of the frequencies and dissociation energies of the respective bonds. Their inclusion increased the density of states by a factor of only 1.25 at energies near the dissociation threshold of 17085 cm^{-1}. Off-diagonal anharmonicites are expected to increase the density of states further, perhaps by a factor of similar magnitude. These off-diagonal anharmonicities were not included in the present density of states calculation because their values are not known. The correction due to these anharmonicities should be reasonably constant over the energy range of only 700 cm^{-1} for which the rates were measured.

5B.2. Model potential energy surfaces for S_0

This method of rate calculations requires knowledge of the potential energy surface. The lack of an *ab initio* surface forced us to model it using analytic functions. Before presenting the numerical results, we describe the procedure used to construct the surface. The conserved modes were treated as harmonic oscillators with an exponential interpolation between the reactant and product frequencies and reactant and product bond distances being used.

$$\lambda_i(R) = \lambda_i^p + (\lambda_i^r - \lambda_i^p)g(R), \qquad (5B.2)$$

where $g(R) = \exp[-\alpha(R-R_e)]$,[4,9] R_e is the equilibrium value of R for the reactants, and λ denotes ν or r_e, i denotes NC or NO, ν_{NC} and $r_{e,NC}$ are the terminal NC stretch frequency and separation distance, and ν_{NO} and $r_{e,NO}$ denote those of NO. The r and p superscripts denote the reactant (NCNO) and products (NC + NO), respectively. A value of 1.0 Å^{-1} for the parameter α, which has been commonly found to provide agreement with experiment in the adiabatic channel model[9] , was used. The properties for the conserved modes are given in Table 5B.1, together with the frequencies and anharmonicities for the transitional modes of the reactant.

In the model of the potential energy surface assumed here for the transitional modes, the sum of a bonding potential for the central NC—NO bond and nonbonding potentials for the other interactions within the transitional modes was used. The nonbonding potential was chosen to be a sum of 6-12 Lennard-Jones potentials for the van der Waals interactions between the nonbonded atoms of the two separate fragments, as in eq 5B.3 below.[10] The bonding potential was approximated by a Varshni potential,[11,12] multiplied by the factor $\cos^2(\theta_{NCN} - \theta_{e,NCN})\cos^2(\theta_{CNO} - \theta_{e,CNO})$ to allow for the loss of bonding which occurs when the fragments are improperly oriented. Here, θ_{NCN} and θ_{CNO} are the NCN and CNO bending angles, respectively, while $\theta_{e,NCN}$ and $\theta_{e,CNO}$ and the e subscript denotes their equilibrium values, as given in Table 5B.1. The Varshni potential rather than a Morse potential was employed since the latter is known[9,12] to decay to zero too slowly at large separation distances, whereas the former is believed to provide a better representation for this region.[12]

Assuming this representation of the nonbonding potential V_{LJ} in terms of van der Waals interactions we have

$$V_{LJ} = \sum_{i,j=1}^{2}{}' 4\epsilon_{ij}\left[(\sigma_{ij}/r_{ij})^{12} - (\sigma_{ij}/r_{ij})^{6}\right], \qquad (5B.3)$$

where i and j label atoms in the NC and NO fragments, respectively, and the prime indicates that the central NC—NO bond is not included in the sum. The parameters σ_{ij} and ϵ_{ij} denote the usual Lennard-Jones parameters for the interaction between atoms i and j; r_{ij} is then the separation distance between atoms i and

j. The Varshni potential V_V for the NC-NO bond, denoted by CN in eq 5B.4, is given by the standard form[11,12]

$$V_V = D_{CN}\left\{1 - \left(\frac{r_{e,CN}}{r_{CN}}\right)\exp\left[-\beta_{CN}\left(r_{CN}^2 - r_{e,CN}^2\right)\right]\right\}^2 - D_{CN}. \qquad (5B.4)$$

The parameters for this model potential energy surface for the transitional modes are given in Tables 5B.2 and 5B.3. The parameters for the Lennard-Jones potential V_{LJ} (Table 5B.2) were taken to be the same as those which gave good results in Monte Carlo simulations of amides and peptides.[13] The parameters D_{CN} and β_{CN} of the Varshni potential were chosen to fit the *total* potential energy function to an assumed Varshni potential surface for the NC—NO separation distance in the range of 3.3 Å. The parameters for this assumed Varshni potential surface are given in Table 5B.3 and were determined here from a consideration of the spectroscopic constants and the force constants determined by Wilson G-matrix analysis of the harmonic frequencies in ref 14. The parameter $r_{e,CN}$ for the fitted potential was held fixed at 1.2 Å. The results were found to be relatively insensitive to this parameter.

We also constructed a second potential surface by similar methods, using an assumed β parameter of 0.7Å^{-2} rather than 0.48Å^{-2}. The resulting parameters for this surface, denoted by (ii), are also given in Table 5B.3.

5B.3. Results of rate calculations

The results of the present k_{EJ} calculations are compared with the experimental results of ref 1 in this section. Unless otherwise specified, the results given here are for the case of reaction on only the ground singlet state. Also, all reaction rate calculations were performed for a total angular momentum quantum number J of 3, which is the estimate of its average value given in refs 1 and 7.

Results for k_{EJ} calculations for the above model of the potential energy surface are given in Figure 5B.2, where the dissociation rates are plotted versus energy. Also given in the same figure are results for the case in which T_1 is included (but with no barrier) and in which the intersystem crossing rate in the transition state region is assumed to be much larger than the dissociation rates. Recent *ab initio*

calculations show that the triplet state T_1 is even more repulsive than this simplified model. Thus the contribution from the T_1 state is even less than that shown in Figure 5B.2 and will also be negligible at lower excess energies. Results are also given (Figure 5B.3) for the potential surface labelled (ii).

Figure 5B.4 shows results of three types of PST calculations. They are (i) a classical PST, (ii) a quantum PST, and (iii) a calculation in which $N_{EJ}(\infty)$ is used for $N^{\dagger}_{EJ}$ in eq 5B.1. The third method corresponds to a PST calculation in which the l-dependent barriers are all at "infinite" separation. While the effective barriers can never be at infinity, they can be at such a large separation distance that the effective barrier energy, a centrifugal potential plus an attractive potential, is negligible. These calculations have all been performed using a C_6 potential parameter of 1.6×10^5 cm $^{-1}$Å^6, as in refs 1 and 7.

5B.4. Discussion

The results in Figure 5B.2 corresponding to the singlet plus triplet deviate significantly from the singlet state calculation only in the low energy region, namely, for E less than about 400 cm^{-1}. This disappearing contribution of the triplet state occurs as the rate changes from being determined mainly by the number of states at $R = \infty$ to being determined mainly by the the number of states at the inner minimum in N_{EJ}. Also, this effect reflects the R of the inner minimum in the number of states being small enough that the singlet-triplet gap for the present model surfaces is comparable to or larger than the excess energy. That is, when this inner minimum in N_{EJ} is less than about 4 Å the difference between the minimum potential energy for a given R on the singlet and triplet states becomes quite large, while at the same time the orbital kinetic energy of the two fragments is becoming relatively large, resulting in a much lower number of states for the triplet potential surface. In PST the R-value of the purely l-dependent barrier of PST does not become this small until much higher energies are reached and so the contribution from the triplet remains considerable until much higher energies.

The results given for the low energies E in Figure 5B.2 for dissociation on the singlet state only are quite similar to the PST results for the singlet state shown in

Figure 5B.4. This similarity arises because at these energies the inner minimum in the number of states N_{EJ} is about the same or more than the number of PST states (and because the triplet state is being neglected). At higher energies the value of this minimum of N_{EJ} actually becomes less than that for PST and so, within the framework of the present potential energy surface, this new minimum represents a better transition state. This effect can be seen in Figures 5B.5 - 5B.7, where plots of $N_{EJ}(R)$ versus R are given for the $\beta = 0.7\text{Å}^{-2}$ potential energy surface at the the three energies, 50 cm^{-1}, 700 cm^{-1} and 2348 cm^{-1}. These results indicate that the inner minimum becomes more dominant with increasing energy.

There are two parts of the potential energy surface function which can significantly affect the calculated rates: the dissociative and the hindered rotational potentials. If the dissociative (bonding) potential actually approaches zero more rapidly than that given by the Varshni potential energy surface considered in Figure 5B.2 the results start to deviate from PST results at lower energies. This effect can be seen in Figure 5B.3, where results are given for the different values of the β parameter. In this case for a $\beta = 0.70$ Å^{-2} the RRKM results already differ from those of PST by a factor of 0.69 at an $E = 700$ cm^{-1}. The calculated rates also depend on the strength and location of the attractive wells of the Lennard-Jones potentials describing the hindered rotation of the fragments. While results for this case are not presented here, when one simply increases σ_{ij} by about 0.3Å, the results are analogous to those obtained for the larger β parameter study.

The results in Figure 5B.4 indicate that classical PST and the $N_{EJ}(\infty)$ treatments of the transitional modes are very similar for these energies, with the differences being only about one to two percent. This similarity occurs because for the energies employed in the experimental work in ref 1 the assumed attractive potential in PST is essentially such a long range potential that $R^{\dagger}(l)$ is so large that the effective barrier is negligible for even the largest l's present. If these l-dependent barriers were completely negligible then the $N_{EJ}(\infty)$ and PST calculations would give identical results. Similarly, the classical and quantum phase space theory results are in good agreement, with the classical calculation being typically 10 to 15

percent below the quantum one. Finally, it also interesting to note that when only the singlet surface S_0 is considered as here, the present results using the different types of PST or using RRKM theory are in better agreement with the experimental results than the PST calculations given in Figure 14 of ref 1, where the electronic degeneracy was treated simply as some constant over the energy range with a second contribution arising from the upper singlet and triplet states shifted by 120 cm^{-1}.

In the expression for k_{EJ} given in eq 5B.1, we assumed that there is one dominant minimum in the number of states N_{EJ} as a function of the dissociation coordinate R. The results presented above indicate two local minima in the plot of N_{EJ} versus R. In Figure 5B.8 the results from three methods for taking into account the presence of two minima in the $N_{EJ}(R)$ plot are given. The simplest method is to take $N^{\dagger}_{EJ}$ as the overall minimum in $N_{EJ}(R)$ and this is what has been done in Figures 5B.2 and 5B.3. In another method, termed unified statistical theory,[15] statistical reflection and transmission probabilities are introduced to obtain $N^{\dagger}_{EJ}$. In a third method[16] a lower bound is determined (within certain dynamical assumptions) to $N^{\dagger}_{EJ}$. Formulae for these different treatments are summarized in ref 6. The results plotted in Figure 5B.8 for potential surface (i) indicate that in the present case the effect of there being two minima was never larger than a factor of 1.4. Similar results for potential surface (ii) indicate that the effect was never larger than a factor of 2.0.

In Figures 5B.9 - 5B.12 the dependence of the present potential energy surfaces on certain bending angles are presented for typical $R^{\dagger}$'s. These figures are given for a range of R where an *ab initio* determination of the potential surface for the transitional modes would be particularly useful for obtaining improved bending and hindered rotational potential energy surfaces. In particular, from this figure it is seen that in the TS region the absolute minimum in the potential for a given R is negative and has a magnitude of a few thousand cm^{-1} while the rotational barriers are positive and have a much larger magnitude.

5B.5. Conclusions

An implementation of RRKM theory for highly flexible transition states has been applied to the dissociation of NCNO. The ground singlet state S_0 is most likely the only state contributing to the determination of the rate constants. The results also indicate that the rate constants determined from RRKM theory are similar to the PST results for the S_0 state only with minor differences at the highest energies studied. The results of these calculations are quite sensitive to the PES. An accurate *ab initio* potential energy surface for the transition state region is therefore highly desirable.

5B.6. References

1. L. R. Khundkar , J. L. Knee and A. H. Zewail, *J. Chem. Phys.*, **87**, 77, (1987.).

2. P. Pechukas and J. C. Light, *J. Chem. Phys.*, **42**, 3281, (1965).
   P. Pechukas, R. Rankin and J. C. Light, *J. Chem. Phys.*, **44**, 794, (1966).
   C. Klotz, *J. Phys. Chem.*, **75**, 1526, (1971).
   C. Klotz, *Z. Naturforsch, Teil***A**, **27**, 553, (1972).
   W. J. Chesnavich and M. T. Bowers, *J. Chem. Phys.*, **66**, 2306, (1977).

3. P. J. Robinson and K. A. Holbrook, in *Unimolecular Reactions* Wiley, New York, (1972).
   W. Forst, *Theory of Unimolecular Reactions* Acad. Press, NY, (1973).
   R. E. Weston and H. A. Schwarz, *Chemical Kinetics* Prentice-Hall, Englewood Cliffs, NJ, (1972).
   R. A. Marcus, *J. Chem. Phys.*, **20**, 359, (1952).
   R. A. Marcus and O. K. Rice, *J. Phys. Colloid. Chem.*, **55**, 894, (1951).
   R. A. Marcus, *J. Chem. Phys.*, **43**, 2658, (1965).
   R. A. Marcus, *ibid.*, **52**, 1018, (1970).

4. D. M. Wardlaw and R. A. Marcus, *Chem. Phys. Lett.*, **110**, 230, (1984).
   D. M. Wardlaw and R. A. Marcus, *J. Chem. Phys.*, **83**, 3462, (1985).
   D. M. Wardlaw and R. A. Marcus, *J. Phys. Chem.*, **90**, 5383, (1986).
   D. M. Wardlaw and R. A. Marcus, *Adv. Chem. Phys.*, **70**, 231, (1988).

5. S. J. Klippenstein and R. A. Marcus, *J. Phys. Chem.* **1988**, in press.

6. S. J. Klippenstein and R. A. Marcus, *J. Phys. Chem.* **1988**, submitted.

7. See references 6 and 28 in part A.

8 Y. Y. Bai and G. A. Segal, private communication.

9. M. Quack and J. Troe, *Ber. Bunsenges. Phys. Chem.*, **78**, 240, (1974).
J. Troe, *J. Phys. Chem.*, **88**, 4375, (1984).

10. The effect of the Coulombic potentials between the partial charges on the different atoms, which are typically included in molecular dynamics simulations, were also considered here. They were found to have a negligible effect on the number of states and so were neglected in the calculations presented here.

11. Y. P. Varshni, *Rev. Mod. Phys.*, **29**, 664, (1957).

12. R. J. Duchovic, W. L. Hase, B. Schlegel, M. J. Frisch and K. Raghavachari, *Chem. Phys. Lett.*, **89**, 120, (1982).
R. J. Duchovic and W. L. Hase, *Chem. Phys. Lett.*, **110**, 474, (1984).
D. Steele, E. R. Lippincott and J. T. Vanderslice, *Rev. Mod. Phys.*, **34**, 239, (1962).

13. W. L. Jorgensen and C. J. Swenson, *J. Am. Chem. Soc.* , **107**, 569, (1985).

14. B. Bak, F. M. Nicolaisen, O. J. Nielsen and S. Skaarup, *J. Mol. Struct.*, **51**, 17, (1979).

15. J. O. Hirschfelder and E. Wigner, *J. Chem. Phys.*, **7**, 616, (191939).
W. H. Miller, *J. Chem. Phys.*, **65**, 2216, (1976).
W. J. Chesnavich, L. Bass, T. Su and M. T. Bowers, *J. Chem. Phys.*, **74**, 2228, (1981).
S. N. Rai and D. G. Truhlar, *J. Chem. Phys.*, **79**, 6046, (1983).

16. E. Pollak and P. Pechukas, *J. Chem. Phys.*, **70**, 325, (1979).
E. Pollak, M. S. Child and P. Pechukas, *J. Chem. Phys.*, **72**, 1669, (1980).

Table 5B.1 : Spectroscopic Parameters for NCNO

Parameter		Reactants[a] Value	Products[a] Value
(i) Frequencies	NC stretch	2170	2068.7
(cm^{-1})	NO stretch	1501	1904.03
	CN stretch	820	
	CNO bend	216.5	
	NCN bend	588.5	
(ii) Anharmonicities[b]	NC stretch	13.1	13.1
(cm^{-1})	NO stretch	14.1	14.1
	CN stretch	9.4	
	CNO bend	0.2	
	NCN bend	0.5	
Coordinates	R_e	2.4Å	
	$r_{e,NC}$	1.163 Å	1.1718 Å
	$r_{e,NO}$	1.217 Å	1.1508 Å
	$\theta_{e,CNO}$ [c]	120°	
	$\theta_{e,NCN}$ [c]	180°	

[a] Unless stated otherwise, all values are as specified in ref 7.

[b] Anharmonicities have been obtained from ref 7 or estimated from the dissociation energy.

[c] The values used correspond to sp and sp^2 bonding geometries rather than to the equilibrium bending angles.

Table 5B.2: Lennard-Jones Potential Parameters

Parameter	Value[a]	Units
σ_{CO}	3.36	Å
σ_{NN}	3.25	Å
σ_{NO}	3.11	Å
ϵ_{CO}	51.9	cm^{-1}
ϵ_{NN}	59.5	cm^{-1}
ϵ_{NO}	46.7	cm^{-1}

[a] All values have been obtained from reference 13 making use of the combination rules $\epsilon_{ij} = (\epsilon_{ii}\epsilon_{jj})^{1/2}$ and $\sigma_{ij} = \frac{1}{2}(\sigma_{ii} + \sigma_{jj})$.

Table 5B.3: Varshni Potential Parameters

Surface	Parameter	Assumed potential[a]	Effective potential
(i)	$r_{e,CN}$	1.418 Å	1.2 Å
	β_{CN}	0.48 $Å^{-2}$	0.517 $Å^{-2}$
	D_{CN}	17880 cm^{-1}	32110 cm^{-1}
(ii)	$r_{e,CN}$	1.418 Å	1.2 Å
	β_{CN}	0.70 $Å^{-2}$	0.7725 $Å^{-2}$
	D_{CN}	17880 cm^{-1}	42600 cm^{-1}

[a] The parameter β_{CN} was obtained by setting $\partial^2 V_{varsh}/\partial^2 r_{CN} = k$ where k is the force constant for the central CN stretch given in reference 14. For surface (ii) β_{CN} was arbitrarily set to 0.70 Å. All other parameters of the assumed potential are as determined spectroscopically in ref. 7

Relevant Potential Energy Surfaces of NCNO

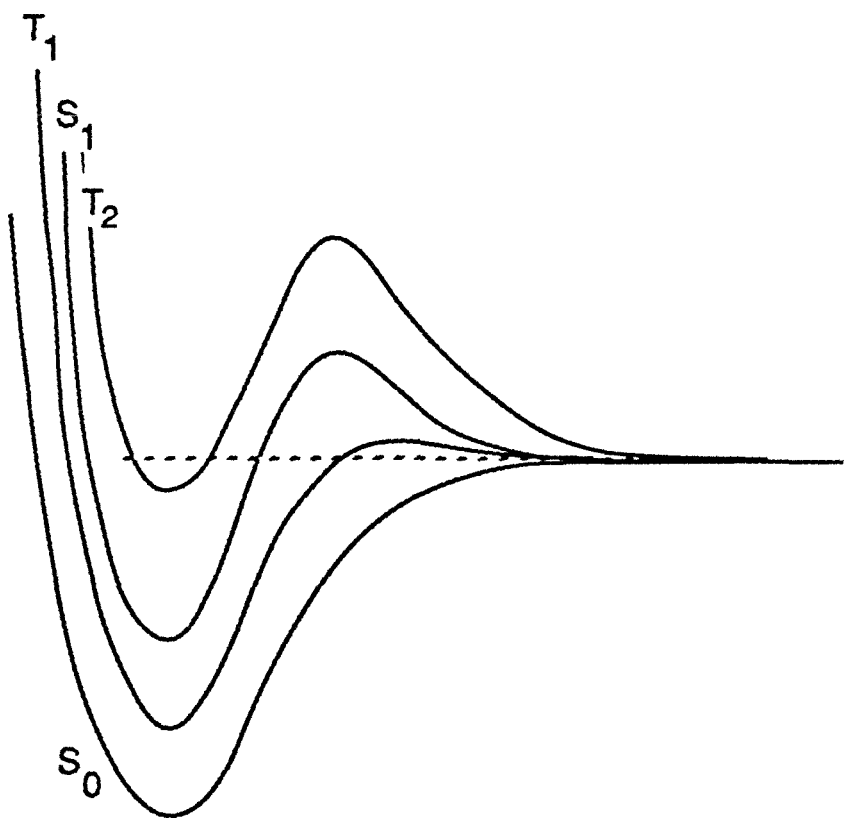

Figure 5B.1. Schematic potential energy diagram for the dissociation of NCNO into NC and NO, indicating singlet and triplet states.

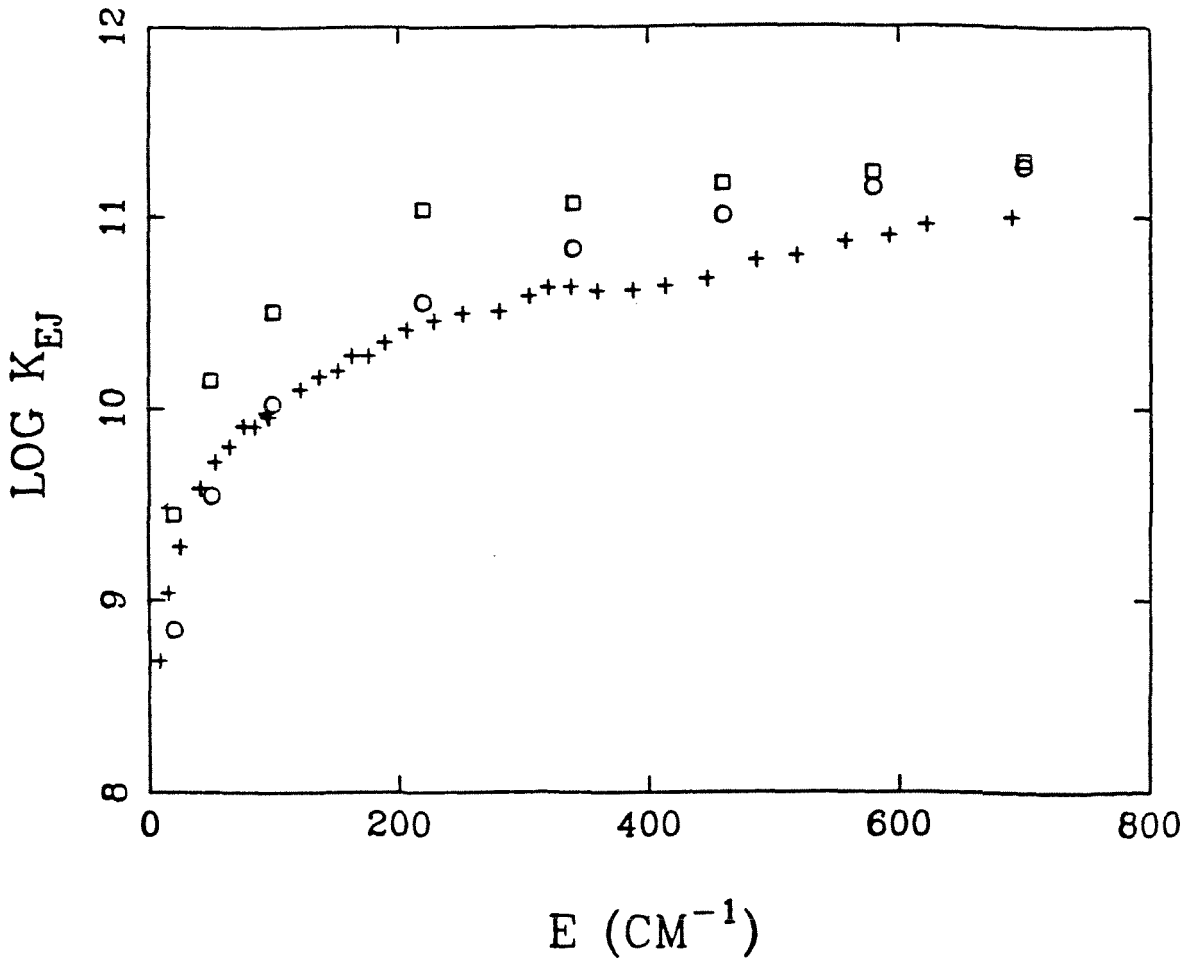

Figure 5B.2. Plot of theoretically determined rate constants log k_{EJ} vs. energy for a variety of treatments of the T_1 triplet surface, and plot of the experimentally determined rate constants (plus signs). The circles denote RRKM calculations on the singlet surface only, boxes denote RRKM calculations including singlet and triplet surfaces with a degeneracy of three for the triplet.

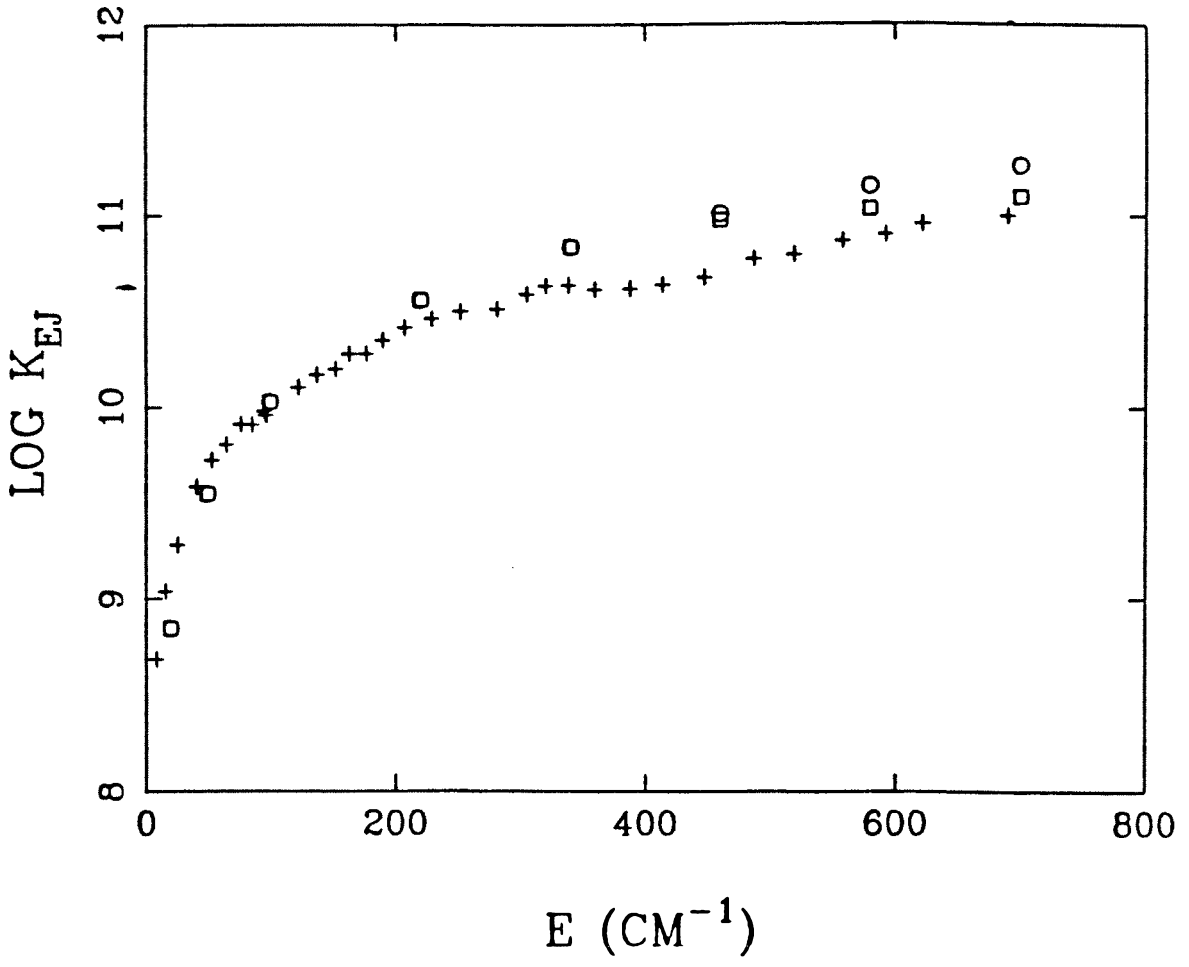

Figure 5B.3. Plot of theoretically determined rate constants log k_{EJ} vs. energy for two different assumed parameters for the Varshni bonding potential, and a plot of the experimentally determined rate constants (plus signs). Also included is a calculation which uses $N_{EJ}(\infty)$. The circles denote RRKM calculations for an assumed potential with a β parameter of 0.48 $Å^{-2}$, boxes denote RRKM calculations for an assumed potential with a β parameter of 0.70 $Å^{-2}$.

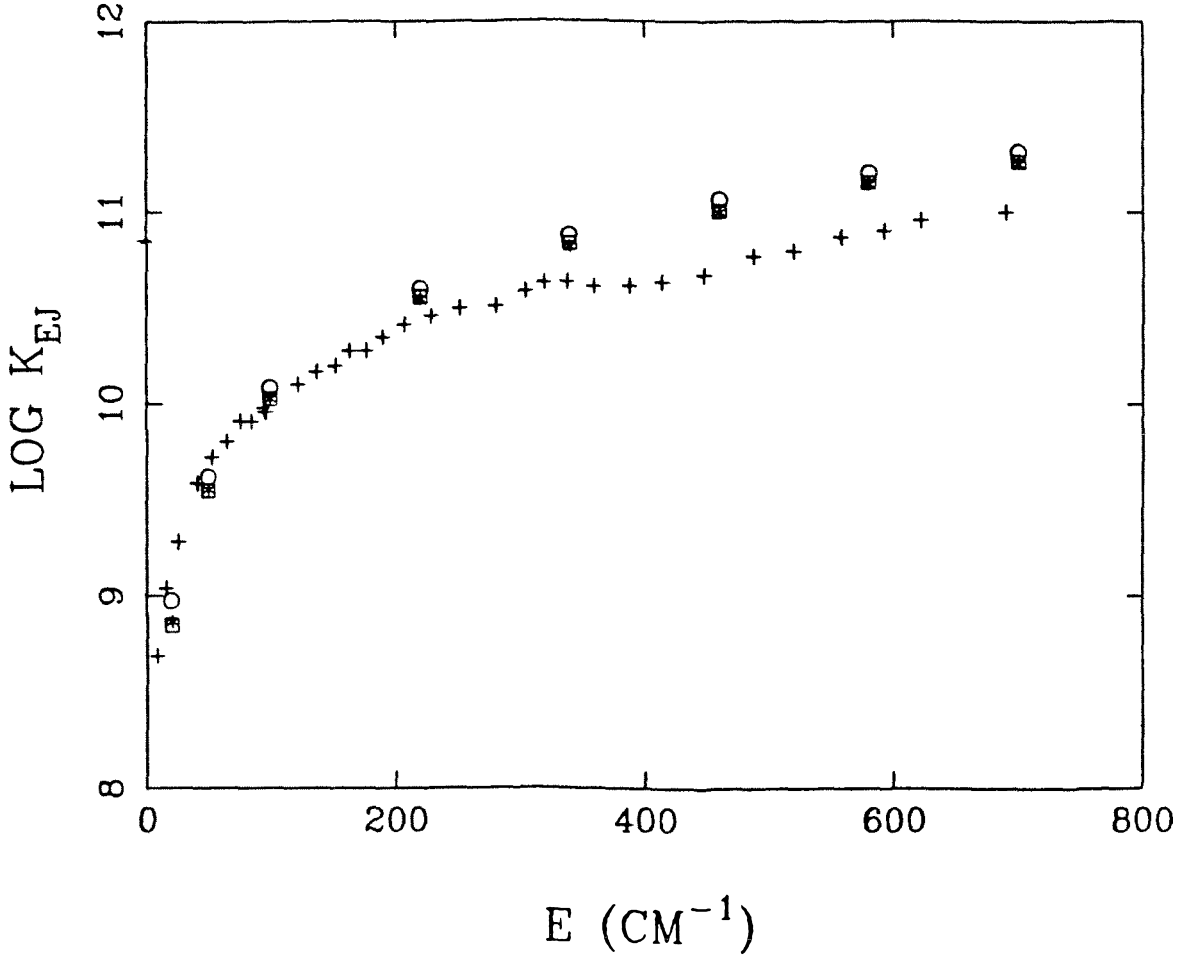

Figure 5B.4. Plot of rate constants log k_{EJ} vs. energy as determined via quantum PST, classical PST and $N_{EJ}(\infty)$ and a plot of the experimentally determined rate constants (plus signs). Circles denote quantum PST calculations, asterisks the classical PST calculations, and boxes the $N_{EJ}(\infty)$ calculation.

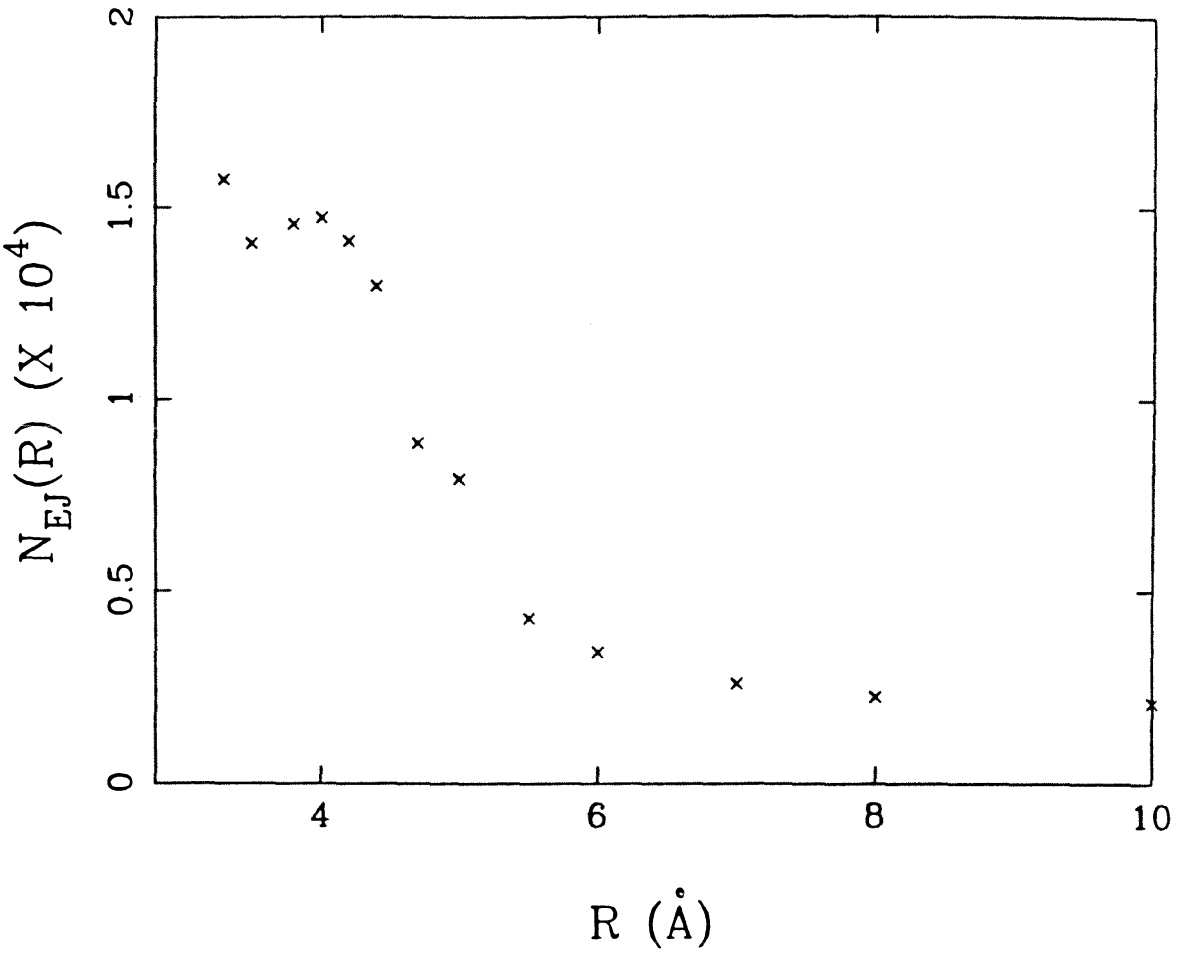

Figure 5B.5. Plot of number of states $N_{EJ}(R)$ vs. separation distance R for potential energy surface (ii) for an excess energy of 50 cm^{-1}.

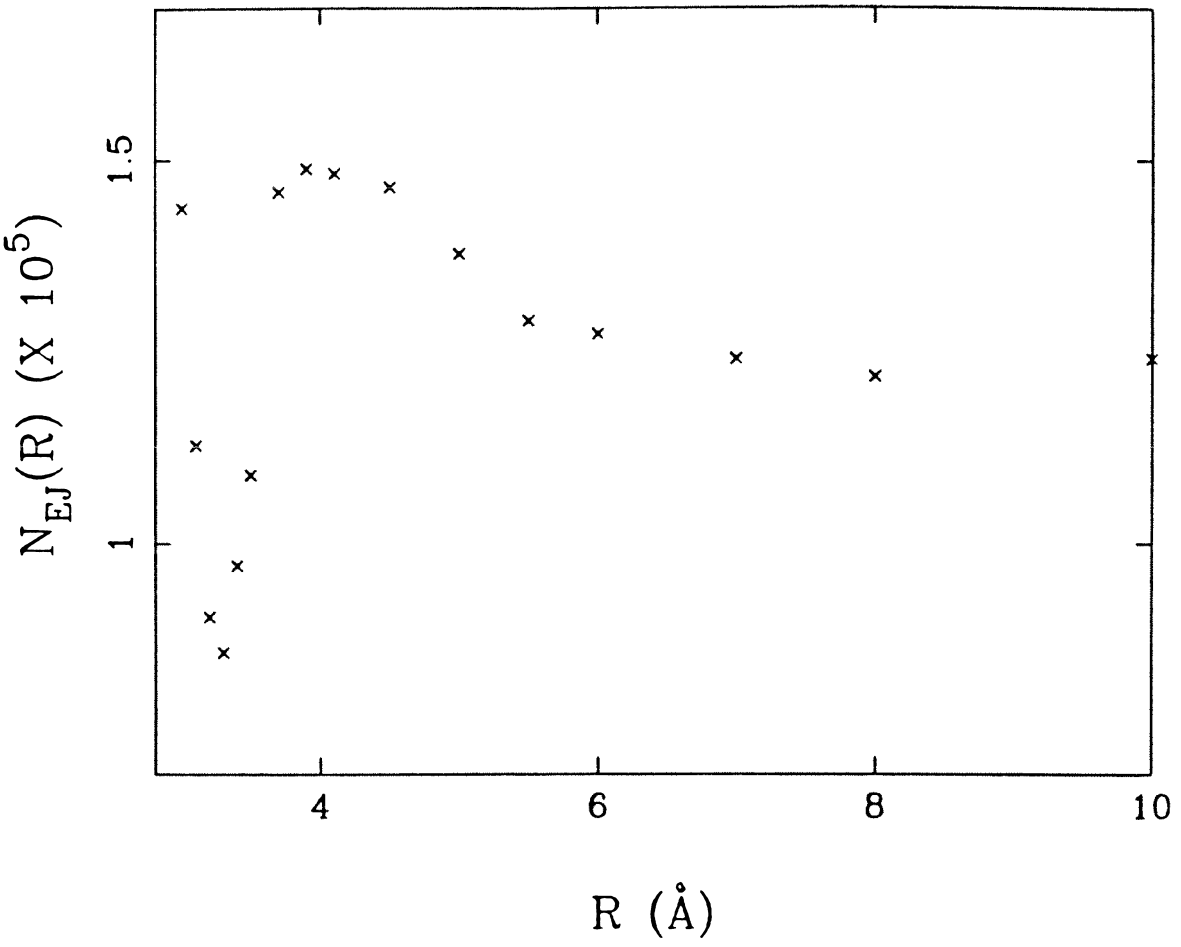

Figure 5B.6. As in Figure 5 but for an excess energy of 700 cm^{-1}.

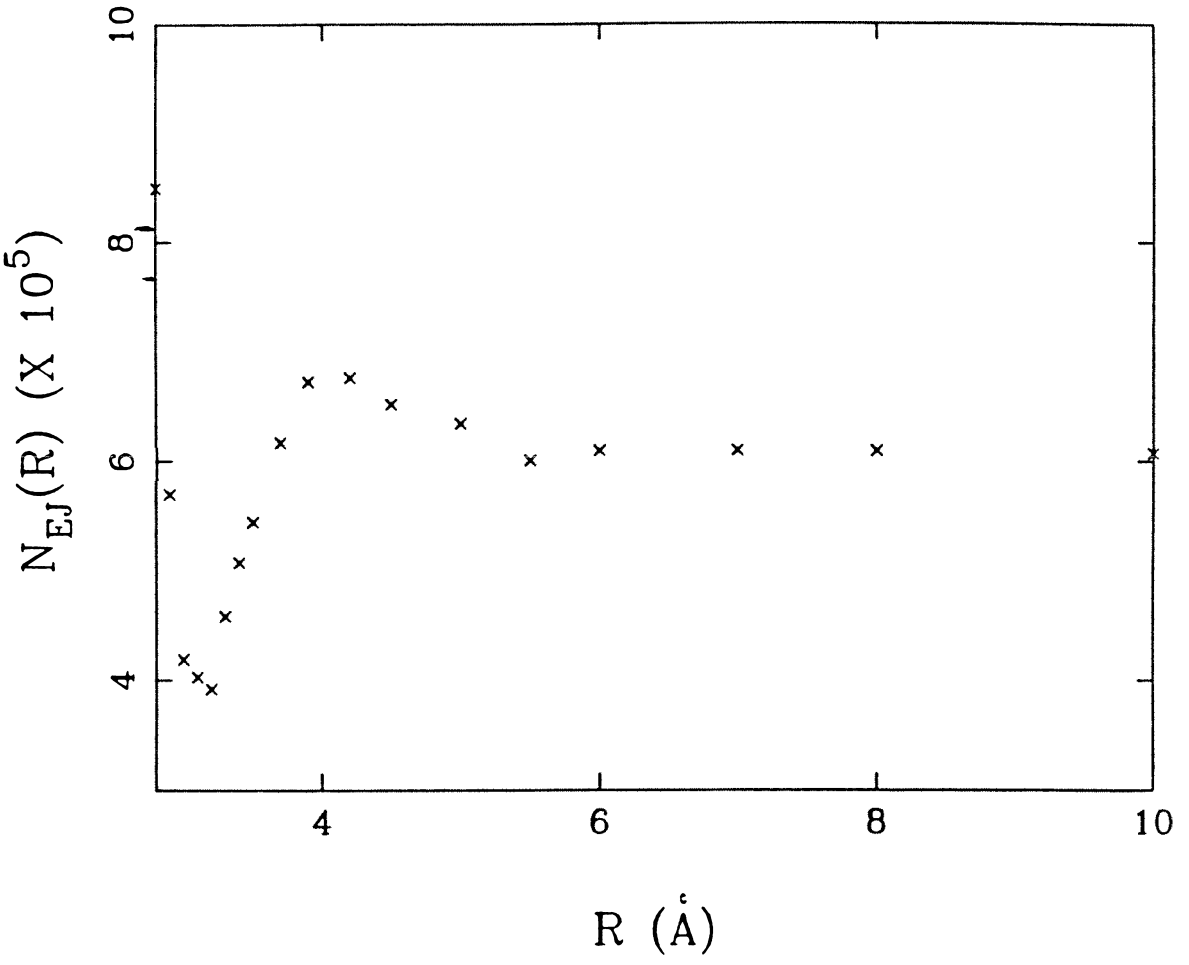

Figure 5B.7. As in Figure 5 but for an excess energy of 2000 cm^{-1}.

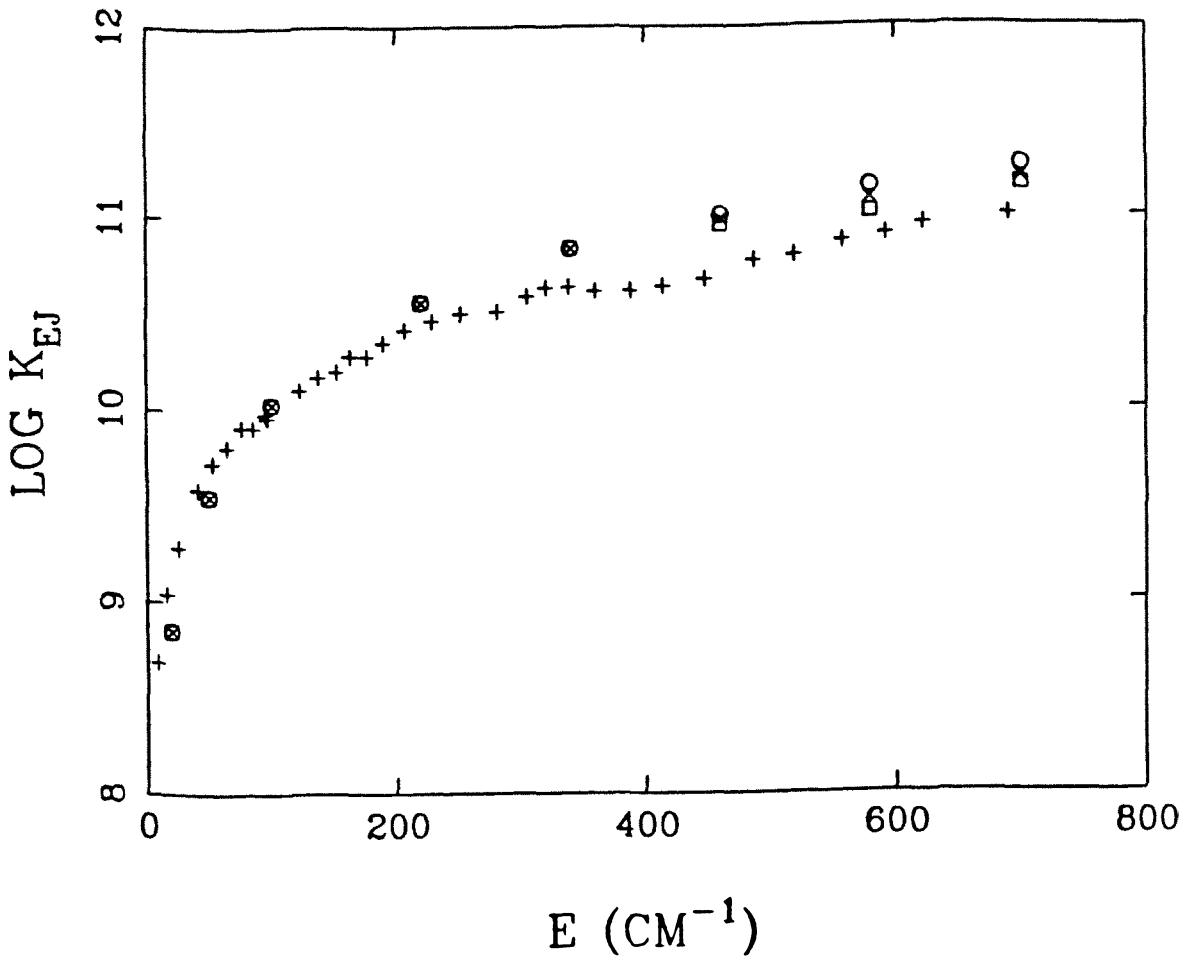

Figure 5B.8. Plot of rate constants log k_{EJ} vs. energy when the two minima in the $N_{EJ}(R)$ plot are taken into account, and a plot of the experimentally determined rate constants (plus signs). Crosses denote the use of the unified statistical theory of ref 14, boxes refer to the use of the lower bound of ref 15, and circles are for the use of the overall minimum.

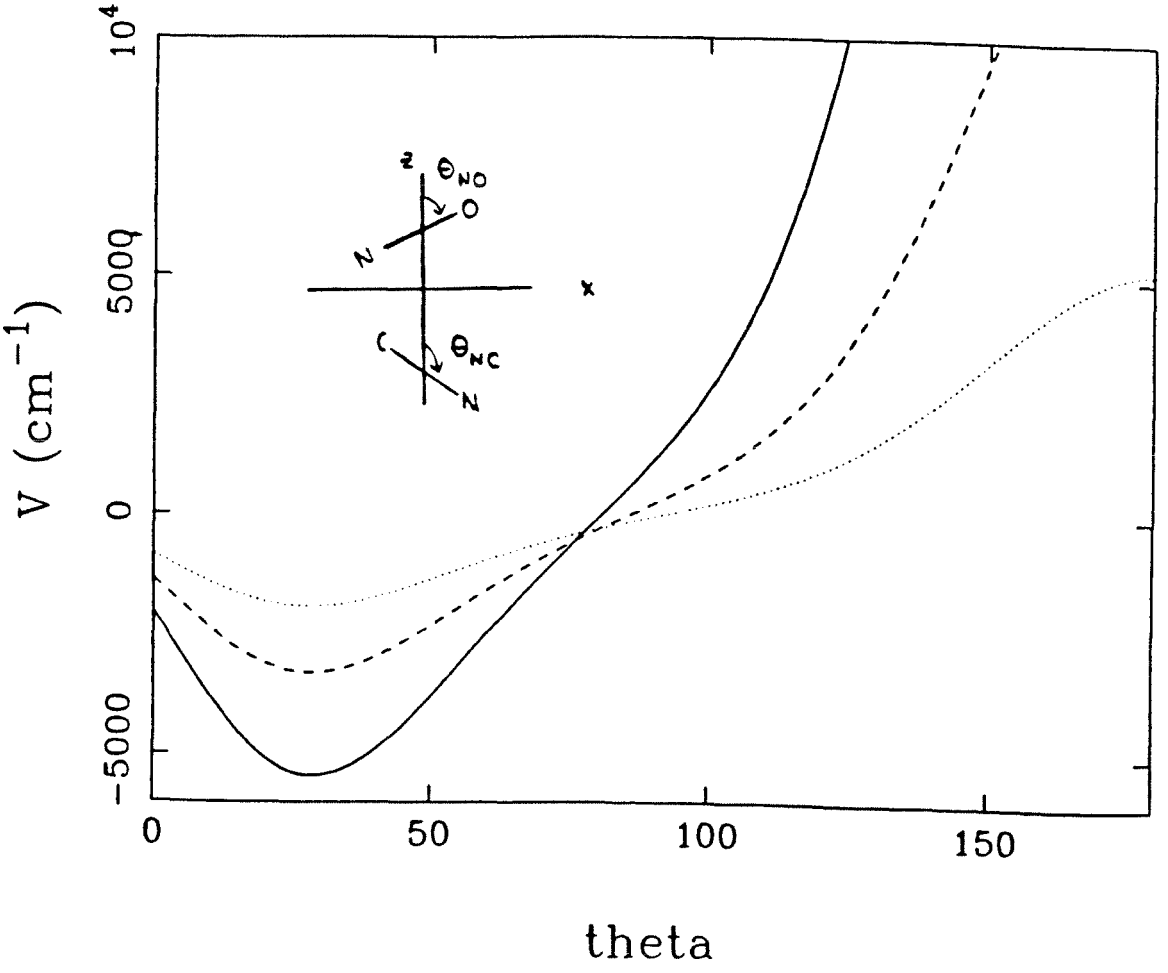

Figure 5B.9. Plot of potential energy surface (i), as a function of θ_{NC}, and θ_{NO} for a variety of R's in the transition state region. θ_{NO} and θ_{NC} are the angles defining the orientation of the fragments NC and NO for a planar NCNO molecule and are illustrated in the inset. The equilibrium orientation is for $\theta_{NO} \approx 30°$ and $\theta_{NC} \approx 180°$. The dependence of the potential energy on θ_{NO} for $\theta_{NC} = 180°$ and $R = 3.3$, 3.5, and 3.7 Å is given by the solid, dashed and dotted lines, respectively.

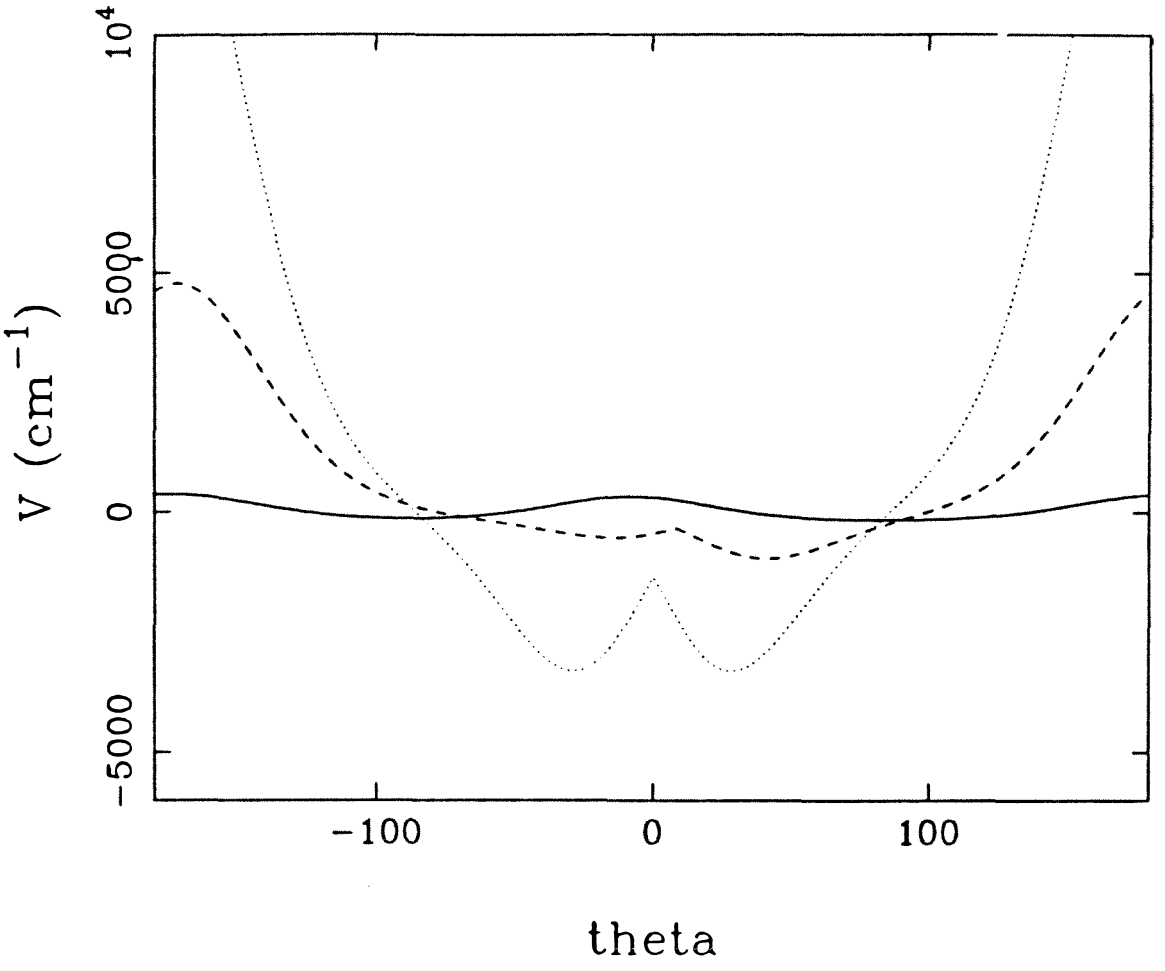

Figure 5B.10. The dependence of potential energy surface (i) on θ_{NO} for R = 3.5 Å and $\theta_{NC} = 90°$, 135°, and 180° is given by the solid, dashed and dotted lines, respectively.

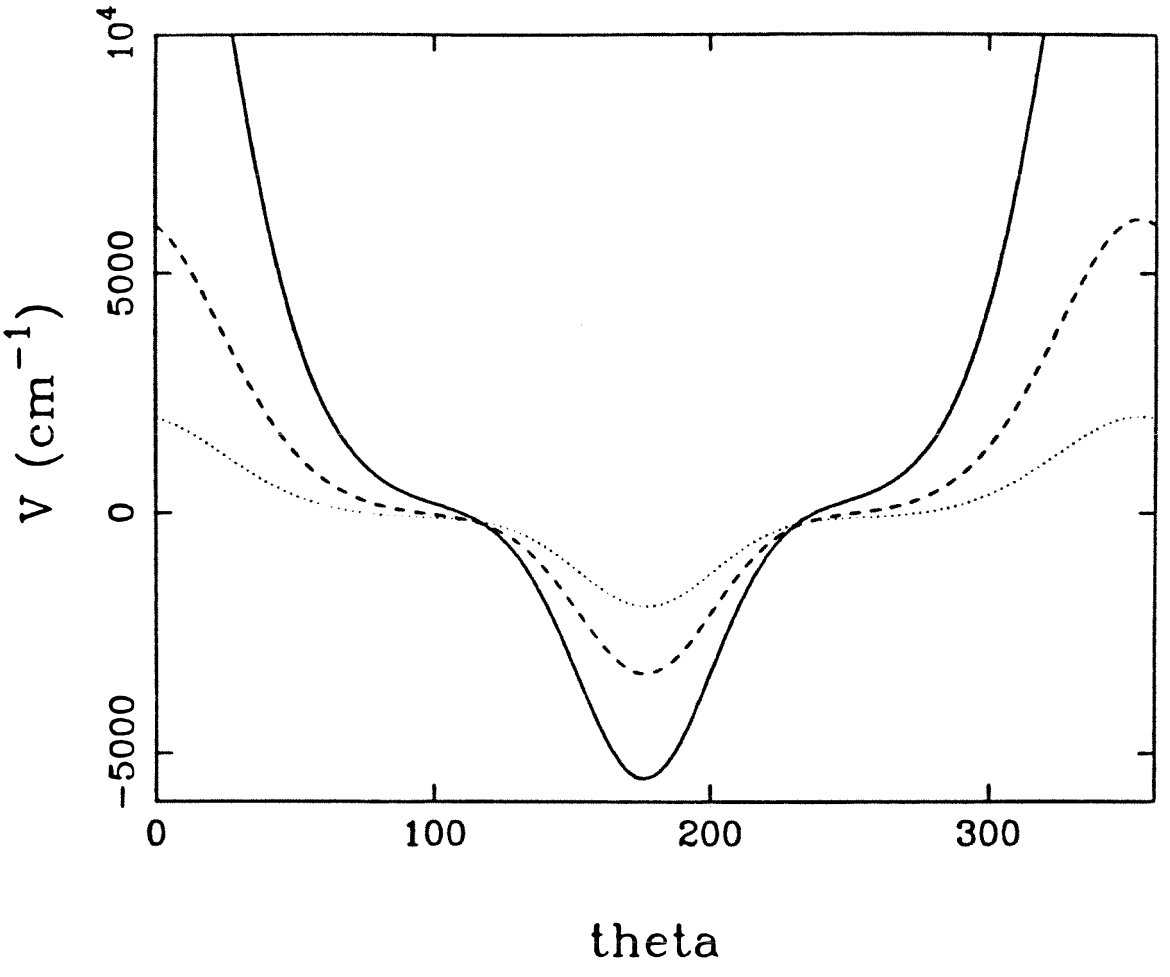

Figure 5B.11. The dependence of potential energy surface (i) on θ_{NC} for θ_{NO} = 30 and R = 3.3, 3.5, and 3.7 Å is given by the solid, dashed and dotted lines, respectively.

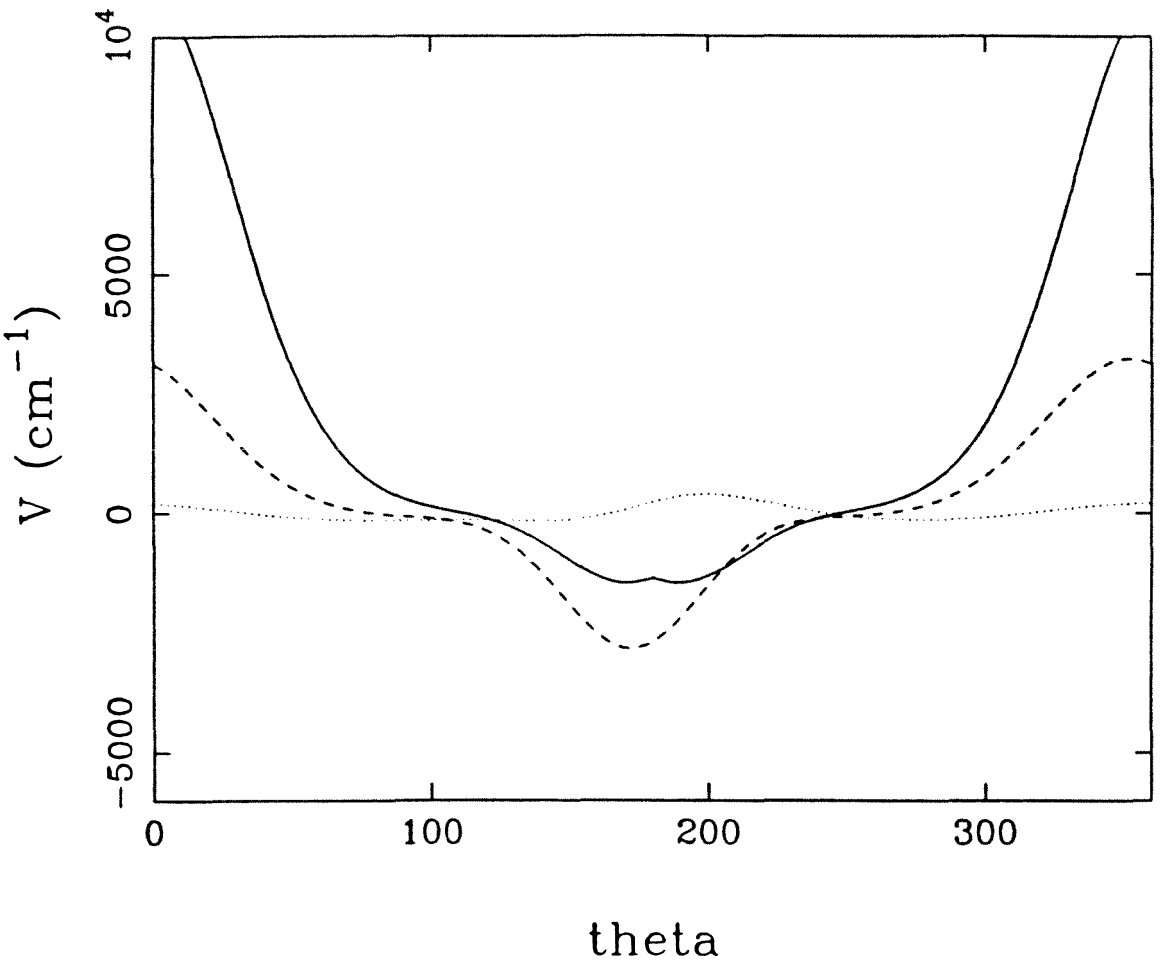

Figure 5B.12. The dependence of potential energy surface (i) on θ_{NC} for R = 3.5 Å and θ_{NO} = 0°, 45°, and 90° is given by the solid, dashed and dotted lines, respectively.

CHAPTER 6

TIME-RESOLVED PHOTOFRAGMENT SPECTROSCOPY: II.

Dissociation Dynamics of 1,2–diiodotetrafluoroethane ($C_2F_4I_2$).

6.1. Introduction

Molecular beam studies of reactive scattering have shown that simple bond dissociation reactions can be categorized as being either *direct* mode or *complex* mode.[1] The primary distinguishing factor is that the complex mode mechanism involves an intermediate that exists for many rotational periods, whereas a direct mode reaction does not. The two types of reactions lead to characteristic patterns in their respective product angular distribution, from which one may infer a crude estimate of the lifetime of the intermediate. Detailed studies on product alignment in photodissociation also yield estimates of these lifetimes.[2]

Such indirect methods yield, at best, order of magnitude estimates. We have recently used pump-probe methods to study unimolecular reactions in real time.[3] Accurate rate constants can be measured as a function of reagent internal energy as well as product internal energy states (electronic, vibrational and rotational). This method can determine the lifetime of intermediates on the sub-picosecond scale[4] and hence has the capability of measuring the rates of both direct and complex mode reations.

The photodissociation of alkyl halides by UV radiation in the 200-300 nm range has been studied extensively.[5] In the case of the iodide, the excitation involves the promotion of a non-bonding electron from the iodine $5p\pi$ atomic orbital to a σ^* molecular orbital. The absorption is broad and the upper state is believed to be repulsive. Photofragment angular distribution measurements suggest that the dissociation is one of the direct mode type. Many of the polyhalo-alkanes show absorption spectra that appear to be superpositions of the individual monohalo-alkanes, indicating that the different chromophores are only weakly coupled and that bond-selective dissociation may be possible. Such experiments have met with mixed success. Lee and coworkers have found that photodissociation of C_2F_4IBr at 248 nm[6] yields I atoms in the first step, even though the photo-excitation involves a Br electron. They also found that in the case of CH_2IBr[7] , one could get almost exclusively I or Br, depending on the excitation wavelength.

We have previously reported dissociation rates of $C_2F_4I_2$ into the two accessible electronic states of the I atom.[8] Signal from I* atoms showed a prompt rise, corresponding to prompt breakage of the first C–I bond, presumably the one selected by optical excitation. Population of ground state iodine atoms was observed to buildup with an apparent biexponential form. This paper represents a more complete study of the dissociation processes occurring in this molecule. The results are analyzed in terms of a two-step mechanism, involving a short-lived intermediate — the C_2F_4I radical. The first step is a direct dissociation, while the second one is the complex mode unimolecular dissociation of internally excited C_2F_4I. Possible explanations of the observed biexponential behavior are discussed, including sequential multiphoton absorption and ensemble effects arising from the distribution of internal energies from the initial dissociation. Our conclusions are in good agreement with recent measurements of velocity and angular distributions of the products of photodissociation.[9,10]

The dependence of the long component of the rise on the excitation energy follows our intuition — lower total energy leads to lower internal energy in the intermediate radical, which therefore decays more slowly. However, the relative fraction of the fast component is seen to increase at lower excitation energies. The commonly used impulsive models[11] for predicting energy disposal in a direct mode reaction are applied to estimate the average internal energy in the radical following the initial dissociation, which is then used to estimate rates. Simulations of the temporal behavior of I atoms using estimated energy distributions and rates indicate that the observed biexponential is consistent with a non-negligible quantum yield of ground state I atoms in the initial dissociation.

The rest of the paper is structured as follows. The next section describes the details of the experiment. The results are presented along with their interpretation in section 6.3. This section is divided into two main parts. The first one treats the primary dissociation step. The second section discusses the transient behavior of the ground-state I atoms as a function of the excitation energy. The pump and probe power dependence is used to rule out involvement of multiple photon

dissociation pathways. The impulsive models for energy disposal are reviewed briefly, in preparation for simulations of the transients using estimated rates and distributions.

6.2. Experimental

Details of the experimental apparatus have been presented elsewhere[3] and we provide only a brief description here. The output of a mode-locked YAG laser was frequency doubled and used as the source for two independently tunable, synchronously pumped dye lasers (R6G). The tuning element in each case was an intracavity quartz birefringent filter (2 or 3 plates). The output of each laser was amplified (3 stages) and doubled to obtain the desired pump and probe frequencies. Cross-correlations of the visible output were typically gaussian, with $\sim$ 10 ps full-width at e^{-1} of the maximum.

The two (amplified) beams were passed along separate arms of a Michelson interferometer, recombined on a dichroic mirror and propagated collinearly from there on. The beams were then focused in the ionization region of a TOFMS (mounted on a molecular beam apparatus) with a fused silica lens (focal length 25 cm). One of the arms of the interferometer also had a nominal $\times 1$ telescope that was adjusted to compensate for the slight difference in the focal length of the two colors, thereby improving the efficiency of probing the species created by the pump beam. Efficient recombination for the similar pump and probe wavelengths was achieved by using one doubling crystal in one arm of the interferometer and placing the other crystal beyond the recombiner. A polarization rotator and a polarizer were installed in each arm of the interferometer to enable fine control of the intensity in each beam.

1,2-diiodotetrafluoroethane ($C_2F_4I_2$) was obtained from Specialty Chemicals ($\geq$ 97%) and used without further purification for most of the experiments described below. The sample was kept in a stainless-steel bomb maintained at 0 °C . Helium gas (20 psig) was flowed over the sample and the mixture expanded through a pulsed nozzle (Kel-F) with a 500 μ aperture. The expansion was skimmed $\sim$ 1 cm from the valve and the total distance from the nozzle to the ionization region

was $\sim$ 10 cm. The transient signal from the ion-multiplier could be recorded every shot using a fast (100 MHz) transient digitizer and many shots averaged in a minicomputer to build up a mass-spectrum. Mass-spectra obtained using laser MPI showed no evidence of clusters. The signal was normally averaged in a boxcar with the gate set to sample only the m/e channels corresponding to the species of interest, in this case I^+.

The sample had a slight violet coloration due to the presence of molecular iodine which is obtained when $C_2F_4I_2$ decomposes. The following tests were performed to determine the contribution of iodine to the signal. First, it is known[5] that I_2 absorption at the pump wavelengths is weak. We performed the experiments with sample that had been treated with metallic copper (I_2 scavenger) and used a glass trap with teflon stopcocks and lines. The results were identical to those obtained with the sample in the steel bomb, implying that the observed signal had no significant contribution from I_2. ^{19}F NMR of the sample showed a single peak to greater than 99% abundance, in accordance with published NMR data[12] for $C_2F_4I_2$. The absence of other significant peaks in the spectrum show that no other fluorinated species were present in the sample. We therefore assumed that the signal measured was from $I - CF_2CF_2 - I$ alone.

The probe laser (DL1) was tuned to a two-photon neutral atomic iodine transition.[13] The transition could be chosen to originate from either the ground state ($^2P_{\frac{3}{2}}$, I) or the excited spin-orbit state ($^2P_{\frac{1}{2}}$, I^*) using light at 3047 or 3040 Å respectively, thus offering a means of distinguishing the two channels. The resonance enhancement with the probe alone was quite evident. The pump laser (DL2) was tuned to frequencies convenient for amplification. Transients were recorded over a range of pump wavelengths from 280 nm to 300 nm.

The rotator-polarizer combination was particularly useful in measuring the intensity dependence of each laser. The output of the boxcar averager was sampled at $\sim$ 300 Hz with a microprocessor controlled 12 bit analog-to-digital converter. This allowed for the determination of average values as well as standard deviations

(quoted errors) for a given level of pump and probe intensity. The background was carefully compensated by measurements of the signal with each laser alone.

The correct system response function is a difficult entity to measure experimentally. A truly instantaneous process which involves the same orders of nonlinearity for the pump and probe as in these experiments is required. A process which is known to occur in less than 100 fs may be used as an approximation. A likely candidate would be the dissociation of methyl-iodide (believed to be $\sim$ 70 fs). Another candidate is dissociation of $C_2F_4I_2$ into the I* channel. The first involves the risk of contamination of the beam, and the rate of the latter is an unknown quantity. It also involves tuning DL1, which introduces a possible source of error. For the majority of the fits reported here, we assumed that the system response function was gaussian and attempted to fit the initial rise by varying the width of the response. The typical width determined this way was $\sim$ 8 ps. This is shorter than the visible cross-correlations, most likely because the signal depends non-linearly on the intensities of both visible beams.

The raw data was fit to biexponential rises using the standard algorithm for non-linear least-squares, as elaborated in chapters 3 and 5A above. Each transient was fitted multiple times to avoid bias from the choice of initial parameters for the algorithm. Many transients recorded at the same pump and probe wavelengths were analyzed to determine the accuracy of the results reported here.

6.3. Results and Discussion

Figure 6.1 shows typical results for the buildup of population in the two lowest spin-orbit states of iodine. The characteristic risetime in the $^2P_{\frac{1}{2}}$ (I*) channel is instantaneous ($\leq$ 1 ps) on our timescale. The ground state (I, $^2P_{\frac{3}{2}}$) shows a rise which can be modelled as a two-component exponential buildup. The fast component is essentially instantaneous, while the slower component changes from $\sim$ 30 ps to $\sim$ 80 ps as the pump frequency is lowered.

The simplest scheme for photodissociation of 1,2-diiodotetrafluoroethane is a two-step, sequential bond-fission. The results reported here are discussed in terms of this scheme below.

$$C_2F_4I_2 \longrightarrow C_2F_4I^{\dagger} + I^{(1)} \quad (6.1)$$

$$C_2F_4I^{\dagger} \longrightarrow C_2F_4 + I^{(2)} \quad (6.2)$$

Superscripts on the I atom are to differentiate between the products of each step.

A. Primary dissociation

The *A* continuum in alkyl-monoiodides is a spin-forbidden $n\sigma^*$ transition. The analysis for methyl iodide reveals five underlying states, three of which are symmetry allowed. According to the analysis of Mulliken[5,14] , one of these states ($^3Q_0$, transition moment parallel to the C–I bond) correlates to I* products, while the other two (^1Q and $^3Q_1$, transition moments perpendicular to the C–I bond) correlate to ground state I. In most iodoalkanes, the state carrying the oscillator strength is believed to correlate to excited iodine atoms, ground state atoms being formed *via* a surface crossing. Fluorine substitution on these alkanes apparently reduces the strength of the coupling between the excited states and results in high quantum yields in the I* channel.[15] For instance, CF_3I, C_2F_4IBr have I* quantum yields of almost unity at 266 nm.

$C_2F_4I_2$ is a symmetric, bichromophoric molecule. The chromophores are quasi-degenerate, the splitting determined by the strength of the interaction between the two absorbers. From a spectroscopic point of view, the two chromophores must interact with each other, at least to the extent of removing the strict degeneracy, since the point group of $C_2F_4I_2(C_{2h})$ does not have degenerate representations. A simple dipole-dipole interaction between the two halves would give rise to exciton states, which are the molecular eigenstates of the system if the coupling with the dissociative continuum is ignored. The absorption spectrum of diiodomethane and iodoform has been described in terms of such a model.[16] If the equilibrium conformation of $C_2F_4I_2$ is *anti*, the two transition moments are parallel and one of

the exciton states will be optically allowed (parallel) while the other one will be dark. For the *gauche* molecule, both states are allowed and the direction of the transition moment is no longer along the direction of the C–I bond. This would lead to a value of β which is significantly less than the predicted 2.0 for a purely parallel transition. Since the measured β is 1.8[10] , we assume that the predominant conformer in the expansion is *anti*, which is the most stable form.

The absorption maximum for $C_2F_4I_2$ vapor is at 266 nm[17] , essentially the same as for CF_3I, suggesting that the interaction between the two chromophores is weak. The weak dipole interaction is unlikely to couple electronic states that are not closely degenerate and therefore the correlations will be unaffected by this coupling. Since they interact only weakly, one may expect that each of the two chromophores would behave as the corresponding mono-chromophoric molecule (in this case CF_3I). In particular, the quantum yield in the I* channel from the first step (equation 6.1) should then be unity; the measured quantum yields at 266 and 308 nm are ≥ 0.95.

Product translational energy distributions from the photodissociation of $C_2F_4I_2$ using 266 nm light measured by Reid *et al.*[9] show a sharp peak centered roughly at the same value of absolute translational velocity as observed in a similar study of C_2F_4IBr.[6] A second, broad peak was ascribed to I atoms from secondary dissociation. The important point is the lack of additional peaks at higher translational energies, as observed by Minton *et al.*[10] in the case of $C_2F_2H_2IBr$, where multiple pathways for primary dissociation are accessible. This is strong evidence that in dissociation with 266 nm light, the initial step leads primarily to I* atoms.

Extrapolation of these results to lower excitation energies is made complicated by the contradictory results on the quantum yield of I* from $C_2F_4I_2$. A study of the IR fluorescence[17] using $n - C_2F_7I$ as a standard concluded that the yield of I* was 0.9 at 308 nm. However, kinetic spectroscopy[10] of $C_2F_4I_2$ shows a much lower quantum yield for excited I atoms (0.6), which is outside the claimed range of experimental error. In our discussion below, we will consider both alternatives.

The direct dissociation step is expected to be fast, on the order of a vibrational period. Our observation of a prompt rise of population in both ground and spin orbit excited states corroborates this directly. These measurements alone cannot verify what fraction of the ground state I atoms is formed in the initial step for reasons discussed below. We may argue that no significant amount of I* is produced in the secondary reaction in the following manner. Suppose some I is formed in the first step, which is fast. This would result in an additional 22 kcal/mol that will have to be dispensed between translation and internal degrees of freedom. If most of this energy appeared as internal energy, I* atoms could be formed in the second step. The energy available for this mode of breakup would be close to threshold, and we would expect to observe a slow component in the rise of signal in the I* channel, similar to that seen in the buildup of the I atoms. This is contrary to our observations, within the limits of sensitivity of measurement, thus precluding it as a significant pathway in the mechanism for dissociation.

B. Secondary Fragmentation

The fate of the nascent radical C_2F_4I which is formed in the primary dissociation step is considered next. Thermodynamic estimates suggest that the radical is bound ($\sim$ 8 kcal/mol).[10] The average internal energy (vibrational and rotational) with 266 nm excitation is 11 kcal/mol. Assuming that this value does not change drastically on reducing the pump energy (see discussion below), the internal energy in the radical is sufficient for radical predissociation (equation 6.2). This process must lead to I ($^2P_{\frac{3}{2}}$) atoms exclusively if only I* atoms are formed in the first step, based simply on energy conservation. On monitoring I, we observe a temporal behavior that can be modelled as a two-component exponential rise (figure 6.1). The fast component appears to be on the time-scale of our pulse ($\leq$ 3 ps) while the slow component is many tens of picoseconds. The rate equations appropriate for the proposed mechanism (equations 6.1 and 6.2) are readily solved. Assuming that the system starts with population only in $C_2F_4I_2$, we obtain

$$[C_2F_4I_2](t) \quad = \quad Ne^{-k_1 t} \tag{6.3}$$

$$[C_2F_4I](t) = \frac{Nk_1}{k_1 - k_2}\left(e^{-k_2 t} - e^{-k_1 t}\right) \quad (6.4a)$$

$$[I^{(1)}](t) = \frac{N}{k_1}\left(1 - e^{-k_1 t}\right) \quad (6.4b)$$

$$[C_2F_4](t) = [I^{(2)}](t) = \frac{Nk_1}{k_1 - k_2}\left[\left(1 - e^{-k_2 t}\right) - \frac{k_2}{k_1}\left(1 - e^{-k_1 t}\right)\right] \quad (6.5)$$

where $N = [C_2F_4I_2](0)$. We associate $I^{(1)}$ with I* and $I^{(2)}$ with I atoms for convenience in the discussion below. Equation (6.5) shows that the expected behavior of the the products of the secondary fragmentation is a biexponential buildup, with relative amplitudes inversely proportional to their rates. In our results for I, $k_1 \geq 10^{12}$ s^{-1} and $k_2 \leq \frac{1}{30}k_1$, while their respective amplitudes are approximately equal. In the following sections, we consider possible schemes that appear consistent with the observation of a greater proportion of the fast component than is predicted by equation 6.5.

B.1. Sequential Multiphoton Absorption

Unstable radicals such as CH_2I[18] and $C_2F_2H_2Br$[10] have been shown to absorb 266 nm radiation.[18] The cross-section is generally comparable to that of the parent molecule. Radicals which absorb a second photon are highly internally excited and are liable to dissociate quite rapidly. The kinetic scheme shown in figure 6.2 shows all pathways that may lead to ground state I atoms. We neglect pathways that lead directly to I^+ since the detected signal is resonantly enhanced.

An approximate treatment of the effect of absorption of photons by any of the dissociating species on the subsequent evolution may be done in the following way. If either $C_2F_4I_2$ or C_2F_4I absorbs a pump photon, we may assume that the initial conditions for solving the kinetic scheme are different from those leading to equations 6.3 to 6.5. The correction involves adding a term

$$N'\alpha\left(1 - e^{-k_1' t}\right)$$

to equation (6.5). If the parent molecule absorbs the photon, $N' = N$, whereas if it is absorbed by the radical, $N' = N\frac{k_1\sigma}{k_1 - k_2}\alpha\left(1 - e^{-k_1' t}\right)$. Here, α is the product of the absorption cross-section and the average intensity, as in chapter 2, and k_1' is

the dissociation rate of the upper state, which is assumed to be fast (instantaneous). σ is a function of the two rate constants which is related to how many radicals are present during a pulse, and what fraction of them dissociate to form I atoms in that period. If k_1 is fast compared to the pulse duration and k_2 is slow, $\sigma \sim 1$.

Similarly, if either of these species absorbs a probe photon, the observed signal is the sum of equation (6.5) and a fraction, α of either equation (6.3) or (6.4a). In either case, we see that the relative fraction of fast to slow increases by $\sim \alpha$.

Transients obtained with pump pulses of different intensities are shown in figure 6.3. The fraction of the fast component is clearly higher when the intensity is high. This is in qualitative agreement with the discussion above. The amount of change (~20 % of the total signal) is quite high, suggesting that the absorption cross-section for the radical is large.

Figure 4a shows a log-log plot of signal *vs.* pump power while a similar plot of the probe power dependence is given in figure 4b. These measurements show linear dependence on the pump and a cubic dependence on the probe at low intensities. At higher pump intensities (not shown), one can see deviations from these simple power laws. This behavior suggests the involvement of other channels at these increased intensities. Transients measured with low pump and probe intensities clearly show the biexponential behavior. This establishes that although sequential multiphoton absorption is possible in this system, the biexponential character is not solely due to this process.

B.2. Radical internal energy distribution and excitation energy

A recent estimate of the stability of C_2F_4I claims that the radical is bound by $\sim$ 8 kcal/mol (2830 cm^{-1}).[10] Energy conservation dictates that radicals are formed with a distribution of internal energies, complementary to the spread in translational energy of the iodine atom. Since they are in a collisionless environment, they dissociate with individual rate constants, $k_2(E)$, which depend on the internal energy. The corresponding distribution of lifetimes often results in apparent biexponential behavior.[3,8] The signal may be represented as a sum of

exponential transients (equation 6.5) weighted by the probability density. In the limit of a continuous distribution of internal energies, the sum may be written as an integral

$$S(t) = \int_{E_0}^{\infty} \frac{P(E)}{1-\zeta(E)} \left[\left(1 - e^{-k_1 \zeta(E) t}\right) - \zeta(E) \left(1 - e^{-k_1 t}\right) \right] dE \qquad (6.6)$$

$$\approx \int_{E_0}^{\infty} \left[1 - e^{-k_1 \zeta(E) t}\right] P(E) dE \qquad \zeta(E) \leq\leq 1 \qquad (6.7)$$

where $\zeta(E) = k_2(E)/k_1$ and $P(E)dE$ is the probability that the radicals have energy in the range $(E,\ E+dE)$. E_0 is the threshold for radical dissociation. In our previous report[8] we have shown that $S(t)$, when convoluted with an instrument response function, could explain our observation of a biexponential rise.

In this series of studies, we have measured the buildup of I atoms for a number of pump wavelengths. The purpose behind this is to change the internal energy distribution in the intermediate radical, and thereby affect the rate of its decay. In figure 6.5, we show the results of experiments at three different excitation energies from 280 nm to 307 nm. The transients show a trend toward longer lifetimes with less available energy, with a concomitant increase of the fraction of the fast component. In view of the discussion of the previous section, we performed the experiments reported here under low power conditions, well into the region of the proper intensity dependence, i.e., linear for the pump and cubic for the probe.

In order to develop a self-consistent picture of the dissociation processes, we need to know the following:

(i) The distribution of internal energy in the radicals at each excitation energy and the relative amounts of vibrational *vs.* rotational excitation.

(ii) The unimolecular rates as a function of energy and angular momentum.

(iii) The rate of formation of C_2F_4I, k_1.

We discuss these points in the next few sections.

B.2.1. Impulsive models for energy distributions

A classical mechanical model for predicting the average kinetic energy released in a direct dissociation has been applied to the UV fragmentatiom of many alkyl

halides with a fair degree of success. The alkyl fragment is treated as being 'soft', i.e., the α C atom being weakly attached to the rest of the radical. The available energy is released into translational energy of the I and C atoms, energy and linear momentum conservation principles being applied to determine the relative speeds of their separation. The motion of the radical is determined by the α C atom 'crashing' into the rest of the radical, conserving linear momentum, the energy of the C atom being partitioned into translational and internal energy of the radical. It can be shown that

$$\frac{E_{vr}}{E_{av}} = 1 - \frac{\mu_a}{\mu_f} \tag{6.8}$$

where μ_a is the reduced mass of the partners in the initial recoil of the C and I atoms and μ_f is the reduced mass of the I atom and the radical. E_{av} is the total energy available for disposal and E_{vr} is the energy that eventually ends up as internal motions of the C_2F_4I. The division of the internal energy into rotations and vibrations is obtained from conservation of angular momentum — the torque applied to the radical is simply the initial linear momentum of the α C atom multiplied by the perpendicular distance of the radical center of mass from the line of centers of the dissociating atoms.

The *rigid radical* approximation is a variation on this theme. As in the other model, the impulse during bond scission involves only the C and I atoms which were previously bonded. The bonds in the radical are assumed to be infinitely stiff and the energy of the recoiling C atom is converted into rotational and translatonal energy of the fragment. The amount of rotational energy is given by

$$\frac{E_{vr}}{E_{av}} = \frac{E_{rot}}{E_{av}} = \left[1 + \frac{I_a}{\mu_f r_{cm}^2 \sin^2 \chi}\right]^{-1} \tag{6.9}$$

where E_{rot} is the average rotational energy, I_a is the moment of inertia of the fragment radical about an axis perpendicular to the plane containing the C and I atoms and the center of mass of the radical. r_{cm} is the distance of the α C atom from the axis of rotation and χ is the angle between the two lines defining the plane of rotational motion at the instant of scission.

The following comments about the application of these models to the dissociation of $C_2F_4I_2$ may be made. First, these models predict the average energy in vibrations and rotations, but do not provide a description of the distribution of internal energy, a knowledge of which is crucial to the analysis of our data. Second, some authors have used a 'united atom'[19] in place of the C atom as the initial recoil partner. For simple alkyl halides, this amounts to including the H atoms attached to the α carbon. Finally, it is useful to note that both models predict the average energy released as translational energy is a constant fraction of the available energy.

B.2.2. Estimation of $k_2(E)$

The unimolecular rates may be calculated as a function of the excess energy using statistical theories (e.g. RRKM)[20] , provided the frequencies and rotational constants of the radical and its 'transition state' are known. C_2F_4I is a very weakly bound molecule whose structure and vibrational frequencies are unknown. We avoid the pitfalls of estimating sixteen vibrational frequencies for the parent and fifteen for the transition state by choosing a different route for predicting $k_2(E)$. It has been empirically shown that rates of unimolecular reactions under isolated conditions may be represented by an Arrhenius-like formula[21]

$$k_2(E) = A \exp\left[-\frac{\alpha}{E - E_0}\right]. \tag{6.10}$$

The pre-exponential factor, A, is easily recognized. α is an adjustable parameter which may be interpreted as the product of the threshold energy, E_0, and the number of effective oscillators. This imposes as upper bound of $\sim$ 120 kcal/mol. for the value of α.

B.2.3. The magnitude of k_1

The kinetic scheme used in this analysis is adequate in describing the dynamics provided the fitted values of the fast component is not taken at face value. The intrinsic assumption in any kinetic model is that the individual steps occur with a random distribution of lifetimes. This may not be an accurate description of

direct mode reactions. In a recently described classical model[22] , one considers the rise time in terms of the relative velocity of separation and the distribution of rise times is related to the distribution of fragment translational energy. We found that equation 6.7 is a good approximation of equation 6.6 as long as $k_2 \leq 0.10k_1$. Since the initial dissociation is prompt, we have assumed that this condition holds for all rate constants considered.

B.2.4. Details of numerical simulations

As pointed out above, the impulsive models are good for estimating average energies only. Although statistical distributions may be calculated, they tend to overestimate the amount of internal excitation. The amount of internal excitation is best obtained from measured kinetic energy distributions by energy conservation.

$$E_{vr} = E_{h\upsilon} - D_0^0(C_2F_4I - I) - E_{so}(I^2P_{3/2}) - E_{trans} \qquad (6.11)$$

The photon energy is $E_{h\upsilon}$, the translational and internal energy are E_{trans} and E_{vr} respectively. E_{so} is the electronic energy of I^* and D_0^0 is the bond dissociation energy. Reid *et al.* have measured the distribution of kinetic energy in the initial step of dissociation at 266 nm.[9] They found that the peak of the kinetic energy distribution was at 14 kcal/mol, which is 42 % of the available energy at that wavelength. The distribution was fairly symmetric and broad, having a full-width at half maximum (FWHM) value of 11 kcal/mol.

The impulsive models predict 86% of the available energy appears as translation for the rigid radical and 14 % for the soft one, the experimental value lying between these limits, which cover almost the full range of possibilities. In passing, it may be noted that a 'united atom' model using the mass of $-CF_2-$ instead of the bare C atom predicts 44% of the available energy should appear as translation, a value which is much closer to the observed value. This approach corresponds to having the C–F bonds of the α carbon atom being rigid, while the rest of the radical is flexible.

In our attempt at simulating the experimental transients, we calculated radical energy distributions with the following assumptions.

(i) The average energy in relative motion, and therefore the average internal energy in C_2F_4I, is a wavelength independent fraction of the available energy, as predicted by the impulsive models. This implies that the rigidity of the radical does not change with excitation energy. We also used the measured fraction[9] of 42 % in estimating the average translational energy at each wavelength.

(ii) The internal energy distribution is gaussian, with width proportional to the average energy, i.e., the available energy.

(iii) The effects of angular momentum on the rates are not significant.

The rates of dissociation as a function of energy were estimated using equation 6.10. These rates were then used with appropriate weights to simulate the transient behavior of the ensemble of C_2F_4I using equation 6.7. These simulated buildups were convoluted with the typical system response and the results analyzed by the method used for the experimental transients. The values of A and α were adjusted to match the two exponential components and their relative amplitudes that were measured for dissociation at 279 nm (Table 6.1). As can be seen from the simulated transient shown in figure 6.6, the agreement was fair.

The A and α values obtained above were used to simulate the expected behavior at lower energies using calculated distributions. As seen from Table 6.1, the fast component obtained in fits of these simulations is much longer than is obtained for the experimental data. The lower panel of figure 6.6 should be compared with the measured transient at 307 nm (figure 6.5). Changing α to larger values effectively increases the difference in the long components at the limiting energies studied. Decreasing α makes the lifetimes more similar, but the relative amount of the fast component becomes much greater than is observed. The disagreement between the simulations and the measured transients indicates that at least one of our assumptions is not justified.

One may argue that the assumed functional form of the energy dependence is responsible for this discrepancy. Any statistical prediction of the energy dependence of k_2 would claim that the rates increase with energy. The fact that the fraction of fast component increases with less available energy suggests that the

energy dependence of the rates is not the sole factor that is of significance in determining the shape of the measured transients. One is therefore forced to conclude that the assumed distributions of internal energies in the radical do not reflect the true distributions present during reaction.

B.2.5. Initial dissociation into the I channel

In the last section, we implicitly assumed that initial dissociation into the I channel occurred with too low a probability for it to affect our results, in accord with the measurements of Gerck.[17] Kinetic energy analysis of I atoms from the dissociation of $C_2F_4I_2$ at 308 nm[10] indicates that $\sim$ 40 % of the initial dissociation leads to ground state I atoms, contradicting the high (0.9) quantum yield of I* measured by IR fluorescence. The magnitude of this discrepancy is difficult to reconcile. However, if the energy analysis study of Minton *et al.*[10] is correct, then the assumptions used in our simulations of the previous section are clearly not justified. In this section we consider the effects of this channel being open on our measurements.

The basic results from the study of Minton *et al.*[10] are that the distribution of kinetic energies is bimodal. One of the peaks (attributed to I* formation) appears at 13.1 kcal/mol and has a FWHM of $\sim$ 5 kcal/mol, while the second one (due to I atoms) appears at 21.6 kcal/mol and has a FWHM $\sim$12.5 kcal/mol. A number of conclusions may be drawn from a comparison of these results and those of Reid *et al.*[9] First, since dissociation at 266 nm leads to no significant amount of I atoms, their production must be wavelength dependent. Similar behavior has been observed in other alkyl halides and is surprising only to the extent that it also occurs in perfluorinated compounds, which generally tend to have high quantum yields of I* . Second, the average kinetic energy released into the I* channel is 69 %, significantly higher than the observed 42 % at 266 nm. Thus our assumption that the rigidity of the radical is independent of excitation energy is erroneous. Finally, the width of the peak is narrower for dissociation at lower energies, proportional to the available energy, in concurrence with the *ad hoc* assumption made in the last section.

The data shown here is qualitatively consistent with an increasing quantum yield of I atoms at longer excitation wavelengths. Since the electronic energy (21.7 kcal/mol) is now available for internal motion, the radicals from this channel are formed with significantly higher internal energy and dissociate rapidly. In addition, the I atoms from the initial step will also be detected, leading to an expected transient shape given by the sum of equations 6.4b and 6.5, weighted by the relative quantum yields. A greater yield of I atoms at lower excitation energies would lead to a larger contribution to the signal from equation 6.4b and, conceivably, a larger relative fraction of the fast component.

A more quantitative comparison requires an interpolation scheme for estimating the quantum yield of I atoms as a function of wavelength, as well as a second one for the peak positions and shapes of the energy distributions as a function of wavelength. The simplest scheme would be to assume zero yield of I for dissociation at 280 nm and a distribution similar to the one observed at 266 nmm scaled by the available energy. The parameters of the measured distribution at 308 nm may be used to simulate the expected transient at 307 nm. Results, shown in figure 6.7, are in much better agreement with the observed transient behavior. The simulation reproduces the initial fast rise and relative amplitude quite well, but fails to predict the long component correctly. Given the simplicitly of our model, the agreement appears remarkable.

Finally, a few relevant points may be mentioned. Our results show that production of I atoms affects the internal energy distribution of C_2F_4I. This suggests that the surface crossing responsible for the production of the ground state radical occurs while the two fragments are still interacting strongly, since almost 50 % of the additional available energy appears as internal energy in C_2F_4I.

The product angular distribution (PAD) measured by Reid *et al.* for C_2F_4 is strongly forward-backward peaked, with pronounced asymmetry favoring backward scattering of the ethylene fragment with respect to the velocity vector of C_2F_4I. This is characteristic of an *osculating* complex[23] , one that lives for a period

comparable to the rotational period of the complex. This is consistent with our observation of a fraction of complexes dissociating rapidly.

6.4. Conclusions

In this chapter, we have presented product electronic state dependent rates of the dissociation of $C_2F_4I_2$ as a function of excitation energy. The dynamics of this reaction can be described in terms of a two step mechanism, the first one leading to an internally excited radical, C_2F_4I, the second step being the dissociation of these energized radicals. The electronically excited I atom showed a pulse-limited rise independent of wavelength, which we interpret as indicating that I^* is formed only in the initial step step. The buildup of ground state I atoms appears biexponential, partly because radicals formed with different amounts of internal energy dissociate with different rate constants. Our results support the hypothesis that both I and I^* atoms can be produced in the initial dissociation, their relative quantum yields being a function of the excitation energy.

6.5. References

1. R. D. Levine and R. B. Berstein, in *Molecular Reaction Dynamics and Chemical Reactivity*, Oxford Univ. Press, NY, (1987).

2. M. Dzvonik, S. Yang and R. Bersohn, *J. Chem. Phys.*, **61**, 4408, (1974).
   J. H. Ling and K. R. Wilson, *J. Chem. Phys.*, **65**, 881, (1976).
   R. N. Zare, *Molec. Photoshem.*, **4**, 1, (1972).

3. L. R. Khundkar , J. L. Knee and A. H. Zewail, *J. Chem. Phys.*, **87**, 77, (1987).
   N. F. Scherer and A. H. Zewail, *J. Chem. Phys.*, **87**, 97, (1987).
   J. L. Knee, L. R. Khundkar and A. H. Zewail, *J. Chem. Phys.*, **87**, 115, (1987).

4. M. Dantus, M. J. Rosker and A. H. Zewail, *J. Chem. Phys.*, **87**, 2395, (1987).

5 S. R. Leone, *Adv. Chem. Phys.*, **44**, 255, (1982).
   S. J. Riley and K.R. Wilson, *Farad. Disc. Chem. Soc.*, **53**, 132, (1972).

6. D. Krajnovich, L. J. Butler and Y. T. Lee, *J. Chem. Phys.*, **81**, 3031, (1984).
   T. K. Minton, G. N. Nathanson and Y. T. Lee, *J. Chem. Phys.*, **86**, 1991, (1987).

7. L. J Butler, E. J. Hintsa, S. F. Shane and Y. T. Lee, *J. Chem. Phys.*, **86**, 2051, (1987).

8. J. L. Knee, L. R. Khundkar and A. H. Zewail, *J. Chem. Phys.*, **83**, 1996, (1985).

9. Brian Reid, Ph. D. Thesis, C.I.T., (1986).

10. Timothy K. Minton, Ph. D. Thesis, Univ. of Cal., Berk., (1986).

11. G. E. Busch and K. R. Wilson, *J. Chem. Phys.*, **56**, 3626, 3638, (1972).

12. V. Wray, *Ann. Rep. NMR Spec.*, **14**, 1, (1983).

13. J. J. Tiee, M. J. Ferris, G. W. Loge amd F. B. Wampler, *Chem. Phys. Lett.*, **96**, 422, (1983).

14. R. S. Mulliken, *Phys. Rev.* , **51**, 310, (1937).
   R. S. Mulliken, *J. Chem. Phys.*, **8**, 382, (1940).

15. C. A. Wright and S. R. Leone, *J. Phys. Chem.*, **87**, 5299, (1983).
   H. B. Schlegel and C. Sosa, *J. Phys. Chem.*, **88**, 1141, (1984).
   T. Donahue and J. R. Wiesenfeld, *J. Chem. Phys.*, **63**, 3130, (1975).

16. M. Kawasaki, S. J. Lee and R. Bersohn, *J. Chem. Phys.*, **63**, 809, (1975).

17. E. Gerck, *J. Chem. Phys.*, **79**, 311, (1983).

18. P. M. Kroger, P. C. Demou and S. J. Riley, *J. Chem. Phys.*, **65**, 1823, (1976).

19. A. J. Tuck, *Farad. Diss. Chem. Soc.*, **62**, 689, (1976).

20. See chapter 4 for a review and references, .

21. A. H. Zewail, *Farad. Diss. Chem. Soc.*, **75**, 315, (1983).

22. R. Bersohn and A. H. Zewail, *Ber. Bun. Phys. Chem.*, in press.

23. W. B. Miller, S. A. Safron and D. R. Herschbach, *Farad. Diss. Chem. Soc.*, **44**, 108, (1967).

Table 6.1 : Fitted parameters for transients and simulations

Wavelength (nm)	τ_1 (ps)	τ_2 (ps)	Fraction[a]	Remarks
279	0.5± 2.	36. ± 5.	0.35 ± .05	Experimental
	1.6± 0.8	35. ± 4.	0.40 ± .02	Simulation[b]
290	1.0± 2.5	45. ± 8.	0.65± .1	Experimental
307	0.5± 2.	69. ± 10.	0.56 ± .08	Experimental
	15.0± 3.	130. ± 12.	0.06 ± .05	Simulation[b]
	0.8± 1.	35. ± 4.	0.74 ± .05	Simulation[c]

[a] Ratio of amplitude of fast component to total amplitude

[b] Simulation as in 6.B.2.4. The rate parameters for the simulations are $\alpha = 50$ kcal/mol, and $A = 5.0 \times 10^{12}$ s^{-1}.

[c] Simulation as in 6.B.2.5. Parameters were the same as in the other model.

Table 6.2 : Parameters for the distributions used in simulations

Model	Wavelength (nm)	Average E (kcal/mol)	Width (kcal/mol)
(a)	279	17.3	12.5
	307	11.2	6.6
(b)	279	17.3	12.5
	307	19.2; 6.0	15.; 5.0

Model(a) refers to the calculations of 6.B.2.4 while model (b) refers to those of 6.B.2.5. For the latter, a bimodal distribution was used. Hence the two numbers in each column.

Figure 6.1. Transient behavior of I and I* channels

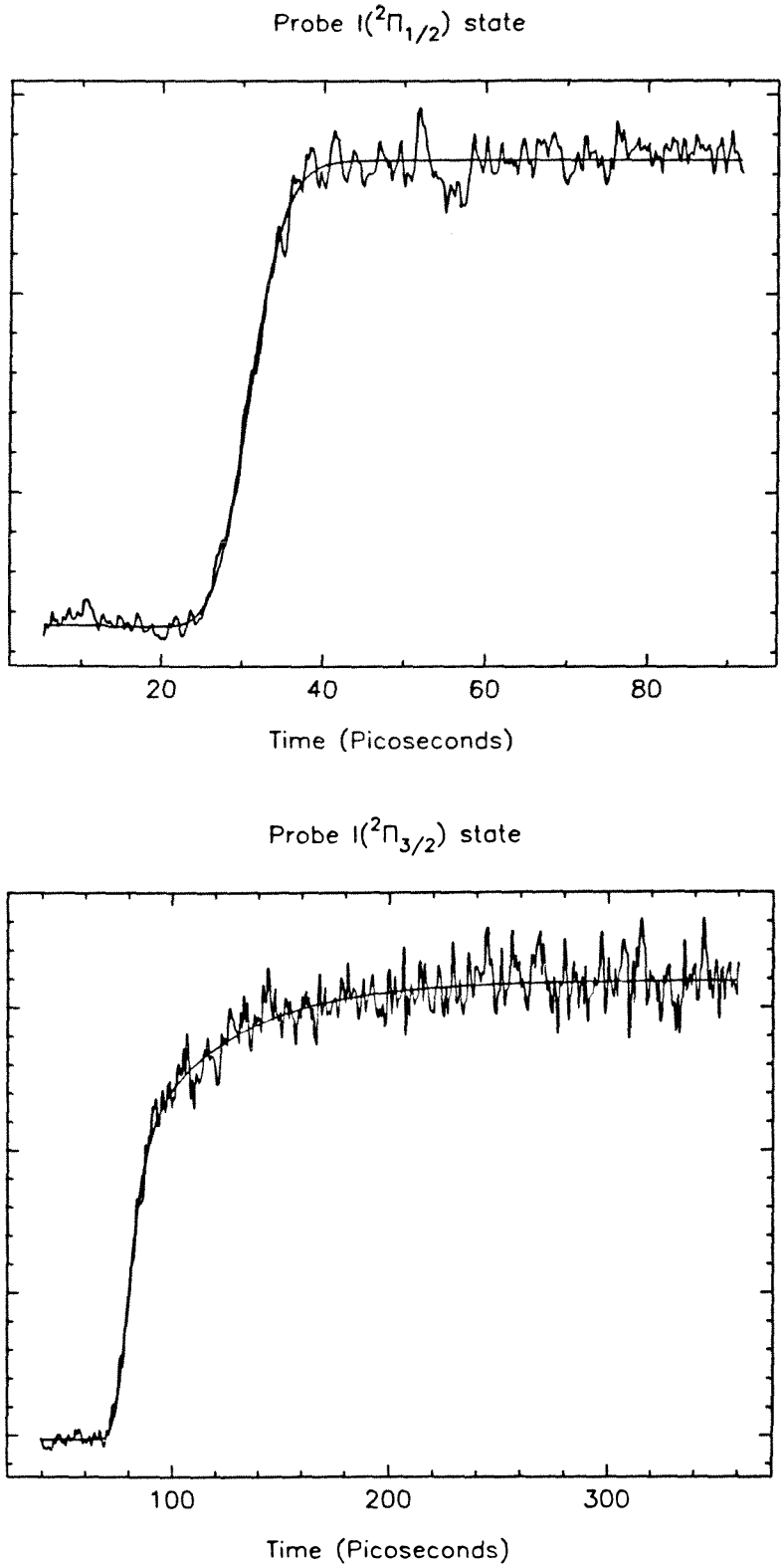

Figure 6.2. Kinetic scheme for dissociation of neutral $C_2F_4I_2$ including pathways for multiphoton dissociation. The shaded arrows indicate optical transitions.

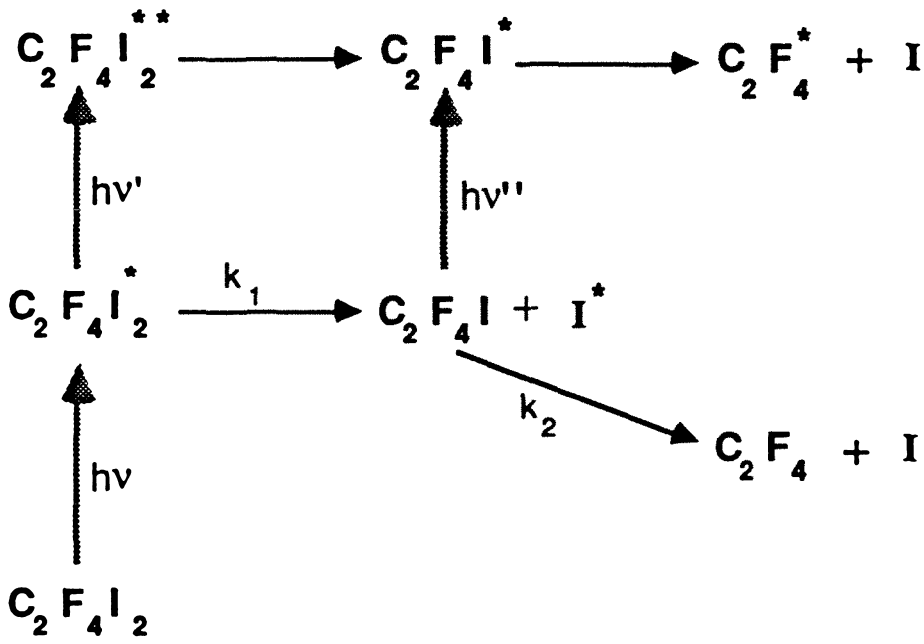

Figure 6.3. Transients obtained with (a) weak and (b) intense pump pulses. The relative amplitude of the fast component is significantly higher in (b) than in (a).

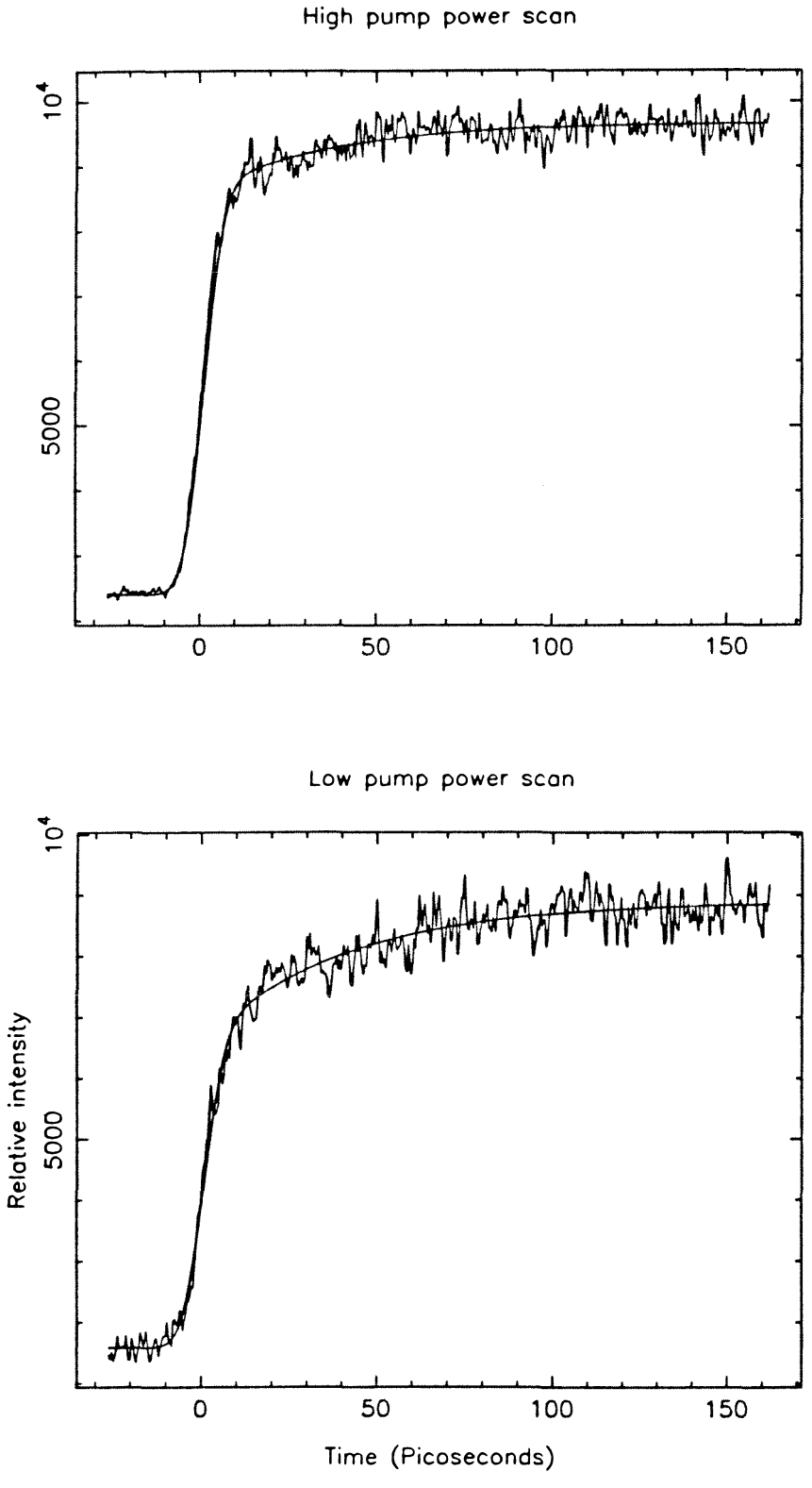

Figure 6.4. (a) Dependence of the signal on the pump intensity. The slope of the best fit line shown is 1.1. (b) Probe-power dependence. The slope of the best fit line shown is 3.1.

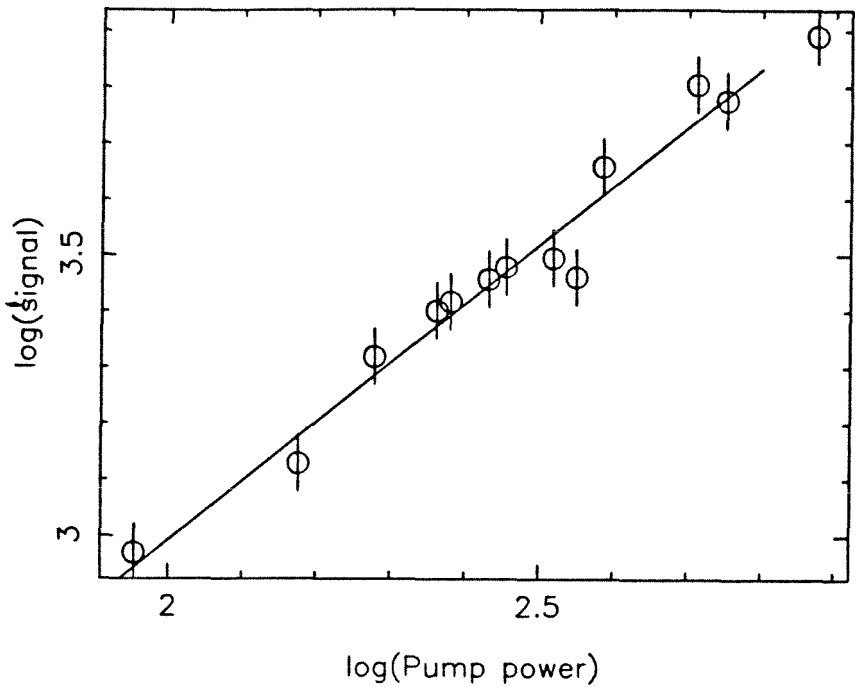

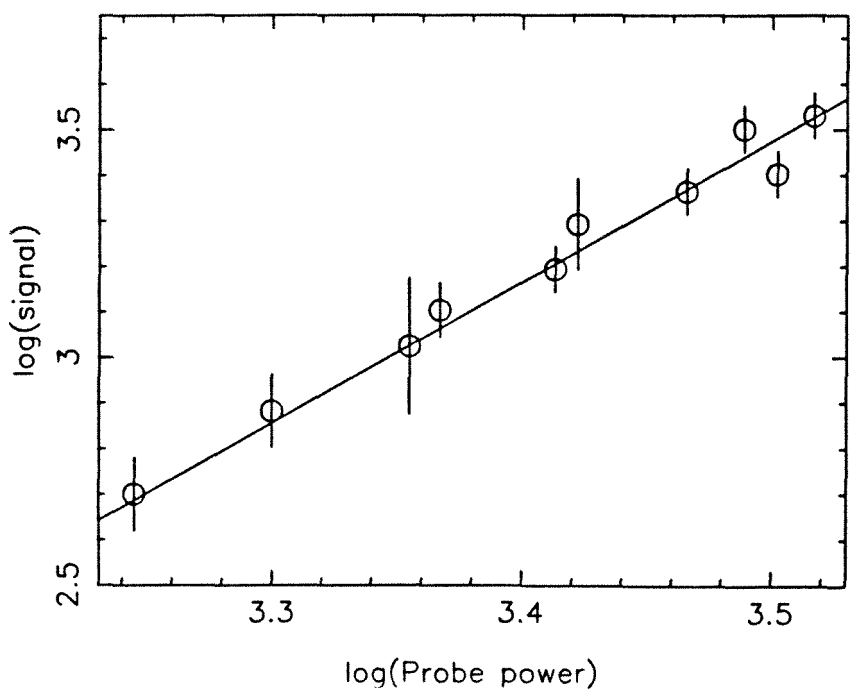

Figure 6.5. Transient buildup of I atoms as a function of the pump wavelength. (a) 279 nm; (b) 290 nm and (c) 307 nm. The solid line in each plot represents the fitted biexponential rise convoluted with an assumed gaussian instrument response. Results of the fits are given in Table 6.1.

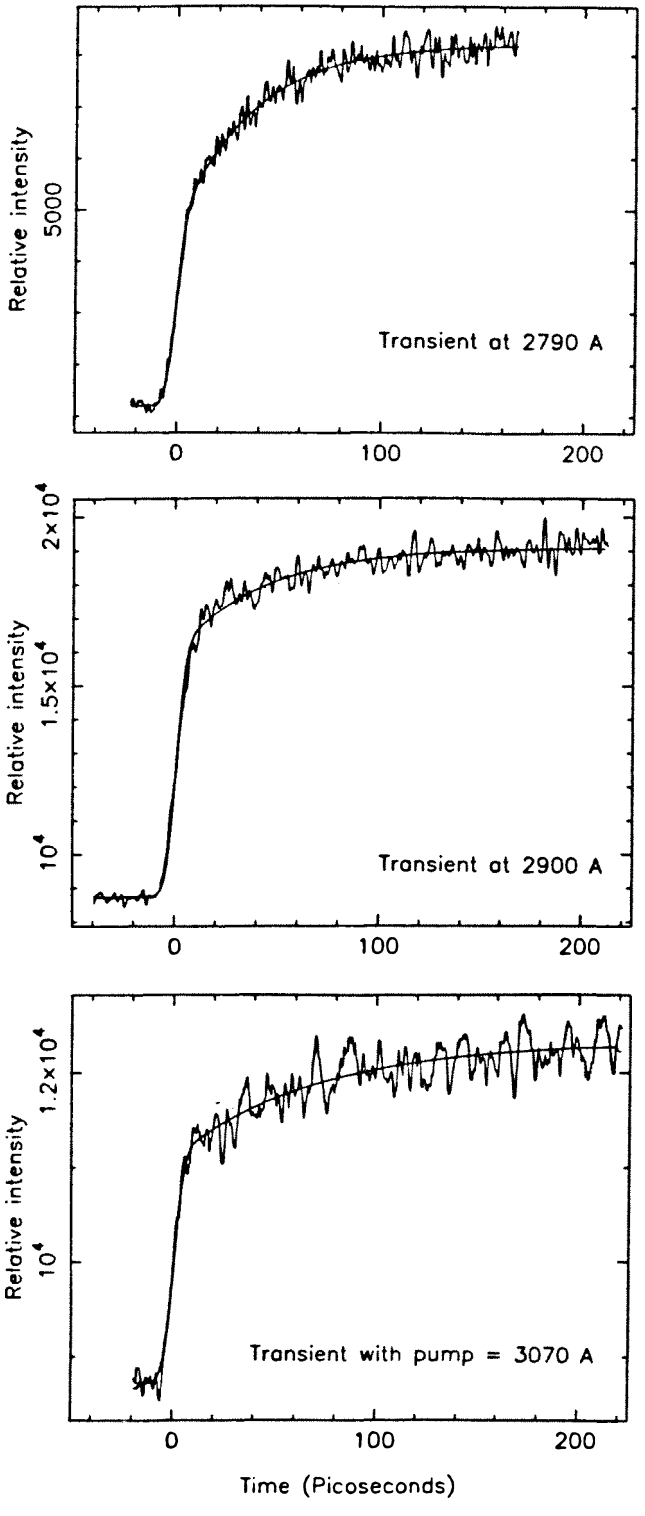

Figure 6.6. Simulated transient buildup of I atoms for excitation energies of (a) 279 nm and (b) 307 nm. 2% white noise is added to the simulations to mimic the random error in the experimental transients and its effect on the fitting procedure. The solid lines represent best fits, results of which are in Table 6.1.

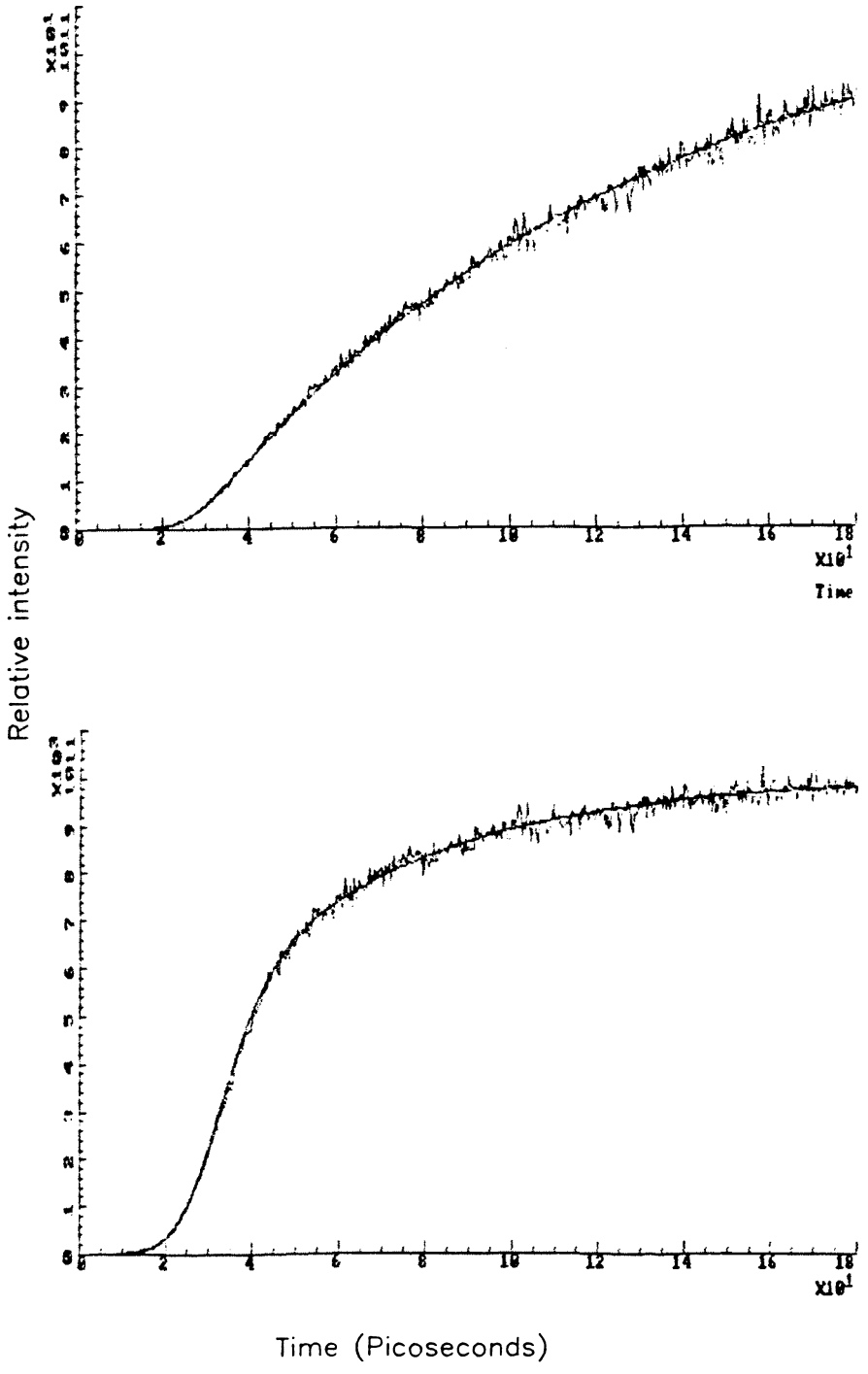

Figure 6.7. Simulated transient behavior of I on excitation at 307 nm, assuming the quantum yield of I in the initial dissociation is 0.4.

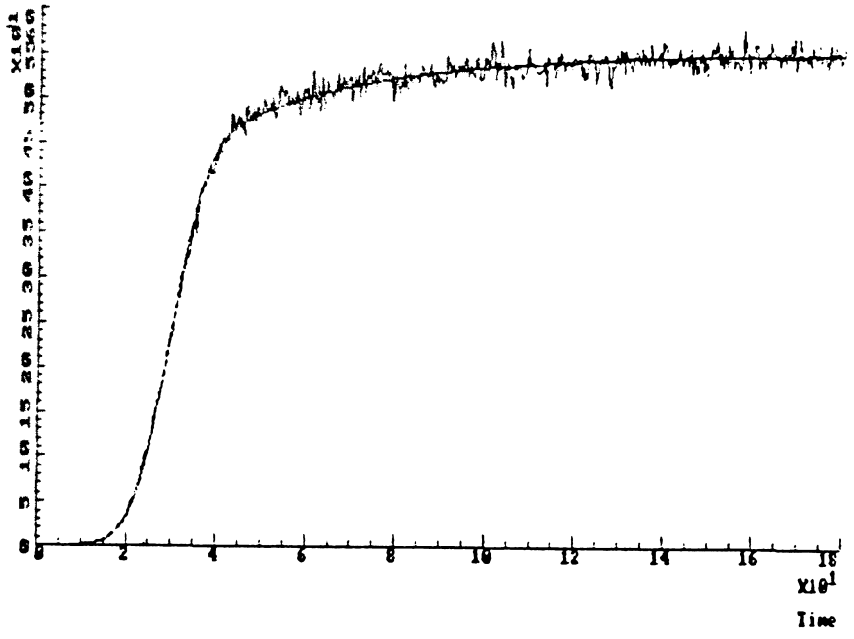

CHAPTER 7

OBSERVATION OF INTRA-COLLISION PROCESSES BY TIME AND FREQUENCY DOMAIN MEASUREMENTS

CHAPTER 7A

PICOSECOND MPI MASS SPECTROMETRY OF CH_3I IN THE PROCESS OF DISSOCIATION

Luftur R. KHUNDKAR and Ahmed H. ZEWAIL [1]

Arthur Amos Noyes Laboratory of Chemical Physics [2], California Institute of Technology, Pasadena, CA 91125, U.S.A.

Received 5 November 1987

Picosecond multiphoton ionization and time-of-flight mass spectrometry has been used to monitor the dissociation of methyl iodide excited to its A continuum. The measured signals show a rapid buildup when the probe laser is tuned to a resonance of free atomic iodine and a sharp feature at zero time delay when it is tuned off-resonance. Enhanced signal is also observed in the parent ion channel. These results illustrate the possible use of this technique for the probing of fragment species before they are completely separated from their partners in a half-collision process.

1. Introduction

The technique of femtosecond "transition state" spectroscopy (FTS) has been recently applied to the bond-breaking process in ICN [1,2]. Two ultrashort pulses ($\leqslant 100$ fs) are employed in the standard pump–probe scheme. The difference is that in FTS, the probe is tuned to either side of the transition in the free product, thereby accentuating the contribution of perturbed states of fragments in the process of falling apart. We have extended this concept experimentally to the picosecond domain [3]. In both the earlier femtosecond [1] and the picosecond [3] experiments, we employed LIF to probe the separating species. Here, we report on the use of multiphoton ionization (MPI) followed by mass-selective detection of fragment ions as a complementary detection method. MPI mass spectrometry allows us to probe non-fluorescing systems, and therefore makes the technique applicable to a larger set of molecular systems. Experimental results on methyl iodide are presented and interpreted in terms of probing the system during the half-collision, i.e. while the dissociating fragments exert forces on each other.

Methyl iodide has been the subject of extensive spectroscopic [4–8] and theoretical [9] investigations over the past two decades. Excitation to the low-lying singlet state (A_1) has often been considered the prototype of direct photodissociation reactions. This state is repulsive and the rate of formation of products (<0.5 ps) [8] is consistent with a rapid release of kinetic energy [5,7]. Some higher lying states of the neutral molecule have been characterized, and the energetics [10] and MPI fragmentation patterns [11] of the corresponding positive ion determined.

2. Experimental

The experimental apparatus has been described in detail elsewhere [12]. Briefly, the 1064 nm output of an actively mode-locked Nd–YAG laser was frequency doubled and used to pump two independent dye lasers synchronously. The output wavelength of each dye laser was selected by an intracavity three-plate quartz birefringent filter. One of these (DL1) was used to generate the pump while the other (DL2) was used for the probe. Each picosecond pulse was amplified in multi-stage dye amplifiers pumped by a *Q*-switched amplified Nd–YAG laser operating at 20 Hz. The final pulse energies were typically 0.5 mJ/pulse and were attenuated for the experiments. The temporal shape of the amplified pulses is very similar to that of the input pulses. The visible pulse cross-correlations are typically Gaussian, with pulsewidths ≈ 7 ps.

The amplified pulses were directed through the two

[1] John Simon Guggenheim Foundation Fellow.

[2] Contribution No. 7695.

0 009-2614/87/$ 03.50

arms of a Michelson interferometer, one fixed (pump), the other variable (probe). The beams were frequency-doubled in KD*P crystals and focused with a 50 cm fused silica lens in a singly skimmed molecular beam. The photoions were deflected into a time-of-flight mass spectrometer. The gate of a boxcar averager was set for selected mass peaks (I^+ or CH_3I^+) and the time delay scanned to measure the temporal behavior of the mass species of interest. Mass spectra can be obtained at fixed time delays using a 100 MHz digitizer to sample the transient ion signal for each laser shot and averaging many such spectra.

Iodomethane (99%, Aldrich) was cooled to 0°C. Helium gas was flowed over the cooled sample and expanded through a pulsed valve (nominal aperture 500 μm) made of Kel-F. Typical expansion conditions were 25 psig stagnation pressure and 2×10^{-4} Torr ambient pressure in the first chamber. The pressure in the ionization chamber was 5×10^{-6} Torr. The expansion was skimmed ≈ 2 cm from the nozzle and ions formed another 9 cm downstream. The trigger to the pulsed valve was adjusted to minimize signal from dimers and larger clusters. Checks were made for dimer contributions [13] to the reported results in the following way. Transients were measured with the lasers sampling different parts of the expansion, i.e. for higher concentrations of dimers (as evidenced by mass spectra). The results showed no qualitative difference between transients obtained when the expansion contained dimers and when it contained no discernible amounts of dimers. Our expansion conditions (≈ 120 Torr CH_3I in 1800 Torr He) are not as favorable for forming dimers as those of ref. [13] (100 Torr neat CH_3I).

3. Results

Transients were obtained by monitoring I^+ as a function of the delay time for different probe wavelengths near known free atomic I two-photon transitions [6,14]. The pump wavelength was held fixed at 292 nm for all scans. The transients (fig. 1) show a fast rise and decay when the probe laser is tuned away from the resonance in either direction. On resonance, the transient shows no evidence of such a feature near zero delay (t_0). For small changes in wavelength, the profile appears to be a combination of both a t_0 feature and residual signal at long (~ ns) delay. The resonance has been assigned [14] to a two-photon transition ($5p^2\ P^\circ_{1/2} \rightarrow 6p^4\ D^\circ_{1/2}$, 304 nm) originating from the excited spin–orbit state ($^2P_{1/2}$) of atomic iodine (I*). Similar behavior has been observed for wavelengths near resonances of ground-state ($^2P_{3/2}$) atomic iodine (I).

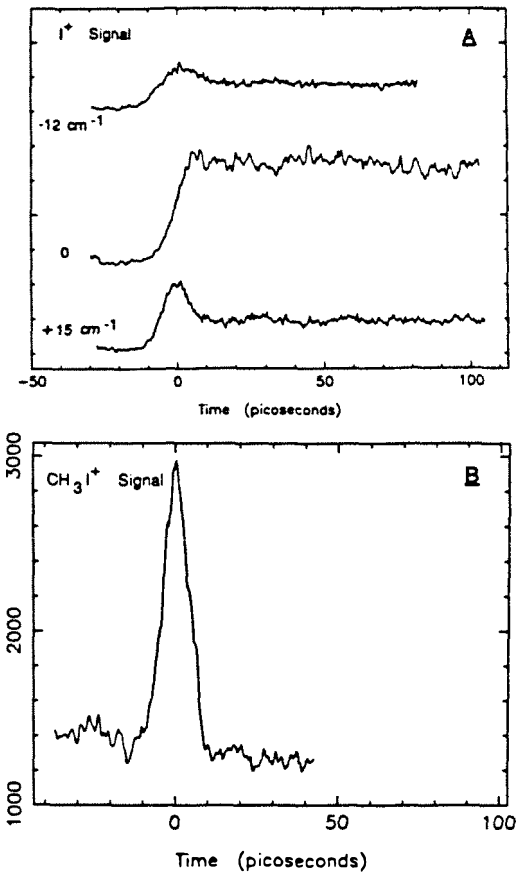

Fig. 1. Time-resolved transients detected by mass selection of (A) I and (B) CH_3I. The three transients in (A) were taken using different probe wavelengths: 0 indicates on-resonance (304 nm), ± indicates relative shifts in cm^{-1} from resonance.

The transient behavior of the parent molecule was measured by monitoring CH_3I^+. A sample transient is shown in fig. 1B. The temporal behavior is characteristic of a fast decay process. These transients do not show as marked a wavelength dependence over the range studied.

Mass spectra obtained at negative, zero and positive time delays clearly reflect the buildup of I (I^*) atoms and the fast decay of CH_3I occurring simultaneously.

The temporal behavior reported here is very similar to that observed in the femtosecond experiment [1]. However, the buildup and decay observed in the picosecond experiments is limited by our time resolution.

4. Discussion

The A continuum of methyl iodide is the band arising from the promotion of a non-bonding electron from the valence shell of the bound I atom into a molecular orbital of antibonding character. The band consists of a number of overlapping states of different symmetries (E, A_1, A_2 in C_{3v}). The transition moment is predominantly parallel to the C–I bond, the axis of symmetry of the molecule. The angular distribution of products [5] and the rate of product formation [8] show that the dissociation is direct. Both ground state atomic iodine and the spin–orbit excited species are formed,

$$CH_3I \rightarrow CH_3 + I,$$

$$CH_3I \rightarrow CH_3 + I^*.$$

The branching ratio varies slightly with energy, and at the energies of interest, it is approximately 2 : 1 (I^*/I) [4,5]. In strict C_{3v} symmetry, the I channel correlates with A_2 and E states (perpendicular transition) while the I^* channel correlates with an A_1 state. The fact that experimentally both I and I^* products appear to be derived from parallel transitions implies that the initial absorption is dominated by the A_1 state and the I atom is produced as a result of the intersection of the A_1 and E or A_2 surfaces. Recent studies on aligned CH_3I molecules [15] corroborate this and suggest that the intersection occurs at a C–I distance larger than the equilibrium bond length in the ground state.

4.1. Probing the fragment species

The competition between photodissociation and photoionization followed by dissociation in the ion has been well documented [11,16]. We observe distinct resonances corresponding to well-known two-photon transitions in free atomic iodine. The major contribution to the ion signal ($m/e = 127$) is derived from two-photon resonant, one-photon ionization of I atoms resulting from the dissociation of CH_3I in the A band. The transient obtained with the probe laser tuned to the peak of an I^* resonance shows a prompt rise in signal ($\tau \leqslant 0.5$ ps) and no subsequent decay. This has been observed and reported previously [8]. As the probe laser is tuned away from the resonance in either direction (red or blue), the transients start to show a distinct peak at t_0 (within our cross-correlation), superimposed on the constant signal at long times. The amplitude of the long time signal decreases as the laser is tuned further off-resonance and eventually reaches background levels. Such behavior has been observed in recent femtosecond experiments [1] and shown to be due to absorption by dissociating species that are still in close proximity [2].

The average kinetic energy release in the I^* channel was measured to be 28 kcal/mol for excitation at 266 nm [5]. Assuming the same fraction of the available energy appears as translational energy at the excitation wavelength of interest, we estimate ≈ 20 kcal/mol released as kinetic energy of both fragments at 292 nm. In the center-of-mass frame, the relative speed (terminal) of separation of the fragments is ≈ 35 Å/ps. The speed of recoil at close distances is smaller than the terminal one. Van der Waals minima at large internuclear separations would also tend to slow down the separation process. Thus for a small fraction (≈ 1–10%) of our pulse duration the dissociating species I...CH_3 are perturbing each other.

A schematic is shown in fig. 2A solely for illustrative purposes. At point A, the fragments are essentially non-interacting and the spectroscopy of the species is that of free fragments. At point B, the van der Waals attraction results in lower energy for the lower surface and the resonance energy is slightly blue-shifted. At point C, the repulsive part of the dissociation potential dominates while the upper surface is not as strongly affected. The resonance is then slightly redder than at point A. Clearly, this is only one of many possible combinations. The salient point is that the perturbations must be different for the two surfaces involved; the experiment is sensitive to the

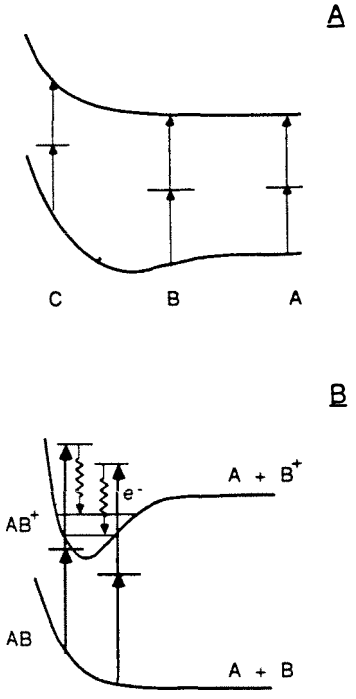

Fig. 2. (A) Schematic of two PES describing blue- and red-shifts in the probing process (see text). (B) Schematic for "trapping" dissociating AB (CH_3–I) by excitation to the ion.

energy difference between them. Such a description has been invoked previously to account for "wing emission" in dissociation reactions [17].

4.2. Probing the parent species

MPI using nanosecond lasers requires significant pulse energies to compete with the rapid dissociation in the A continuum when this is used as an intermediate resonance. Consequently the balance between ionization and subsequent absorption by the ion leads to significant fragmentation to smaller ionic species. As discussed later, we observe primarily the parent ion, CH_3I^+, in our studies and ascribe this to the high peak power at a given average pulse energy for our picosecond pulses.

It is interesting to note that allowing for only vertical excitations, the ionization process should be able to sample a finite part of the repulsive surface (fig. 2B). Vertical transitions from different regions of the repulsive surface will leave the ion with enough energy to fragment. A certain fraction of the excited species will eject photoelectrons with sufficient kinetic energy so as to stabilize the resulting positive ion. The process is similar to radiative-trapping or recombination [18] in that the fragments are trapped (in the ion) before they are able to separate.

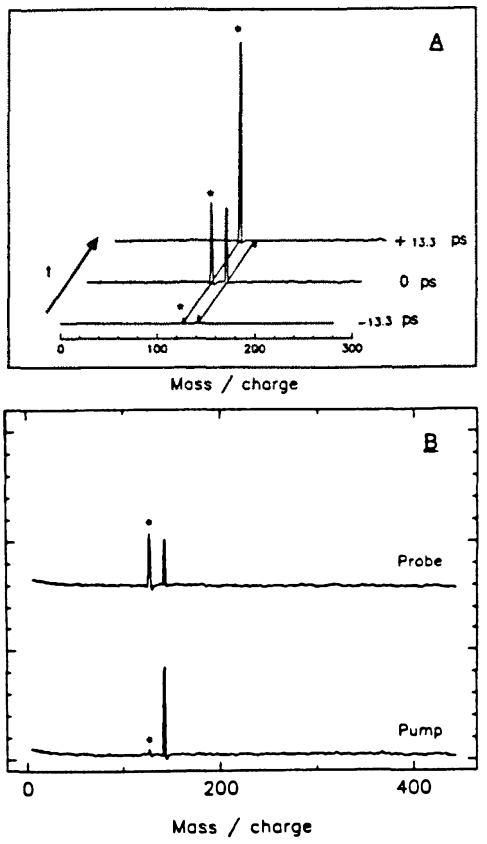

Fig. 3. (A) Picosecond time-gated mass spectra. The • indicates I^+ (m/e=127). The other peak is CH_3I^+ (m/e=142). The background has been subtracted for each spectrum (see text for details). (B) Mass spectrum obtained from each laser individually.

4.3. Mass spectra and fragmentation schemes

In fig. 3A we show mass spectra obtained at time delays of −13.3, 0 and +13.3 ps. The probe laser was tuned to a resonance of I^*, where the temporal behavior is simply a buildup.

The spectrum at long negative times has been subtracted from each in an effort to remove background

signal (the raw data show the same trend). The change in the spectrum as a function of time is dramatic – large signal in the CH_3I^+ channel at t_0 and almost negligible signal at positive delays [#1]. The signal in the I^+ channel is largest at long positive delay, consistent with a buildup of I^* as discussed above. The relative magnitudes of the ion signal in different channels are worthy of note. At t_0, the two channels have comparable intensity implying that a significant fraction of the molecules excited by the pump remain bound long enough to be probed. At positive time, only neutral I (I^*) atoms are left to be probed.

A few alternative schemes have also been considered to verify the uniqueness of the explanation proposed above. First, the pump may leave significant population in some high-lying neutral (Rydberg) state of CH_3I. The probe could ionize these highly excited molecules. Recent multiphoton studies on CH_3I show no significant absorption in the 290 nm region although molecular states abound at higher and lower energies [6]. Thus the probability of forming highly excited neutral CH_3I is small. If such a state were to exist, our results imply that the state is very short-lived (fig. 1B). The dynamics is probably qualitatively similar to that occurring in the A continuum, and the arguments of the previous sections hold equally well. However, the low probability of populating high-lying states implies that this channel cannot be the major contributor to the observed signals.

Second, our experiments may be probing the dynamics of the ions. Clearly, the enhanced signal in the parent mass-channel must be due to dynamics in a neutral CH_3I. One may argue that the t_0 feature in the I^+ channel is derived from fragmentation of excited CH_3I^+. Fig. 3B shows mass spectra obtained using each laser separately. Note that the pump laser creates very little I^+ or CH_3^+. Thus the dominant mechanism is to create stable parent ion. This suggests that subsequent absorption of a photon by the parent ion is not a very probable process. The spectrum due to the probe laser alone shows the same features, but a much greater amount of I^+ signal. We presume that this signal comes primarily from the resonant ionization of free I from dissociated neutrals. Tuning the probe off-resonance causes the signal in this channel to decrease by a factor of 5, which is comparable to the I^+ signals observed in the mass spectrum due to the pump laser alone. Thus we conclude that fragmentation of CH_3I^+ by absorption of additional probe photons cannot be a major source for the t_0 feature observed in this channel.

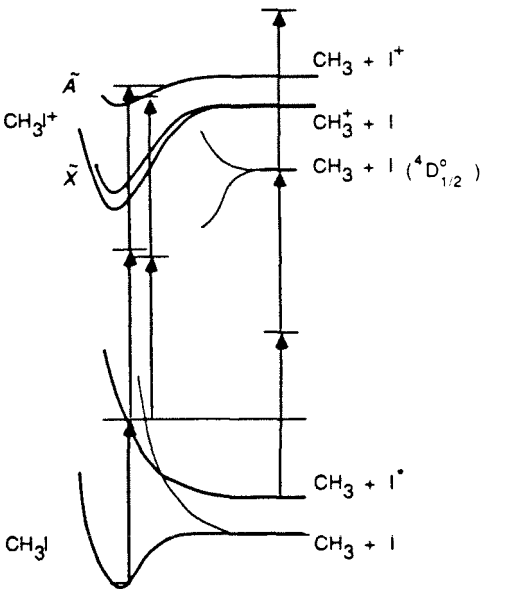

Fig. 4. Energetics of neutral and ion states of CH_3I. The solid arrows correspond to transitions excited by the pump, while the shaded (lighter) arrows indicate those due to the probe.

The energetics of the ion are known from MPI fragmentation and photoion photoelectron coincidence studies. A schematic diagram is shown in fig. 4. Two photons of the probe are required to ionize molecules that have absorbed one pump photon. The total energy obtained from the sum of three photons is in the region of the $\tilde{A}$ state of the ion. If the photoelectron leaves with low kinetic energy, the ion will be left in the $\tilde{A}$ state, while higher energy photoelectrons correspond to ground state CH_3I^+ stable to further fragmentation. The ionic $\tilde{A}$ state is believed to undergo rapid internal conversion to the $\tilde{X}$ state [10], which has two fragmentation channels accessible: $CH_3I^+ \rightarrow CH_3^+ + I$ and $CH_3I^+ \rightarrow CH_2I^+ + H$. The first has a lower threshold and is likely to dominate. Neither of these channels give rise to signal in

[#1] The small amount of "negative" signal in the parent ion channel at positive delay is an artefact of the background subtraction procedure. It represents the error limits of our results.

the I^+ channel. A third probe photon would leave the ions with enough energy to form I^+, but the cross section for this process should be many orders of magnitude smaller.

Finally, it should be noted that any off-resonance effect of the I atom ionization will only be observed if the ionization signal is monitored in real time. The pump–probe signal [#2] is sensitive only to the delay time between the two pulses and hence to formation of the fragment.

5. Conclusions

These studies demonstrate that the process of separation of fragments of direct photodissociation reactions can be probed using tunable, ultrashort pulses in combination with MPI–mass spectrometry. Mass selection of ions allows us to identify bound species and fragments unambiguously and also to probe non-fluorescing species. Wavelength tunability provides another degree of freedom which may be exploited to obtain detailed information on the perturbed fragment species. The extension of this detection scheme to the femtosecond time domain promises to make FTS [1] versatile in probing the "transition state" of reactions.

Note: Two very recent studies are relevant to this work. (a) El-Sayed and co-workers [19] have found that with one pulse (≈ 50 ps) at 266 nm, absorption to the ion competes effectively with dissociation on the repulsive surface, consistent with our work. (b) Polanyi and co-workers have reported [20] the use of MPI to detect HD_2 produced in the hot atom reaction of H with D_2, with nanosecond lasers. It is interesting that even long (nanosecond) pulses can detect species with ≤ 1 ps lifetime.

Acknowledgement

This work was supported by the Air Force Office of Scientific Research, Contract No. AFOSR-87-0071. We thank Professor J.C. Polanyi for providing us with a preprint of his work on HD_2. One of us (AHZ) wishes to acknowledge fruitful and enlightening discussions with Professor R. Bersohn on absorption during dissociation while here at Caltech.

[#2] Coherence effects between pump and probe pulses are not significant because of the large difference in wavelengths.

References

[1] M. Dantus, M.J. Rosker and A.H. Zewail, J. Chem. Phys. 87 (1987) 2395.

[2] R. Bersohn and A.H. Zewail, Ber. Bunsenges. Phys. Chem., submitted for publication.

[3] N.F. Scherer, C.N. Sipes and A.H. Zewail, in preparation.

[4] A. Gedanken and M.D. Rowe, Chem. Phys. Letters 34 (1975) 39;
S.L. Baughcum and S.R. Leone, J. Chem. Phys. 72 (1980) 6531;
H.W. Hermann and S.R. Leone, J. Chem. Phys. 76 (1982) 476;
T.F. Hunter, S. Lunt and K.S. Kristjansson, J. Chem Soc. Faraday Trans. II 79 (1983) 303;
J.D. Scott, W. Sid Felps, G.L. Findley and S.P. McGlynn, J. Chem. Phys. 68 (1978) 4678.

[5] S.J. Riley and K.R. Wilson, Faraday Discussions Chem. Soc. 53 (1972) 132;
R.K. Sparks, K. Shobatake, L.R. Carlson and Y.T. Lee, J. Chem. Phys. 75 (1981) 3838;
G.N.A. van Veen, T. Baller, A.E. de Vries and N.J.A. van Veen, Chem. Phys. 87 (1984) 405;
M. Dzvonik, S. Yang and R. Bersohn, J. Chem. Phys. 61 (1974) 4408.

[6] D.H. Parker, R. Pandolfi, P.R. Stannard and M.A. El-Sayed, Chem. Phys. 45 (1980) 27;
A. Gedanken, M.B. Robin and Y. Yafet, J. Chem. Phys. 76 (1982) 4798;
J. Danon, H. Zacharias, H. Rottke and K.H. Welge, J. Chem. Phys. 76 (1982) 2399;
J.W. Hudgens, T.G. DiGiuseppe and M.C. Lin, J. Chem. Phys. 79 (1983) 571.
P.L. Houston, unpublished results.

[7] D. Imre, J.L. Kinsey, A. Sinha and J. Krenos, J. Phys. Chem. 88 (1984) 3956.

[8] J.L. Knee, L.R. Khundkar and A.H. Zewail, J. Chem. Phys. 83 (1985) 1996.

[9] M. Shapiro and R. Bersohn, J. Chem. Phys. 73 (1980) 3810;
E.J. Heller, Accounts Chem. Res. 14 (1981) 368;
S.-Y. Lee and E.J. Heller, J. Chem. Phys. 76 (1982) 3035;
R.L. Sundberg, D. Imre, M.O. Hale, J.L. Kinsey and R.D. Coalson, J. Phys. Chem. 90 (1986) 5001.

[10] J.H.D. Eland, R. Frey, A. Kuestler, H. Schulte and B. Brehm, Intern. J. Mass Spectrom. Ion Phys. 22 (1976) 155;
H.M. Rosenstock, K. Draxl, D.W. Steiner and J.T. Herron, J. Phys. Chem. Ref. Data 6 (1977) suppl. 1;
L. Karlsson, R. Jadrny, L. Mattson, F.T. Chan and K. Siegbahn, Physica Scripta 16 (1977) 225;
D.M. Mintz and T. Baer, J. Chem. Phys. 65 (1976) 2407;

A.M. Woodward, S.D. Colson and W.A. Chupka, J. Phys. Chem. 90 (1986) 274.

[11] D.H. Parker and R.B. Bernstein, J. Phys. Chem. 86 (1982) 60;
K.R. Newton, D.A. Lichtin and R.B. Bernstein, J. Phys. Chem. 85 (1981) 15;
D.A. Lichtin, R.B. Bernstein and K.R. Newton, J.Chem. Phys. 75 (1981) 5728.

[12] L.R. Khundkar, J.L. Knee and A.H. Zewail, J. Chem. Phys. 87 (1987) 77;
N.F. Scherer and A.H. Zewail, J. Chem. Phys. 87 (1987) 97;
J.L. Knee, L.R. Khundkar and A.H. Zewail, J. Chem. Phys. 87 (1987) 115.

[13] D.J. Donaldson, V. Vaida and R. Naaman, J. Chem. Phys. 87 (1987) 2522.

[14] C.E. Moore, Atomic energy levels, Vol. 3, NBS Circular No. 467 (US Govt. Printing Office, Washington, 1958);
J.J. Tiee, M.J. Ferris, G.W. Loge and F.B. Wampler, Chem. Phys. Letters 96 (1983) 422;
J. Berkowitz, C.H. Batson and G.L. Goodman, Phys. Rev. A24 (1981) 149.

[15] S.R. Gandhi and R.B. Bernstein, private communication; Chem. Phys. 105 (1986) 423.

[16] Y. Jiang, M.R. Giorgi-Arnazzi and R.B. Bernstein, Chem. Phys. 106 (1986) 171;
K. Tsukiyama, B. Katz and R. Bersohn, Chem. Phys. Letters 124 (1986) 309.

[17] H.-J. Foth, J.C. Polanyi and H.H. Telle, J. Phys. Chem. 86 (1982) 5027.

[18] T.F. George, J. Phys. Chem. 86 (1982) 10;
A.M.F. Lau, Advan. Chem. Phys. 50 (1982) 191.

[19] M.A. El-Sayed, private communication.

[20] B.A. Collings, J.C. Polanyi, M.A. Smith, A. Stolow and A.W. Tarr, private communication.

Chapter 7B

Time- and frequency-resolved measurements of transition states

7B.1. Introduction

Electronic excitation of molecules from a bound ground state to a repulsive (unbound) state leads to dissociation on a time-scale which is often much faster than the molecular rotational period. Recent pump-probe experiments using ultrashort pulses ($\sim$ 100 fs) have shown that a small, but finite, time-lag is associated with the evolution of the unperturbed fragment states.[1] This may be interpreted as the time taken by the fragments to physically separate along a classical path. A simple model[2] for interpreting the time-dependence of the absorption of light by dissociating fragments has been developed and used to model this delay.

These experiments[1,3] have also shown that the so-called "transition-state" species may be detected via their characteristic absorption profiles. Since time and frequency constitute a Fourier transform pair, these effects should also be observable in energy-resolved experiments. Polanyi and coworkers[4] have used carefully scaled measurements over a large dynamic range of signal intensity to show that light emitted by fragments during dissociation have spectral profiles that are non-Lorentzian as a result of the mutual perturbation of the separating species.

Here, we extend the classical model of light absorption during fragmentation of Bersohn and Zewail (BZ)[2] to the frequency domain and show by numerical simulation how parameters such as initial energy, spectral and temporal bandwidths of the pulses employed affect the outcome of a pump-probe experiment. As a concrete example, we compare the predictions of this simple model with recent experimental measurements on methyl iodide.

In the previous chapter[3] , we presented transients at different wavelengths near a non-resonant two-photon transition of the iodine atom. Results obtained with the laser tuned slightly off-resonance showed a sharp feature at zero time which is not

present when the laser is properly tuned to resonance. This has been attributed to absorption by iodine atoms which are perturbed by their recoil partners, the methyl radicals. If our analysis is correct, the absorption spectrum near a resonance of the atoms should appear broader when both pulses are overlapped in time than when they are separated by finite delays long enough to ensure that all recoiling species are far removed from each other. Here, we present results of spectral measurements at various delays to corroborate the observations of the previous section.

7B.2. Experimental

The apparatus used was essentially the same as the one described earlier. The primary difference was that instead of the time delay being varied to map the evolution of the system, the probe laser wavelength was tuned for fixed delay times. A few other variations in the experimental setup are described briefly.

Instead of two independent dye lasers, we used a single synchronously pumped one and amplified its output in four stages to obtain pulses of high energy (~1 mJ) picosecond light at 608 nm. Approximately 80% of this light was focused into a 5 cm long water cell. The intensities obtained were high enough to generate a white-light continuum.[5] The remaining 20% of the first pulse was propagated through the delay line and a nominal ×1 telescope (50 cm quartz lenses), as described earlier. A thin KDP crystal was placed near the beam waist to generate the second harmonic, which was used as the probe.

The white-light continuum was collimated with a spherical achromatic lens and the beam dispersed with a grating. A double pass arrangement with a slit in the path of the beam is capable of selecting a narrow portion of the spectrum[6] (FWHM of the spectral bandwidth was ~ 10 Å). The wavelength selected beam was amplified in another three stages, doubled and used as the pump in the usual way. Since the color of the pump light is determined almost entirely by the geometry of the grating arrangement, the wavelength of the light used to generate the continuum does not affect the frequency of the pump. The two beams are therefore still independently tunable.

The REMPI spectrum of I^* atoms was obtained by tuning the sync-pump laser with a stepper motor. The steps of the motor were synchronized with the channel advance of the multichannel analyzer. A typical set of spectra was obtained in the following sequence of steps. The laser was tuned to the peak of the resonance and a transient of the parent CH_3I was obtained by stepping the delay line. Once a reasonable transient had been obtained, the delay was set to correspond to the peak of the transient. The gate of the boxcar was adjusted to sample only ions with the same mass as the I atom and the spectrum was obtained by varying the wavelength of the dye laser systematically. This was repeated for both positive and negative delays (40 ps). A number of such scans were averaged for improved S/N ratios, with appropriate measures taken to correct for changes in the laser intensities during the experiment. The spectra shown in the figures below were optimally filtered in fourier space.[7]

7B.3. Theory

A schematic of the 1-dimensional potential energy surfaces (curves) relevant to this discussion is shown in figure 7B.1. As in the BZ model, we assume Born-Oppenheimer separability of electronic and nuclear motions and use classical mechanics to describe the evolution of a molecule placed on the repulsive surface. We choose an exponential form for the surface since the equations of motion have analytic solutions.

The potential curves as a function of the fragment separation, R ($R \geq R_0$), are

$$V_1(R) = V_1(R_0)\, exp[-(R - R_0)/L_1] \qquad (7B.1)$$

$$V_2(R) = V_2(R_0)\, exp[-(R - R_0)/L_2] + h\nu^{\infty} \qquad (7B.2)$$

where $h\nu^{\infty}$ is the energy of an excited electronic state of the free fragments. Optical excitation is assumed to be vertical in the Franck-Condon sense, and is therefore parametrized by R. The intrinsic molecular absorption profile, m, is also a function of R.

$$m(\epsilon, R) = \frac{\gamma}{\gamma^2 + [\epsilon - \phi(R)]^2} \qquad (7B.3)$$

where we have chosen a Lorentzian profile for the absorption. $\phi(R)$ is simply the difference in energy between the two electronic surfaces at R.

$$\phi(R) \quad = \quad V_2(R) \; - \; V_1(R) \tag{7B.4}$$

The homogeneous linewidth of the transition, γ, is typically very narrow for long-lived fragment species.

The dynamics of nuclear motion is most easily derived from conservation of energy

$$\frac{1}{2}\mu\left(\frac{dR}{dt}\right)^2 \; + \; V_1(R) \quad = \quad E. \tag{7B.5}$$

In this equation, E is the terminal kinetic energy, μ the reduced mass of the system and dR/dt is the radial velocity of separation. The appropriate initial conditions are $V_1(R_0) = E$ and $t(R_0) = 0$, i.e., the system starts from the classical turning point, R_0. If we consider only 1-dimensional motion, R is a well-defined, single-valued function of time, given implicitly by

$$exp(-[R - R_0]/L_1) \quad = \quad sech^2\left(\frac{vt}{2L_1}\right) \tag{7B.6}$$

where v is the terminal radial velocity, $\sqrt{2E/\mu}$. Under these conditions, eqn. (7B.3) represents a time-dependent molecular absorption function which may be used to model both time and frequency scans.

1. Transient behavior

We will first show that the formalism used here reduces to the BZ model under the appropriate conditions. In pump-probe measurements of the temporal behavior, one maintains a constant spectral profile for the probe while scanning the relative delay between the pump and probe pulses. The absorption at time t, $A(t)$, is given by the integral of the time- and frequency-dependent molecular absorption profile over all frequencies.

$$A(t) \quad = \quad \int_{-\infty}^{\infty} m(\epsilon, t) S_{prb}(\epsilon - \epsilon_0) d\epsilon \tag{7B.7}$$

Assuming that γ (eqn 7B.3) is much smaller than the bandwidth of the probe laser, i.e., S_{prb} is a slowly varying function of energy, one may replace m by the delta function, $\delta(\epsilon - \phi(R(t)))$. Eqn 7B.7 then reduces to

$$A(t) \quad = \quad S_{prb}\left(\phi[R(t)] - \phi[R(t^*)]\right) \qquad (7B.8)$$

where t^* is defined to satisfy $\epsilon_0 = \phi[R(t^*)]$. If the laser frequency profile, S_{prb}, were Lorentzian, one would recover eqn 7 of BZ (ref 2) exactly. In this section , we consider effects of both temporal and spectral bandwidths on the predictions of the model and choose gaussian profiles for simplicity. Using eqn 7B.6 and 7B.7 and neglecting $V_2(R)$ as in BZ, we get

$$A(t) \quad = \quad exp\left(-\left(\frac{E}{\sigma_s}\right)^2\left[sech^2\left(\frac{vt}{2L_1}\right) - sech^2\left(\frac{vt^*}{2L_1}\right)\right]^2\right) \qquad (7B.9)$$

The full width at half the maximum value (FWHM) of the spectral profile is $2\sigma_s\sqrt{\ell n\, 2}$. For a proper comparison with experiment, $A(t)$ should be convoluted with the response function, ρ. Thus the observed transient, D, is

$$D(T) = \int_{-\infty}^{T} A(T-s)\rho(s)ds \qquad (7B.10)$$

$$= \int_{-\infty}^{T} exp\left(-\left(\frac{E}{\sigma_s}\right)^2\left[sech^2\left(\frac{vt}{2L_1}\right) - sech^2\left(\frac{vt^*}{2L_1}\right)\right]^2\right) e^{-(s/\sigma_t)^2}\, ds \qquad (7B.11)$$

Plots of $A(t)$ and $D(T)$ are shown in figure 7B.2 for various values of t^*. It is important to note that the abscissa is the dimensionless variable $vt/2L_1$, which may be interpreted as time in units of $v/2L_1$. Thus σ_t, the temporal width of the response function, is also given in these units. The unit of energy is chosen to be σ_s, the spectral width of the probe.

From figure 7B.2, we see that the effect of the convolution with the temporal response function ($\sigma_t = 0.5$) is to broaden the observed widths and decrease the contrast ratio of the maximum absorption to the value at long positive delays. A

more dramatic change of this ratio is observed when the spectral bandwidth is increased by a factor of 2, corresponding to pulses that are not transform-limited (fig 7B.3). This serves to illustrate the advantage of using pulses having the minimum energy spread for a given temporal width.

2. *Spectral profiles*

In measuring time-dependent spectral profiles, the delay between the two pulses is held fixed while the wavelength of the probe laser is scanned through a resonance of the fragment. The measured bandshape at a given time, t, is the convolution of the molecular absorption with the laser frequency profile, S_{prb}.

$$M(\epsilon,t) \quad = \quad \int_{-\infty}^{\infty} m(\xi,t) S_{prb}(\epsilon-\xi) d\xi \qquad (7B.12)$$

which reduces to eqn 7B.13 when the delta function approximation is used.

$$M(\epsilon,t) \quad = \quad S_{prb}\left(\epsilon - \phi[R(t)]\right) \qquad (7B.13)$$

$$\approx \quad \frac{1}{\sigma_s} exp\left(-\frac{1}{\sigma_s^2}\left[\epsilon + E\, sech^2\left(\frac{vt}{2L_1}\right)\right]^2\right) \qquad (7B.14)$$

The zero of energy has been redefined as the transition energy of the unperturbed fragment. Convolution of M with the temporal response function then yields the observed signal

$$D_s(\epsilon,T) = \int_{-\infty}^{\infty} \frac{1}{\sigma_s} exp\left(-\frac{1}{\sigma_s^2}\left[\epsilon + E\, sech^2\left(\frac{v(T+s)}{2L_1}\right)\right]^2\right) e^{-(s/\sigma_t)^2} ds \qquad (7B.15)$$

The integration over time implies that the absorption corresponding to a specific value of R is proportional to the time the system spends in this configuration. The constant of proportionality has been chosen to be unity and eqn 7B.15 is thus transparent to this bit of detail.

It is instructive to consider the behavior of D_s for long positive delays. We assume that the molecular absorption spectrum has ceased to change and treat M

as a constant. The integral is then simply the area of the pulse and the measured bandshape is the spectral response function.

$$D_s(\infty) \quad \approx \quad M(\epsilon, \infty) \quad = \quad S_{prb}(\epsilon - h\nu^{\infty})$$

A simulation of $D_s(\epsilon, 0)$ is shown in fig 7B.4. The bandshape shows an overall shift of the peak of the absorption to lower energies, along with a tail of significant amplitude to even redder energies. The structure seen is an artifact of the calculation arising from the discrete sum approximation of the integral. The trend seen in these simulations is consistent with our intuition. If the temporal response is increased and the spectral width reduced simultaneously such that their product remains the same, the magnitude of the shift in the peak position decreases and the tail loses intensity. The effect is greater than the figure suggests as the scale of the abscissa has been reduced by choosing a smaller σ_s. If σ_t is further increased with σ_s held constant, the same qualitative trend is seen — the amplitude of the tail is reduced (fig. 7B.5).

The effect of the pulse width on the spectrum can be easily understood. For a fixed bandwidth, the function $\left(\frac{E}{\sigma_s}\right) sech^2 \frac{vt}{2L_1}$ describes the detuning as a function of time. At times greater than some value $t = t_\infty$, the function is zero for all practical purposes, and the spectrum is that of the free fragment. Figure 7B.6 shows a plot of the energy remaining as a function of reduced time. The fractional absorption due to the transient species is thus $\sim erf(t_\infty/\sigma_t)$. As σ_t increases, the relative amount of time during which these species can absorb is reduced (scaled by the length of the pulse width) and the amplitude of the tail (wing-absorption) is decreased. Thus the signal has to be recorded over a larger dynamic range in order to resolve these off-resonance features.

Although the integral in eqn 7B.15 can be evaluated numerically, one may derive a simpler form for the predicted absorption when $\sigma_t \gg 1$ and the contribution

to the spectrum is dominated by the asymptotic region of the potential. It may be broken into two parts

$$D_s(T) = \int_{-\infty}^{t_\infty} M(\epsilon, T+s) e^{-(s/\sigma_t)^2} ds + M(\epsilon,\infty) \int_{t_\infty}^{\infty} e^{-(s/\sigma_t)^2} ds \quad (7B.16)$$

$$= \int_{-\infty}^{t_\infty} M(\epsilon, T+s) e^{-(s/\sigma_t)^2} ds + M(\epsilon,\infty)\sigma_t erfc(t_\infty/\sigma_t) \quad (7B.17)$$

When $\sigma_t \gg 1$, the gaussian term in the first integral is approximately unity. Deconvolution of this integral with the spectral response function results in

$$m(\xi) = \int_{-\infty}^{t_\infty} \delta \left[\xi + E sech^2 \left(\frac{v(T+s)}{2L_1} \right) \right] ds \quad (7B.18)$$

The integral over time of the delta function in energy space is a mathematical statement of a physical assumption mentioned earlier. It means that the absorption at a given energy is proportional to the amount of time the system spends in that region. Thus equation 7B.18 simplifies to

$$m(-\xi) = \left[2\xi \sqrt{1 + (\sigma_s \xi / E)} \right]^{-1} \quad (7B.19)$$

where the domain of ξ, the detuning energy, is the interval $(0, E)$. The measured spectrum will then be the convolution of S_{prb} with $\tilde{m}$.

$$\tilde{m}(-\xi) = \left[2\xi \sqrt{1 + (\sigma_s \xi / E)} \right]^{-1} + erfc(t_\infty/\sigma_t)\delta(0) \quad (7B.20)$$

This predicts a tail which diminishes as the reciprocal of the energy near the resonance.

7B.4. Application to methyl iodide

The spectral lineshapes measured for zero time delay and large positive delay are shown in figure 7B.7. The difference spectrum shown in figure 7B.8 was obtained by subtracting the average of the spectra at large positive and negative delays. This difference represents absorption by dissociating species, as discussed below.

The observed spectrum is the sum of contributions of various species, each convoluted with the laser linewidth. Since methyl iodide dissociates when it absorbs

304 nm photons, the probe is capable of giving rise to signal on its own. In measuring a transient response, this appears as background, and we do not need to take it into account explicitly. As we are now considering absolute signals, we must subtract out the contribution of this process to the signals we are interested in.

The spectrum at large positive time has contributions from the probe alone and from free I* atoms created by the pump. At time t=0, the signal has contributions from the probe alone, I atoms produced by the initial part of the pump-pulse being probed, as well as transient species that are still in the neighborhood of their dissociation partners. The contribution of these transient species to the spectrum can be obtained only when signal from the other processes have been properly subtracted.

If the cross-correlation of the pump and probe pulses is symmetric, its integral reaches half the maximum value at t=0. We use this as an estimate of the number of free I* atoms that are contributing to the signal at zero delay. It then follows that the contribution of free atomic iodine and background from the probe alone is the average of the spectra at large positive and negative delays. Thus the difference spectrum shown in figure 7B.8 should be the spectrum of dissociating species, convoluted with the probe spectral bandwidth.

The shape of the absorption feature in figure 7B.7a is slightly broader at the base than the one in figure 7B.7b, the bandshape measured at long positive delays. The residual signal is $\sim$ 10% of the total signal observed at long times. One may therefore argue that small errors in determining the zero of time could lead to an incomplete cancellation of the contribution from the free I* atoms when the procedure described above is used. We have attempted to check this by subtracting an arbitrary fraction of the T_{pos} spectrum, i.e., the one obtained at long positive delay, from the one obtained at zero relative delay. This fraction was chosen so that the value of the residual spectrum at the maximum of the absorption is zero. This over-estimates the contribution of free atoms, but we still observe a non-zero residual on either side of the absorption peak (figure 7B.9). This is strong evidence

in support of the t=0 spectrum having a measurable contribution from molecules in the process of dissociation.

With this preamble on the analysis of our data, we attempt to compare the measured spectra with predictions of the simple model described in the previous section. Sundberg *et al.*[8] have recently formulated a two parameter analytic function that approximates the $^3Q_0$ state which is primarily responsible for the absorption band at 260 nm. Using the average value of the β parameters described by these authors, we estimate a value of 0.25Å for L_1. Kinetic energy analysis[9] of the photofragmentation process using 266 nm light showed that most (90 %) of the available energy in the I* channel is released as kinetic energy. For our excitation wavelength, we estimate $E \sim 7200$ cm^{-1}. Given a two photon bandwidth of $\sim$ 7 cm^{-1} for our probe laser, we get $E/\sigma_s \sim 1000$. At these kinetic energies, the terminal relative speed is $\sim 4 \times 10^5$ cm/s, which implies that the unit of time is $\sim$ 12 fs. With our temporal response of $\sim 6 - 8$ ps, $\sigma_t \sim 50 - 70$.

Simulations of the bandshape for zero time delay using these parameters are shown in figure 7B.10. The dotted lines indicate the spectrum at long positive times, i.e., our spectral response function. On careful study, one can observe a slight difference between the two curves on the red wing of the spectrum. In order to quantify this variation, we show the difference spectra, normalized to the measured value of the t=0 spectrum at each energy in figure 7B.11. The ordinate is given as a percentage and the peak of the response function has been shifted ($0.009\sigma_s$) to make the difference spectrum a positive function. These simulations show the same qualitative features as our experimental results — the $t = 0$ spectrum shows a very small tail to the red. The relative magnitude of the wing absorption is significantly less in the simulations ($\sim$ 1%) than in the observed spectra ($\sim$ 10 %). Simulations with different values of σ_s and σ_t show that a narrower temporal response would lead to greater amounts of absorption in the wing, which extends to many multiples of σ_s to the red.

Two further comments must be made. First, the measured difference spectrum shows a non-zero background which is due in part to fragmentation in the parent ion

$$CH_3I^+ \longrightarrow CH_3 + I^+$$

This process should show no dependence on the wavelength near the resonance of a free I atom. Second, the amplitude of the residual on the blue edge of the resonance has some contribution from a very slight shift in the peak of the absorption profile at $t = 0$ but the ratio of the amplitudes of the blue and red lobes of the difference spectrum is larger in the experimental results than in the simulations. Also, the model developed by BZ and extended here cannot explain the temporal behavior observed (i.e., peak at $t = 0$) when the probe is tuned to energies slightly higher than resonance if we assume that $\phi(R)$ is a monotonically decreasing function. A more complex form, including some of the other surfaces that participate in the dissociation as well as those correlating to the two-photon I atom resonant states, could acoount for some of the intensity in the blue wing.

7B.5. Conclusions

We have extended the BZ model for time-resolved pump-probe measurements on direct dissociation reactions to model time-dependent spectral bandshapes of the fragments. The predictions of the model has been compared with such measurements of the spin-orbit excited iodine atom produced during the dissociation of methyl iodide.

7B.6. References

1. M. J. Rosker, M. Dantus and A. H. Zewail, submitted.

2. R. Bersohn and A. H. Zewail, *Ber. Bun. Ges. Phys. Chem.*, **92**, 373, (1988).

3. M. Dantus, M. J. Rosker and A. H. Zewail, *J. Chem. Phys.*, **87**, 2395, (1987).

4. See, e.g., J. C. Polanyi, *Ang. Chem. Int. (Eng.) Ed.*, **26**, 952, (1987).

5. R. L. Fork, C. V. Shank, C. Hirlimann and R. Yen, *Opt. Lett.*, **8**, 1, (1983).

6. O. E. Martinez, *IEEE J. Quan. Electron.*, **QE-23**, 59, (1987).
Norbert F. Scherer, Ph. D. Thesis, C.I.T., to be submitted.

7. W. H. Press, B. P. Flannery, S. A. Teukolsky and W. T. Vetterling, .
in *Numerical Recipes*, Camb. Univ. Press, Cambridge, (1986)
8. R. L. Sundberg, D. Imre, M. O. Hale, J. L. Kinsey and R. D. Coalson, *J. Phys. Chem.*, **90**, 5001, (1986).

9. R. K. Sparks, K. Shobatake, L. R. Carlson and Y. T. Lee, *J. Chem. Phys.*, **75**, 3838, (1981).

Figure 7B.1 Schematic of potential energy curves relevant to light absorption during dissociation.

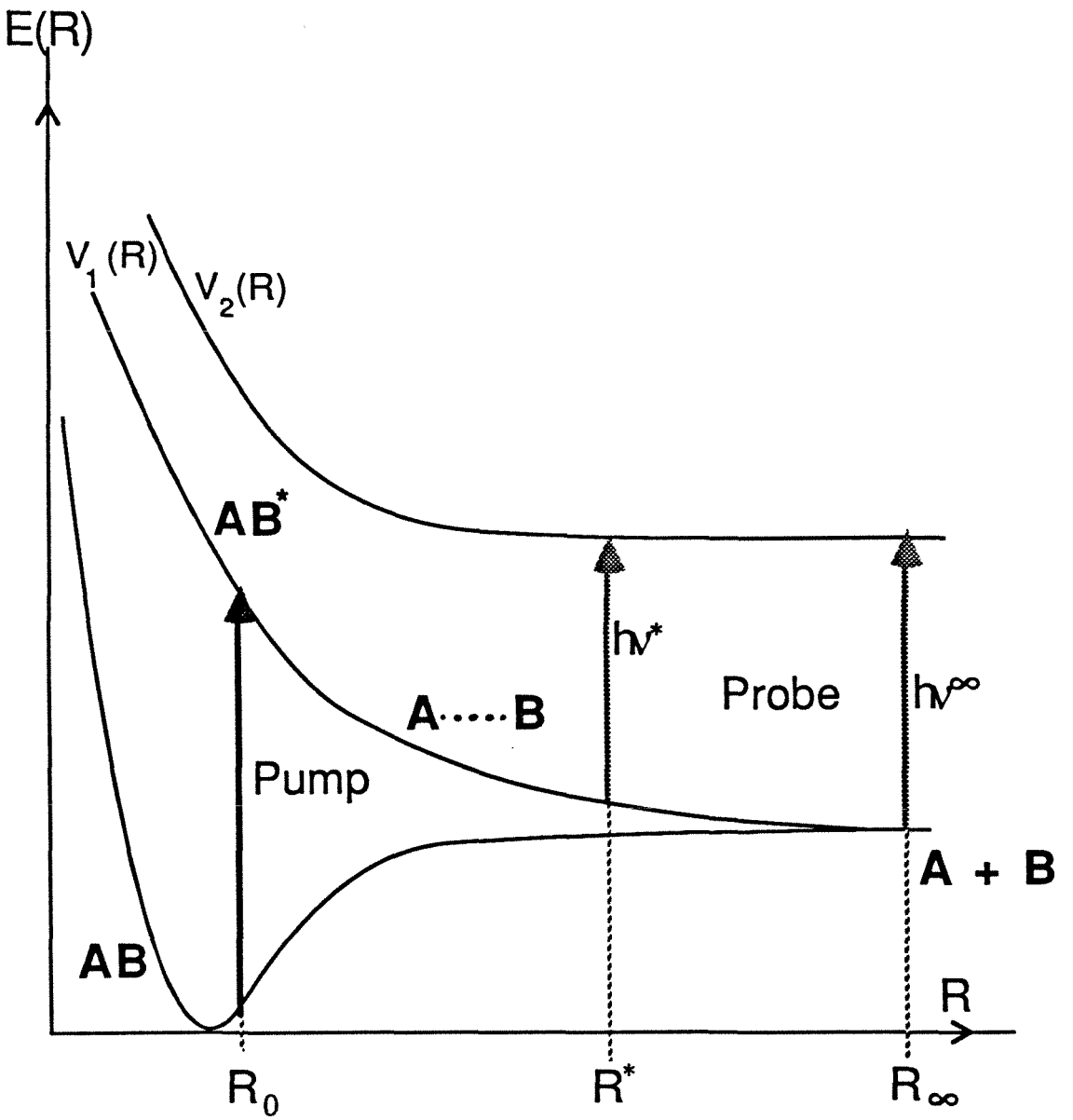

Figure 7B.2 Transient behavior predicted by the BZ model for various values of t^*. The solid curves (numbered 1 - 4) show the molecular absorption profile while the dotted curves (a - d) represent the absorption after convolution with a gaussian response. The values used were $\sigma_t = 1.0$ and $E/\sigma_s = 32.0$. (1,a) $t^* = 0.5$, (2,b) $t^* = 1.8$, (3,c) $t^* = 2.1$ (4,d) $t^* = 2.4$. The abscissa is reduced time (units of $2L_1/v$); the ordinate is the relative absorption. Each curve has been individually normalized to its maximum value.

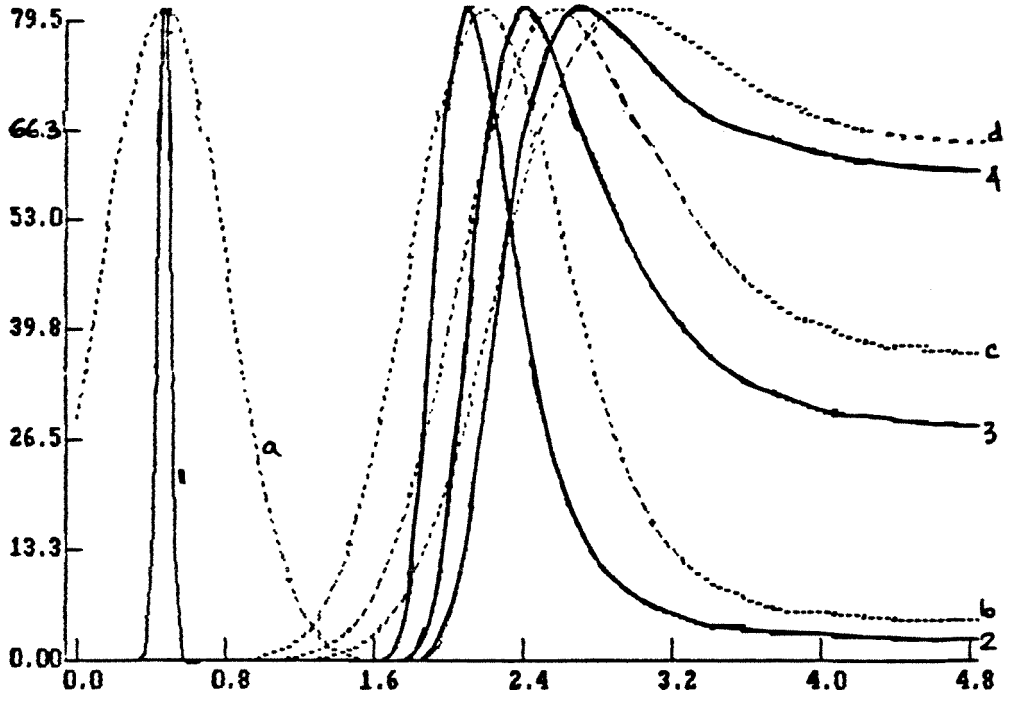

Figure 7B.3 Same as figure 7B.2 except $E/\sigma_s = 16.0$. This corresponds to a spectral width twice that employed in the previous figure, reflecting the effect of using pulses that are not transform limited.

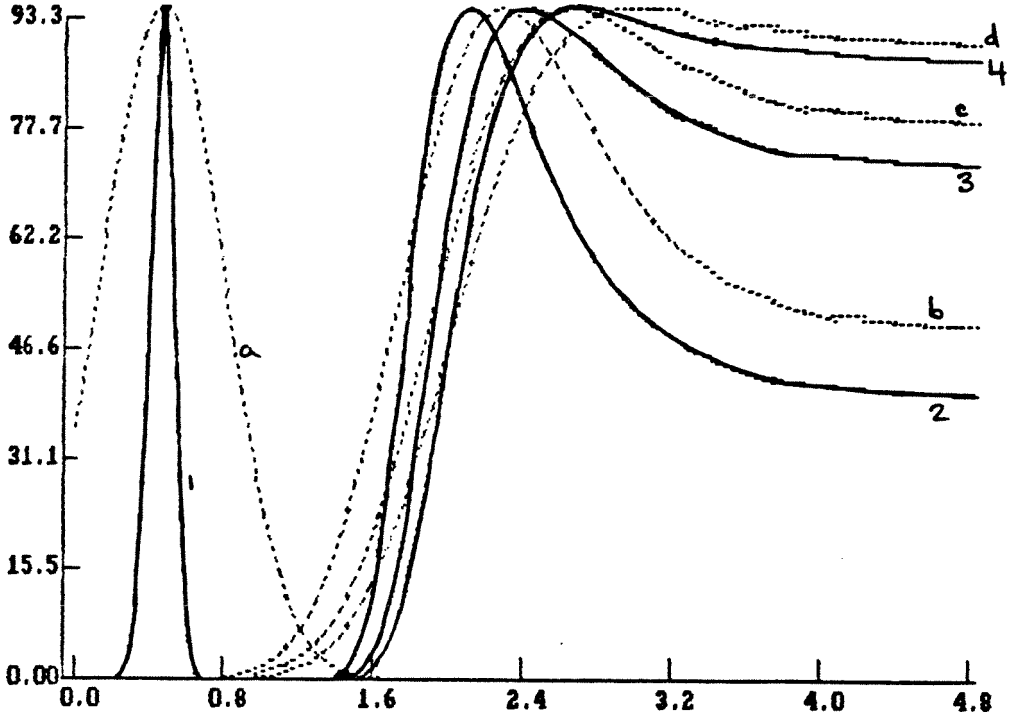

Figure 7B.4 Simulations of the spectral response for two values of σ_t and E/σ_s. The solid curve correspond to zero delay between pump and probe pulses. The dotted curves are the spectral response function. The abscissa is the detuning energy, in units of σ_s, and the ordinate is absorption intensity in arbitrary units. The structure at negative detuning is an artifact of the numerical integration and the dashed curve is extrapolated from the smooth part of the spectrum to estimate the true prediction of the model. The lower spectra are for a pulse twice as long and having half the bandwidth as that used to obtain the upper spectra. Note that the absolute energy scale for the two sets of spectra are therefore different.

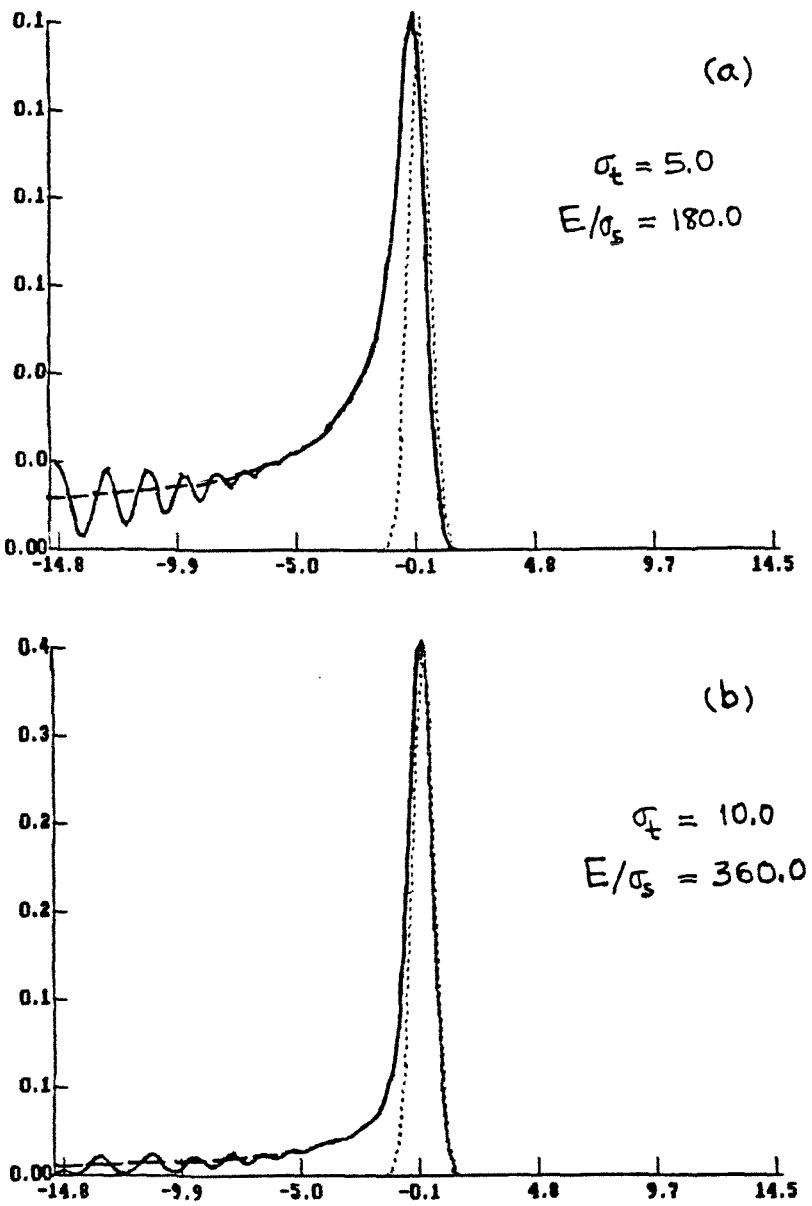

Figure 7B.5 Same as figure 7B.4 except $\sigma_t = 15.0$ and $E/\sigma_s = 360.0$, demonstrating the effect of a longer pulse which is not transform limited.

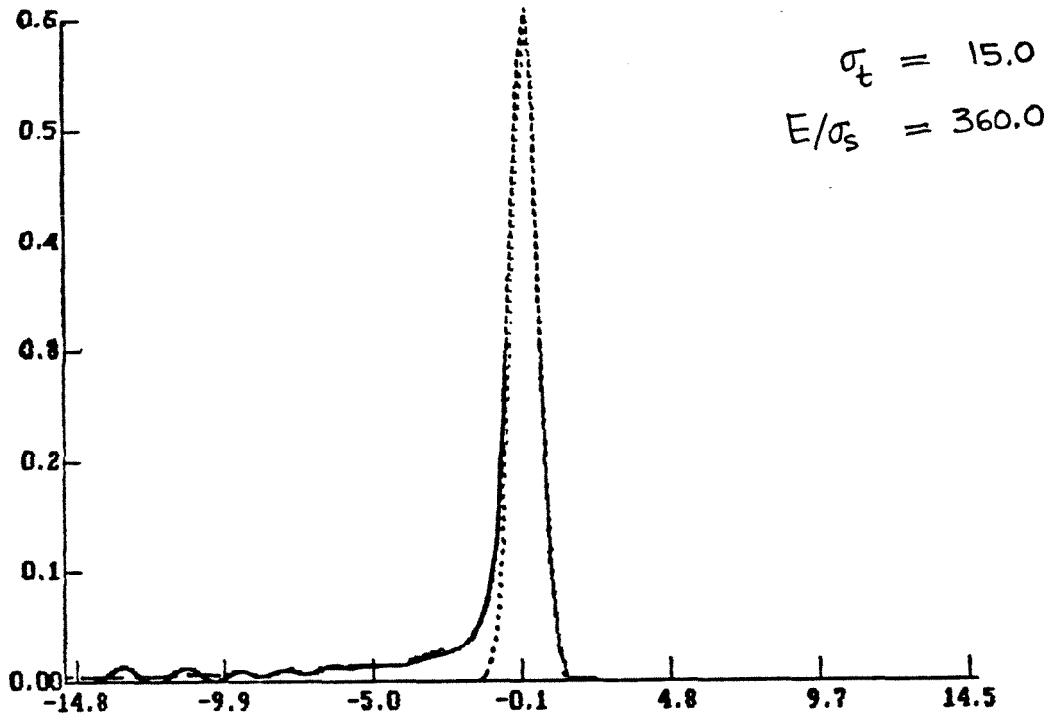

Figure 7B.6 The solid curve shows the amount of potential energy remaining as a function of time. The dotted curve shows the amplitude of the response function on the same time scale.

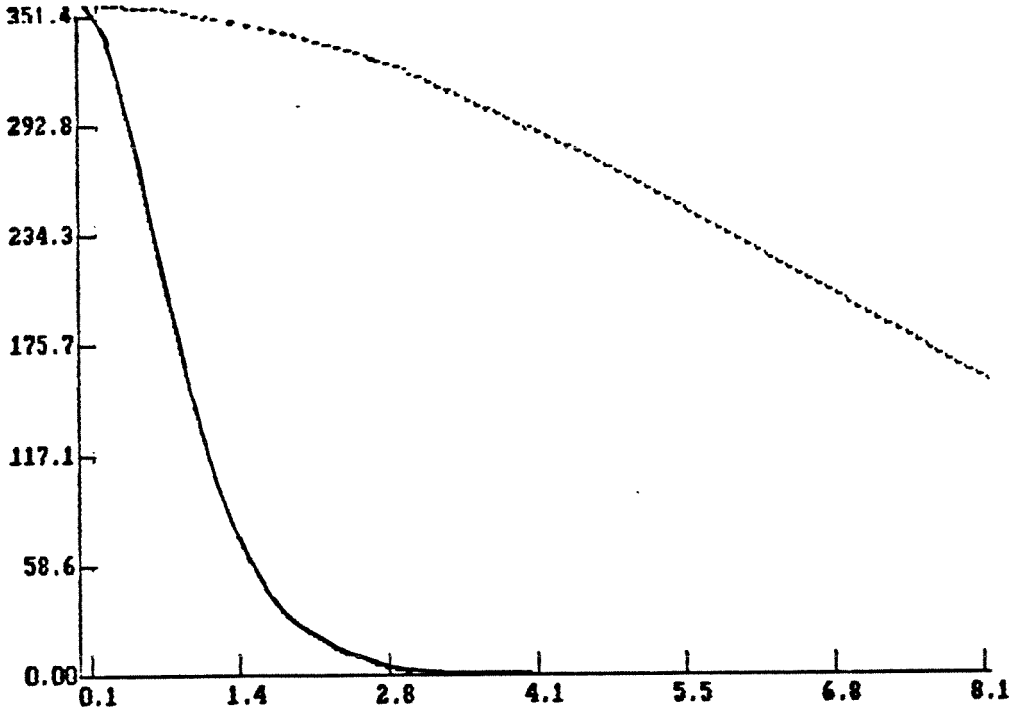

Figure 7B.7 Spectral lineshapes of I atoms obtained from the dissociation of methyl iodide, measured as a function of the time delay. (a) zero-delay spectrum, (b) positive delay (40 ps) spectrum.

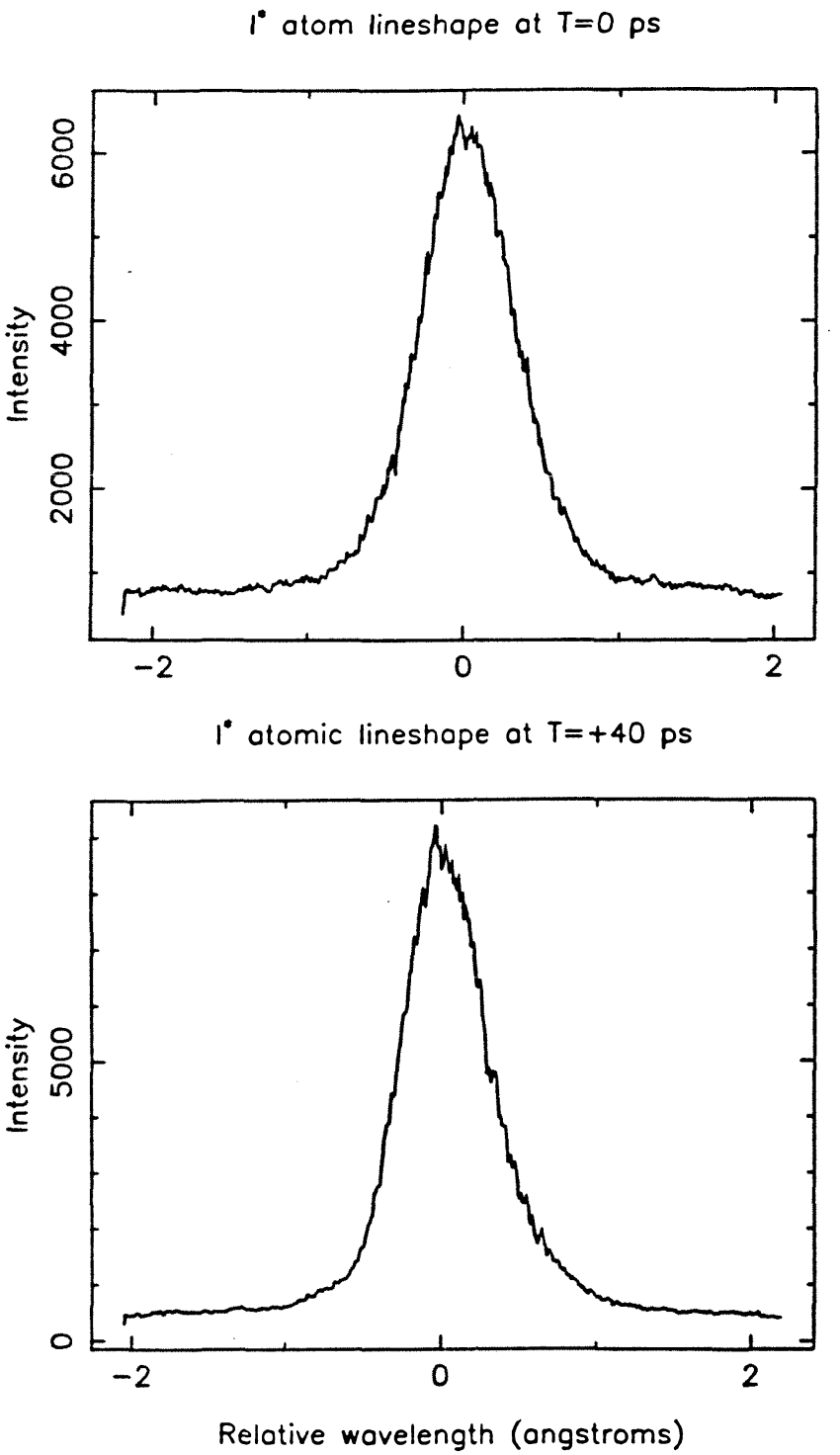

Figure 7B.8 The spectrum of transient species, as obtained from the difference of fig. 7B.7a and the average of fig. 7B.7b and the spectrum at negative delays.

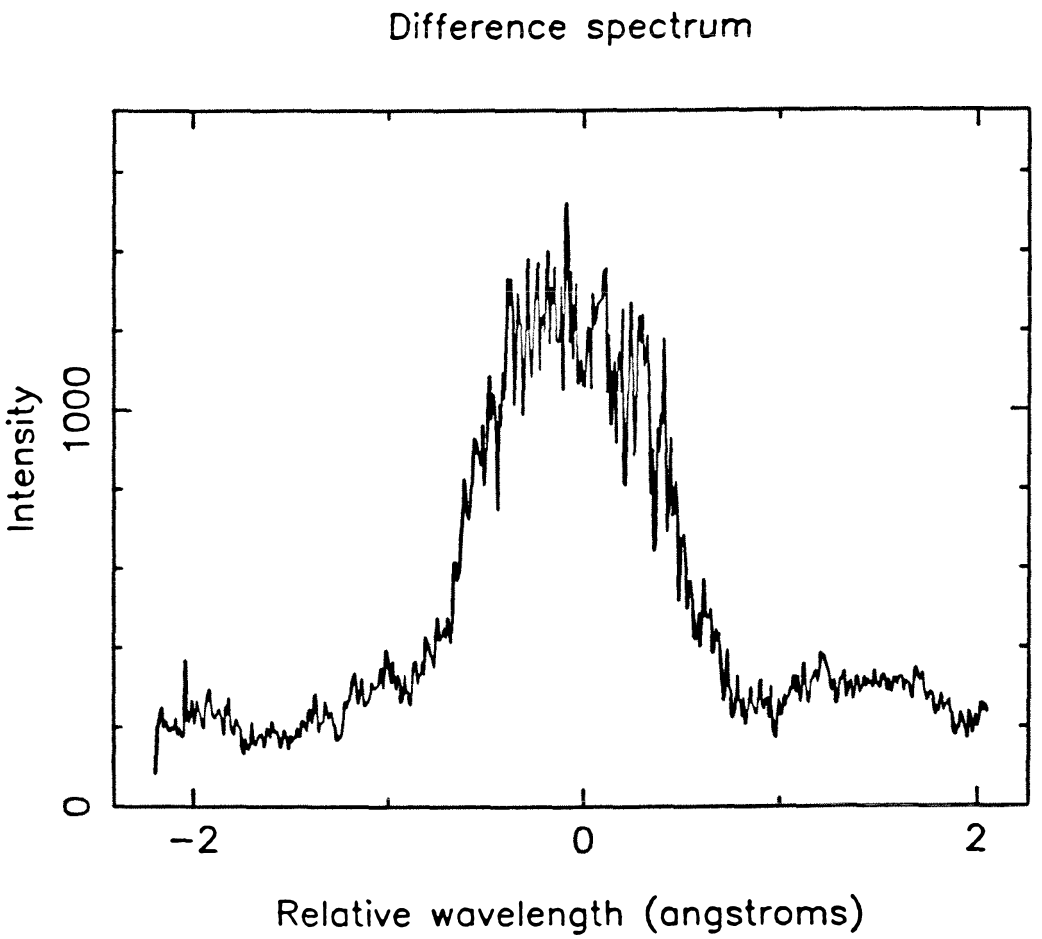

Figure 7B.9 Difference spectrum with a larger fraction of the positive-delay spectrum subtracted to show the 'wing' character of the absorption.

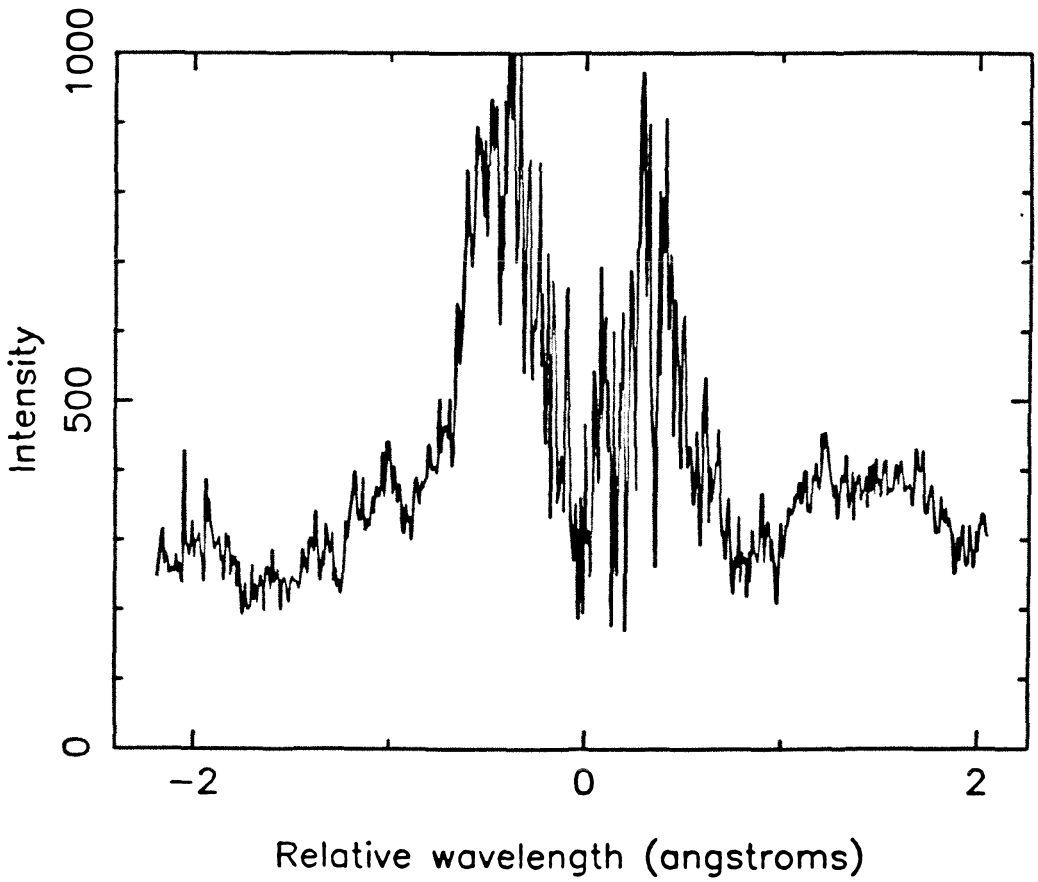

Figure 7B.10 Simulated spectra for methyl iodide. See captions of figure 7B.4 for comments and text for further details.

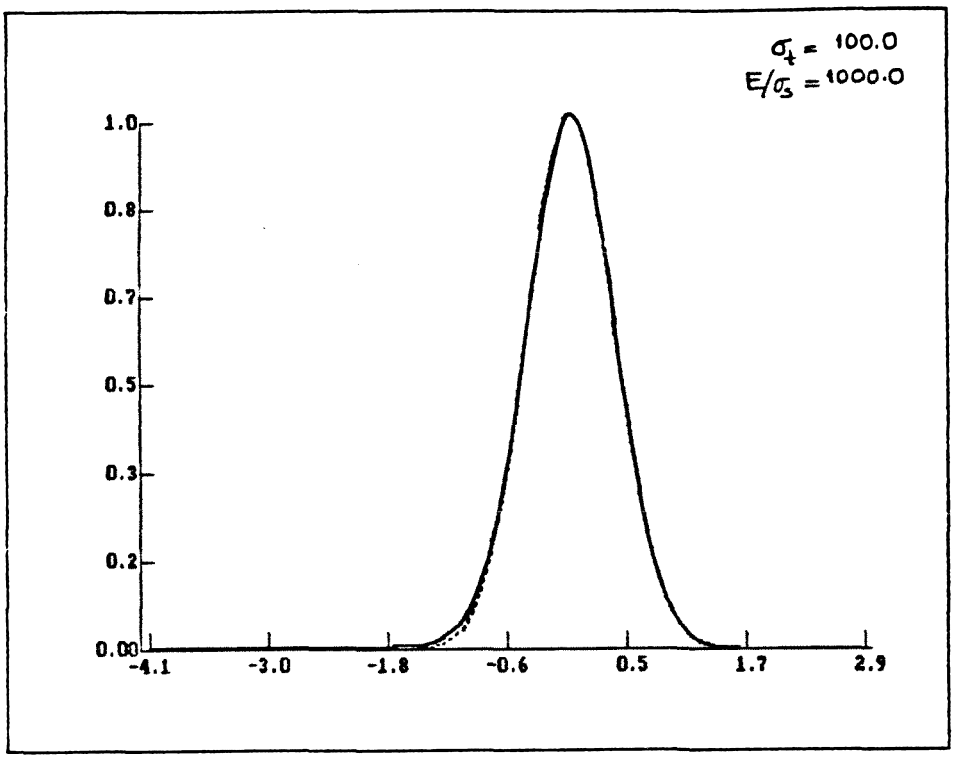

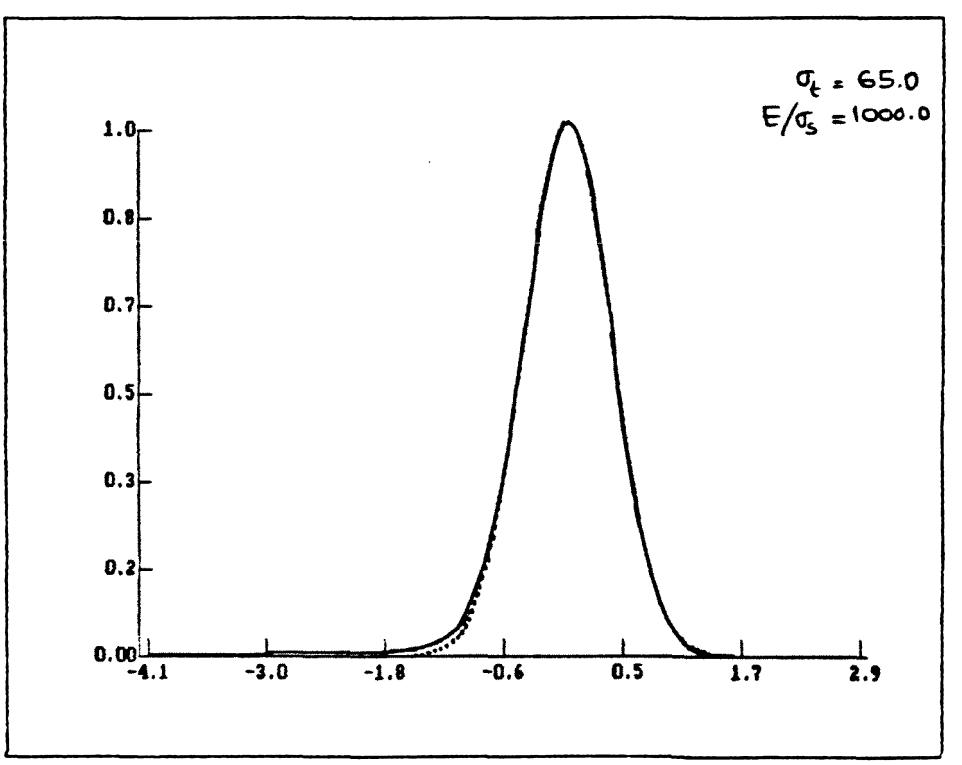

Figure 7B.11 Difference spectra generated from figure 7B.10. The ordinate is in percentage units of the solid curve in the previous figure.

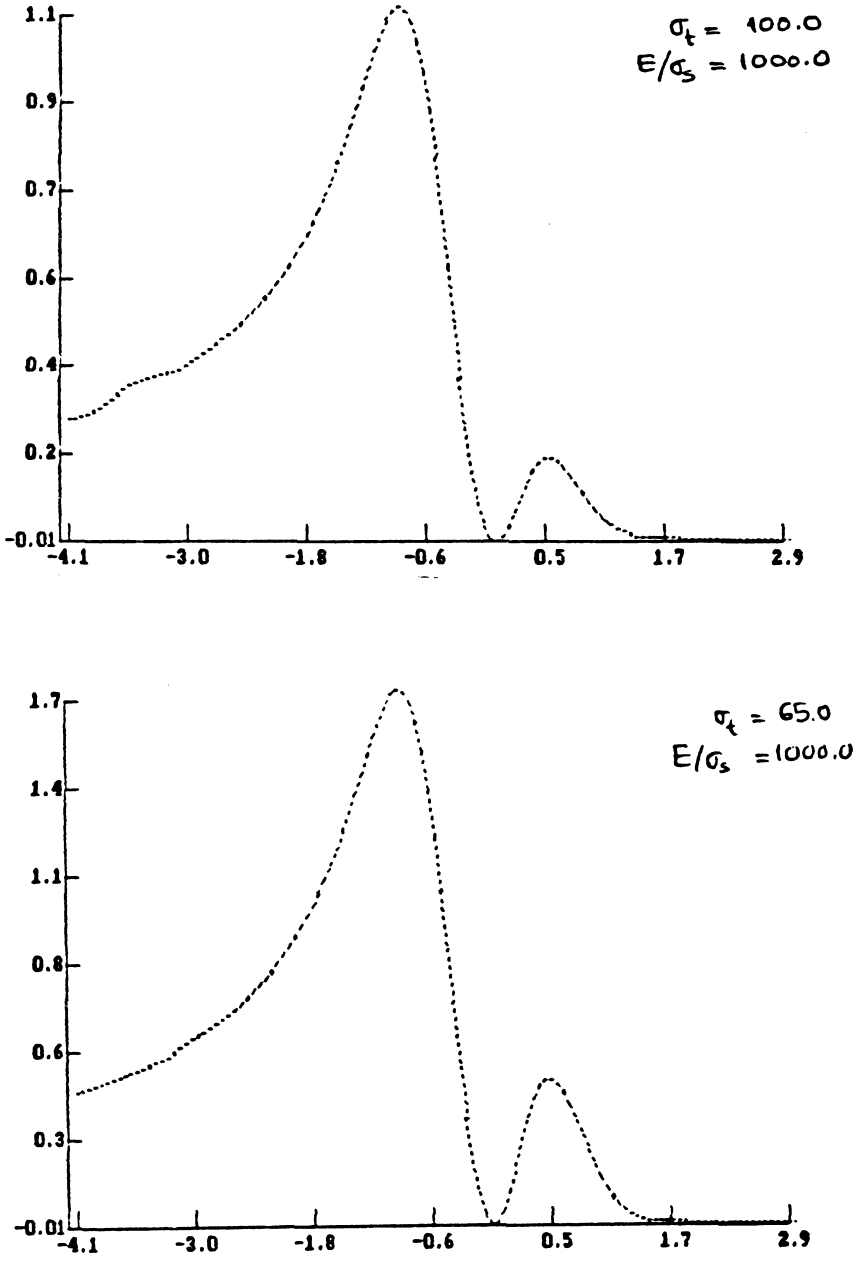

APPENDICES

APPENDIX I

Picosecond photofragment spectroscopy. III. Vibrational predissociation of van der Waals' clusters

Joseph L. Knee,[a] Lutfur R. Khundkar, and Ahmed H. Zewail
Arthur Amos Noyes Laboratory of Chemical Physics,[b] California Institute of Technology, Pasadena, California 91125

(Received 9 December 1986; accepted 11 February 1987)

This paper, last in this series, reports on the picosecond dynamics of vibrational predissociation in beam-cooled van der Waals' clusters. Reaction rates have been measured for clusters (1:1) of phenol and cresol (*p*-methylphenol) with benzene by the picosecond pump–probe photoionization mass-spectrometry technique. Dissociation to form phenol (cresol) and benzene takes place from vibrational levels of the S_1 state of phenol (cresol) prepared by the pump laser. The predissociation rates were measured for a number of different excess energies upto $\sim 2500\ cm^{-1}$, and the reaction threshold was found to be $1400\ cm^{-1}$ above the S_1 origin for phenol–benzene and $\sim 1795\ cm^{-1}$ for cresol–benzene, respectively. For phenol–benzene, the predissociation rates, following excitation of ring-type modes, vs excess energy vary more or less smoothly. Cresol–benzene exhibits biexponential decay, with the fast component becoming more dominant at higher energies. A non-RRKM model involving division of the vibrational phase space is discussed to explain this observation.

I. INTRODUCTION

van der Waals molecules have been the focus of intense study since the development of supersonic molecular beams and sensitive spectroscopic tools for measuring their properties.[1] The interest stems from the fact that these are simple systems dominated by long range attractive forces which are manifested as small perturbations of the constituent molecules. Studying such systems may allow one to understand interactions which are important to energy flow in dissociating complex systems and to the structure of more strongly bound chemical species. Much of the work to date has focused on the spectroscopy of these species as a means of determining the structure, interaction potentials, stabilization energies and induced perturbations present which all help to describe the bonding in these model systems.

Our primary interest in van der Waals molecules is their use as model systems for studying chemical reactivity, specifically IVR dynamics and unimolecular dissociation. The presence of a van der Waals bond between two constituent molecules induces only a small perturbation allowing the system to be approximated by the states of the uncomplexed molecules. The important feature for unimolecular dissociation of such species is that the van der Waals bond is much weaker than any of the covalent bonds in the system and therefore only a moderate amount of energy need be deposited in one of the constituent molecules to exceed the van der Waals dissociation energy. This amount of energy places the chromophore on an excited part of its potential energy surface which is still adequately described by the normal vibrational modes of the system. In other words, the small amount of energy to break the van der Waals bond can be deposited in the system by exciting a well defined initial state whereas to break a chemical bond in a strongly bound species, the system has to be excited to a portion of the potential energy surface where anharmonic and Coriolis couplings are important. Thus van der Waals molecules should be simple model systems to test theoretical descriptions because one can be more concerned with the influence of the few intermolecular modes than with describing a highly excited region of a multidimensional potential surface. They also provide a testing ground for the fundamental problem of energy flow to the reaction coordinate. If energy redistribution is complete prior to vibrational predissociation, one should observe dynamical behavior predicted by statistical theories. On the other hand, if dissociation rates are comparable to the rate of redistribution, then mode specific (selective) effects may be present.

Until now almost all of the information on van der Waals molecule predissociation has come from spectroscopic measurements which fall into two categories. The first is the measurement of electronic state spectra where predissociation occurs on an excited state potential. Here, the presence of predissociation is observed as either a broadening in the absorption spectrum (either fluorescence excitation or MPI spectra) or a change in the fluorescence from the excited state due to vibrational (but not electronic) relaxation of the initially prepared excited state caused by the predissociation process. A prototype study of this kind is that of I_2–He,[2] and a large number of systems have now been studied.[3] The information one can obtain includes the van der Waals binding energy (by observation of the predissociation threshold) and possibly the product states of the dissociation, observed by monitoring the fluorescence spectrum of the initially excited molecule which has now been vibrationally relaxed. The second type of experiment is direct excitation to vibrational states in the ground electronic state of one of the constituent molecules. Although these experiments are more attractive because one does not have to be concerned with influences of excited electronic states, they are technically more difficult. A number of such experiments have been done with available lasers,[4] often line tunable ones such as

[a] Present address: Dept. of Chemistry, Wesleyan University, Middletown, CT 06547.
[b] Contribution No. 7515.

 0021-9606/87/130115-13$02.10

CO_2, and they have been mostly concerned with measuring linewidths to determine the spectral broadening due to the presence of relatively fast predissociation processes. One advantage of this approach is that small molecules can be studied which is often not the case with the electronic state spectroscopy approach because the smaller molecules (unlike I_2) generally do not absorb in wavelength regions conveniently accessed by present day lasers (>200 nm). From doing either type of spectroscopy one can learn about the energetics of the predissociation process such as the reaction barrier height and product state distributions. One could also obtain the rates for the predissociation process if the relationship between linewidths and rates is well defined.

In general, linewidths and lifetimes are not related unless one knows with certainty that the line is homogeneously broadened and that no dephasing is involved.[5] In diatomics, the relationship is clear and has been confirmed experimentally.[6] In larger systems, contributions to the measured linewidths from inhomogeneous broadening, power saturation effects, and pure dephasing are difficult to ascertain, and care must be exercised in relating linewidths to dynamics.[7]

Several reports have appeared where time resolved fluorescence has been used to measure vdW molecule dissociation rates by monitoring fluorescence decay rates. Spectral and time resolution of the fluorescence on the picosecond time scale[8] allows one to obtain the rates of intramolecular vibrational redistribution (IVR) and vibrational predissociation (VP). When one measures the VP process directly in time the actual rate, and not the dephasing time of the initially prepared state, is obtained. The van der Waals systems studied by this technique are isoquinoline–water,[9] tetrazine–Ar,[10] dimethyl tetrazine dimer,[11] stilbene–He and –Ar,[12] and anthracene–Ar.[12] In these studies the stoichiometry of the complex is inferred spectroscopically. Only very recently, a high-resolution sub-Doppler method has been used to measure the stoichiometry of these large complexes.[12] The time resolution of these fluorescence experiments is ~100–40 ps.

In a recent communication,[13] we reported our results on the direct measurement of van der Waals molecule VP rates using picosecond pump–probe mass spectrometry. This technique uses two picosecond pulses, one to excite the vdW complex and the second, delayed in time, to ionize the excited complexes. The ions are identified by their mass in a time-of-flight spectrometer. The time resolution is a few picoseconds in this case, limited by the temporal width of the laser pulses. The system studied was phenol–benzene.

In this paper we give a full account of the study of the phenol–benzene complex (Ph–Bz) and extend it to the cresol–benzene (*p*-methylphenol–benzene) system; the binding energy of the complexes (Fig. 1) is ~4 kcal/mol. Substituting phenol with a methyl group allows us to control the density of states in the system without making substantial changes in the electronic structure. The results can then be compared in a relative sense which is particularly important for RRKM calculations. Furthermore, in both systems the excitation is to phenol type modes and this permits the study of energy redistribution from the phenol moiety to the reaction coordinate. The questions pertinent to the dynamics

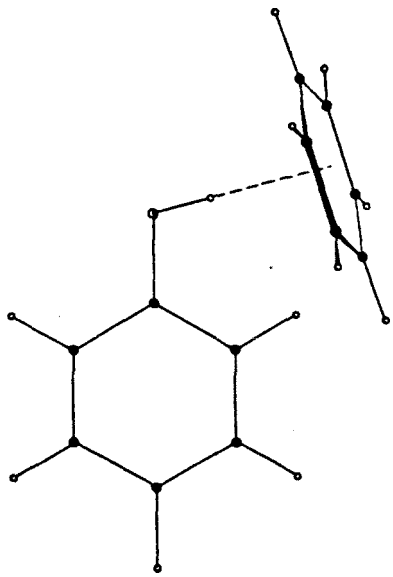

FIG. 1. Representation of the phenol–benzene van der Waals binding geometry. The interaction is π electron hydrogen bonding with the phenol "donating" a proton to the π cloud of benzene. This structure is supported by both thermodynamic and spectroscopic data and should be almost identical in the *p*-cresol–benzene system. The binding energy is estimated to be 1400 cm^{-1} (see the text).

are: (1) What is the extent of intramolecular vibrational redistribution prior to dissociation? (2) Are the dissociation rates dependent only on excess energy or are they mode specific? (3) Can the rates in these simple systems be predicted by statistical reaction rate theories?

The paper is outlined as follows. The experimental scheme is described in detail first (Sec. II). A brief survey of the decays (Sec. III A) is followed by excitation spectra of cresol and its complex with benzene (Sec. III B). Discussion of our interpretation of the observed transient behavior is presented next (Sec. III C), followed by discussion of the VP rates for each of the two systems in the last four subsections.

II. EXPERIMENTAL

A. General

The aim of the experiments is to measure the unimolecular dissociation rates of the Ph–Bz system when vibrational energy is deposited initially in the phenol moiety. The excitation of phenol is an electronic transition which allows a variety of vibrational states in the S_1 manifold to be accessed from which predissociation occurs on the excited electronic surface. To measure the unimolecular dissociation rates we use a picosecond pump–probe photoionization technique which is described as follows (Fig. 2). The Ph–Bz species is excited via the phenol $S_0 \rightarrow S_1$ transition with a UV picosecond laser pulse. A second, red-shifted, picosecond pulse then excites this species above its ionization threshold. The resulting product ions are mass analysed in a time of flight

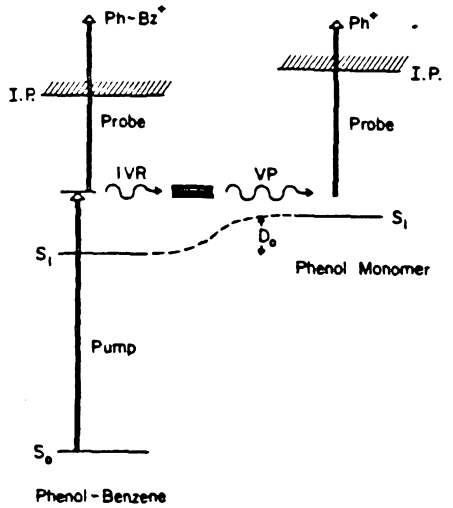

FIG. 2. Schematic energy level diagram of the phenol–benzene system showing the correlation from the bound system to free phenol along the reaction coordinate. The pump and probe scheme is shown. The case described here is that of IVR followed by VP. The second channel, not shown, is that of the initial state undergoing direct VP to products.

mass spectrometer. By monitoring the amount of parent ion formed ($[Ph\text{-}Bz]^+$) as a function of pump–probe pulse delay we can measure directly the vibrational predissociation rates because any dissociation which takes place in the neutral, between the pump and probe pulses, will be observed as a loss of signal in the parent ion mass channel. A discussion of possible alternative processes which may lead to similar observations will be presented below but they can be ruled out, leaving the observation of decay of the parent ion signal as being a measure of vibrational predissociation of the complex from the S_1 state of phenol. The dissociation rates can then be measured as a function of excess energy and vibrational state character by pumping a variety of vibrational states in phenol. The same experiments were also performed on cresol–benzene van der Waals molecules.

B. Laser system: Pump and probe

The pump–probe laser arrangement is described in the preceding papers I and II.[14] The picosecond system used in this work is different from that given in papers I and II. In the previous papers we used two separate dye-laser/amplifier units, starting with a mode-locked cw YAG laser. Here, a mode-locked Ar^+ laser and one dye-laser/amplifier system was used. The experimental apparatus with MPI detection has been described only briefly in several publications[15] so a more detailed description will be given here. To perform the ionization experiments outlined above, high peak power picosecond laser pulses are required with the necessity also of having pump and probe pulses in the UV but different wavelengths for greater sensitivity. This is accomplished using a pulse amplified picosecond laser system. The picosecond pulses originate in a mode locked argon ion laser which is synchronously pumping a dye laser. This dye laser produces a train of pulses at 82 MHz having pulse energies of $\lesssim 1$ nJ and pulse widths of from 2 to 5 ps depending on the frequency tuning element used. These pulses are propagated through a three-stage dye amplifier which is pumped by the second harmonic of a Q-switched Nd:YAG laser operating at 20 Hz (140 mJ/pulse at 532 nm). The Q switch of the YAG laser is synchronized to the mode-locking frequency synthesizer of the argon ion laser so that a 532 nm pulse and a picosecond pulse arrive at the dye amplifier simultaneously. The overall gain of this amplifier is approximately 1×10^6 yielding a pulse train of visible pulses at 20 Hz which are from 0.5–1.0 mJ/pulse. The temporal shape of the amplified pulses is very similar to that of the input pulses as long as the gain of the amplifier is not much greater than 1×10^6.

As mentioned above, two colors are necessary to perform the pump–probe experiment. In this case, Raman shifting in methane was used to produce a second color. It also serves another purpose and that is to allow the generation of wavelengths blue enough to excite the S_1 state of phenol. The tuning range of the synchronously pumped dye laser extends only to ~ 550 nm, the second harmonic of which, 275 nm, can only excite phenol to the S_1 origin. The anti-Stokes Raman line was used to extend this to higher energies. The output of the amplified dye laser was focused (1 m lens) into a 1 m long high-pressure Raman cell. The light, Raman orders, and fundamental, was recollimated with a 0.5 m lens. Normally to obtain the anti-Stokes shifted UV one would first generate the dye laser second harmonic then use Raman shifting. However, it was found that with these relatively low energy picosecond pulses the second harmonic could not be successfully anti-Stokes Raman shifted. Instead, the fundamental dye laser pulses were scattered in methane ($\Delta\nu = 2914\ cm^{-1}$) and the first anti-Stokes line was mixed with the fundamental in a KDP crystal immediately after the recollimating lens to obtain the desired UV wavelengths. Best conversion efficiency for mixing was obtained with the recollimating lens close to the output window of the Raman cell as the anti-Stokes radiation diverges, and good overlap with the fundamental is lost quickly as the beams propagate. This mixed frequency UV pulse was then separated from the remaining frequencies and propagated along a fixed optical delay and eventually used for one-photon resonant excitation of the phenol moiety. The remaining frequencies, fundamental, and Stokes-shifted radiation, could be used as the probe. In practice two frequencies were used as the probe: the second harmonic of the dye laser fundamental or the fundamental mixed with the Stokes-shifted light to yield a probe which was further to the red. The generated probe beam was directed to a variable optical delay line which was controlled by a stepper motor driven translation stage. The pump and probe pulses were then recombined on a dichroic mirror so they could be directed to the sample collinearly.

C. The molecular beam and experimental arrangement

The experiment was performed in a supersonic molecular beam which is required to form the van der Waals molecules and as a benefit the internal degrees of freedom in the vdW molecules are extensively cooled resulting in a well defined initial state. The beam apparatus consists of two cham-

bers each of which is pumped by a 6 in. diffusion pump. The first chamber contains a pulsed nozzle which operates at the laser repetition rate, 20 Hz. The nozzle was constructed in our laboratory[16] and can be heated substantially, > 250 °C, which is often required for nonvolatile compounds. Under typical operating conditions with 20 psi He behind the nozzle the pressure in this chamber rises to $\sim 2\times10^{-4}$ Torr. The central portion of the expansion passes through a skimmer, 1.3 mm diam, to the second chamber where the steady state pressure is typically 1×10^{-6} Torr when the valve is in operation.

The laser enters the second chamber perpendicular to the molecular beam and intersects it ~ 10 cm downstream of the nozzle. The intersection of the laser and molecular beam is in the acceleration region of a time of flight mass spectrometer which is similar in design to that of Wiley and McLaren.[17] The drift tube of the mass spectrometer is 3/4 of a meter and contains an ion multipler, EMI 9642/3B, to detect the ions which have been dispersed in time. The arrival of the ions can be recorded by a transient waveform digitizer, Lecroy TR8818, which is based in a CAMAC crate interfaced to an LSI 11/23 + minicomputer. The signal from a number of laser shots can be recorded and averaged in the computer to build up a mass spectrum. In cases where just one mass is to be observed, the output of the ion multiplier is input to a gated integrator/boxcar averager (EG&G 162/164), and the gate positioned to sample the mass peak of interest, with near unit mass resolution in the region of interest.

A pump–probe transient is obtained by sampling the signal in a particular mass channel as a function of the position of the stepper motor controlled optical delay line. This is recorded in a multichannel analyzer whose channel advance is enslaved to the stepper motor driver. The optical delay line can be repetitively scanned for signal averaging.

An experiment was performed in the following way. The wavelength of the transition was obtained from the literature and the laser tuned to this value using a monochromator. Then, using the pump beam alone, the resonance enhanced ionization was maximized to find the transition. The amount of ionization would be reduced to a barely observable level by introducing appropriate neutral density filters. At this point the probe was introduced and the spatial and temporal overlap adjusted to maximize the two laser signal. Enchancements of greater than 3:1 were usually easy to obtain (often > 10:1).

Samples were handled as follows. Phenol (Mallinckrodt AR) and cresol (Aldrich > 99%) both required heating (60 and 70 °C, respectively) to obtain sufficient densities in the beam so these were introduced into a sample chamber contained in the pulse valve whose temperature could be controlled. The benzene was held in an external vessel through which the He carrier gas flowed and was saturated with the vapor pressure of benzene. Reducing the number of larger clusters $(Ph–Bz)_n$, in the beam was of primary importance so the concentration of benzene was lowered as far as possible without losing all signal from the Ph–Bz species. This was done by maintaining the vessel containing benzene at − 45 °C, thereby reducing its vapor pressure to < 1 Torr. Ito and co-workers[18] have measured the phenol–benzene spectrum and observed that at benzene pressures of < 1 Torr there was almost no signal from the phenol–$(benzene)_2$ species or larger clusters.

III. RESULTS AND DISCUSSION

A. Picosecond transients

The transient behavior of phenol–benzene has been measured for nine vibrational bands. The observed decays

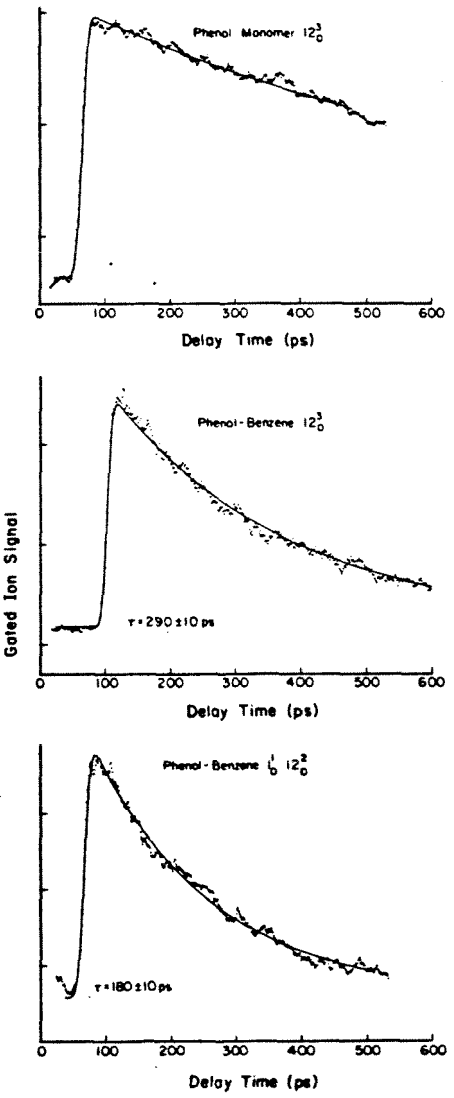

FIG. 3. Phenol–benzene mass-gated ion signal as a function of pump–probe delay time. In the top figure the phenol monomer 12_0^3 resonance (2345 cm^{-1} excess energy) is pumped and signal collected by gating at the monomer mass (m/e = 94). The lower two figures were obtained by pumping the phenol–benzene complex (2345 and 2500 cm^{-1}) and collecting signal at the complex mass (m/e = 172). A summary of the phenol–benzene data is given in Table I.

TABLE I. Phenol–benzene predissociation rates.

Mode	Energy[a] (cm^{-1})	Δ Energy[b] (cm^{-1})	Rate ($10^9 s^{-1}$)
12_0^2	1564	164	0.42
$1_0^1 12_0^1$[c]	1716	316	0.38
1_0^2[d]	1818	418	1.12
$7a_0^1 12_0^1$	2056	656	2.1
$1_0^1 7a_0^1$	2207	807	3.4
12_0^3	2345	945	3.3
$1_0^1 12_0^2$	2500	1100	5.7

[a] Energy above S_1 origin of phenol.
[b] Energy above the predissociation barrier.
[c] Alternative assignment $4_0^1 10b_0^1 12_0^1$.
[d] Alternative assignment $1_0^1 4_0^1 10b_0^1$.

(Fig. 3) were fit to a single exponential decay with a nonlinear least-squares routine based on the Marquardt algorithm (see paper I). In all cases, a single exponential fit the data (in the time range studied) quite well with little or no improvements being obtained with biexponential fitting. The results are summarized in Table I. As mentioned earlier, several wavelengths were used to probe the reaction but since no difference was observed this will not be referred to in the discussion. The monomer was measured at a number of different excess energies but its decay did not appear to depend sharply on excess energy. Since our accuracy in measuring these longer (ns) lifetimes is limited, these values cannot be usefully quantified but it was clear that they did not decrease significantly at higher energies and so the bare molecule contribution was negligible compared to the complex decay from predissociation.

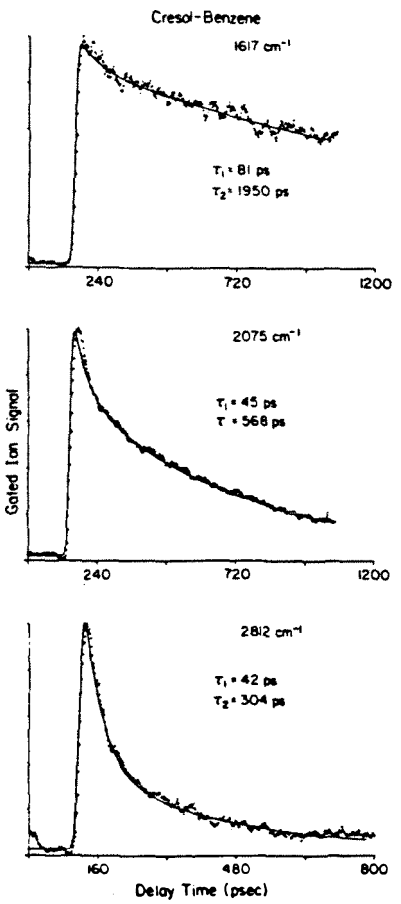

FIG. 4. Cresol–benzene mass-gated ion signal as a function of pump–probe delay time. The lower two transients are clearly biexponential and are representative of the transients obtained above approximately 1700 cm^{-1}. The data for cresol–benzene is summarized in Table II.

TABLE II. Cresol–benzene decay parameters.

Vibrational energy (cm^{-1})	Δ Energy[a] (cm^{-1})	τ_1 (ps)	τ_2 (ps)	Ratio[b]
1617	217	81	1950	0.15
2002	602	46	620	0.38
2075	675	45	568	0.37
2135	735	53	492	0.34
2190	790	46	561	0.48
2420	1020	35	358	0.51
2424	1024	38	266	0.44
2472	1072	34	229	0.44
2635	1235	63	534	0.7
2770	1370	80	690	0.74
2812	1412	42	304	0.70
3195	1795	18	160	0.60

[a] Energy above the predissociation barrier.
[b] Ratio of the fast component intensity to the total signal.

The particular complex transitions studied were chosen because the corresponding monomer bands are known to absorb strongly. The complex bands were found to be shifted $\sim 145\ cm^{-1}$ to the red of the monomer transitions at each of the excess energies studied, in agreement with the value reported by Ito *et al.*[18] for the origin. At low excess energies, distinct resonant enhancements of the complex signal were observed. At higher energies, where the transitions were somewhat weaker and there was considerable spectral congestion, the resonant enhancement was not as distinct. In these cases, the actual wavelength, as measured by a monochromator, was used to tune to the transitions. There were several points taken where the excitation was "off-resonance" meaning excitation into a region where no particularly strong assignable bands were present. No significant deviation was observed from the expected transient behavior for this off-resonant excitation. The highest energy band excited in phenol, 2500 cm^{-1} excess energy, was at the blue limit of the experimentally obtainable wavelengths.

In the cresol–benzene system, 14 vibrational band decays were measured. As can be seen in Fig. 4, at higher energies the transient behavior is no longer a simple exponential. These higher energy transients could be fit well to biexponential decay. In Table II, the data for cresol–benzene is presented with the measured single or biexponential decay constants. For the cases of biexponential decay the contribution of the fast decay component is listed as the ratio of the fast component to the total signal. Again for cresol, a number of measurements were made for the bare molecule at different

excess energies and no dramatic change in rate with excess energy was observed.

B. Structure and spectroscopy

The $\pi\pi^*$ absorption band at 2750 Å of phenol vapor has been analyzed[19] and complexes of phenol with various solvents have been studied previously.[18] Here, we briefly present our studies on the excitation spectrum of *p*-cresol and its complex with benzene.

1. Bare molecule excitation spectrum

The fluorescence excitation spectrum (275–285 nm) of *p*-cresol cooled in a supersonic jet is shown in Fig. 5. The strongest band in the spectrum (35 334 cm^{-1}) is assigned as the electronic origin of the $S_1 \leftarrow S_0$ transition. This corresponds to $\sim 1000\ cm^{-1}$ red shift of the origin as compared to phenol due to 4-methyl substitution and is consistent with shifts on methylation observed in other aromatic molecules.[20] Some of the other bands observed are assigned by comparison with phenol, and we use the notation of Bist *et al.*,[19] namely the same as for benzene. These results are in general agreement with previous analyses of the absorption spectra of the vapor.[21] The 421 cm^{-1} fundamental is a substituent sensitive ring mode ($6a_0^1$). The band at 372 cm^{-1} may be assigned as $16a_0^2$, by analogy with the corresponding band in phenol. It should be noted that the 217 cm^{-1} fundamental assigned by previous authors is not present in this excitation spectrum and should be assigned as a hot or sequence band. The bands having S_1 vibrational energy greater than 700 cm^{-1} reported here correspond to observed resonances closest to those reported by previous authors. These numbers were determined using the picosecond pump–probe apparatus described above. The wavelength obtained for each resonance was converted to absolute wave numbers without vacuum corrections and the value of the S_1 origin subtracted from it to get the relative energies. The assignments for these modes were derived from correlations of published data[21,22] for S_1 and S_0 fundamentals of cresol.

The origin region warrants a careful analysis. The 4-methyl group in toluene is believed to be essentially a free internal rotor.[23] The peaks at 5, 16, and 52 cm^{-1} are very similar to ones observed in the excitation spectrum of jet-cooled toluene and assigned to free internal rotation of the methyl group.[23] These bands derive their intensities from the coupling of internal rotation with overall rotation of the molecule and the band at $-5\ cm^{-1}$ is likely a hot band of this progression. Therefore, this set of bands is probably due to the progression arising from the rotation of the methyl group about the bond connecting it to the aromatic ring.

A low resolution emission spectrum of the vibrationless level of S_1 shows features that may be readily assigned as overtones and combinations of the strongly active 6*a*, 7, and 12 fundamentals.

2. Excitation spectrum of complex with benzene

The ability of aromatic (and olefinic) compounds to form hydrogen bonds with proton donors has been recognized for some time.[24] The spectroscopic studies of Ito and co-workers[18] on 1:1 complexes of phenol with various solvents show a correlation of the shift of the electronic origin and the intermolecular stretching frequencies with thermodynamic data on H-bond strengths. On the basis of comparative evidence, they proposed the structure for the phenol–benzene complex shown in Fig. 1. In this model, OH function points toward the center of the benzene (solvent) ring. Similar data are not available for cresol, but the spectral red shift of the origin and intensity distribution about it are both very similar to the phenol–benzene complex. Since the methyl group is substituted in the *para* position, steric effects are not of importance, and the structure of the complex of benzene with cresol is expected to be the same as with phenol.

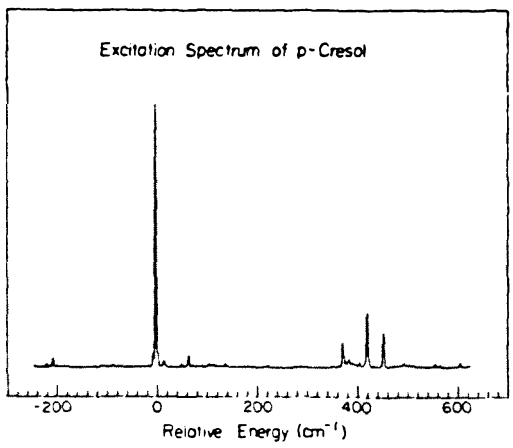

FIG. 5. Fluorescence excitation spectrum of *p*-cresol in a pulsed supersonic jet. The energy scale is referenced to the origin of S_1 in *p*-cresol, 35 334 cm^{-1}.

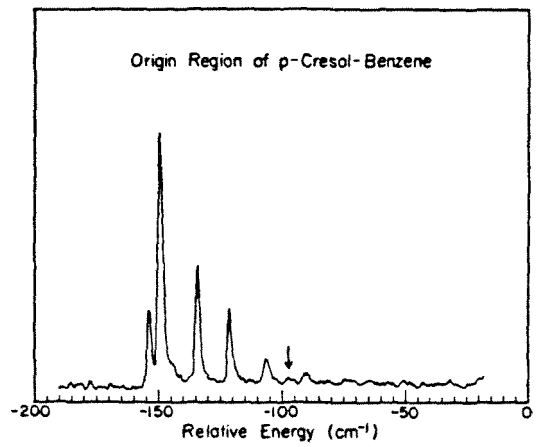

FIG. 6. Fluorescence excitation spectrum of the cresol–benzene van der Waals complex. The energy scale is referenced to the origin of the cresol monomer, 35 334 cm^{-1}. The origin of the complex is ascribed to the largest feature at $-147\ cm^{-1}$. The structure to the blue of the complex origin corresponds to excitation of the intermolecular modes. The arrow marks a feature at $-50\ cm^{-1}$, which is probably the fundamental of the intermolecular stretch.

The excitation spectrum of cresol expanded in Ne saturated with benzene at -15 °C was obtained in the same range as for the bare molecule. Prominent bands showing well-resolved progressions appearing at 35 187 and 35 612 cm^{-1} are assigned to the origin and the $6a_0^1$ transitions of the 1:1 complex respectively. The origin region is shown in greater detail in Fig. 6. The most intense band in this progression is the 0–0 transition shifted 147 cm^{-1} to the red of the origin of free cresol. The set of bands (0, 15, 28, 43, 59) cm^{-1} is tentatively assigned as the progression of an intermolecular bending mode, consistent with a similar progression in the phenol complex. The length of the progression implies a large change in geometry on excitation. Bist *et al.*[19] have shown that the rotational constants of phenol in S_1 are consistent with an increase in the COH bond angle. If this is also true in the case of cresol and complexation with benzene does not affect the equilibrium geometries of the two moieties, a long progression in the "in-plane" intermolecular mode supports the assignment above.

3. Rotational profiles of origin transitions

A high resolution scan of the origin region of cresol shows *P* and *R* branches only. As in phenol, the electronic transition moment is directed along the short in-plane axis, which is also the axis of intermediate moment of inertia of the molecule. Thus the transition is a *B*-type band. A simulation of the rotational profile[25] using structural parameters of phenol for the molecular frame[18] and those of toluene[23] for the methyl rotor agrees well with the measured contour. This comparison is only approximate as the calculations were performed for a rigid molecule of C_{2v} symmetry and the free internal rotation of the methyl group is expected to affect the finer features of the calculations.[26] A similar study of the origin transition of the 1:1 complex shows unresolved *P*, *Q*, and *R* branches. Using the model structure proposed by Ito *et al.*[18] and approximating the H-bond length as the sum[24] of the O–H bond and the half-thickness of the aromatic π-system[27] (crude estimate of the effective van der Waals' radius of benzene), one calculates the principle moments of inertia to be 301(298), 1285(1465), and 1406(1582) amu·Å^2.[28] The numbers in parenthesis are the values for the excited state of the complex. The *a* and *b* principle axes are inclined at $\sim -28°$ to the *y* and *z* axes in the plane of the ring of cresol and the *c* axis is perpendicular to the ring. Thus the excitation in cresol–benzene corresponds to a hybrid band of *A* and *B* types. A simulation of the rotational profile of the complex using these parameters is in qualitative agreement with the measured contour.

The intensity of the band slightly red of the complex origin (-4.5 cm^{-1}) is insensitive to expansion conditions (varying backing pressure from 5–30 psi in different carrier gases) which would suggest that it is not a hot or sequence band. It is possible that this band belongs to the well-developed progression in the bending mode; uneven level spacings have been reported in other molecules with hindered rotors.[20] Abe *et al.*[18] have concluded that a similar pair of closely spaced levels in phenol–benzene are derived from two different conformations. A similar explanation could also be true for the case at hand.

4. Bond dissociation energies

Estimates of the H-bond enthalpy of the phenol complex in the ground state vary from 1.56 to 4.1 kcal/mol. Adiabatic dissociation energies correspond to bond enthalpy at absolute zero and may be derived from enthalpies measured at higher temperatures.[30(a)] The spectral red shift of the S_1 electronic origin implies that the excited state complex is more tightly bound (145 cm^{-1}) than the ground state complex. The reported range of values for the bond enthalpy translates to 875 to 1760 cm^{-1} for the bond dissociation energy in the excited state. Assuming that the transition state involved in the reaction is fairly loose, contribution of tunneling to dissociation rates is negligible. Our experiments therefore show that the energetic threshold to dissociation lies between 1250 and 1550 cm^{-1}, which is well within the range quoted in the literature. In all discussions below, we choose 1400 cm^{-1} as the van der Waals' bond energy for Ph–Bz.

No measured values of the bond enthalpy for cresol–benzene are available, but estimates may be derived from comparisons of systems involving phenol or cresol with a common solvent. The free energies of complexation of phenol and cresol with benzene differ by ~ 0.05 kcal/mol (~ 20 cm^{-1}).[30(b)] Assuming the entropy change is the same in each case, the H-bond energies of the two compounds should account for the difference in free energies. The dissociation energy of the cresol–benzene complex is therefore chosen to be the same as that of Ph–Bz, i.e., ~ 1400 cm^{-1}. This choice is also supported by the spectral red shift in the cresol complex, 147 cm^{-1}, provided the correlation with bond energies is valid.

C. Ionization and electronic state dynamics

The question of how the observed decays are ascribed to vibrational predissociation from the S_1 state of phenol is addressed first. Typical transient ion signals are shown in Fig. 3. In the lower transient the initial excitation is 2500 cm^{-1} above the phenol origin, which should be safely above the predissociation barrier estimated to be approximately 1400 cm^{-1}. In this figure, the ion signal of the mass corresponding to phenol–benzene is plotted as a function of pump–probe delay time. At the same excess energy the phenol monomer lifetime is considerably longer, ~ 2 ns, indicating that the fast decay is associated with dynamics which occur only in the complex. The approximately 2 ns decay is the excited electronic state lifetime. The most straightforward interpretation is that the complex is predissociating in the neutral molecule causing a loss of signal from the Ph–Bz complex mass channel. A conclusive check of this would be the observation of a corresponding rise in intensity in the phenol monomer mass channel as the reaction proceeds because the dissociated phenol fragment remains electronically excited and should absorb the probe to give monomer ions. Unfortunately this was not possible because a large background of monomer ions was found to be always present. It comes from two sources. First, the absorption by phenol monomer molecules at the wavelength where the complex absorbs. Even though the resonance favors the complex there is a much greater concentration of monomers and particularly at higher ener-

gies there are always small absorption features present even in the cold supersonic beam. Second, there is contribution to the monomer ion channel from fragmentation of the complex ions. $[Ph\text{-}Bz]^+ \rightarrow Ph^+ + Bz$. This occurs because the probe excites the complex 7285 cm^{-1} above the ionization threshold,[31] certainly exceeding the complex ion binding energy. The ionization process results in a distribution of ion vibrational states determined by Franck–Condon factors (as would be observed in the photoelectron spectrum) leaving some complex ions above the dissociation barrier and others below it. This determines the fraction of complex ions which dissociate and it appears from our observations that a substantial amount do fragment. It should be emphasized that these dissociation processes cannot contribute to the observed dynamic behavior because ionization occurs after the absorption of two photons and thus any post ionization events are independent of pump–probe delay time.

There are several alternative explanations of the observed decay which have been considered and can be shown to be improbable. One possibility is that the observed decay is due to intramolecular vibrational energy redistribution of the initially prepared well defined vibrational state. It might be argued that the initially prepared state has a larger cross section for ionization than the redistributed states thereby leading to a decrease in the ionization signal as population goes into the redistributed states.[15(a)] One simple argument against this is that uncomplexed phenol does not exhibit this type of behavior even at the maximum excess energy studied, 2500 cm^{-1}. Of course it is possible that the presence of the van der Waals bond could induce IVR at a lower excess energy. One must then consider the specifics of what the cross section for ionization should be for one vibrational state vs another. The ionization cross section is the product of the electronic transition moment between S_1 and the ion ground state, the vibrational Franck–Condon factors and an electron continuum function. The effect of the Franck–Condon factors may give rise to a difference in cross section from one S_1 vibrational state to another, which will depend on the probe photon wavelength. If one probes near the ion threshold only some vibrational states of the ion will be accessible and these will determine the Franck–Condon factors. On the other hand, when one excites substantially above the ionization threshold all the ion vibrational states become accessible. In this case, the ionization cross section becomes the same for all vibrational states because the integrated F–C factors from any one vibrational state to all other states in another electronic manifold are equal. So when one is exciting sufficiently above the ionization threshold the behavior can be compared to that of a fluorescence spectrum in this regard. In the experiments on phenol and cresol several probe wavelengths were used to investigate the effect, if any, of the probe photon energy on the transient behavior of the complexes. The redder probe excited to approximately 4370 cm^{-1} above the threshold while the blue probe was 7285 cm^{-1} above it, certainly well beyond the point at which there might be increasing intensity due to F–C overlap with highly excited ion vibrational states. Transients obtained using either probe wavelength showed identical behavior suggesting that the decay in the ionization signal was not due to vibrational redistribution in the neutral molecule.

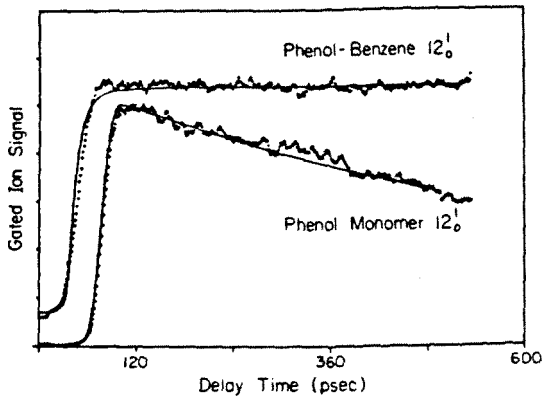

FIG. 7. Comparison of the transient behavior of the phenol monomer to that of the phenol–benzene complex when pumping the 12_0^1 transition (782 cm^{-1}). The population is monitored by ionizing the intermediate state with a probe pulse and measuring the mass-gated ion signal, $m/e = 94$ for phenol and $m/e = 172$ for the complex.

Another possible explanation for the observation of decay in the phenol–benzene complex is that some nonradiative electronic decay is induced by the presence of the van der Waals partner. Quantum yield and absorption measurements of phenol in solution[32] showed that in cyclohexane the S_1 state of phenol has a fluorescence lifetime of ~ 2 ns and a quantum yield of 0.08, whereas in methanol the lifetime is lengthened considerably to 7 ns with a quantum yield of 0.22. This should be compared to our measurements of the lifetime of phenol and phenol–benzene complexes near the origin of S_1 where no vibrational predissociation occurs. As can be seen in Fig. 7, the phenol monomer has a lifetime of 1 to 2 ns (the picosecond system is set up for measurement of short time intervals and cannot accurately measure lifetimes greater than 1 ns) while the complex is showing essentially no decay on our time scale and must have a lifetime > 5 ns. There is some mechanism, electronic or vibrational,[33] which is reducing the nonradiative decay in the complex. These observations are consistent with earlier work on hydrogen bonding of water and alcohol with isoquinoline.[9] This suggests that the interactions observed in the isolated van der Waals species are similar to those present in solution, supporting the idea presented above that the structure of phenol–benzene is a π hydrogen bonding interaction. The point is that the formation of the van der Waals bond actually inhibits nonradiative decay and it is unlikely that this changes dramatically with excess energy to the point where nonradiative decay is much faster than in the monomer.

Further evidence that vibrational predissociation is being measured comes from the observation of rates vs excess vibrational energy. First, the onset of measurable decay in the phenol–benzene complex is between 1275 cm^{-1}, where no decay is observed, and 1564 cm^{-1} which is the first complex band to decay appreciably. The observed threshold behavior agrees with the thermodynamic data, as discussed above. Second, the trend of the rates is also consistent with a

predissociation process. RRKM calculations presented below show the same trend as the measured dissociation rates of the phenol–benzene system. To summarize, there is substantial evidence that vibrational predissociation is being directly measured in the phenol–benzene system and by analogy in cresol–benzene as well.

D. Phenol–benzene predissociation

The single exponential decay constants observed for the phenol–benzene species are listed in Table I and plotted as a function of excess vibrational energy in Fig. 8. As discussed above, the decay mechanism has been ascribed to vibrational predissociation so the excess energy scale is relative to the reaction threshold. From examining Fig. 8, one can see that the rates are following a consistent trend—increasing predissociation rate as a function of excess energy. This is to be expected if the reaction is statistical, i.e., the initially deposited energy is completely randomized prior to reaction. The question now is are there any mode specific effects which would show unexpected behavior in the trend of the rates. Data points showing marked deviation from the trend or an irregular distribution of rates with no clear excess energy dependence would imply that the dynamics include nonstatistical effects. There are several data points which do not follow the trend exactly, in particular the decay at 1818 cm^{-1} (i.e., 418 cm^{-1} above threshold), which is decidedly biexponential, but these are fairly small deviations and given the confidence limits one has to conclude that there are no obvious mode specific effects. Subtle effects may be present but cannot be asserted with the present data set. The question now is: What is the degree of statistical behavior among modes in the complete vibrational phase space?

Since phenol–benzene must dissociate following energy redistribution, we chose to model the rates using standard routines[34] based on RRKM theory. A PST calculation (see papers I and II) is perhaps more appropriate since we expect the TS to be fairly loose, but we do not attempt it here. The purpose of these calculations is to see if the order of magnitude of the observed rates can be reproduced and if the trend is as expected. In order to do a meaningful calculation, all the vibrational frequencies in the molecule must be known as well as the frequencies of the transition state. In a system the size of phenol–benzene this is obviously difficult particularly because the intermolecular modes, van der Waals bond stretch, four bends and a free or hindered rotation, are difficult to determine accurately. Fortunately, two of the intermolecular modes, the vdW stretch and one of the bends, have been observed spectroscopically for phenol–benzene, 50 and 20 cm^{-1}, leaving only four others to be estimated. The modes for phenol have been determined almost completely and so are not a problem. As alluded to in the introduction, the constituent molecules of the complex are not highly excited by the energy deposited to break the van der Waals bond and thus anharmonic corrections for these modes are relatively unimportant and were not included in the calculation. We assume that in the transition state, the vibrational frequencies of the constituent molecules change very little because the breaking of the weak van der Waals bond is only a small perturbation. However, our poor knowledge of the intermolecular modes means that a rigorous calculation is not possible. As a first attempt a standard RRKM calculation was performed in which the frequencies of the transition state were chosen to be the same as in the reactant molecule. Reasonable values were chosen for the intermolecular modes and the calculation (for adiabatic rotations, i.e., counting vibrational density of states only) performed without adjusting any of the parameters to fit the data. This should give an estimate of the reaction rates and their excess energy dependence without a bias from adjusting parameters. One point which needs to be addressed is whether or not the benzene vibrational modes play a role in the dynamics, i.e., does vibrational energy transfer across the weak vdW bond to the benzene in the IVR process. It seems rather unlikely that the energy necessary to excite the relatively high frequency modes of the benzene moiety would transfer efficiently across the weak vdW bond, but as a check the calculation was done with and without these modes. The results of the calculations are shown in Fig. 8 where RRKM rates are plotted with experimental results for phenol–benzene. A much better fit of the data is obtained if the transition state is made somewhat loose by decreasing the frequencies of the intermolecular modes by 20%. A loose transition state is certainly expected in this case as there should be no appreciable barrier to dissociation in the long range attractive van der Waals' potential. The important point is that the trend in the experimental rates can be reproduced by the

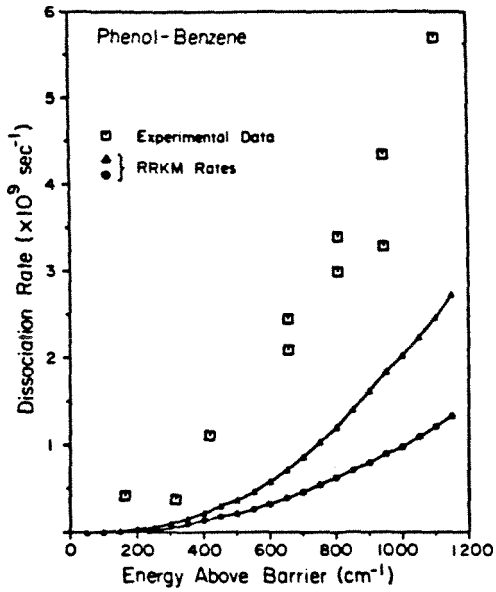

FIG. 8. Plot of the vibrational predissociation rates of the phenol–benzene van der Waals molecule as a function of excess energy above the dissociation threshold, 1400 cm^{-1}. The squares are the rates from a single exponential fit of the experimentally measured decay curves. The plotted data includes results from our earlier work (Ref. 13) as well as more recent results. The triangles are the rates obtained using standard RRKM calculations on the phenol–benzene system with the exclusion, however, of the benzene vibrational frequencies. The circles are the same calculation including the benzene modes. See the text for details of the calculations.

calculation, which implies fast energy redistribution. However, energy redistribution is not necessarily complete and this may account for deviations (observed rates faster than calculated ones). Since the energy is being deposited selectively through optically active transitions, IVR must be occuring on a time scale fast compared to the predissociation process but to a subset of states in the vibrational phase space. Unfortunately the calculations are not accurate enough e.g., to determine if the benzene modes are involved except to show that in the standard RRKM calculation inclusion of these modes gives results that are even further from the experimental results than without them.

The phenol–benzene system can now be used as a point of reference for comparison to the behavior of substituted phenol–benzene vdW molecules. The idea is that although the RRKM calculations might be subject to problems in calculating the absolute rates and the degree of statistical behavior they should be quite accurate for relative rates between similar systems particularly where the unknown quantities, vdW mode frequencies, are the same in each system. The system used for comparison is cresol–benzene, where a methyl group is "added" to the phenol–benzene complex.

E. Cresol–benzene predissociation

In the cresol–benzene system, some evidence of decay is seen below the barrier that was chosen (*vide supra*) which is probably due to fluorescence from the complex (ns). The decays at ~ 1200 cm^{-1} are dominantly single exponential with some hint of a faster process. At low energies, the fast component is only a small fraction of the total signal. Limited signal-to-noise and fluctuations during signal averaging makes it difficult to make any strong assertions at these energies. As the excess energy above the barrier is increased, a biexponential fit of the transient becomes signficantly better than a single exponential one and the fast component of the decay becomes a larger fraction of the total signal. (In fact the ratio of the fast component to the total signal, Table II, is one of the most predictable variables of the excess energy; it increases systematically with almost no deviations).

The lifetime of the fast component does not show a regular trend with excess energy but instead appears to fluctuate. The long component of the decay shows a more regular trend—decreasing lifetime with increasing excess energy but these values also fluctuate at higher energies. The origin of this biexponential behavior as compared to the apparently simple behavior of phenol is addressed below.

There is spectroscopic evidence of at least two different conformations of the Ph–Bz[18] complex which raises the possibility that for cresol–benzene two conformations, with different decay rates, are responsible for the biexponential behavior. If there are two types of binding sites for the benzene, each with its own barrier, the observed signal will be the sum of two individual ensembles of complexes. In order to account for the observed behavior, one has to assume that the complexes which give rise to the fast component have a much lower barrier and are not formed with phenol. A number of observations argue strongly against this as the source of the measured biexponentials. First, the fast component does not appear until 1617 cm^{-1} which is the opposite of what would be expected for a complex with a lower barrier. Secondly, the fast component does not show an excess energy dependence that would be indicative of a simple additional contribution from a separate ensemble of complexes. Finally, there does not seem to be a change in the ratio of the fast to slow components by tuning on and off known complex resonances which should favor one ensemble of complexes over another.

Next we consider the behavior of a complex with one well defined structure. The appearance of more complicated decay behavior is then indicative of several competing processes which contribute to the experimental observations. These might be processes such as intramolecular vibrational redistribution or interelectronic nonradiative decay which do not directly involve dissociation but can lead to a loss of observed signal due to decreased ionization probabilities from the redistributed (dark) states. This point was addressed in some detail above in ascribing any decay to dissociation and the arguments against these mechanisms are just as valid for cresol–benzene dissociation. One cannot rule out the possibility that these processes are occurring, especially since in the case of phenol–benzene there is at least some IVR prior to dissociation. If this redistribution process is very fast compared to dissociation then no evidence for it will be observed in the transient decay (as in the Ph–Bz case). Energy redistribution processes occuring on timescales comparable to the dissociation rate can show multiexponential decay behavior if the initial and redistributed states have different dissociation rates. This situation would exclude the use of simple statistical models which require total redistribution to be fast compared to any dissociation process. The data for cresol–benzene is indeed biexponential, and in the model presented below we discuss our results taking into account energy redistribution prior to vibrational predissociation. Certainly other, more complicated, models can be introduced but the point here is to show how these competing processes can lead to the observation of biexponential decays. The possible nature of state distributions before and after this redistribution process will then be discussed.

F. Energy redistribution and vibrational predissociation

The model which we have used (see also papers I and II) to describe the cresol–benzene decay is as follows. The pump pulse initially prepares a state(s), $\{|s\rangle_i\}$, which has two nonradiative channels open to it. One of the channels is vibrational predissociation which results in a decrease in the experimentally observed signal. The second channel is energy redistribution to isoenergetic states of the complex, denoted by $\{|l\rangle_i\}$. The states $\{|l\rangle_i\}$ also have a vibrational predissociation channel open. The kinetic scheme is

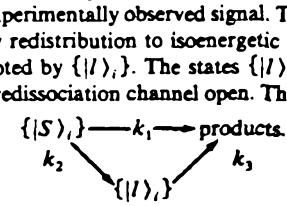

The validity of a kinetic model for describing dissociation has been considered in paper I, and here we ignore coherence effects and reversible processes for reasons discussed earlier

in papers I and II. The concept of dividing the phase space to account for biexponential decay kinetics follows from previously described models of IVR[15(a)] and non-RRKM behavior.[35]

As was mentioned before, we expect that vibrationally redistributed states, $\{|l\rangle_i\}$, have the same cross section for ionization as the initial states, $\{|s\rangle_i\}$ (because of the energetics of the experiments), and thus the observed signal will not reflect the population in $\{|s\rangle_i\}$ but will rather give the sum of population in $\{|s\rangle_i\}$ and $\{|l\rangle_i\}$. Therefore, to model the experimental observable kinetic equations are solved for the quantity $[\{|s\rangle_i\} + \{|l\rangle_i\}]$, which yields

$$[\{|s\rangle_i\} + \{|l\rangle_i\}] = \frac{I_0}{k_1 + k_2 - k_3}\left[(k_1 - k_3)e^{-(k_1+k_2)t} + k_2 e^{-k_3 t}\right].$$

The experimental measurements on cresol–benzene dissociation at higher energy can be fit with a biexponential decay which yields three unique parameters. The time-dependent signal, $I(t)$, is given by

$$I(t) = Ae^{-\alpha t} + Be^{-\beta t},$$

where the fast component decay rate is α, the slow component decay rate is β, and the ratio of the fast component to the total signal, $F_A = A/(A+B)$. These experimentally observed quantities can be related to the kinetic model parameters as follows:

$$k_1 = F_A(\alpha - \beta) + \beta,$$
$$k_2 = \alpha - k_1 = (\alpha - \beta)(1 - F_A),$$
$$k_3 = \beta.$$

Thus, within the limits of this model one can identify the predissociation rates from the initial states k_1, the redistribution rate to $\{|l\rangle_i\}$, k_2, and the predissociation rate from the $\{|l\rangle_i\}$ states k_3. The physical rationale behind this model can now be investigated to see if the results obtained appear reasonable. First, the nature of the initial states, $\{|s\rangle_i\}$ must be addressed. By analogy to phenol–benzene one would expect there to be a redistribution process which is fast compared to dissociation. Therefore it is likely that the initial state in the kinetic model $\{|s\rangle_i\}$ is not the optically prepared state but some set of states formed by an initial rapid (much faster than dissociation) redistribution. Competing with predissociation (k_1) would be redistribution to available bath states of the complex $\{|l\rangle_i\}$ with a rate constant k_2. These redistributed states dissociate more slowly, k_3, in this model (see below).

The exact nature of the division of the vibrational phase space is difficult to ascertain. Here, we consider two cases. First, we consider case (a), where k_1 is the dissociation rate from the initial, partially randomized, set of states, k_2 is the slower redistribution rate which populates the entire phase space, and k_3 is the predissociation rate from this distribution. As can be seen from Table III the values for k_1 and k_2 vary considerably and do not show a regular trend. This is understandable if one examines the expressions for k_1 and k_2. They depend on all three experimental parameters, α, β, and F_A, in a complicated way and the experimental uncertainties are compounded. The predissociation rate k_3 is directly measured experimentally as β, the long-component of the biexponential decay and should, therefore, be a more reliable figure. Accordingly, k_3 is the decay rate from the "equilibrated" phase space of the cresol–benzene, $\{|l\rangle_i\}$, which is consistent with the predictions of the models in Refs. 15(a) and 35. If this is the case, then the RRKM calculations should yield k_3. As mentioned earlier, we can use the relative RRKM calculations obtained to fit the phenol–benzene complex decay and modify it by just including the additional methyl vibrational modes. The barrier and other modes, including those of the transition state, are assumed to be the same. The results of this calculation are plotted in Fig. 9 along with the experimentally obtained values of k_3. Although the calculations do seem to give the average trend, there is definite deviations in the experimental data around the RRKM curve. In case (b), we consider the $\{|l\rangle_i\}$ states to represent bath modes of the methyl group. Accordingly, k_3 is the predissociation rate from the bath states and again they should be slower than $k_1 + k_2$. The biexponential behavior in cresol–benzene is therefore reflecting phenol–benzene behavior in addition to predissociation from physically remote methyl bath modes. More experiments involving partial deuteration and longer alkyl chains (or other substituents) would be of extreme interest to learn about the nature of vibrational energy redistribution in these prototype systems.

TABLE III. Cresol–benzene kinetic model rates.

Vibrational energy (cm^{-1})	Δ Energy[a] (cm^{-1})	$k_1 \times 10^9$ (s^{-1})	$k_2 \times 10^9$ (s^{-1})	$k_3 \times 10^9$ (s^{-1})
1617	217	2.3	10.1	0.5
2002	602	9.3	12.5	1.6
2075	675	9.3	12.9	1.8
2135	735	7.8	11.1	2.0
2190	790	11.4	10.4	1.8
2420	1020	15.9	12.6	2.8
2424	1024	13.7	12.6	2.8
2472	1072	15.4	14.0	4.4
2635	1235	11.7	4.2	1.9
2770	1370	9.6	2.9	1.5
2812	1412	17.6	6.2	3.3
3195	1795	11.4	10.4	1.8

[a] Energy above the predissociation barrier.

G. Homogeneous linewidth and VP rates

As mentioned in papers I and II, in large molecular systems one must be careful in relating the apparent linewidth to IVR and VP dynamics. The present study indicates that the contribution of VP/IVR rates to the homogeneous linewidth is 0.01 to 0.1 cm^{-1}, (the apparent rotational contour is, of course, much larger than this value) above the barrier to dissociation. Below the barrier, the width is less, being ~ 0.005 cm^{-1}. It would be interesting to perform high-resolution contour analysis on these systems below and above the barrier and compare with time-resolved data reported here.

The biexponential behavior reported here is different

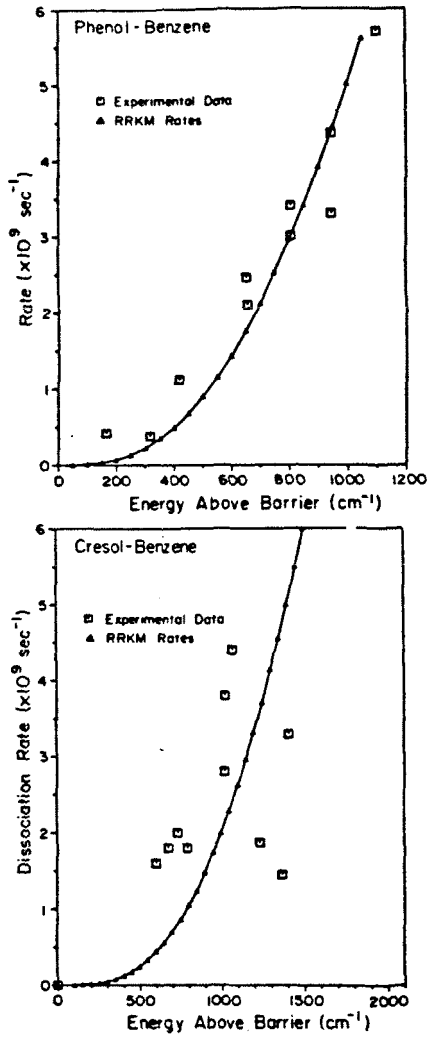

FIG. 9. Comparison of experimental rates to adjusted RRKM rates. The upper half shows the observed rates and calculations for the phenol–benzene complex, while the lower one shows the same for the complex of cresol. Calculated rates are for a transition state with frequencies 20% smaller than in the reactant and are plotted as a solid line. The fundamental frequencies for cresol were chosen to be the same as the corresponding ones in phenol, augmented by those for a methyl substituent. See the text for further details.

from that observed in gaseous benzene in the channel 3 region. As discussed elsewhere,[7,36] thermal congestion can lead to inhomogeneous superposition of transitions and to biexponential decay. In our case, the system is cooled by supersonic-beam expansion and inhomogeneous vibrational excitations are essentially eliminated. Inhomogeneous rotational excitation could, however, be significant. If there were a strong rotational dependence for VP, nonexponential decays would be observed even in a beam experiment.

A final comment regarding VP rates is now made. Throughout the paper we compared our experimental results with RRKM rates. In the literature,[37] the classical RRK expression was used to describe VP of van der Waals molecules. The argument applied to the system *n*-octylbenzene–Ar was as follows. Using the classical RRK expression

$$k = A\left(1 - \frac{E_0}{E}\right)^{s-1}$$

the prefactor A was estimated to be $\sim 10^{13}\,s^{-1}$ and $s = 24$ to obtain $k \approx 0.1\,s^{-1}$—ten orders of magnitude slower than the inferred experimental rate. The author used this large disparity to claim deviation from statistical behavior. However, as discussed in this paper, the RRKM theory (semiclassical) is more appropriate for comparing with experiment than the classical RRK theory.

IV. CONCLUSIONS

This paper, the third in the series, presents picosecond time-resolved fragmentation of van der Waals clusters. Using a picosecond pump–probe mass-spectrometry technique, we have measured the dissociation rates for the weakly bound beam-cooled systems phenol–benzene and cresol–benzene. Excitation was to specific vibrational states in the S_1 state of phenol (cresol) and dissociation proceeds on this electronic surface.

The main findings are:

(a) for the case of phenol–benzene the rates of dissociation increased smoothly with increasing excess energy. The trends could be modeled using simple RRKM calculations although restricted IVR is also included.

(b) The cresol–benzene system showed markedly different behavior, exhibiting *biexponential* decays as the energy is increased above reaction threshold. This we describe using a model for partitioning phase space, with each part exhibiting its own dissociation rate. At least partial energy redistribution occurs prior to vibrational predissociation.

(c) The binding energy of benzene to phenol is ~ 1400 cm^{-1}, as measured from rates vs excess energy, and dissociation contributes at most 0.1 cm^{-1} to homogeneous broadening above threshold.

Picosecond photofragment spectroscopy using photoionization mass spectrometry or LIF techniques should be general for studying a large number of dissociation reactions, including other van der Waals clusters. Our current apparatus (see papers I and II) offers independent tunability for both pulses, and this provides additional sensitivity for probing the dynamics of recoil as a function of energy in the reagent or fragments.

Note added in proof: Using fluorescence detection, mode-selective (non-RRKM) behavior have been observed recently for the vdW system stilbene–He. For more details see: D. Semmes, J. S. Baskin, and A. H. Zewail, J. Am. Chem. Soc. (in press).

ACKNOWLEDGMENT

This work was supported by a grant from the National Science Foundation (DMR 85-21191).

[1](a) For reviews see: D. H. Levy, in *Photoselective Chemistry*, edited by J. Jortner, R. D. Levine, and S. A. Rice (Wiley, New York, 1981), part 1, p.

323. (b) J. A. Beswick and J. Jortner, Ref. 1, p. 363. (c) K. C. Janda, Adv. Chem. Phys. 60, 201 (1985).

[2]R. E. Smalley, D. H. Levy, and L. Wharton, J. Chem. Phys. 64, 3266 (1976).

[3]See, e.g., (a) D. V. Brumbaugh, J. E. Kenny, and D. H. Levy, J. Chem. Phys. 78, 3415 (1983). (b) C. A. Hayman, D. V. Brumbaugh, and D. H. Levy, J. Chem. Phys. 81, 2282 (1984). (c) T. A. Stephenson and S. A. Rice, *ibid.* 81, 1083 (1984). (d) N. Halberstadt and B. Soep, Chem. Phys. Lett. 87, 109 (1982). (e) A. Amirav, U. Even, and J. Jortner, J. Chem. Phys. 25, 2489 (1981). (f) J. Wanna and E. R. Bernstein, *ibid.* 84, 927, 1981; K. S. Law and E. R. Bernstein, *ibid.* 82, 2856 (1985), and references therein.

[4]See, e.g. (a) A. Mitchell, M. J. McAuliffe, C. F. Giese, and W. R. Gentry, J. Chem. Phys. 83, 4271 (1985). (b) M. P. Casassa, D. S. Bomse, and K. C. Janda, *ibid.* 74, 5044 (1981). (c) G. T. Fraser, D. D. Nelson, A. Charo, and W. Klemperer, *ibid.* 82, 2535 (1985). (d) A. S. Pines and W. J. Lafferty, *ibid.* 78, 2154 (1984). (e) T. E. Gough, R. E. Miller, and G. Scoles, *ibid.* 69, 1588 (1985). (f) D. S. King and J. C. Stephenson, *ibid.* 82, 5286 (1985). (g) For a recent review, see R. E. Miller, J. Phys. Chem. 90, 3301 (1986).

[5]A. H. Zewail, Acct. Chem. Res. 13, 360 (1980).

[6]See, e.g., M. J. Burns, W. K. Liu, and A. H. Zewail, in *Spectroscopy and Excitation Dynamics of Condensed Molecular Systems*, edited by V. M. Agranovish and R. M. Hochstrasser (North-Holland, New York, 1983), Vol. 4.

[7]A. H. Zewail, Ber. Bunsenges. Phys. Chem. 89, 264 (1985); R. Gentry, in *NATO Advanced Research Workshop*, edited by A. Weber (Reidel, Dordrecht, 1987).

[8]P. M. Felker and A. H. Zewail, in *Applications of Picosecond Spectroscopy to Chemistry*, edited by K. B. Eisenthal (Reidel, Dordrecht, 1983), and references therein.

[9]P. M. Felker and A. H. Zewail, Chem. Phys. Lett. 94, 454 (1983); J. Chem. Phys. 78, 5266 (1983).

[10](a) J. F. Ramaekers, J. Langelaar, and R. P. H. Rettschnick, in *Proceeding of the Third International Conference on Picosecond Phenomena* (Springer, Berlin, 1982). (b) J. F. Ramaekers, L. B. Krijnen, H. J. Lips, J. Langelaar, and R. P. H. Rettschnick, Laser Chem. 2, 125 (1983). (c) M. Heppener, A. G. Kunst, D. Bebelaar, and R. P. H. Rettschnick, J. Chem. Phys. 83, 5341 (1985).

[11]D. D. Smith, A. Lorincz, J. Siemon, and S. A. Rice, J. Chem. Phys. 81, 2295 (1984).

[12](a) J. S. Baskin, P. M. Felker, and A. H. Zewail, J. Chem. Phys. 84, 4708 (1986); J. S. Baskin, D. H. Semmes, and A. H. Zewail, *ibid.* 85, 7488 (1986). (b) D. H. Semmes, J. S. Baskin, and A. H. Zewail (to be published).

[13]J. L. Knee, L. R. Khundkar, and A. H. Zewail, J. Chem. Phys. 82, 4715 (1985).

[14]L. R. Khundkar, J. L. Knee, and A. H. Zewail, J. Chem. Phys. 87, 77 (1987), paper I in this series. (b) N. F. Scherer and A. H. Zewail, J. Chem. Phys. 87, 97 (1987), paper II in this series.

[15](a) J. W. Perry, N. F. Scherer, and A. H. Zewail, Chem. Phys. Lett. 104, 1 (1983); N. F. Scherer, J. W. Perry, F. E. Doany, and A. H. Zewail, J. Phys. Chem. 89, 894 (1985). (b) J. L. Knee, L. R. Khundkar, and A. H. Zewail, *ibid.* 89, 3201 (1985). (c) J. L. Knee, F. E. Doany, and A. H. Zewail, J. Chem. Phys. 82, 1042 (1985). (d) J. L. Knee, L. R. Khundkar, and A. H. Zewail, *ibid.* 83, 1996 (1985).

[16](a) B. W. Keelan, J. A. Syage, J. F. Shepanski, and A. H. Zewail, in *Proceedings of the International Conference on Lasers* (STS, Mclean, VA, 1985), p. 718. (b) B. W. Keelan and A. H. Zewail, J. Chem. Phys. 82, 3011 (1985).

[17]W. C. Wiley and I. H. McLaren, Rev. Sci. Instrum. 26, 1150 (1955).

[18](a) H. Abe, N. Mikami, and M. Ito, J. Phys. Chem. 86, 1768, (1982). (b) H. Abe, N. Mikami, M. Ito, and Y. Udagawa, 86, 2567 (1982). (c) Chem. Phys. Lett. 93, 217 (1982). (d) A. Oikawa, H. Abe, N. Mikami, and M. Ito, J. Phys. Chem. 87, 5083 (1983).

[19](a) H. D. Bist, J. C. D. Brand, and D. R. Williams, J. Mol. Spectrosc. 21, 76 (1966). (b) H. D. Bist, J. C. D. Brand, and D. R. Williams, J. Mol. Spectrosc. 24, 413 (1967).

[20]J. A. Syage, P. M. Felker, D. H. Semmes, F. al Adel, and A. H. Zewail, J. Chem. Phys. 82, 2896 (1985).

[21](a) S. Imanishi and M. Ito, Bull. Chem. Soc. Jpn. 25, 153 (1952). (b) P. R. Rao, Proc. Ind. Acad. Sci. Sect. A 55, 232 (1962).

[22]R. J. Jacobsen, Spectrochim. Acta 21, 433 (1965).

[23]H. D. Rudolph, H. Driezler, A. Jaeschke, and P. Wendling, Z. Naturforsch. Teil A 22, 940 (1967). (b) J. Murakami, M. Ito, and K. Kaya, Chem. Phys. Lett. 80, 203 (1981). (c) M. Ito, J. Phys. Chem. 91, 517 (1987).

[24]G. C. Pimentel and A. I. McClellan, in *The Hydrogen Bond* (Freeman, San Francisco, 1960).

[25]Ref. 16(b); H. Selzle, W. E. Howard, and E. W. Schlag, *Rotational Band Contour Program* (Technische Universität, München), (implemented on a VAX 11/780).

[26](a) T. Cvitas and J. M. Hollas, Mol. Phys. 20, 645 (1971). (b) T. Cvitas, J. M. Hollas, and G. H. Kirby, *ibid.* 19, 305 (1970).

[27]*Handbook of Physics and Chemistry*, edited by P. Weast, 60th ed. (Chemical Rubber, Boca Raton, FL, 1980).

[28]The eigenvalues of the inertia tensor were obtained from the cubic characteristic equation using Cardan's formulas. The eigenvectors were obtained numerically using iterative deflation with orthogonalization in each iteration.

[29](a) D. Werst, R. Gentry, and P. Barbara, J. Phys. Chem. 89, 730 (1985). (b) L. R. Khundkar and A. H. Zewail, J. Chem. Phys. 86, 1302 (1986).

[30](a) L. R. Khundkar, R. A. Marcus, and A. H. Zewail, J. Chem. Phys. 87, 2473 (1983). (b) D. Blaser, J. Murphy and J. N. Spencer, Can. J. Chem. 49, 3913 (1971); Z. Yoshida and N. Ishiba, Bull. Chem. Soc. Jpn. 42, 3254 (1969).

[31]N. Gonobe, H. Abe, N. Mikami, and M. Ito, J. Phys. Chem. 89, 3642 (1985).

[32]I. B. Berlman, *Handbook of Fluorescence Spectra of Aromatic Molecules* (Academic, New York, 1971).

[33]A. Sur and P. M. Johnson, J. Chem. Phys. 84, 1206 (1986).

[34]W. L. Hase and D. L. Bunker, program QCPE-234 (California Institute of Technology, Pasadena, CA).

[35]R. A. Marcus, W. L. Hase, and K. N. Swamy, J. Phys. Chem. 88, 6717 (1984); R. A. Marcus, J. Chem. Phys. 85, 5035 (1986).

[36]U. Schubert, E. Riedle, H. J. Neusser, and E. W. Schlag, J. Chem. Phys. 84, 6182 (1986).

[37]R. E. Smalley, J. Phys. Chem. 86, 3504 (1982).

APPENDIX II

Real-time picosecond clocking of the collision complex in a bimolecular reaction: The birth of OH from H+CO_2

Norbert F. Scherer,[a] Luttur R. Khundkar, Richard B. Bernstein,[b] and Ahmed H. Zewail[c]

Arthur Amos Noyes Laboratory of Chemical Physics,[d] California Institute of Technology, Pasadena, California 91125

(Received 13 April 1987; accepted 12 May 1987)

Picosecond (and femtosecond) photofragment spectroscopy[1-5] has recently provided time-resolved, state-to-state dynamics of molecular photofragmentation.[6-8] The focus of these experiments was on unimolecular reactions, where two main issues are fundamental to the dynamics: the nature of the "half-collision" and the degree to which statistical theories account for the time evolution of product state distributions (PSDs).

In contrast to unimolecular fragmentation, bimolecular reactions involve a full collision, and the dynamics[9] of the collision complex is crucial to the fate of product(s). Traditionally, these reactions have been studied by the crossed molecular beam scattering technique.[10,11] From the anisotropy of the products' angular distribution (PAD) in the center-of-mass coordinate system it is possible to infer whether the reaction proceeds by the "direct-mode" (subpicosecond interaction time) or via a "long-lived" (few rotational periods) collision complex.[12,13] In this regard, quasiclassical trajectory calculations on semiempirical potential surfaces[14] and statistical theories[15-24] of formation and decay of collision complexes have been instructive. More recently, spectroscopic methods have been utilized,[25-27] but the main body of experimental information[28-30] has come from *post-collision* observables, i.e., PSDs (via chemiluminescence[31] and LIF[32]), PADs,[33] and products' polarization.[34]

In this Communication, we report the first direct (real-time) measurement of product formation from a bimolecular reaction: the birth of OH from the hot atom reaction H + OCO.[35-37] The reaction steps are: H + CO_2 → HOCO → HO + CO. In our pump–probe experiments, a picosecond laser pulse initiates the reaction via photodissociation of the van der Waals (vdW) molecule $IH\cdots OCO$, prepared in a seeded supersonic beam expansion. The "clocking" of the reaction is accomplished by the use of a picosecond probe pulse (for OH LIF monitoring), delayed in time with respect to the initiation pulse (Fig. 1). UV photolysis of such a vdW precursor molecule ensures that the initial H velocity (~ 20 km s^{-1}) is preferentially directed along the hydrogen bond to the OCO, limiting the range of impact parameters[38-40] and "orienting" the reactants.[38-42] The essential element in our experiment is that the UV photolysis picosecond (pump) pulse acts as a precise trigger setting off the H atom "projectile," thus establishing the *zero of time* for the bimolecular collision.

The experimental apparatus is similar to that employed in Refs. 6–8. The seeded molecular beam was obtained by expanding mixtures of 5% HI and 8% CO_2 in He($P \simeq 1800$ Torr). The beam was characterized by electron impact (15–30 eV) TOF mass spectrometry. The mass spectra displayed peaks for HI, CO_2, $HI\cdot CO_2$, $(CO_2)_n$ and very little of $HI\cdot(CO_2)_2$. Care was taken to trap I_2 (at -15 °C) before nozzle expansion. The complex $HI\cdot CO_2$ concentration was typically 3%–5% relative to HI.

The picosecond pump pulse (239 nm) was generated by mixing the second harmonic of the 616 nm light with the 1.06 μ of a YAG laser. The probe was the second harmonic of the 616 nm pulse. The cross correlation between 616 and 308 nm was obtained using a $LiIO_3$ crystal. The probe was tuned to the $Q_1(1)$ transition of OH using a cell of H_2O_2.[7] On-resonance enhancement for OH LIF was evident from probe wavelength tuning experiments. Typically, for the molecular beam $X/D \sim 40$. The OH signal level was < 0.2 photons/pulse. Following Wittig *et al.*,[38,39] care was taken to optimize the 1:1 vdW complex in the expansion. Signal processing and treatment of the data followed Refs. 6–8.

The experimental results are displayed in Fig. 2. The rise time of the OH signal after deconvolution is found to be ~ 5–15 ps. This first direct observation of the time evolution of the nascent product of a bimolecular reaction represents the transient decay time of the collision complex, formed with

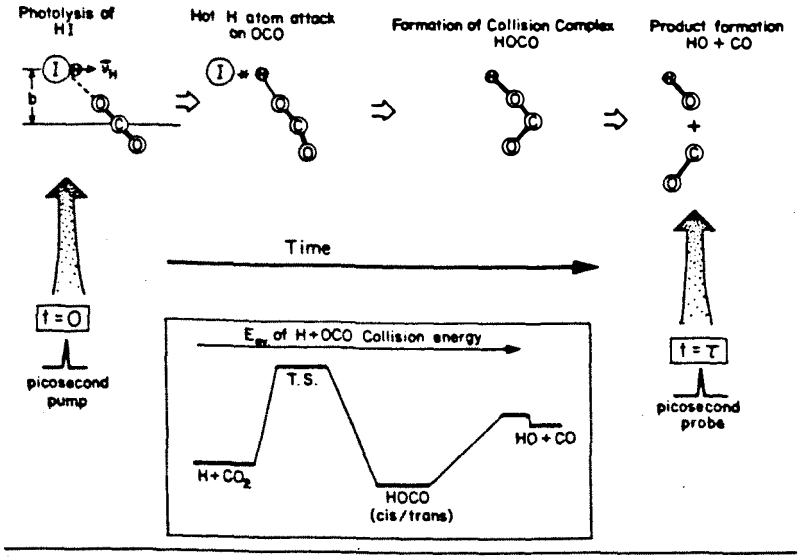

FIG. 1. Scheme of the experiment and potential energy surface (PES) of the bimolecular reaction $H + CO_2$. The picosecond photolysis pulse initiates the hot-atom reaction forming the HOCO collision complex. This dissociates to yield the OH product which is detected by the probe picosecond laser pulse delayed by a time τ with respect to the pump. The insert is a simplified picture of the PES taken from theoretical and experimental work (see the text).

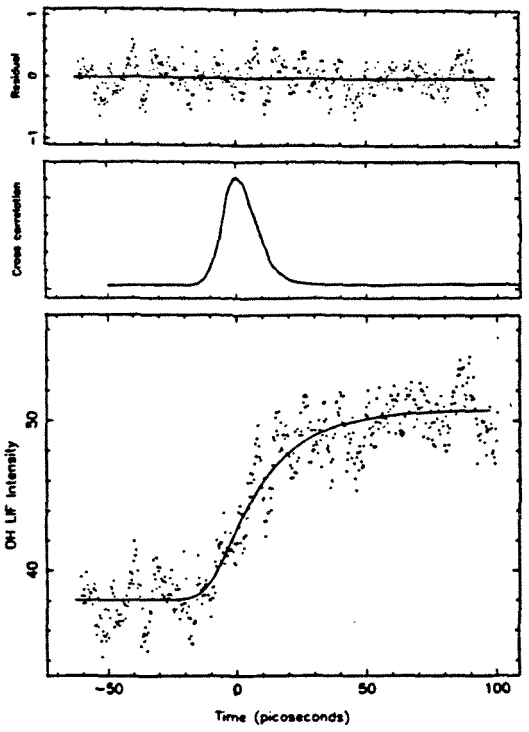

FIG. 2. Experimental results. Typical "transient" showing the OH LIF signal vs delay time τ. The experimental data points have been fitted (solid curve) assuming an exponential risetime (15 ps) and convoluting with the measured cross-correlation function (shown in the insert). The weighted residuals are also plotted (above) vs τ. From a number of experiments, the rise time range is 5–15 ps. More recent results (Ref. 47) deconvoluted with the proper system response function for pump and probe pulses, and obtained with improved S/N, give $\tau_r = 5 \pm 2$ ps.

the given available energy. For the photolysis wavelength used, the initial relative translational energy, E_{tr} ($\simeq E_{av}$) of the H + OCO reagents is calculated to be 200 kJ mol^{-1} assuming collinear incidence. The slower H atoms from the I^* branch, in contrast, yields $E_{tr} = 112$ kJ mol^{-1}, only slightly above threshold.[35]

For the subject reaction there is considerable knowledge of the potential surface based on theory[43] and experiment.[35–40,44,45] The minimum energy path has an entrance barrier corresponding to a threshold energy of ~105 kJ mol^{-1},[35,38] followed by a potential well supporting a complex, HOCO (itself studied by matrix isolation spectroscopy),[46] followed by a small exit barrier[44] to OH + CO. The initial H atom velocity is ~200 Å/ps and the available energy of collision with CO_2 is above the transition state barrier.[39] Thus, the initial step is assumed to be complete within our pulse, but the rapid H-atom attack slows down depending on the vibrational motion in HOCO, which leads to a slower rate for the formation of HO + CO. The measured OH rise time can now be used to model the PSD and possible deviations from statistical behavior. Experiments at different photolysis wavelengths will yield the energy dependence of the formation and decay of the complex.

Planned experiments also include direct detection of the appearance of the HOCO and extension of the technique to the femtosecond time domain.[5,48] This will make it possible to clock not only complex-mode bimolecular reactions, but also subpicosecond, direct-mode hot atom bimolecular reactions.

[a] Recipient of a Procter and Gamble Award, American Chemical Society, 1986.
[b] Sherman Fairchild Distinguished Scholar, Caltech (1986); permanent address: Department of Chemistry, University of California, Los Angeles, CA 90024.
[c] John Simon Guggenheim Foundation Fellow.
[d] Contribution No. 7572; Research supported by the National Science Foundation under Grant No. DMR-8521191.
[1] J. L. Knee, L. R. Khundkar, and A. H. Zewail, J. Chem. Phys. 82, 4715

(1985).
[2]J. K. Knee, L. R. Khundkar, and A. H. Zewail, J. Chem. Phys. 83, 1996 (1985).
[3]J. L. Knee, L. R. Khundkar, and A. H. Zewail, J. Phys. Chem. 89, 4659 (1985).
[4]N. F. Scherer, F. E. Doany, A. H. Zewail, and J. W. Perry, J. Chem. Phys. 84, 1932 (1986).
[5]N. F. Scherer, J. L. Knee, D. D. Smith, and A. H. Zewail, J. Phys. Chem. 89, 5141 (1985).
[6]L. R. Khundkar, J. L. Knee, and A. H. Zewail, J. Chem. Phys. 87, 77 (1987).
[7]N. F. Scherer and A. H. Zewail, J. Chem. Phys. 87, 97 (1987).
[8]J. L. Knee, L. R. Khundkar, and A. H. Zewail, J. Chem. Phys. 87, 115 (1987).
[9]R. D. Levine and R. B. Bernstein, *Molecular Reaction Dynamics and Chemical Reactivity* (Oxford University, N.Y., 1987).
[10]E. H. Taylor and S. Datz, J. Chem. Phys. 23, 1711 (1955).
[11]D. R. Herschbach, Discuss. Faraday Soc. 33, 149 (1962); 55, 233 (1973).
[12]W. B. Miller, S. A. Safron, and D. R. Herschbach, Discuss. Faraday Soc. 44, 108 (1967).
[13]S. Stolte, A. E. Proctor, and R. B. Bernstein, J. Chem. Phys. 65, 4990 (1976).
[14]P. Brumer and M. Karplus, Faraday Discuss. Chem. Soc. 55, 80 (1973).
[15]C. E. Klots, J. Phys. Chem. 75, 1526 (1971).
[16]S. A. Safron, N. D. Weinstein, D. R. Herschbach, and J. C. Tully, Chem. Phys. Lett. 12, 564 (1972).
[17]M. Quack and J. Troe, Ber. Bunsenges. Phys. Chem. 78, 240 (1974); 79, 170 (1975).
[18]R. A. Marcus, J. Chem. Phys. 62, 1372 (1975).
[19]G. Worry and R. A. Marcus, J. Chem. Phys. 67, 1636 (1977).
[20]J. C. Light, in *Atom–Molecule Collision Theory*, edited by R. B. Bernstein (Plenum, N.Y., 1979), p. 647.
[21]R. D. Levine and J. L. Kinsey, in *Atom–Molecule Collision Theory*, edited by R. B. Bernstein (Plenum, N.Y., 1979), p. 693.
[22]I. Nadler, M. Noble, H. Reisler, and C. Wittig, J. Chem. Phys. 82, 2608 (1985).
[23]C. Wittig, I. Nadler, H. Reisler, M. Noble, J. Catanzarite, and G. Radhakrishnan, J. Chem. Phys. 83, 5581 (1985).
[24]C. X. Qian, M. Noble, I. Nadler, H. Reisler, and C. Wittig, J. Chem. Phys. 83, 5573 (1985).
[25]P. Hering, P. R. Brooks, R. Curt, R. Judson, and R. S. Lowe, Phys. Rev. Lett. 44, 687 (1980).
[26]H.-J. Foth, J. C. Polanyi, and H. H. Telle, J. Phys. Chem. 86, 5027 (1982).
[27]T. C. Maguire, P. R. Brooks, R. F. Curl J. H. Spence, and S. J. Ulvick, J. Chem. Phys. 85, 844 (1986).
[28]R. N. Zare and R. B. Bernstein, Phys. Today 33 (No. 11), 43 (1980).
[29]Y. T. Lee and Y. R. Shen, Phys. Today 33 (No. 11), 52 (1980).
[30]R. B. Bernstein and A. H. Zewail, J. Phys. Chem. 90, 3467 (1986).
[31]A. M. Ding, L. J. Kirsch, D. S. Perry, J. C. Polanyi, and J. L. Schreiber, Faraday Discuss. Chem. Soc. 55, 252 (1973).
[32]H. W. Cruse, P. J. Dagdigian, and R. N. Zare, Faraday Discuss. Chem. Soc. 55, 277 (1973).
[33]J. M. Farrar and Y. T. Lee, Annu. Rev. Phys. Chem. 25, 357 (1974); D. M. Neumark, A. M. Wodtke, G. N. Robinson, C. C. Hayden, and Y. T. Lee, J. Chem. Phys. 82, 3045 (1985).
[34]R. Altkorn and R. N. Zare, Annu. Rev. Phys. Chem. 35, 265 (1984).
[35]G. A. Oldershaw and D. A. Porter, Nature 223, 490 (1969).
[36]C. R. Quick, Jr. and J. J. Tiee, Chem. Phys. Lett. 100, 223 (1983).
[37]K. Kleinermanns and J. Wolfrum, Chem. Phys. Lett. 104, 157 (1984).
[38]S. Buelow, G. Radhakrishnan, J. Catanzarite, and C. Wittig, J. Chem. Phys. 83, 444 (1985).
[39]G. Radhakrishnan, S. Buelow, and C. Wittig, J. Chem. Phys. 84, 727 (1986).
[40]S. Buelow, M. Noble, G. Radhakrishnan, H. Reisler, C. Wittig, and G. Hancock, J. Phys. Chem. 90, 1015 (1986).
[41]C. Jouvet and B. Soep, J. Chem. Phys. 80, 2229 (1984).
[42]C. Jouvet and B. Soep, Chem. Phys. Lett. 96, 426 (1983).
[43]L. B. Harding (unpublished), quoted in Ref. 39, G. Schatz and L. Harding (to be published).
[44]I. W. M. Smith and R. Zellner, J. Chem. Soc. Faraday Trans. 2 69, 1617 (1973).
[45]I. W. M. Smith, Chem. Phys. Lett. 49, 112 (1977).
[46]D. E. Milligan and M. E. Jacox, J. Chem. Phys. 54, 927 (1971).
[47]N. F. Scherer, L. R. Khundkar, R. B. Bernstein, and A. H. Zewail (to be published).
[48]M. Dantus, M. Rosker, and A. H. Zewail (submitted for publication).

APPENDIX III

```
      PROGRAM INPUT
      DIMENSION NV(99),ID(99),VIB(99),SUM(500),ANH(99),DENS(250)
      DIMENSION LABEL(4),FREQ(2),NUM(2)
      CHARACTER*8 FREQ,NUM
      CHARACTER*16 LABEL
      DATA ANH/ 99*0./
      DATA SUM/ 500*0./
      DATA LABEL/'DIRECT COUNT','WHIT.-RABINOVITCH','DIRECT COUNT',
     *          'DIRECT  COUNT'/
      DATA FREQ/'HARMONIC','MORSE'/
      DATA NUM/'ZERO','ONE'/
      CVF=1./1400.
       sum(1) = 1
C*****************************************************************
C                                                                *
C   The input program asks questions relevant to subsequent program
C   control.                                                     *
C              M       : The number of frequencies               *
C              MODE    : The mode of the calculation             *
C                    0         Harmonic direct count            *
C       **           1         Whitten-Rabinovitch count        *
C                    2         Anharmonic direct count          *
C       **           3         Anharmonic, internal rotor d. count
C                                                               *
C              IORDER  : 0 orders the frequencies               *
C                        1 assumes frequencies in ascending order
C                                                               *
C              ANHFLG  :  1 assumes reduced anharmonicities     *
C                        -1 assumes anharmonicities in wavenumbers
C                                                               *
C                                                               *
C                                                               *
C*****************************************************************
      READ (5,101) M,MODE,IORDER
      READ (5,102) (VIB(J),J=1,M)
      READ (5,103) (ID(J),J=1,M)
      READ (5,104) XMIN,XMAX,XINC
      IF (MODE.LT.2) GOTO 15
      READ (5,*) ANHFLG
      READ (5,1030) (ANH(J),J=1,M)
      if (anhflg.gt.0.) goto 4
     DO 3 J=1,M
c     IF (ABS(ANH(J)).GT.1.0) ANH(J)=CVF*VIB(J)/ANH(J)
3     anh(j) = anh(j)/vib(j)

4     CONTINUE
      do 5 j=1,m
      jmax = -0.5*(anh(j) - 1.0)/anh(j)
      evmaxm = vib(j)*jmax*(1.0-(1.0+jmax)*anh(j))
      if (evmaxm .gt. xmax) goto 5
      write(6,110) j, jmax, evmaxm, vib(j), anh(j)
      goto 55
c
5     CONTINUE
110   format ( '  F A T A L   W A R N I N G --- Anharmonicity
      1 too large ',2i5,3x,2f6.1,3x,f8.4  )
C5    IF (XMIN.EQ.0.) XMIN=0.5*XINC
15    G=(XMAX-XMIN)/XINC
      NP=G+0.5
      G=0.5*(XMAX-XMIN)/FLOAT(NP)
      NP=NP+1
C
      WRITE (6,77) LABEL(MODE+1)
      MOD=1
```

```
      IF (MODE.GE.2) MOD=2
      WRITE (6,78) M
      WRITE (6,79) FREQ(MOD)
       WRITE (6,102) (VIB(J),J=1,M)
       WRITE (6,103) (ID(J),J=1,M)
     IF (MODE.GE.2) WRITE(6,1032) (ANH(J),J=1,M)
      MOD=1
      IF (MODE.EQ.3) MOD=2
      WRITE(6,1033) NUM(MOD)
       WRITE (6,1045) XMIN,XMAX,NP
C
      IF (MODE.EQ.1) CALL WRCOUNT(M,ID,VIB,SUM,DENS,XMIN,XMAX,NP)
      IF (MODE.NE.1) CALL DCOUNT(M,ID,VIB,ANH,SUM,DENS,XMAX,NP,G)
      IF (MODE.EQ.3) CALL ROTOR(SUM,DENS,XMIN,XMAX,NP,G)
C
C
      WRITE (6,201)
      IF (MODE.NE.1) GOTO 27
      DO 23 L=1,NP
      E=xmin + 2.*G*FLOAT(L-1)
23     WRITE (6,202) E,SUM(L),DENS(L)
      GOTO 55
27    S = SUM(1)
      WRITE (6,202) EMIN,S,DENS(1)
      DO 30 L=1,(NP-1)
      J=L*2+1
       S = S + SUM(J-1) + SUM(J)
       E = 2.*G*FLOAT(L)
30     WRITE (6,202) E,S,DENS(L+1)
C
C
55     CONTINUE
C
77     FORMAT (' The following program calculates the sum and
     * density of states using the ',A16,'  method')
78     FORMAT (/ ' The following ',I5,'  frequencies are considered
     * in the calculation' )
79     FORMAT (/ ' These frequencies are treated as ',A8,'
     * oscillators')
1032   FORMAT (' Anharmonic corrections used (WeXe/v) :'/
     *          7(E10.4,3X) )
1033   FORMAT (/' This system has ',A8, ' internal rotor ' / )
101    FORMAT (3I2)
102    FORMAT (7F10.0)
103    FORMAT (14I5)
1030   FORMAT (7F10.4)
104    FORMAT (3F10.0)
1045   FORMAT (' The calculation is for the energy range   ',
     *          2F10.0, '  in', I5,'  increments' //
     *          10X, 50(' *') //)
201    FORMAT (3X,' EXCESS ENERGY',4X,' SUM OF STATES',10X,
       1' DENSITY OF STATES'/)
202    FORMAT (5X,F10.0,7X,E12.5,12X,E10.4)
       STOP
       END


      SUBROUTINE DCOUNT(M,ID,VIB,ANH,SUM,DENS,EMAX,NP,EINC)
      DIMENSION ID(1),VIB(1),ANH(1),SUM(1),DENS(1),NV(99)
C*************************************************************
C
C   This subroutine uses a quantum stepping algorithm to perform
C   a direct count of the sum and densities of states for a
C   specified range of energies.  As the program steps through
C   the possible sets of quantum numbers, it evaluates the energy
C   and adds a number (combinatoric degeneracy) to the sum of
C   states in one of the energy bins that have been set up.
C       After all possible combinations of quantum numbers that
C   satisfy the energy upper bound have been exhausted, these
C   bins contain the number of states within the energy boundaries
C   of each bin. Division by the energy range gives an average
C   density of states.
```

```
C*********************************************************************
C
C       INITIALIZE COUNTERS AND OTHER LIMITING PARAMETERS
C
        DEN0 = 0
        MM=M
        SPT = 2.*EINC
        EV = EMAX + EINC
C
       IF (IORDER.EQ.0) GOTO 2
C   ORDER FREQUENCIES IN INCREASING ORDER
C
        DO 1 I=1,MM-1
        DO 1 J=(I+1),MM
        IF (VIB(J).GT.VIB(I)) GO TO 1
        SAV = VIB(I)
        VIB(I) = VIB(J)
        VIB(J) = SAV
        ISV = ID(I)
        ID(I) = ID(J)
        ID(J) = ISV
        SAV = ANH(I)
        ANH(I) = ANH(J)
        ANH(J) = SAV
1       CONTINUE
C
C       CALCULATE LARGEST FREQ WITH NON-ZERO QUANTA AT GIVEN ENERGY
C
2       CONTINUE
        DO 3 I = 1,M
        IF (VIB(I).GT.EV) GO TO 4
3       CONTINUE
4       M = I-1
C
C       MODULE FOR CALCULATING SUM AND DENSITY
C
        KC = 2
        DO 5 J = 1,MM
5       NV(J) = 0
C
6       K = 2
c       NV(1) = NV(1) - 1
7       NV(1) = NV(1) + 1
        E = 0
        DO 8 J=1,KC
8       E = E + NV(J)*VIB(J)*(1.0 - (1.+NV(J))*ANH(J))
        IF(E-EV) 10,10,11
C10     SUM = SUM + 1
C       IF(E.GT.EMIN) DEN=DEN+1
10      CALL COUNT(SUM,NV,ID,DEN0,KC,E,EMIN,EINC)
c       write(6,*) (nv(j3),j3=1,mm),e
        GO TO 7
11      NV(K) = NV(K) + 1
        DO 12 J=1,(K-1)


12      NV(J) = 0
C
        E = 0
        DO 14 J=1,KC
14      E = E + NV(J)*VIB(J)*(1.0 - (1.+NV(J))*ANH(J))
        IF(E-EV) 15,15,16
C15     SUM = SUM + 1
C       IF(E.GT.EMIN) DEN=DEN+1
15      CALL COUNT(SUM,NV,ID,DEN0,KC,E,EMIN,EINC)
c       write(6,*) (nv(j3),j3=1,mm),e
        GO TO 6
16      K = K + 1
        IF(KC.LT.K) KC=K
        IF(K.GT.M) GO TO 17
        GO TO 11
17      CONTINUE
```

```
C       OUTPUT SECTION
C
       L=1
       DENS(1) = (DEN0+SUM(2))/SPT
        DO 18 J=3,(2*NP),2
       L=L+1
        DENS(L) = (SUM(J) + SUM(J+1))/SPT
18      CONTINUE
C
       RETURN
        END



       SUBROUTINE COUNT(SUM,NV,ID,DEN0,KC,E,EMIN,GRID)
       DIMENSION NV(1),ID(1),SUM(1)
C ***************************************************************************
C
C   This subroutine is designed to calculate the combinatoric degeneracies
C   for modes with degenerate frequencies.
C
C ***************************************************************************
C
C       CALCULATE THE DEGENERACIES
        COLL = 1
        DO 1 KK=1,KC
        DGN = 1
        IF (ID(KK).EQ.1) GO TO 1
        IF (NV(KK).EQ.0) GO TO 1
        DO 2 J=1,(ID(KK)-1)
2       DGN = DGN*FLOAT(NV(KK)+J)/FLOAT(J)
1       COLL = COLL*DGN
C
C       PARTITIONING SECTION
C
        XP = (E/GRID) + 0.5
1001    FORMAT (4(3X,F10.4),5X,I5 )
        IN = XP
        IF (XP.GT.0.) GO TO 3
        IN = -1
        IF (XP.GT.-1.) DEN0=DEN0+1.
3       IN = IN + 2
        SUM(IN) = SUM(IN) + COLL
C       IF (E.GT.EMIN) DEN=DEN+COLL/TOL
        RETURN



      SUBROUTINE WRCOUNT(M,ID,VIB,SUM,DENS,EMIN,EMAX,NP)
      DIMENSION ID(1),VIB(1),SUM(1),DENS(1)
C  ***************************************************************************
C                                                                             *
C   This section calculates the density of states using the semi-             *
C   classical empirical approach proposed by Whitten and Rabinovitch.         *
C                    BETA       (frequency dispersion parameter)            *
C                    XSFAC      logarithm of M!                             *
C                    XHNU       logarithm of product of freq.               *
C                                                                             *
C  ***************************************************************************
C
C               Calculate the zero-point energy
      EZERO=0.
      DO 1 J=1,M
      DO 1 K=1,ID(J)
1      EZERO=EZERO+VIB(J)
      EZERO=0.50*EZERO
C               Calculate BETA, XSFAC, XHNU
      S=0
      SNU=0
      SNU2=0
      XSFAC=0
      XHNU=0
```

```
      DO 5 L1=1,M
      DO 5 L2=1,ID(L1)
      S = S + 1
      SNU = SNU + VIB(L1)
      SNU2 = SNU2 + VIB(L1)**2
      XSFAC = XSFAC + ALOG(S)
      XHNU = XHNU + ALOG(VIB(L1))
5      CONTINUE
      BETA = (S-1)*SNU2/(SNU**2) !S does not appear because it
C                                appears twice for snu**2
C
C
       txsfac = exp(xsfac)
       type *, beta,txsfac
      EINC=(EMAX-EMIN)/FLOAT(NP-1)
      E = EMIN
      DO 50 I=1,NP
      EP = E/EZERO
           EPS = EP**0.5
      IF (EP.GE.1.0) GOTO 25
           W=5.00*EP + (2.73*EPS) + 3.51
           W=1./W
           DW = 1.365/EPS
           DW = - (5.00+DW)*W**2
       GOTO 35
25         EPSS = SQRT(EPS)
           W = EXP(-2.4191*EPSS)
           DW = -W*(0.60478/(EPS*EPSS))
35     CONTINUE
      A = 1.00 - BETA*W
      EX = E + A*EZERO
      DEN = (S-1.)*ALOG(EX) - XSFAC - XHNU
      DENS(I) = (EXP(DEN))*(1.-BETA*DW)*S
      SUM(I) = EX*DENS(i)/S
      E = E + EINC
50     CONTINUE
      RETURN
      END
```

APPENDIX IV

```
C       This program calculates the phase space theory product state
C       distributions for the photodissociation of ABCD ---> AB + CD for
C       comparison with product (AB) N dependent rates/dist. observed
C       experimentally.  The simplest approximations are used. The
C       contributions from the electronic degeneracy of AB are ignored.
C
C  ************************************************************************
C
        PROGRAM PSRATE
C       DIMENSION RATE(5,100),PROB(5,100),VIB(20),SODGN(2)
        DIMENSION ES(500),JTOT(500),TPROB(20),LABEL(4),RPROB(20)
        DIMENSION AMPL(500),NTRAN(500)
        DOUBLE PRECISION TPROB,TNORM,AMPL
        BYTE FIL(11)
        COMMON /PARAM/ BAB,B2(2),EFAB,EFCD(2),CADJ,D0,LJ,EISO(2),NISO
        COMMON /OUTP/ RATE(5,100),PROB(5,100),VIB(20),BB(3),XJ(2)
        COMMON /OUTP2/ E,I,J0,K,SUMJ,MAXJ, SRATE
        DATA NAB,JAB,NCD,JCD / 4*0/
        DATA RATE,RPROB / 500*0.,20*0. /
C       DATA SODGN / 1.,1. /
        LJ = 12
        DO 5 I=1,20
5       TPROB(I) = 0.0
C   The spin-orbit degeneracies (SODGN) are to account for the J quantum
C   number (2J+1) of the electron motion in the two fragments. For this
C   series of calculations, the electronic angular momentum is not
C   considered as a degree of freedom. The degeneracies are set to unity
C       DATA NVIB,VIB / 6,2170.,1501.,820.,588.,217.,264.,14*0. /
C       DATA NVIB,VIB / 8,3608.,3599.,1402.,1266.,877.,243.,14*0. /
C
C                The input section is first
C
C       TYPE *,'Enter the name of the data file'
        READ(5,1000) (FIL(I),I=1,11)
1000    FORMAT (11A1)
C       CALL ASSIGN(4,FIL)
      OPEN(UNIT=4,FILE=FIL,STATUS='OLD',
     1  ACCESS='SEQUENTIAL', DISPOSE='SAVE')
        READ (4,60) LABEL
60      FORMAT( 1X, 4A3)
        READ (4,*) MODE,ITYPE
        READ (4,*) (BB(I),I=1,3), D0
        READ (4,*) EFAB,BAB,CSIX,DM1
        READ (4,*) EFCD(1),B2(1),DM2,NISO,XJ(1)
        EISO(1)=0.
        I=2
6       CONTINUE
        IF (I.GT.NISO) GOTO 7
        READ (4,*) EFCD(I),B2(I),XJ(I),EISO(I)
        I=I+1
        GOTO 6
7       CONTINUE
        DM=(DM1*DM2)/(DM1+DM2)  !The reduced mass of the fragments
        CADJ=(6.0)*CSIX*DM
        BCK=(BB(1)-BB(2))
C
        WRITE(6,1001) LABEL
1001    FORMAT(1X,'The following parameters were used as input for
     1  calculating' /5X, 'distributions for the reaction'/
     2 20X,2A3,2X,'------>'2X,A3,'   +   ',A3)
        WRITE (6,1012) LABEL(1),LABEL(2),D0
        WRITE (1,1012) LABEL(1),LABEL(2),D0
1012    FORMAT (/1X, ' Parent ',2A2, ' :',10X,'Diss. energy ',F8.0)
        WRITE (6,1013) BB
```

```
      WRITE (1,1013) BB
1013  FORMAT (1X, 'Rotational constants  ',3(F8.4,X) )
      WRITE (6,1011) LABEL(3)
      WRITE (1,1011) LABEL(3)
1011  FORMAT(/1X, 'Fragment ',A4,':')
      WRITE (6,1002) DM1,EFAB,BAB
      WRITE (1,1002) DM1,EFAB,BAB
1002  FORMAT(20X,'Mass:',F5.0,2x,'Vib. Freq.:',F7.0,2X,
     1 'B cons.:',F8.4 )
      WRITE(6,1011) LABEL(4)
      DO 10 I=1,NISO
      WRITE (6,1003) XJ(I), EISO(I),DM2, EFCD(I),B2(I)
1003  FORMAT(1X,F4.1,2X,'Ener ',F6.2,2X,'Mass:',F5.0,2x,'Vib. Freq.:'
     1 ,F7.0,2x,'B cons.:',F8.4 )
10    CONTINUE
      WRITE (6,1004)
1004  FORMAT (1X, 80('*'), /,/)
C
C
      IF (MODE.EQ.1) GOTO 300
      IF (MODE.EQ.2) GOTO 400
      READ (4,*) ITER
      DO 1 I=1,ITER
1     READ(4,*) ES(I),JTOT(I)
C
      IF (ITYPE.EQ.0) WRITE(6,100)
      IF (ITYPE.EQ.1) WRITE(6,101)
100   FORMAT (//3X,' The following distributions have been
     1 calculated by PHASE SPACE THEORY using quantum counts. ')
101   FORMAT (//3X,' The following distributions have been
     1 calculated using quantum counts '/
     2 5X,'conserving J,E at infinite separation. ')
C
      WRITE (6,121)
121   FORMAT (1X,'Energy',2x,'J',5x,'Rate', 6x,
     1 '  C    N         D i s t r i b u t i o n ')
      DO 50 NITER=1,ITER
      E=ES(NITER)
      J0=JTOT(NITER)
      CALL PSDIST(E,J0,MAXJ,SUMJ,ITYPE)
      CALL WRDENS(E,D0,BCK,J0,DENS)
      SRATE = SUMJ/DENS
      SRATE = 3.0E10*SRATE
      E = E + BB(2)*(FLOAT(J0*(J0+1)))
      CALL OUTPUT(MODE)
C     WRITE (6, 102) SRATE
102   FORMAT (1X, 'The rate of reaction is ',E10.4)
50    CONTINUE
      GOTO 999
C
C
300   READ(4,*) T,EMAX, ELASER,NVIB
      WRITE(6,*) T,EMAX, ELASER
      READ (4,*) (VIB(I),I=1,NVIB)
C
      EXQ = ELASER-D0
      LUN=6
      WRITE (LUN,3001)
      WRITE (LUN,3002) T, ELASER, EMAX
      WRITE (LUN,3003) (VIB(I),I=1,NVIB)
      WRITE (LUN,3004)
C
3001  FORMAT (/1X,'The following results are from a PST calculation
     1 for an initial',/' Boltzmann distribution ')


3002  FORMAT (3X, 'Temperature',F5.0,' K',5X,'Min Ex ',F7.1,5X,
     1 'Max initial Ex ',F7.1)
3003  FORMAT (1X,'The initial state vibrational energies are '/7F8.1)
3004  FORMAT (/2x,'Ener',3x,'v',4x,'K',4x,'J', 8x,'Rate',5x,'Boltz'
     1 ,20x, 'P S T   D i s t r i b u t i o n ')
```

```
c               This section computes the average of PST distributions
c
        LJ=0
        QFNC=0.
        AVRATE=0.
        BETA = 1.4388/T
        DO 395 I=1,NVIB                    !Loop over vibrational energies
C       PVIB=EXP(-BETA*VIB(I))
        IF (EMAX.LT.VIB(I)) GOTO 395
        KMAX=SQRT((EMAX-VIB(I))/(BCK))
        DGNK=1.
        DO 390 K=0,(KMAX+1)
        EK=BCK*(FLOAT(K**2))
        IF ((EMAX-VIB(I)).LT.EK) GOTO 390
        JMAX = SQRT((EMAX-VIB(I)-EK)/BB(2))
        ICOUNT=0
        DO 385 J=K,(JMAX+1)
        DGNJ=2*J+1
        J0=J
        E=VIB(I)+BB(2)*FLOAT(J*(J+1))+EK
        BFAC=DGNJ*DGNK*EXP(-BETA*E)
CD      TYPE *, VIB(I),J,EK,E,BFAC
        IF (BFAC.LT.1.E-04) GOTO 385
        QFNC = QFNC + BFAC
        EXQ = E + ELASER - D0
        E = E + ELASER - D0 - (BB(2)*(FLOAT(J*(J+1))) )
        IF (E.LE.0.) GOTO 385
C       E=E-D0
        CALL PSDIST(E,J0,MAXJ,SUMJ,ITYPE)
        CALL WRDENS(E,D0,BCK,J0,DENS)
        TRATE=SUMJ/DENS
        AVRATE = AVRATE + TRATE*BFAC
        IF (LJ.LT.MAXJ) LJ=MAXJ
C       IF (ICOUNT.EQ.0) CALL OUTPUT(MODE)
        DO 384 N=1,(MAXJ+1)
        RPROB(N)=RPROB(N) + PROB(1,N)*BFAC*TRATE
384     TPROB(N)=TPROB(N)+PROB(1,N)*BFAC
C       WRITE (6,*) E,J0,K,DENS, TRATE
        ICOUNT=ICOUNT+1
        RLIFE = 3.0E10*TRATE
c       RLIFE = 1./RLIFE
        if (icount.ne.0) goto 3849
        WRITE(6,3010) EXQ,MAXJ,K,J0, RLIFE,BFAC,(PROB(1,IJ),IJ=1,MAXJ)
3010    FORMAT(1X,F6.0,1X,3(I2,3X), 2X,E10.4,1X, F7.4, 3X,
     1  5(20(1X,F6.3),/ ) )
3849    IF (ICOUNT.GE.4) ICOUNT=0
385     CONTINUE
390     DGNK=2.
395     CONTINUE
C
C
        TNORM=0
        DO 396 I=1,LJ+1
396     TNORM=TNORM+TPROB(I)
        DO 397 I=1,LJ+1
        IF (TPROB(I).LT. 0.001) GOTO 397
        RPROB(I)=(RPROB(I)/TPROB(I) )*3.0E10
397     TPROB(I)=TPROB(I)/TNORM

        AVRATE=3.0E10*AVRATE/QFNC
        ELASER = ELASER - D0
        WRITE (6,9004) elaser,(RPROB(J),J=1,LJ+1)
9004    FORMAT (1X, 'The thermally averaged rates at', F7.0,3x,'are'
     1  ,/, 5(3x,E10.4) )
        GOTO 9009
C
C               This section looks up the initial state distributions
C               from a data file and does the thermal average
400     READ(4,*) T,EMAX,NVIB
        READ (4,3001) (VIB(I),I=1,NVIB)
C       READ (4,3002) (BB(I),I=1,3)
C       LJ=0
       CLOSE(UNIT=9, DISPOSE='SAVE')
```

```
      ICOUNT = 0
401   READ (9,*,ERR=405) I
      READ (9,*) GEX,TEX,EXS,KV0,JV0,K5,J5,TP
      E=EXS-D0
      IF (TP.LT.1.E-04) GOTO 401
      IF (E.GE.EFAB) GOTO 401
      TYPE *, GEX,EXS,KV0,JV0,K5,J5,TP
      ICOUNT = ICOUNT + 1
      ES(ICOUNT) = E
      JTOT(ICOUNT) = J5
      AMPL(ICOUNT) = TP
      NTRAN(ICOUNT) = I
      GO TO 401
405   TYPE *,ICOUNT
      DO 415 I=1,ICOUNT
      CALL PSDIST(ES(I),JTOT(I),MAXJ,SUMJ,ITYPE)
C     MJ=MAXJ
C     IF (LJ.LE.MJ) LJ=MJ
      DO 411 N=1,LJ
411   TPROB(N) = TPROB(N) + AMPL(I)*PROB(1,N)
      E = ES(I)
      K = NTRAN(I)
      SUMJ = AMPL(I)
415   CALL OUTPUT(1)  !TYPE *, ES(I),EFAB,EFCD,BAB,BCD,CADJ,MAXJ
      TNORM=0
      DO 417 I=1,LJ
417   TNORM=TNORM+TPROB(I)
      DO 418 I=1,LJ
418   TPROB(I)=TPROB(I)/TNORM
9009  WRITE(6,9010) QFNC
      WRITE(6,9011) (TPROB(I),I=1,LJ)
9010  FORMAT (//1X,'The calculated partition function is ',F8.2/
     1  '                  The thermally averaged distribution is ')
9011  FORMAT (1X,7(F8.4,2X))
999   CONTINUE
      CLOSE(UNIT=4,DISPOSE='SAVE')
      STOP
      END
C
C
C
C
C
      SUBROUTINE PSDIST(ENER,J0,MAXJ,SUMJ,ITYPE)
      COMMON /PARAM/ BAB,B2(2),EFAB,EFCD(2),CADJ,D0,LJ,EISO(2),NISO
      COMMON /OUTP/ RATE(5,100),PROB(5,100),VIB(20),BB(3),XJ(2)
      DO 11 IK=1,2
      DO 11 IK2=1,20

      PROB(IK,IK2) = 0
11    RATE(IK,IK2) = 0
C     TYPE *, D0,EFAB,EFCD,BAB,BCD,CADJ,MAXJ,LJ
C
C     TYPE *,E,J0,ITER
      E=ENER + BB(2)*(FLOAT(J0*(J0+1)) )
C     TYPE *,E
      MNAB = E/EFAB
C     IF (MNAB.GT.5) TYPE *,'MNAB is greater than 5'
      DO 69 NAB=0,MNAB
      NDGNAB=1
      ER1= E - FLOAT(NAB)*EFAB        !Energy left after AB vibration
      XJAB = 0.50*( (ABS(SQRT(1+(4.*ER1/BAB)))) - 1.) !Calculate max JAB
      MJAB = XJAB
C     CALL TESTMJ(MJAB,BAB,ER1)
      IF (NAB.EQ.0) MAXJ=MJAB
C     IF (MJAB.GT.100) TYPE *,'MJAB is greater than 100'

c     EJAB0 = 0.      ! Include this line for NCNO
      EJAB0 = BAB*(1.5*(2.5)) ! Zero energy for OH (2P3/2) rotations
      DO 59 JAB=0,MJAB
D     WRITE (6,200)
200   FORMAT (1X, '  ' )
      xj1 = float(jab) + 1.5  ! Rot q # for (2P3/2) OH
      JDGNAB=2*JAB + 1
```

```
c       ER2=ER1-BAB*(FLOAT(JAB*(JAB+1))) + EJAB0
        ER2=ER1-BAB*( xj1*(xj1+1) ) + EJAB0  ! J q # for H2O2 is 1/2 int.

C                       !Energy left after AB vib. + rot.
        RATE12 = 0.
c       DO 585 ISPIN=1,2        ! Include next three lines for NCNO (1)
c       XJ1 = FLOAT(JAB) + 0.50*(-1.0)**ISPIN   !                   (2)
c       IF (XJ1.LT.0.) GOTO 585 !                                   (3)
c
        DO 58 ISO=1,NISO
        IF (ER2.LE.EISO(ISO)) GOTO 585
        BCD=B2(ISO)
        ER22=ER2-EISO(ISO)
        MNCD = ER22/EFCD(ISO)
        RATE1 = 0.
C
C
        IF (MNCD.GT.5) TYPE *,'MNCD is greater than 5'
        DO 49 NCD=0,MNCD
        NDGNCD=1.
        ER3 = ER22 - FLOAT(NCD)*EFCD(ISO) ! Energy left for CD rot and orbit L
        MJCD=IFIX(0.50*( (ABS(SQRT(1+(4.*ER3/BCD))))-1.)) !Calculate max JCD
C       CALL TESTMJ(MJCD,BCD,ER3)
C
        IF (MJCD.GT.100) TYPE *,'MJCD is greater than 100'
        EJCD0=BCD*(XJ(ISO)*(XJ(ISO)+1.)  )
        DO 39 JCD=0,MJCD
        XJ2 = XJ(ISO) + FLOAT(JCD)
        JDGNCD = 2*JCD + 1
        ER4=ER3-BCD*(XJ2*(XJ2+1.)) + EJCD0
        IF (ER4.LT.0.) GOTO 39
C               ! Energy left for orbital motion
        LDGN=0
        IF (ER4.LT.0.) GOTO 39
201     FORMAT (2X,4(I3,X),2F10.2,4I5 ,F7.0)
        JPMIN=IFIX(ABS(XJ1-XJ2) + 0.499)
C       IF (JPMIN.LT.0) JPMIN=JAB-J0
        JPMAX=IFIX(ABS(XJ1+XJ2) + 0.499)
        DO 40 JPRIME=JPMIN,JPMAX

        CALL MINMAX(J0,JPRIME,ITYPE,JMIN,JMAX,ER4,BCD,CADJ,IERR)
        IF (JMIN.LT.0) GOTO 40
        LDGN = LDGN + (JMAX-JMIN+1)
40      CONTINUE
491     RATE1=RATE1 + FLOAT(NDGNCD*LDGN)
C       WRITE (6,201) JAB,JCD,JPMIN,JPMAX,E,ER4,JMIN
C       &  ,JMAX,JPRIME,LDGN,RATE1
C                       !Calculates part contribution to k
39      CONTINUE
49      CONTINUE
58      RATE12 = RATE12 + RATE1
585     CONTINUE
59      RATE(NAB+1,JAB+1)=RATE12 + RATE(NAB+1,JAB+1)
C ***************************************************************************
C       The last statement calculates the relative rate constant for a fixed
C       n(AB) and J(AB). The rotational degeneracies of AB and CD are not
C       explicit in the rate formula since they are (2*JAB+1) and (2*JCD+1)
C ***************************************************************************
C
69      CONTINUE
C       Calculate the probability distribution for different j's assuming
C       distribution proportional to rates.
        SUMJ=0
        MAXJ=MAXJ+1
        DO 72 L1=1,(MNAB+1)
        DO 72 L2=1,MAXJ
72      SUMJ=SUMJ+RATE(L1,L2)
        IF (SUMJ.EQ.0.) GOTO 95
        DO 73 L1=1,(MNAB+1)
        DO 73 L2=1,MAXJ
        PROB(L1,L2)=RATE(L1,L2)/SUMJ
C73     RATE(L1,L2) = RATE(L1,L2) * RFAC
73      RATE(L1,L2) = RATE(L1,L2)
C   OUTPUT SECTION
        GOTO 96
```

```
95      TYPE *,'Energy below threshold'
96      CONTINUE
C       DO 79 L=0,MNAB
C       WRITE (6,102) L,SUMJ
C       WRITE (6,103) (RATE(L+1,LK), LK=1,MAXJ)
C79     CONTINUE
C       WRITE (6,*) E,(PROB(1,L),L=1,26,5)
85      CONTINUE
C
102     FORMAT (/3X,'Rates for n(OH) = ',I3 /' N(E,J) ',F8.0)
        RETURN
        END
C
C
C
        SUBROUTINE OUTPUT(MODE)
        COMMON /OUTP/ RATE(5,100),PROB(5,100),VIB(20)
        COMMON /OUTP2/ E,I,J0,K,SUMJ,MAXJ,ERATE
        IF (MODE.EQ.1) GOTO 200
        WRITE (6,101) E,J0,MAXJ,ERATE
        DO 80 L=0,MNAB
C       WRITE (6,105) L
        WRITE (6,106) (PROB(L+1,LK), LK=1,MAXJ)
80      CONTINUE
        GOTO 99
200     CONTINUE
        WRITE(6,301) VIB(I),E,J0,K, SUMJ,(PROB(1,L),L=1,MAXJ)
301     FORMAT (3X,F5.0,X,F8.2,2(2X,I3),5X, F7.0,12(X,F6.3) )
C101    FORMAT  ( 100('-')///3X,'Total excess energy in the parent ',
C       &  F8.0,5X,' and the J quantum number',I4, '.')
101     FORMAT (1X, F5.1,2I3,1X,E10.4, $)
103     FORMAT ( 20 (/ 5X,5(E10.4,3X)) )
C105    FORMAT (/ 3X,'Distribution for n(CN) =',I3,15X,'N(E,J)',F8.0)
105     FORMAT ( 2X, I2, $)
106     FORMAT ( 8( 3X,12(F7.4,2X) / 10X) )
99      RETURN
        END
C
C
C
        SUBROUTINE MINMAX(J0,J,ITYPE,JMIN,JMAX,E,B,C,IERR)
C  ***********************************************************************
C       This subroutine calculates the maximum and minimum allowed J'
C       quantum numbers allowed with total energy and angular momentum
C       conservation. The potential used is the van der Waal's attractive
C       r**-6 potential plus the rotational repulsion.
C  ***********************************************************************
        LMAX=1000
        IF (ITYPE.EQ.1) GOTO 12
        IF (E) 91,91,10
10      X1 = (ALOG10(0.5*E))*0.6666667
        X2 = C*(10.**X1)
C
        X = ABS(SQRT(1. + 4.*X2))       ! Finding LMAX by solving a quadratic
        X = 0.5*(X-1.)                  ! equation of energy constraint
        LMAX = X
C
12      JMAX=LMAX
        JCD0=J+J0
        IF (JMAX.GT.JCD0) JMAX=JCD0
        IF (J-J0) 21,21,23
21      JMIN = J0-J
        GOTO 25
23      JMIN=J-J0
25      CONTINUE
C
        IF (JMIN.GT.LMAX) JMIN=-100
C       TYPE *,' JMIN',JMIN,'   JMAX',JMAX,'   LMAX',LMAX
        GOTO 99
91      JMAX = JMIN
        IERR = 1
        TYPE *, 'Residual energy is negative'
99      CONTINUE
        RETURN
        END
```